
The Nanoscale Characterization and
Interparticulate Interactions of Pharmaceutical
Materials

Jennifer Hooton BPharm (Hons) MRPharmS

Thesis submitted to the University of Nottingham for the degree of
Doctor of Philosophy, September 2003

“I do not know whether it ought to be so, but certainly silly things do cease to be silly if they are done by sensible people in an impudent way. Wickedness is always wickedness, but folly is not always folly. It depends upon the character of those who handle it.”

Emma, Jane Austin

Table of Contents

Table of Contents	i
-------------------------	---

Table of Figures	viii
------------------------	------

Abstract	xiii
----------------	------

Abbreviations	xvii
---------------------	------

Introduction

Chapter 1	1
-----------------	---

1.1. Crystallization.....	1
---------------------------	---

1.1.1. Need for Control of Particle Size and Distribution	2
---	---

1.1.2. Particle Size Generation.....	3
--------------------------------------	---

1.2. Supercritical Fluids.....	5
--------------------------------	---

1.2.1. Phase Diagrams	5
-----------------------------	---

1.2.2. Supercritical Fluids	5
-----------------------------------	---

1.2.3. SCF Selection	7
----------------------------	---

1.2.4. Particle Formations with Supercritical Fluids	8
--	---

1.2.4.1. Supercritical Fluid used as a solvent.....	8
---	---

1.2.4.2. Gas Saturated Solution.....	9
--------------------------------------	---

1.2.4.3. Supercritical Fluid Used as an Antisolvent.....	9
--	---

1.2.5. Mechanisms of Particle Formation	11
---	----

Table of Contents

1.2.6.	Solution Enhanced Dispersion with Supercritical Fluids	11
1.2.7.	Applications of SEDS™	13
1.3.	Forces Between Particles	15
1.3.1.	Van der Waals Forces	15
1.3.2.	Lifshitz Theory	17
1.3.3.	Capillary Forces	18
1.3.4.	Contact Potential Forces	18
1.3.5.	Coulomb Forces	19
1.3.6.	Specific Forces	19
1.3.7.	Other Important Factors	20
1.3.7.1.	Surface Roughness	20
1.3.7.2.	Surface Energy	20
1.3.7.3.	Mechanical Properties of the Surface	23
1.4.	Adhesion theory	24
1.4.1.	Hertz Theory	24
1.4.2.	JKR Theory	25
1.4.3.	DMT Theory	26
1.4.4.	Tabor Equation	29
1.5.	Methods of Measuring Forces	31
1.5.1.	Surface Force Apparatus	31
1.5.2.	Impaction Methods	32
1.5.3.	Centrifuge Technique	32
1.6.	Scanning Probe Microscopy	33
1.6.1.	Atomic Force Microscopy	34
1.6.2.	Modes of Operation	36
1.6.2.1.	Imaging Modes	36
1.6.2.2.	Force Measurements	39
1.7.	Aims of the Project	39

Materials and Methods

Chapter 2	41
-----------------	----

Table of Contents

2.1	Imaging of Samples	41
2.1.1.	Scanning Electron Microscopy (SEM)	41
2.1.2.	Atomic Force Microscopy (AFM)	41
2.2	Force Measurements and Tip Characterisation	42
2.2.1.	Addition of Particles onto Tips	42
2.2.2.	Force Measurements.....	44
2.2.3.	Control of Humidity	48
2.2.4.	Force Measurement Substrates	50

Characterization and Quantification of Particle

Contact Area

Chapter 3	54
3.1. Introduction	54
3.1.1. Contact Area	54
3.1.2. Pressurised Metered Dose Inhalers	55
3.1.3. Aim	55
3.2. Methods	57
3.2.1. Tip Imaging.....	57
3.2.2. Image Analysis	58
3.2.3. Force Per Unit Area.....	62
3.2.4. Contact Mechanics Calculation of Particle Against Surface ...	62
3.2.5. Work of Adhesion	65
3.2.6. Reproducibility.....	66
3.3. Results	66
3.3.1. Images.....	66
3.3.2. Force Distance Data.....	76
3.3.3. Tip Imaging.....	76
3.3.4. Half Sphere Approximation.....	79
3.3.5. Contact Mechanics Approach.....	79
3.3.6. Work of Adhesion	82
3.3.7. Reproduceability.....	82

3.4. Discussion.....	85
3.4.1. Images.....	85
3.4.2. Force Data.....	86
3.4.3. Tip Imaging Data.....	86
3.4.4. Corrected Data.....	86
3.4.5. Reproducibility.....	87
3.5. Conclusions.....	88

Effect of Humidity and Contact Geometry on Adhesion

Chapter 4	91
4.1. Introduction	91
4.1.1. Dry Powder Inhalers.....	91
4.1.2. Capillary Forces	92
4.1.3. Aim of Work.....	97
4.2. Methods	98
4.2.1. Force Measurements.....	98
4.2.2. Work of Adhesion, Surface Energy and Predicted Force Values	99
4.3. Results	100
4.3.1. Blank Tip Against Compressed Disks.....	100
4.3.2. Particles and Blank Tips Against HOPG.....	102
4.3.3. Particles Against Compressed Disks.....	112
4.3.3.1. Micronised Salbutamol.....	112
4.3.3.2. SEDS™ Salbutamol.....	116
4.3.4. JKR/Actual Forces.....	119
4.3.5. Surface Energy Measurements	120
4.4. Discussion	126
4.4.1. Blank Tips on Compressed Disks.....	126
4.4.2. Particles on the HOPG Surface.....	129
4.4.3. Particle Against Particle Force Measurements.....	133

Table of Contents

4.4.4.	JKR Forces.....	135
4.4.5.	Surface Energy Measurements	136
4.5.	Conclusion	137

Comparison of Polymorphs

Chapter 5	139
5.1. Introduction	139
5.1.1. Polymorphism.....	139
5.1.2. Sulphathiazole.....	140
5.1.3. Formation of Sulphathiazole Polymorphs	140
5.1.4. Aim of Work.....	143
5.2. Methods	143
5.2.1. Formation of Particles.....	143
5.2.2. Acquisition of Force Measurements	143
5.3. Results	145
5.3.1. Images of Polymorphs.....	145
5.3.2. Surface Roughness	147
5.3.3. Force Measurements and Surface Energy Calculations.....	155
5.3.3.1. Polymorph I-Met.....	155
5.3.3.2. Polymorph I-Ace	161
5.3.3.3. Polymorph III.....	169
5.3.3.4. Polymorph IV	174
5.3.4. Change of Maximum Contact Force and Rate of Tip-Sample Approach.....	179
5.3.4.1. Polymorph I-Ace	180
5.4. Discussion	183
5.4.1. Polymorph I-Met	183
5.4.2. Polymorph I-Ace.....	185
5.4.3. Polymorph III	187
5.4.4. Polymorph IV	189
5.5. Conclusions.....	190

Force Measurements Using Biological Materials

Chapter 6	192
6.1. Introduction	192
6.1.1. Supercritical Processing of Biological Material	192
6.1.2. Insulin	193
6.1.3. Insulin Administration	193
6.1.4. Aim of this Work	195
6.2. Methods	195
6.3. Results	196
6.3.1. Images.....	196
6.3.2. Force Measurements.....	200
6.3.3. Work of Adhesion and Surface Energy Measurements.....	209
6.4. Discussion	212
6.4.1. Images.....	212
6.4.2. Force Measurements.....	213
6.4.3. Work of Adhesion and Surface Energy Measurements	215
6.5. Conclusions.....	215

The Co-formulation of a Drug Using the SEDS™

Technique

Chapter 7	217
7.1. Introduction	217
7.1.1. Co-Formulation.....	218
7.1.2. Pregabalin	218
7.1.3. X-ray Photoelectron Spectrometry (XPS).....	220
7.1.4. Time of Flight Secondary Ion Mass spectrometry (ToF-SIMS)	220
7.1.5. Aims	222
7.2. Methods	222

Table of Contents

7.2.1. Samples	222
7.2.2. XPS	222
7.2.3. SIMS.....	223
7.3. Results	223
7.3.1. Imaging.....	223
7.3.2. XPS Data.....	227
7.3.3. SIMS Data	232
7.4. Discussion	239
7.4.1. Images.....	239
7.4.2. XPS	239
7.4.3. ToF-SIMS Data	240
7.5. Conclusions.....	242
Final Conclusions	
Chapter 8	243
References.....	246
Acknowledgements	258
Publications.....	259

Table of Figures

FIGURE 1.1. COMPARISON OF CONVENTIONAL METHODS OF PARTICLE PRODUCTION TO SUPERCRITICAL FLUID METHODS.....	4
FIGURE 1.2. PHASE DIAGRAM OF A PURE SUBSTANCE.	6
FIGURE 1.3. APPARATUS USED FOR THE FORMATION OF PARTICLES BY THE SEDS™ TECHNIQUE.	12
FIGURE 1.4. NOZZLES USED IN THE SEDS™ TECHNIQUE.....	14
FIGURE 1.5. EFFECT OF SURFACE ROUGHNESS ON PARTICLE ADHESION.....	21
FIGURE 1.6. THE PHENOMENA OF SURFACE TENSION.....	22
FIGURE 1.7. DIAGRAM SHOWING THE REGIONS OF COMPRESSION (C) AND TENSION (T) ACCORDING TO THE JKR THEORY.	27
FIGURE 1.8. DIAGRAM SHOWING THE REGIONS OF COMPRESSION (C) AND TENSION (T) ACCORDING TO THE DMT THEORY.	28
FIGURE 1.9. THE DIMENSIONS OF THE NECK FORMED WHEN A PARTICLE COMES INTO CONTACT WITH A SURFACE.....	30
FIGURE 1.10. SCHEMATIC DIAGRAM OF AN AFM	35
FIGURE 1.11. AFM IMAGING MODES.....	37
FIGURE 1.12. AFM ARTEFACT OF SWEEPING.	38
FIGURE 2.1. THE ADDITION OF PARTICLES ONTO TIPS.....	43
FIGURE 2.2. TIP WITH PARTICLE ADDED ONTO END.	45
FIGURE 2.3. SEM IMAGES OF BEFORE AND AFTER FLUE ADDED ONTO PARTICLE..	46
FIGURE 2.4. AFM SET-UP IN LIQUID.....	47
FIGURE 2.5. HUMIDITY CONTROL EQUIPMENT SCHEMATIC.	49
FIGURE 2.6. A FORCE MEASUREMENT CURVE.....	51
FIGURE 3.1. CHEMICAL STRUCTURE OF SALBUTAMOL.	56
FIGURE 3.2. TIP IMAGING GRID.....	59
FIGURE 3.3. THE AFM ARTEFACT OF TIP IMAGING.	60
FIGURE 3.4. TIP IMAGING OF PARTICLE ON THE END OF AN AFM CANTILEVER.....	61

Table of Figures

FIGURE 3.5. SCHEMATIC REPRESENTATION OF THE CALCULATIONS UNDERTAKEN TO CALCULATE CONTACT AREA BY CONSIDERATION OF MECHANICAL PROPERTIES AND WORK OF ADHESION.	63
FIGURE 3.6. SEM IMAGES OF MICRONISED SALBUTAMOL.	67
FIGURE 3.7. SEM IMAGES OF SEDS™ SALBUTAMOL.	68
FIGURE 3.8. AFM IMAGES OF MICRONISED SALBUTAMOL.....	69
FIGURE 3.9. CROSS SECTION OF MICRONISED SALBUTAMOL SHOWING RIDGES IN A PARTICLE.	71
FIGURE 3.10. AFM HEIGHT AND PHASE IMAGES OF SEDS™ PROCESSED SALBUTAMOL.	72
FIGURE 3.11. CROSS-SECTION OF SEDS™ PARTICLE IN FIGURE 3.10 (B).	73
FIGURE 3.12. IMAGE OF HOPG SUBSTRATE.	74
FIGURE 3.13. SEM IMAGES OF TIPS WITH (A) MICRONISED AND (B) SEDS™ SALBUTAMOL ADDED ONTO TIPS.	75
FIGURE 3.14. FREQUENCY DISTRIBUTIONS FOR SALBUTAMOL PARTICLES AND CONTROL TIPS.	77
FIGURE 3.15. TIP IMAGES OF CONTACTING ASPERITIES.	78
FIGURE 3.16. DATA CORRECTED FOR HALF SPHERE AREA.	81
FIGURE 3.17. FORCE CORRECTED FOR AREA CALCULATED USING THE CONTACT MECHANICS APPROACH.	83
FIGURE 3.18. WORK OF ADHESION CALCULATED FOR MICRONISED AND SEDS™ SALBUTAMOL.	84
FIGURE 3.19. SOURCES OF ERROR IN DETERMINATION OF RADIUS OF ASPERITIES.	89
FIGURE 4.1. FORMATION OF A CAPILLARY BRIDGE BETWEEN A PARTICLE AND SUBSTRATE.	93
FIGURE 4.2. FORCE MEASUREMENTS USING BLANK AFM TIPS AGAINST COMPRESSED DISKS OF MATERIAL.	101
FIGURE 4.3. SURFACE ROUGHNESS MEASUREMENTS OF SEDS™ AND MICRONISED SALBUTAMOL.	103
FIGURE 4.4. IMAGE AND FORCE DATA FOR MICRONISED SALBUTAMOL TIP A.	104
FIGURE 4.5. IMAGE AND FORCE DATA FOR MICRONISED SALBUTAMOL TIP B.	105
FIGURE 4.6. IMAGE AND FORCE DATA FOR MICRONISED SALBUTAMOL TIP C.	106
FIGURE 4.7. IMAGE AND FORCE DATA FOR SEDS™ SALBUTAMOL TIP D.	108

Table of Figures

FIGURE 4.8. IMAGE AND FORCE DATA FOR SEDS™ SALBUTAMOL TIP E.	109
FIGURE 4.9. IMAGE AND FORCE DATA FOR SEDS™ SALBUTAMOL TIP F.....	110
FIGURE 4.10. ADHESION FORCE MEASUREMENTS OF PLASMA ETCHED AND GLUE ADDED AFM TIPS AGAINST HOPG AT 22% RH.....	111
FIGURE 4.11. IMAGE AND FORCE DATA FOR MICRONISED SALBUTAMOL TIP G. ...	113
FIGURE 4.12. IMAGE AND FORCE DATA OF MICRONISED SALBUTAMOL TIP H.	114
FIGURE 4.13. IMAGE AND FORCE DATA OF MICRONISED SALBUTAMOL TIP I.....	115
FIGURE 4.14. IMAGE AND FORCE DATA FOR SEDS™ PARTICLE TIP J.	117
FIGURE 4.15. IMAGE AND FORCE DATA FOR SEDS™ TIP K.	118
FIGURE 4.16. IMAGE AND FORCE DATA FOR SEDS™ TIP L.....	119
FIGURE 4.17. WORK OF ADHESION AND SURFACE ENERGY OF MICRONISED AND SEDS™ SALBUTAMOL PARTICLES.	125
FIGURE 4.18. THE THREE SCENARIOS OF ADHESION AND HOW THEY CORRESPOND TO BEHAVIOUR.	130
FIGURE 5.1. CHEMICAL STRUCTURE OF SULPHATHIAZOLE.	141
FIGURE 5.2. POSITION OF POINT MEASUREMENTS FOR PARTICLE-PARTICLE MEASUREMENTS.	144
FIGURE 5.3. SEM IMAGES OF POLYMORPH I-MET.	146
FIGURE 5.4. AFM IMAGES OF POLYMORPH I-MET.....	148
FIGURE 5.5. SEM IMAGES OF POLYMORPH I-ACE.....	149
FIGURE 5.6. AFM IMAGES OF POLYMORPH I-ACE.	150
FIGURE 5.7. SEM IMAGES OF POLYMORPH III.....	151
FIGURE 5.8. AFM IMAGES OF POLYMORPH III.....	152
FIGURE 5.9. SEM IMAGES OF POLYMORPH IV.	153
FIGURE 5.10. AFM IMAGES OF POLYMORPH IV.	154
FIGURE 5.11. ROUGHNESS OF POLYMORPHS.	156
FIGURE 5.12. IMAGE AND FORCE DATA FOR POLYMORPH I-MET TIP A.	157
FIGURE 5.13. IMAGE AND FORCE DATA FOR POLYMORPH I-MET TIP B.....	159
FIGURE 5.14. IMAGE AND FORCE DATA OF POLYMORPH I-MET TIP C.	160
FIGURE 5.15. WORK OF ADHESION AND SURFACE ENERGY MEASUREMENTS OF POLYMORPH PARTICLES.	162
FIGURE 5.16. IMAGE AND FORCE DATA FOR POLYMORPH I-ACE TIP D.	163
FIGURE 5.17. IMAGE AND FORCE DATA OF POLYMORPH I-ACE TIP E.	165
FIGURE 5.18. IMAGE AND FORCE DATA OF POLYMORPH I-ACE TIP F.	167

Table of Figures

FIGURE 5.19. TYPICAL FORCE CURVE SEEN FOR POLYMORPH I-ACE.	168
FIGURE 5.20. IMAGE AND FORCE DATA OF POLYMORPH III TIP G.....	170
FIGURE 5.21. IMAGE AND FORCE DATA OF POLYMORPH III TIP H.	172
FIGURE 5.22. IMAGE AND FORCE DATA FOR POLYMORPH III TIP I.....	173
FIGURE 5.23. IMAGE AND FORCE DATA FOR POLYMORPH IV TIP J.....	175
FIGURE 5.24. IMAGE AND FORCE MEASUREMENTS OF POLYMORPH IV TIP K.....	177
FIGURE 5.25. IMAGE AND FORCE DATA FOR POLYMORPH IV TIP L.....	178
FIGURE 5.26. EFFECT OF CHANGE IN PRESS ON FORCE ON POLYMORPH I-ACE.	181
FIGURE 5.27. EFFECT OF CHANGE IN MEASUREMENT RATE ON POLYMORPH I-ACE.	182
FIGURE 6.1. STRUCTURE OF INSULIN.....	194
FIGURE 6.2. SEM IMAGES OF UNPROCESSED INSULIN.....	197
FIGURE 6.3. SEM IMAGES OF SEDS TM INSULIN.	198
FIGURE 6.4. AFM IMAGES OF UNPROCESSED INSULIN.....	199
FIGURE 6.5. AFM IMAGES OF SEDS TM INSULIN.	201
FIGURE 6.6. IMAGE AND FORCE DATA OF UNPROCESSED INSULIN TIP A.....	202
FIGURE 6.7. IMAGE AND FORCE DATA FOR UNPROCESSED INSULIN TIP B.....	203
FIGURE 6.8. IMAGE AND FORCE DATA FOR UNPROCESSED INSULIN TIP C.	205
FIGURE 6.9. IMAGE AND FORCE DATA FOR SEDS TM PROCESSED INSULIN TIP D.	207
FIGURE 6.10. IMAGE AND FORCE DATA FOR SEDS TM PROCESSED INSULIN TIP E.	208
FIGURE 6.11. IMAGE AND FORCE DATA FOR SEDS TM PROCESSED INSULIN TIP F.	210
FIGURE 6.12. WORK OF ADHESION AND SURFACE ENERGY OF UNPROCESSED AND SEDS TM PROCESSED INSULIN.	211
FIGURE 7.1. CHEMICAL STRUCTURES OF PREGABALIN AND DPPC.	219
FIGURE 7.2. SEM IMAGES OF 100% SEDS TM PREGABALIN.	224
FIGURE 7.3. SEM IMAGES OF 50:50 LIPID:PREGABALIN SEDS TM PROCESSED MATERIAL.....	225
FIGURE 7.4. AFM IMAGES OF 100% SEDS TM PREGABALIN.....	226
FIGURE 7.5. AFM IMAGES OF 50:50 LIPID PREGABALIN.....	228
FIGURE 7.6. OVERVIEW SPECTRA OF THE THREE SAMPLES.....	229
FIGURE 7.7. CARBON SPECTRA OF THE THREE SAMPLES.....	230
FIGURE 7.8. OXYGEN SPECTRA OF THE THREE SAMPLES.....	231

Table of Figures

FIGURE 7.9. NITROGEN SPECTRA OF THE THREE SAMPLES.	233
FIGURE 7.10. PHOSPHOROUS SPECTRA OF THE LIPID AND 50:50 LIPID:PREGABALIN SAMPLES.	234
FIGURE 7.11. SIMS SPECTRA OF THE LIPID SAMPLE.	235
FIGURE 7.12. TOF-SIMS SPECTRA OF SEDS™ PREGABALIN.	237
FIGURE 7.13. TOF-SIMS SPECTRA OF 50:50 LIPID:PREGABALIN.	238

Abstract

The aim of this project is to compare pharmaceutical particles made using a Nektar supercritical fluid technology technique called solution enhanced dispersion by supercritical fluids (SEDSTM) to those made using more traditional techniques. This involves a comparison of not only the surface properties of both types of particles, but also the interparticulate interactions. The majority of the work has involved the use of the atomic force microscope (AFM) as both a tool for imaging and for the acquisition of localized force measurements.

The first experimental chapter of this work describes a method developed in order to image the contacting asperities of a particle. The AFM has the potential to provide useful information regarding single particle interactions to complement data generated from bulk techniques. In this chapter, the AFM artefact of tip imaging was used to produce 3D images of the asperities of particles of micronised and SEDSTM salbutamol sulphate, an anti-asthma drug, contacting a model surface of highly orientated pyrolytic graphite (HOPG). These data were recorded in a model propellant environment, used in order to simulate the environment that would be found in pressurised metered dose inhalers, such as those used by asthmatics. From the images generated the contacting area was estimated to be $1.1 \times 10^{-3} \mu\text{m}^2$ for the micronised material, and 1.4×10^{-3} for the SEDSTM material. The work of

adhesion for both of the materials was also calculated, and the values of 19.0 mJm^{-2} and 4.0 mJm^{-2} were obtained for the micronised and SEDSTM samples respectively. This supported available data that indicated the SEDS material had a lower surface energy than the micronised drug, and that it is possible to make comparisons between different modified AFM probes.

The second chapter develops this work so that it can be applied to an air environment, which is applicable to more pharmaceutical systems. Here, force measurements were again performed using AFM, with the same drug samples studied in the first chapter, except a controlled relative humidity (RH) environment was used, so that the variation in adhesion with increasing RH could be studied. Two types of measurement were undertaken. The first involved the use of blank AFM tips on compressed disks of drug material, and the second involved the use of drug particles mounted onto AFM tips on both HOPG and compressed disks of drug. With the blank AFM tip and particle modified AFM tip on HOPG work it was observed that the SEDSTM materials showed a peak in adhesion force at 22% RH while the micronised salbutamol showed a peak at 44% RH. From this, a three-scenario model of linking morphology of contact to adhesion was developed to explain the observed peaks in adhesion. In addition, the surface energies of each of the two samples were calculated using the force measurements acquired against HOPG and compressed disks of material and compared. The micronised material was found to have a higher surface energy than the SEDSTM material (10.8 mJm^{-2} cf 5 mJm^{-2}) when data acquired against HOPG was used. However, when data acquired using the compressed disks of drug were used, the SEDSTM had a higher surface energy than the micronised (29.9 mJm^{-2} cf 22.6 mJm^{-2}). This higher value was attributed to different surface roughness effects found with the compressed disks.

The third chapter uses the techniques and models developed in the previous chapters to examine the effect of polymorphism on surface energy, structure and particulate interactions. Three polymorphs of the drug sulphathiazole (forms I, II and IV) were formed using the SEDSTM technique, one of which (form I) was formed using two different solvents: methanol and acetone.

Force measurements were performed using the AFM at controlled humidity using particles of each of the polymorphs mounted onto AFM tips against substrates of HOPG and the polymorph under analysis. This data was then related to the model developed in the previous chapter, and calculations were undertaken to assess the different surface energies of each of the four samples. For some of the samples it was observed that peaks were again occurring in the data, at 22% RH for polymorphs I-methanol and III, and 44% for polymorph IV. No peak was seen for polymorph I-acetone. These peaks were then related to the surface energy calculated for each of the polymorphs, as polymorphs I-methanol and III were found to have lower surface energy (0.99 mJm^{-2} and 1.17 mJm^{-2} respectively) than polymorphs IV and I-acetone (20.33 mJm^{-2} and 309 mJm^{-2}).

The fourth chapter examines the application of AFM to an industrial problem. When using the SEDSTM process to manufacture insulin, it was observed that the SEDSTM material had poorer flow properties than that of the unprocessed material. Using the AFM as both an imaging and force measurement tool, this chapter explores the application of imaging and the adhesion models and surface energy calculations previously developed to understand this problem. The AFM images showed the presence of highly aggregated particles of SEDSTM insulin, compared to the unprocessed insulin that appeared to be more crystalline. When force measurements were performed against both HOPG and particles of the material under analysis, none of the unprocessed, and only one of the SEDSTM particle tips prepared displayed the peak behaviour seen with previous measurements, and instead displayed a continual increase in adhesion force with humidity. In addition, when the surface energy was calculated, the SEDSTM material was found to be higher than the unprocessed insulin (77.5 mJm^{-2} cf 2.4 mJm^{-2}). The increase in adhesion force was related to the particles agglomerating together, due to the presence of a higher surface energy and high amorphous content of the particles.

The final experimental chapter uses techniques that compliment AFM analysis to examine another industrial problem. The SEDSTM process can be

used to co-formulate drugs with other materials such as polymers. In this chapter, the drug pregabalin has been co-formulated with lipid in order to produce a coating around the drug to mask taste. The use of AFM as an imaging tool, and the additional techniques of X-ray photoelectron spectrometry (XPS) and time-of-flight secondary ion mass spectroscopy (ToF-SIMS) have been used to generate an understanding of surface structure and chemistry of this heterogeneous system. The AFM images showed no areas of surface heterogeneous behaviour, although the largest scan size was only 5 μm x 5 μm . However both the XPS and ToF-SIMS spectra, which samples far larger areas (up to 75 μm x 75 μm) showed the presence of lipid and drug molecules. It was concluded that the lipid was not forming a uniform layer around the drug molecule, but was instead forming large patches that were beyond the resolution of the AFM.

This work aims therefore to provide a fundamental study of the application of AFM to real pharmaceutical systems. In particular models are developed which allow not only ranking of particle interactions but the quantification of factors such as surface energy and work of adhesion. Finally the significance of the morphology of the inter-particulate contact has been explored at the nanoscale.

Abbreviations

AFM	- Atomic force microscope
ASES	- Aerosol solvent extraction system
CO ₂	- Carbon dioxide
DMT	- Derjaguin-Muller-Toporov theory
DPI	- Dry powder inhalers
DPPC	- DL- α -Phosphotidylcholine Dipalmitoyl
Eq	- Equation
GAS	- Gaseous anti-solvent
GABA	- γ aminobutyric acid
HOPG	- Highly orientated pyrolytic graphite
JKR	- Johnson-Kendall-Roberts theory
PCA	- Precipitation with a compressed fluid antisolvent
PGSS	- Particles from gas saturated solutions
pMDI	- Pressurised metered dose inhaler
RESS	- Rapid expansion of the supercritical fluid
SAS	- Supercritical anti-solvent
SEM	- Scanning electron microscope
SEDS TM	- Solution enhanced dispersion by supercritical fluids
SCF	- Supercritical fluid
SFA	- Surface force apparatus
SFCO ₂	- Supercritical carbon dioxide
SPM	- Scanning probe microscopy
STM	- Scanning tunnelling microscope
ToF-SIMS	- Secondary ion mass spectrometry
UV	- Ultra-violet
XPS	- X-ray photoelectron spectroscopy

Symbols

a_0	- Contact radius
a_L	- Area of the liquid
a_{mol}	- Molecular length
a_s	- Separation radius
A	- Contact area
A_H	- Hamaker constant
BE	- Binding energy
C	- Region of compression
C_H	- Hamaker interaction constant
CV	- Coefficient of variation
D	- Distance between particle and surface
D	- Distance of deflection of a AFM cantilever from its rest position
d_m	- Distance between the top of the meniscus to the vase of the particle
E	- Young's modulus
E^*	- Reduced Young's modulus
e	- Minimum height of water required for spreading
F_{on}	- Press on force
F_{ad}	- Force of adhesion
$F_{c,1}$	- Force due to capillary neck circumference surface tension
$F_{c,2}$	- Force due to liquid pressure in capillary meniscus
F_{det}	- Force of detachment
F_{disj}	- Disjoining pressure
G	- Gibb's free energy
Hz	- Hertz
h	- Height of neck formed between particle and surface

$h\nu$	- X-ray energy
l	- Distance between the centres of two charges
k	- Spring constant of and AFM cantilever
KE	- Kinetic energy
kHz	- Kilo-hertz
kV	- Kilo-volts
M	- Meters
M_p	- Mass of a particle
mA	- Milliamps
ml	- Millilitres
mN	- Milli-newtons
N	- Newton
$N(E)$	- Kinetic energy distribution
nm	- Nano-meters
nN	- Nano-newton
P	- Laplace pressure
P_{cap}	- Capillary pressure
P_c	- Critical pressure
q	- Particle charge upon detachment from a surface
Q	- Charge of a particle
R	- Radius of particle
R_C	- Particle contact radius due to surface and particle deformation
R_g	- Gas constant
RH	- Relative humidity
r	- Distance from the axis of rotation in a centrifuge
r_1	- Concave meniscus radius
r_2	- Convex meniscus radius
r_K	- Kelvin radius
R_q	- Root-mean-square roughness
S	- Spreading coefficient
SD	- Standard deviation
T_p	- Temperature
T	- Region of Tension

T_c	- Critical temperature
V	- Molar volume
V_s	- Velocity
W	- Watts
W_l	- Interaction energy
X	- Radius from centre to top of meniscus concave
z_0	- Equilibrium distance of separation between atoms in contact
ϕ	- Angle between centre of gravity of the particle and outer surface of the meniscus
ϕ_0	- Tabor equation defining value
ϕ_w	- Work function of a material
γ	- Surface energy
γ_{12}	- Interfacial energy between two surfaces
γ_{ad}	- Work of adhesion
γ_L	- Surface tension of a liquid
μ_1	- Chemical potential of liquid in gap
μm	- Micro-meters
ν	- Poisson's ratio
ν_0	- Ratio of predicted JKR force divided by actual force obtained
π	- Pi
ρ	- Number density of interacting surface
ω	- Angular velocity

Chapter 1

Introduction

1.1. Crystallization

Crystallization is a widely used process in the pharmaceutical industry as a means of producing drugs and excipients. The ability to form highly crystalline materials, lacking in defects such as *amorphous* regions (areas which lack a regular lattice arrangement), *pseudopolymorphs* (crystals formed when solvent is incorporated into the lattice), or changes in the *crystal habit* (the external shape of a crystal) is a highly desired characteristic (Brittain, 1999; Haleblan, 1975). This is because the presence of such defects may cause changes in the formulation, efficacy and stability of medicines – something that is undesirable for regulatory and safety reasons (Yu *et al.*, 2003). It is well known that such crystal properties are influenced by the crystallisation conditions employed, and hence the ability to control the conditions is important to ensure the same product is reliably achieved.

Unfortunately, the process of conventional crystallization has many limitations, which make the goal of reliable crystal production difficult to achieve. The formation of crystals is determined by a large number of factors, including solubility, supersaturation and temperature (Rodriguez-

Hornedo and Murphy, 1999, Haleblan, 1975). Small changes in these factors caused by poor process control will lead to changes in the crystals produced, as was seen with the HIV drug Indinavir where capsule production was halted due to the sudden formation of new crystalline structures (Rodriguez-Hornedo and Murphy, 1999).

There are also a number of other disadvantages to the traditional crystallization process. Crystallization frequently requires a considerable amount of time, particularly if recrystallization is undertaken to purify a drug (Carstensen, 1993), which when combined with the cost of solvent and recovery, may make the process uneconomical. In addition, the crystals produced may still have residual solvent traces, which is undesirable from a GMP point of view (Shekunov, 2000). Finally, few crystals produced will possess a usable particle size and distribution, which is required for many processes.

1.1.1. Need for Control of Particle Size and Distribution

Many operations in the pharmaceutical industry require particles with controlled shape, size and size distribution. Some of the many examples of such operations include –

- (a) Drug delivery, for example in inhalation products, where delivery to the lung requires a size range of 1 – 5 μ m (Schulz, 1998).
- (b) Dissolution rate of drugs, where changes in the size of particles may affect the rate of dissolution, which will alter drug absorption and hence therapeutic efficacy (Florence and Attwood, 1988).
- (c) Mixing, as differences in particle size are one of the most important factors in the segregation of mixes into their individual components (Rhodes, 1999). This is of particular importance in the preparation of micro-dose drugs (for example digoxin), where good distribution of drugs and excipients is required. By controlling the size and

distribution of particles, therapeutic effectiveness can be achieved with low risk of toxicity.

- (d) Flow properties, for example small sized particles of a regular shape will promote uniformity in dosage forms, as this will increase the number of particles and reduce the variation in powder flow. This is important in processes such as filling tablet dies where uniform drug content is important (Aulton, 1988).

The lack of particle control during production means that further processing may be required, such as milling in order to obtain the desired particle size characteristics (Lachman *et al.*, 1986).

1.1.2. Particle Size Generation

There are many types of mill available for particle size reduction, for example hammer mills, ball mills and fluid energy mills. The method selected depends upon the type of starting material and the product required (Lachman *et al.*, 1986; Aulton, 1988). However, the process of size reduction can create problems in that it will frequently alter the crystallinity of a surface (Buckton, 1995; Buckton *et al.*, 1988). The product may also become charged, cohesive and of a coarse morphology (Winters, 1996).

The process of manufacturing drug particles is shown schematically in figure 1.1 (a). It can be seen that the process consists of many stages and, as discussed above, there are many difficulties associated with each process. If this entire process of manufacturing could be condensed into a single step, where the crystal properties can be controlled and modified simultaneously with the particle properties (as seen in figure 1.1 (b)), this would potentially confer many advantages to the pharmaceutical industry. The use of supercritical fluids may provide a means of achieving this.

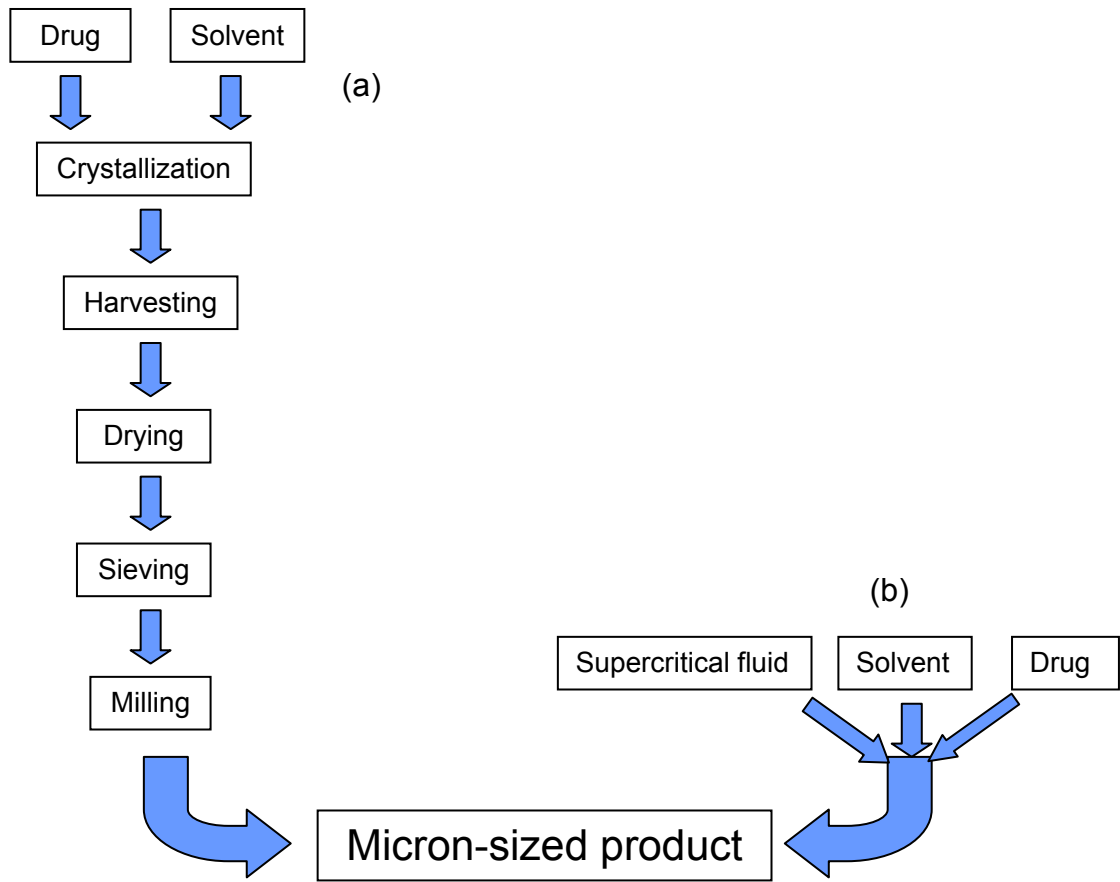


Figure 1.1. Comparison of conventional methods of particle production to supercritical fluid methods. The multi-step process in (a) is both expensive and time consuming, so the ability to use a one step processes as seen in (b) would be highly advantageous.

1.2. Supercritical Fluids

1.2.1. Phase Diagrams

In order to understand the properties of supercritical fluids, it is necessary to understand the conditions of temperature and pressure that are required by a substance to maintain a thermodynamically stable state. To illustrate such conditions, a typical example of a phase diagram of a pure substance is shown in figure 1.2 (Atkins,1996).

The figure shows that each of the three states of solid, liquid and gas is encased by a phase boundary, which shows the temperature and pressure at which two phases can exist in equilibrium. All three phases exist in equilibrium at the triple point. If the liquid-gas curve is followed, it is seen that with an increase in temperature and pressure the density of the liquid decreases while that of the gas increases. At the end of this curve the critical point is found. Beyond this the distinction between the liquid and the gas no longer exists and the substance is now described as a supercritical fluid (SCF) (Clifford, 1998). The critical point co-ordinates are described by the critical temperature (T_c) and critical pressure (P_c), which vary for different substances (Clifford, 1998).

1.2.2. Supercritical Fluids

A SCF is thus defined as a substance that is at a pressure and temperature greater than its critical point (Subramaniam *et al.*, 1997). Above the critical point the SCF demonstrates many useful features. SCFs possess appreciable solvation power due to density values which can be almost liquid-like (Subra and Jestin, 1999). Also, the viscosity of the solutes in SCFs is lower than is found in liquids, which, when combined with the higher diffusivity that SCFs also exhibit allows facilitation of mass transfer (York, 1999). Finally the SCFs are highly compressible, particularly for the 1.0 – 1.2 T_p/T_c range, where T_p is the temperature (Subra and Jestin, 1999).

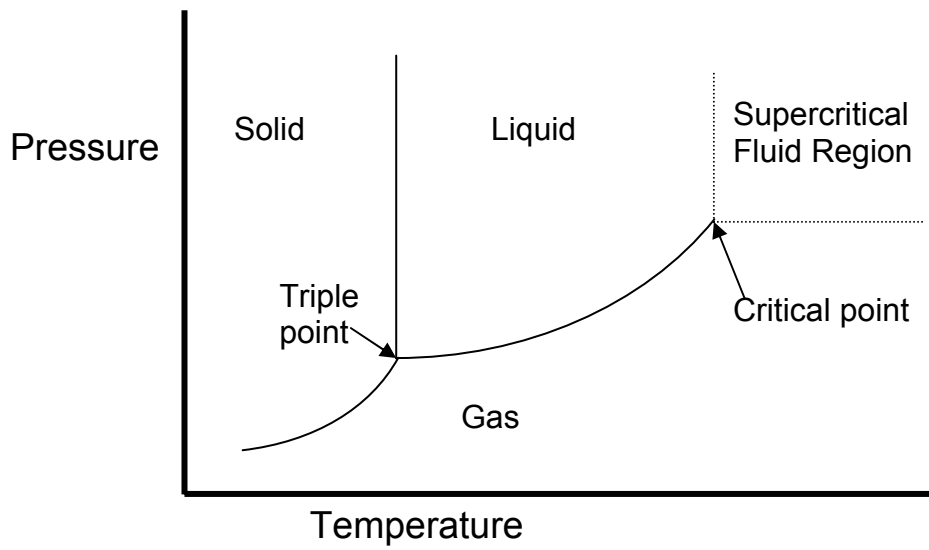


Figure 1.2. Phase diagram of a pure substance. The three phases exist in equilibrium at the triple point. The critical point is located at the end of the phase boundary between the liquid and gas phase, and once this is passed the supercritical region is reached.

These properties have made SCFs a feasible option for the production of pharmaceutical materials both as a solvent and as an anti-solvent. The ability to control their density (and thus the solvation power) by small changes in temperature and/or pressure conditions allows control over the particle formation process at the molecular scale to be exercised (Subramaniam *et al.*, 1997; York, 1999). This means it is possible to control particle size, morphology and crystallinity, consequently providing a means to a one step operation that produces particles free from organic solvent, whilst also using reduced amounts of process solvent. It is also suitable for a wide variety of compounds (Jarzebski *et al.*, 1995; Reverchon, 1999) and has the potential for being GMP compliant (York 1999).

1.2.3. SCF Selection

Although in theory any substance can form a SCF, carbon dioxide (CO₂) is the most widely used for pharmaceutical applications due to the numerous useful properties it possess (Kordikowski *et al.*, 1999; Tom *et al.*, 1991; Tai *et al.*, 1998). It is cheap, leaves no solvent residue, recyclable, generally regarded as safe, non-flammable, non-toxic, environmentally acceptable, has a low critical temperature (31.1°C), has chemical stability and is attractive for heat sensitive materials (Larson *et al.*, 1986; Subra and Jestin, 1999; Clifford, 1998). However, the level of solubility of a solute in a solvent determines the usefulness of a SCF. This is the main disadvantage of CO₂ in that it is a non-polar solvent (Subramaniam *et al.*, 1997), hence compounds that contain polar groups (for example hydroxyl groups) have reduced solubility in the SCF (Phillips *et al.*, 1993).

The solubility properties of a SCF can be altered by the addition of a co-solvent (known as a modifier or entrainer) to the SCF (Dobbs *et al.*, 1986; Dobbs *et al.*, 1987; Alsten *et al.*, 1993). Modifiers (for example methanol) are frequently added to CO₂ in small quantities (5% to 10%) (Clifford, 1998). The addition of a modifier will alter the T_c and P_c of a SCF slightly, but the gains that can be obtained in solvent power can easily offset this loss.

1.2.4. Particle Formations with Supercritical Fluids

The ability of SCFs to facilitate the formation of particles has been known since the 19th Century when Hannay and Hogarth (1879) observed that by reducing the pressure of SCF ethanol, potassium iodide could be precipitated as a “snow” in gas, or as a “frost” on glass. Since then, SCFs have been used in a variety of industrial process including decaffeination of coffee, extraction of edible oils (for example vegetable oil) and chemotherapeutic agent extraction processes (Mchugh *et al.*, 1994). SCFs have also found many uses in the pharmaceutical industry, for example in the precipitation of polymeric material (Randolph *et al.*, 1993), proteins (Yeo *et al.*, 1993) and drug compounds (Kordikowski, 1999; Larson and King, 1986). SCFs can be utilised in one of three ways to form particles – as a solvent, as a gas saturated solution or an anti-solvent for the solute.

1.2.4.1. **Supercritical Fluid used as a solvent**

When the SCF is used as a solvent, the solute is added to the SCF to form a solution. This solution is then passed into a precipitator through a nozzle. This process allows rapid expansion of the SCF, creating a concurrent decrease in its density and hence solvation power. This creates an increase in the level of solute supersaturation, leading to nucleation and particle formation (Phillips *et al.*, 1993). This process is known as rapid expansion of the supercritical fluid (RESS) (Matson *et al.*, 1987).

RESS's main advantage is that it produces large, rapid and uniform supersaturation and can yield small size particles of controlled distribution that are free from traces of organic solvent (Subra and Jestin, 1999). However problems with aggregation and unpredictable morphology have been observed which are dependent on the solute and its concentration (Matson *et al.*, 1987; Tom *et al.*, 1991).

In the pharmaceutical industry RESS has not been favoured due to the lack of solubility of solute in the fluid which is the main limitation of the process. The choice of solvent is limited to those of mild critical properties (for example CO₂) (Subra and Jestin, 1999) because the high temperatures that would be required for other solvents could destroy the labile pharmaceutical compounds. Despite this, RESS has been used successfully for steroid (Larson and King, 1986) and polymer (Matson *et al.*, 1987; Tom *et al.*, 1991) processing.

1.2.4.2. Gas Saturated Solution

The process of producing particles from gas saturated solutions (PGSS) involves dissolving a compressible gas into the melted substance under pressure to create a liquid phase. This is then processed by expansion to create supersaturation and particle formation. PGSS has advantages over RESS: it requires lower levels of CO₂, solubility in SF₆CO₂ is not required, and over SCF use as an antisolvent in that no organic solvent is required. However it has the disadvantage that high temperatures are required, although it has been used to successfully process nifedipine (Sencar-Bozic *et al.*, 1997).

1.2.4.3. Supercritical Fluid Used as an Antisolvent

In this process, the solute is first dissolved in an organic solvent, which is then added to a SCF. As the organic solvent will have a high solubility in the SCF (unlike the solute which will not), the solvent density will reduce, leading to an increase in the solute supersaturation level, which will create nucleation and crystal growth. This approach to particle formation is the most commonly used for pharmaceuticals and has been modified in a number of ways, described below.

The *gaseous anti solvent* (GAS) process involves spraying a solution into a vessel containing SF₆CO₂ (Subramaniam *et al.*, 1997). Although it has been

used to make polymers (Randolph *et al.*, 1993), it has the disadvantages of being a batch process and that it can be difficult to control the morphologies of particles (Tai *et al.*, 1998).

Precipitation with a compressed fluid antisolvent (PCA) is similar to the GAS process, although in this method the antisolvent may be in either a subcritical or supercritical phase. This technique has also been applied to the production of polymers (Dixon *et al.*, 1993).

The *supercritical anti solvent* (SAS) process involves the continual co-current flows of liquid and SCF phase continuum. This then expands in the precipitator, as opposed to GAS where the SCF is added to the solution that already exists in the vessel (Yeo *et al.*, 1993; Reverchon *et al.*, 2001). SAS has been used in the production of proteins, but processing caused some conformational changes in the product, although this did not affect the final biological efficacy (Yeo *et al.*, 1993; Winters *et al.*, 1996).

The *aerosol solvent extraction system* (ASES) is similar to SAS. Here a solution of the solute in an organic solvent is sprayed through a nozzle into the SCF stream for a fixed amount of time. This has been used to produce polymers however agglomeration phenomena and mixed particle morphologies were observed (Bleich *et al.*, 1993).

Although all the processes mentioned above have been successfully used to make particles, they all have the disadvantage of requiring long drying times (2 to 3 hours in some cases) (Winters *et al.*, 1996; Bleich *et al.*, 1993), as well as having problems with aggregation of particles. This is due to low rates of mass transfer, which can be explained by considering the mechanisms of nucleation.

1.2.5. Mechanisms of Particle Formation

Formation of crystals using antisolvents relies upon two processes. The first is the diffusion of the SCF into the droplet, as the antisolvent mass transfer will decrease the solute solubility within the organic phase (York, 1999; Subra and Jestin, 1999). This in turn governs the rate of crystallization within the droplet and thus determines the particle size (Palakodaty *et al.*, 1999).

The second process is the evaporation of the organic solvent into the antisolvent phase, causing an increase in solute concentration (York, 1999; Subra and Jestin, 1999). This determines the nucleation and agglomeration of particles within the droplet and can be influenced by mixing the solvent with the SCF phase (Palakodaty and York, 1999). A narrow size distribution of small sized particles is observed when the solute predominantly undergoes nucleation. However, when nucleation is low, then the opposite situation is observed where a lower number of particles of a larger size are produced (Subra and Jestin, 1999).

In order to be able to control the process of particle formation, the rates of mass transfer need to be increased. This can be achieved by increasing the SCF to solvent ratio, or by using high SCF velocities (York, 1999; Palakodaty and York, 1999), as is found in the Nektar SCF technology process known as solution enhanced dispersion by supercritical fluids (SEDSTM).

1.2.6. Solution Enhanced Dispersion with Supercritical Fluids

The SEDSTM process involves the mixing and dispersing of a drug solution and SFCO₂ within a patent nozzle arrangement (York, 1999). Particles, which are free of solvent, are then precipitated into the collecting vessel (Shekunov and York, 2000). This is shown schematically in figure 1.3.

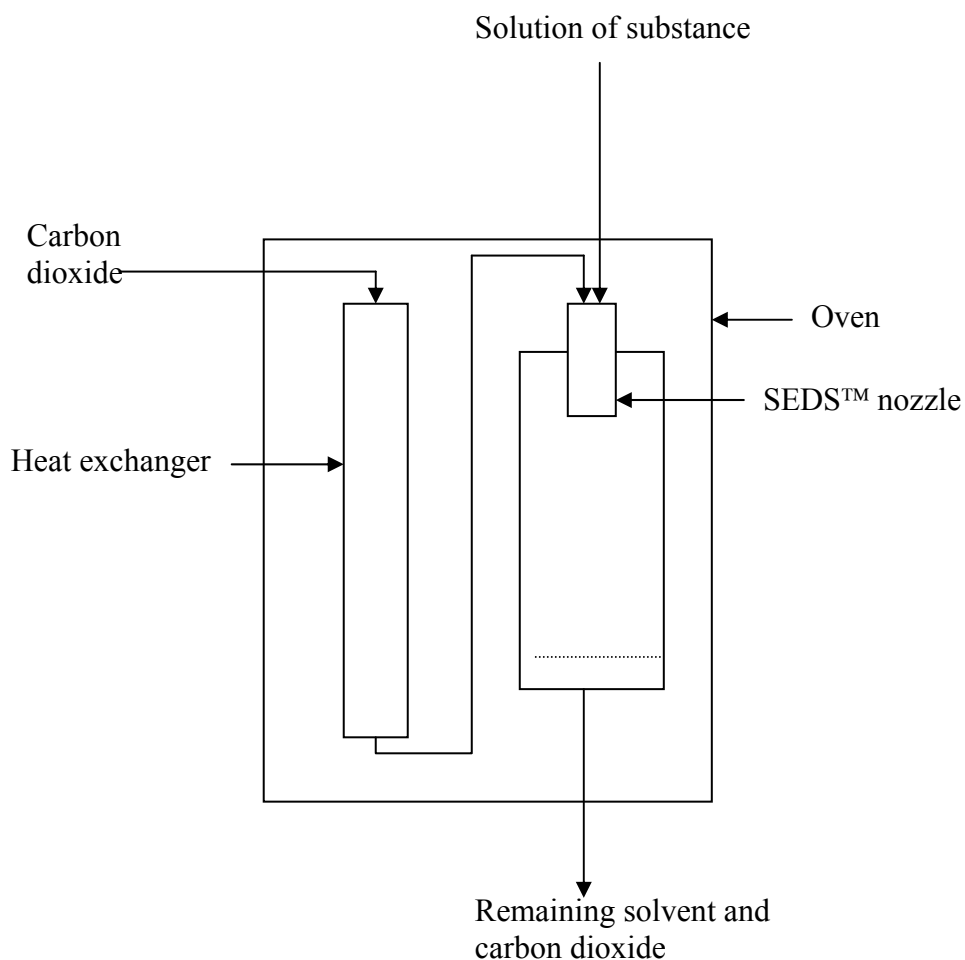


Figure 1.3. Apparatus used for the formation of particles by the SEDS™ technique. CO₂ is pumped into the particle formation vessel via a heat exchanger, where it is converted into the SCF phase. This is then passed to the SEDS™ nozzle, where the substance in solution, and organic modifier (if required) are added. Particles are then precipitated into the collecting vessel, where they are harvested and the remaining solvent and CO₂ are removed for recycling. The whole system is enclosed in an oven, which when combined with the control over the flow rates of the SFCO₂ and drug solution allows for control over the particle formation process.

The SEDSTM process has three main attributes. Firstly, particle formation and mixing are enhanced by the high speed of the CO₂, which is added at the same time as the solution and results in rapid dispersion at the solution. Secondly, to allow for controlled formation of particles, the starting composition of the process feeds is maintained. Finally the pressure and temperature are regulated to maintain stable conditions for particle formation (Shekunov and York, 2000).

SEDSTM has been undertaken using two types of nozzle. These are shown in figure 1.4 (a) and (b). The first (figure 1.4 (a)) is a two component nozzle in which the flows are SFCO₂ (with co-solvent if required) and organic/aqueous solution (Palakodaty *et al.*, 1998; Kordikowski *et al.*, 1999). The second (figure 1.4 (b)) is a three component nozzle consisting of three separate flows of SFCO₂, aqueous solution and organic solvent that can be used for biological material (Sloan *et al.*, 1999; Forbes *et al.*, 1998). In this second nozzle the organic solvent, that will facilitate extraction of H₂O, and is miscible with the SFCO₂ (for example methanol) is the middle feed. Before interacting with the SCF it first mixes with the aqueous feed; the SCF is however rapidly introduced which allows for particle formation with minimal exposure to potentially damaging organic solvents (York, 2000).

1.2.7. Applications of SEDSTM

SEDSTM has been used to control a number of properties of a variety of materials. For example, it has been used in the resolution of chiral drugs (Kordikowski and York, 1999), the controlling of crystal form (Beach *et al.*, 1999) and for the preparation of a wide variety of biological materials (Sloan *et al.*; 1999, Forbes *et al.*, 1998; Sarup *et al.*, 2000; Tservistas *et al.*, 2001; Moshashaee *et al.*, 2000). It has also been shown to be capable of being scaled up to an industrial scale (York *et al.*, 1998).

SEDSTM has also been found to produce particles that are of a narrow, micron sized distribution that are highly crystalline and possess a low level of

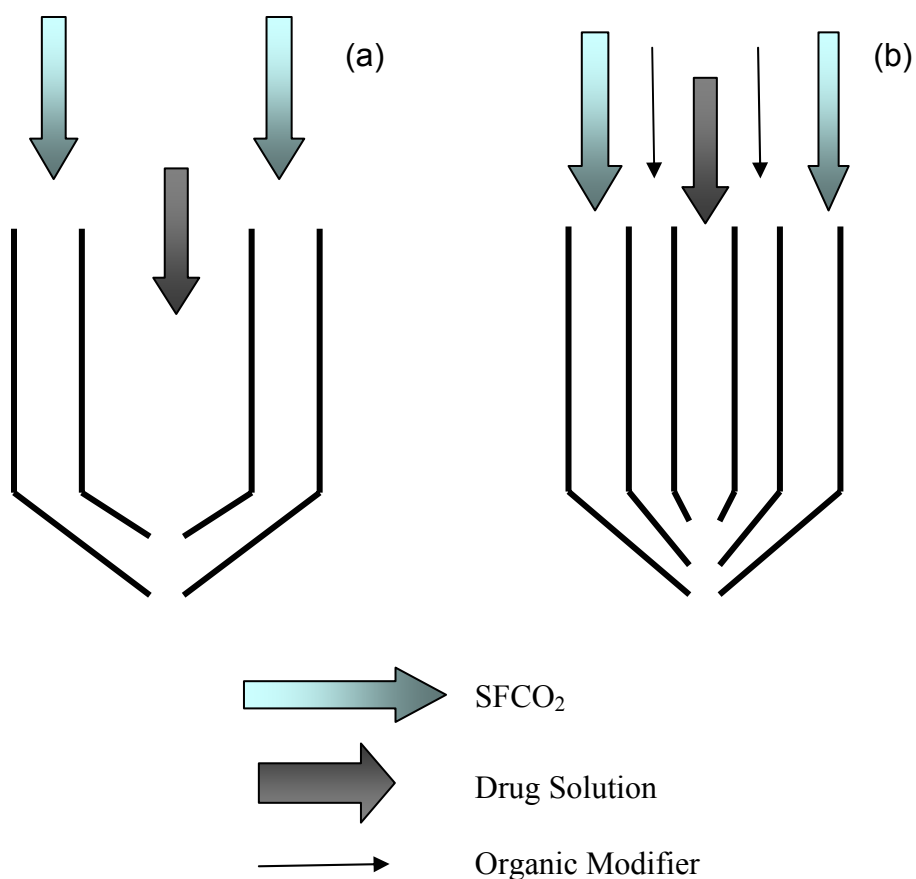


Figure 1.4. Nozzles used in the SEDSTM technique (adapted from Sarup et al., 2000).

- (a) Two component nozzle. This consists of two separate feeds, that of the SFCO₂ and the drug in an organic solvent.
- (b) Three component nozzle. This has three separate feeds, the SFCO₂, the drug in an aqueous solution and an organic modifier to enhance the solubility of the aqueous phase in the SFCO₂.

residual solvent (Forbes *et al.*, 1998; Feeley *et al.*, 1996). As discussed above, these are characteristics that are highly desired. In addition, the particles have been found to be free flowing and of a low surface energy. One of the main aims of this project is to understand the adhesion between these particles and how this is affected by their structure and surface properties. There are many types of forces and factors that influence adhesion, which will be discussed below.

1.3. Forces Between Particles

Adhesion is the result of interactions between the particle and a particular surface. The process of adhesion is a complex one that is affected not only by the fundamental forces that may occur between two molecules such as van der Waals forces, but also properties that are a function of the surface as a whole, for example surface energy. These types of interaction will be discussed below.

1.3.1. Van der Waals Forces

Van der Waals forces are divided into three types, Keesom, Debye and London forces. London forces (or dispersion forces) are of most relevance to this work as they make the most important contribution to the total van der Waals force present, and are always found between atoms and molecules (Israelachvili, 1991). They occur between uncharged, non-polar molecules and arise because of fluctuations in the arrangement of electrons, which gives rise to transient dipoles. The presence of these will generate an electric field, which can polarise a neighbouring molecule, leading to attraction between the dipoles. The first molecule's dipole will change due to the continual changes in the electron distribution and the second molecule's dipole will follow (Atkins, 1998). This leads to an interaction between the two molecules, the strength of which will be proportional to the inverse 6th power of the distance separating the two nuclei (Myers, 1999).

London forces have a number of characteristics -

- (a) In comparison with covalent bonds, they are considered to be long-range forces, and can be found to be present from distances greater than 10 nm to inter-atomic spacing (about 0.2 nm).
- (b) Depending on the situation they may be attractive or repulsive and simple power laws do not apply to their dependence on separation distances.
- (c) The interactions are *non-additive*, in that the field originating from a single molecule will reach the second molecule by both a direct and a 'reflected' route, meaning that the presence of other bodies around will affect the dispersion interaction of the two bodies.

It is possible to calculate the interaction energy (W_i) of a sphere near a planar surface by integrating the energies of all the atoms in a single body with all the atoms in the other, giving the equation –

$$W_i = -\frac{A_H R}{6D}$$

(Eq 1.1)

where R is the radius of the particle, D is the distance between the particle and surface and A_H is the Hamaker constant, which is calculated by the equation -

$$A_H = \pi^2 C_H \rho_1 \rho_2$$

(Eq 1.2)

where C is the interaction constant, and ρ_1 and ρ_2 are the number densities of the two interacting surfaces (Israelachvili, 1991).

This equation ignores the presence of atoms which possess different electronegativities and polarizabilities, which would increase the contribution of the Keesom (dipole-dipole) and Debye (dipole induced dipole) forces. In addition, this calculation also ignores non-additive effects, leading to a disagreement between the calculated and observed forces. Lifshitz has applied quantum field theory to address this problem (Lifshitz, 1956).

1.3.2. Lifshitz Theory

While a detailed discussion of the Lifshitz theory is beyond the scope of this thesis, it can be explained as being a different method of calculating the Hamaker constant in equation 1.2, by treating large bodies as continuous media. In this theory, the resultant forces are considered to be due to normal changes in electron density, which cause alterations in dipole moment appearance. This leads to differences in the electromagnetic field of the atoms. If this field is considered to act over a large distance, it will allow interactions with other atoms fields, leading to attraction between solid bodies (Israelachvili, 1991; Podczec, 1998).

The main limitations of Lifshitz theory are that it does not account for separation distances of molecular dimensions, and that it assumes that the physical properties of the interacting bodies are uniform through the phase (Myers, 1999).

It should be noted that all types of van der Waals forces are affected by the properties of the materials, as well as their contacting surfaces, which will in turn change the adhesion strength. Examples of properties that are important include elasticity (discussed in section 1.3.7.3) and the true area of contact (Podczec, 1998).

1.3.3. Capillary Forces

Capillary forces arise due to the condensation of water at the point of contact between particles, or to pores in hydrophilic materials, which may condense trapped moisture. This water will form a meniscus, which creates relatively large forces between the particle and surface (Coelho and Harnby, 1978). This force will be affected by many factors, which will be discussed in more detail in chapter 4.

The presence of water may also have a physical effect on the materials in contact. If the particle material is soluble in water, then the prolonged presence of capillary forces will cause the surfaces in contact to dissolve. If the material is then dried, crystal bridges may form leading to increased adhesion (Podczecz *et al.*, 1997). Alternatively, the water may act as a plasticizer (Buckton, 1995). This will mean that the surface is easier to deform, leading to an increase in the contact area and hence increases in adhesion force.

1.3.4. Contact Potential Forces

Contact potential forces arise due to electrical charging of a surface caused by differences in the outermost band of electrons, known as the Fermi level. The difference in energy states between these electrons and the vacuum energy level give the work function (ϕ_w) of a material (Pollock *et al.*, 1995). When two different materials contact, a transfer of electrons occurs until both materials have a similar Fermi level, generating a contact potential which is the same as the difference between the work functions of both materials (Stewart, 1986). The strength of the resulting force is given by -

$$F = \frac{2\pi q^2}{A}$$

(Eq 1.3)

where q is the particle charge upon detachment and A is the contact area between the particle and carrier surface. These forces can cause problems in pharmaceutical processing, as different processing conditions can lead to changes in the charge on particle surfaces, which can influence adhesion and mixing (Staniforth, 1987), and be of greater magnitude than coulomb forces (Stewart, 1986).

1.3.5. Coulomb Forces

Coulomb forces can be either attractive or repulsive and are formed from surfaces that acquire a charge, either from friction or artificial charging created by placing a surface in an electric field (Horn *et al.*, 1992; Staniforth *et al.*, 1989). If a charged particle contacts an uncharged surface an equal, but opposite, charge will be induced on the surface causing adhesion, the force of which is given by –

$$F = \frac{Q^2}{l^2}$$

(Eq 1.4)

where Q is the charge on the particle and l is the distance between the centres of the charges. These forces are eliminated by the presence of moisture, which makes the gap between the particles more conductive leading to charge leakage, as well as roughness which will assist in discharge (Coelho and Harnby, 1978).

1.3.6. Specific Forces

Specific forces are strong forces that occur between biological molecules in specific orientations and are due to a range of non-covalent forces, such as those discussed above. These bonds have a very precise stoichiometry similar to the 'lock and key' mechanism observed for enzyme activity (Hasama *et al.*, 1997). However, the presence of forces that are related to

specific orientations of molecules are not thought to be important in this work.

1.3.7. Other Important Factors

1.3.7.1. Surface Roughness

Surface and particle roughness is of great importance in interactions and some of the potential affects are shown schematically in figure 1.5. If the particle adhering to the surface is smaller than the distance between asperities, as seen in (a) and (b), it will fall into the trough, leading to an increase in contact area which may increase adhesion. Also, the asperities will provide 'protection' from lateral forces that may act on the particle to remove it (Podczec, 1998). However, if the particle is larger than the asperity distance, the particle will be unable to come into close contact with the surface, leading to a reduction in the van der Waals contribution to the adhesion force.

The presence of surface roughness can lead to large discrepancies between predicted and actual adhesion forces, for example significant deviations from predicted values were found by Heim *et al.*, (2002) when looking at adhesion forces between spherical polystyrene and gold particles.

1.3.7.2. Surface Energy

A molecule in the centre of a bulk phase, as shown in figure 1.6 (a), is encircled by similar molecules, and so will have no net force acting on it. However, if the molecule was found at the surface, whilst there are other molecules around and underneath, there are none above it, only those of a second, different phase such as a vapour phase as demonstrated in figure 1.6 (b). As the strength of the interaction with this vapour phase will be lower than with the surrounding molecules, there will be an inward attraction of the molecule. Since this force will be acting to contract the surface, it is said to

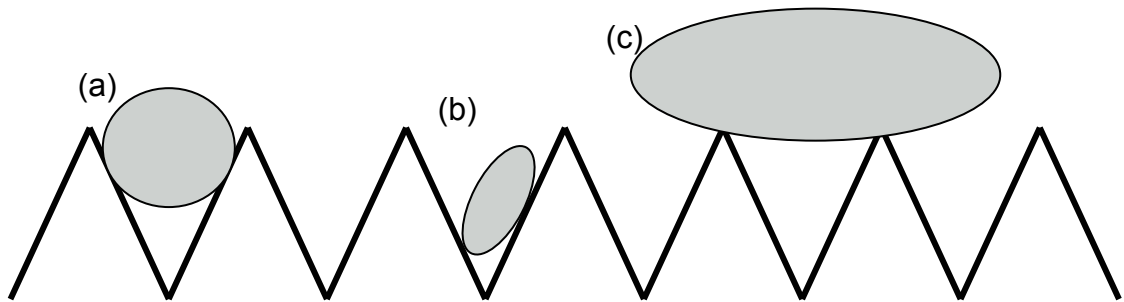


Figure 1.5. Effect of surface roughness on particle adhesion. In (a) and (b), the particle is nested in the valleys between the asperities causing an increase in the adhesion force. In (c) the particle is resting upon the asperities, leading to a decrease in the adhesion force (Taken from Podczec, 1998).

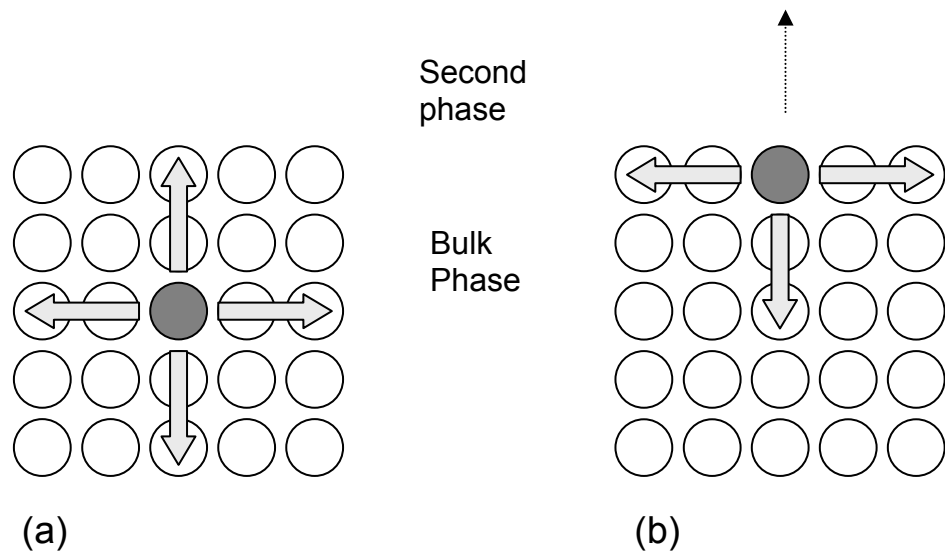


Figure 1.6. The phenomena of surface tension. In (a) the centre molecule is surrounded on all side by similar molecules, meaning that it will experience no net force. However, in (b) the molecule is at the surface, where molecules of a second phase are present which will have a lower interaction than the like molecules. This will lead to a net inward pull, known as surface tension.

exist in a state of tension. If the bulk phase is liquid, the phenomena is known as *surface tension*, as this term refers to the work performed in forming a unit area of surface. However, if the bulk phase is solid then this is known as *surface free energy*, as this describes the work spent in stretching the surface. These terms are thus defined as the amount of work required to increase the surface area of a substance by 1 m² (Buckton, 1995).

With liquids, the terms surface tension and surface free energy (and their respective values) are interchangeable, but this is not the case with solids. The forming of a new surface is the result of two processes: cleaving the phase, and the reconfiguration of the molecules to the most stable arrangement. Liquid molecules are able to perform this simultaneously, whereas solid surface molecules are held in a rigid conformation and are unable to reconfigure in a short timescale. This will mean either that the density of surface molecules will differ from molecules in the most stable state, or that the surface area may have been increased or decreased with no change in the total number of molecules, which will lead to local changes in surface energy (Myers, 1999; Buckton, 1995).

The surface energy is important in many aspects of pharmaceutical processing, because in order to reduce the surface free energy, particles will aggregate together to limit the number of free surfaces available. This may lead to changes in operations such the flow of powders, which is important in such processes as the filing of tablet dies, or may even affect drug delivery by reducing the separation of drug from carrier.

1.3.7.3. Mechanical Properties of the Surface

The mechanical properties of the contacting surfaces, such as hardness and elasticity are important in the adhesion of particles. The hardness of a material is defined as the resistance to indentation (Tabor, 1948) and elasticity as the ability of a material to resume its initial form after removal of an applied stress. In many materials, the plot of elastic stress against elastic

strain results in a linear relationship. The gradient of the slope of this linear region is known as the Young's modulus of a material (Timoshenko and Goodier, 1970; Askeland and Phule, 2003).

These material properties will affect how the particle and surface will deform on contact, which in the absence of surface forces, will be in response to the press-on force (Heuberger *et al.*, 1996). The presence of deformation will generally increase the area of contact, which will affect adhesion in a number of ways, for example by increasing the van der Waals forces (Podczuch, 1998). Explaining the effect of deformation on the resulting adhesion force has been improved by the development of a series of adhesion theories, which are discussed below.

1.4. Adhesion theory

1.4.1. Hertz Theory

Most models developed to describe adhesion are based upon the Hertz theory of contact between two spheres, which assumes that there is no adhesion or friction and that the contact stress is compressive (i.e. repulsive) over the whole area of contact (Briscoe *et al.*, 1998). Hertz demonstrated that at high loads, both the size and shape of the zone of contact between two spheres was related to the elastic deformation between the two bodies by the equation –

$$a_0^3 = \frac{3F_{on}R}{4E^*}$$

(Eq 1.5)

where a_0 is the contact radius, F_{on} is the applied load, R is the radius of the sphere and E^* is the reduced Young's modulus calculated using the following equation -

$$\frac{1}{E^*} = \left(\frac{1-\nu_1^2}{E_1} + \frac{1-\nu_2^2}{E_2} \right)$$

(Eq 1.6)

where E_1 and E_2 are the Young's moduli of the sphere and the surface, and ν_1 and ν_2 are the respective Poisson's ratios (Johnson *et al.*, 1971). The Hertz theory makes a number of assumptions (Briscoe *et al.*, 1998) –

- (a) a normally loaded contact exists between the bodies
- (b) the materials behave as a linear elastic bodies
- (c) the radius of the contact area is small compared with the radius of the sphere
- (d) there is frictionless contact between the surfaces resulting in the transfer of only normal stresses between the contact surfaces

The Hertz theory does not include consideration of adhesive surface forces (Heim *et al.*, 2002), which became important when it was noted by Johnson *et al.*, (1971) that this equation did not hold for low loads, suggesting that attractive surface forces are operating between solids. Although the “additional” contact forces were of little significance at high loads, they became more important as the load was reduced to zero. In subsequent models of adhesion based upon this theory, the presence of surface adhesive forces was corrected for.

1.4.2. JKR Theory

The Johnson-Kendall-Roberts theory (1971) is based upon the consideration that surface forces act inside the contact region causing deformation that is not fully Hertzian, so the contact area is described by the generalised Hertz equation –

$$a_0^3 = \frac{RF_{on}}{E^*}$$

(Eq 1.7)

This deformation is seen as a neck region, due to compression occurring inside the centre of the contact spot, and tension (i.e. attraction) occurring in the outer circle of the contact area, as shown in figure 1.7. This leads to the prediction that the particle and surface in contact will separate abruptly from a finite contact area when the pull-off force is reached (Horn *et al.*, 1987). According to this theory, the pull-off force between two surfaces is given by –

$$F_{ad} = \frac{3}{2}\pi\gamma_{ad}R$$

(Eq 1.8)

where F_{ad} is the force of adhesion and γ_{ad} is the work of adhesion. Separation occurs once the contact radius has decreased to –

$$a_s = 0.63a_0$$

(Eq 1.9)

where a_s is the separation radius. This model has been widely used in adhesion studies (Heim *et al.*, 2002, Schaefer *et al.*, 1995) and has been shown to be useful in describing the adhesion of high surface energy, low-modulus elastomeric bodies at low loads (Muller *et al.*, 1980).

1.4.3. DMT Theory

The Derjaguin-Muller-Toporov theory (1975) also assumes that there are attractive forces deforming the sphere, although compared with the JKR theory, they are acting outside the contact region (see figure 1.8), leading to deformation as predicted by Hertz in equation 1.5 (Briscoe *et al.*, 1998). This calculation also takes into account the energy of molecular attraction in the

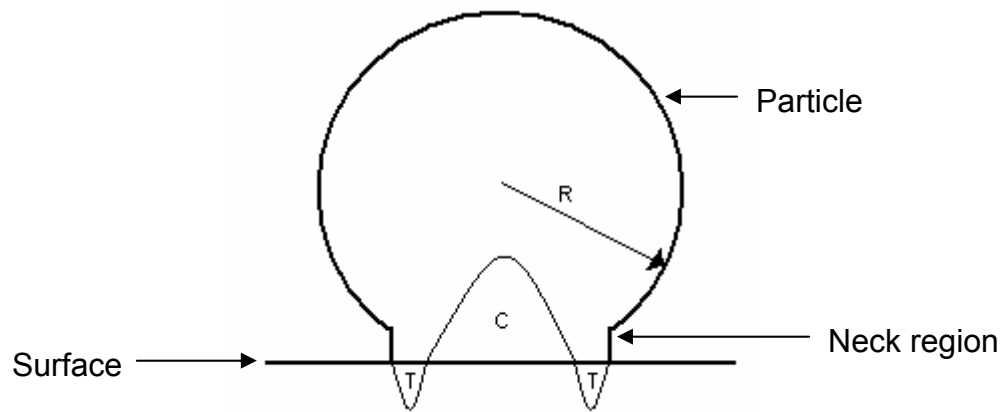


Figure 1.7. Diagram showing the regions of compression (C) and tension (T) according to the JKR theory.

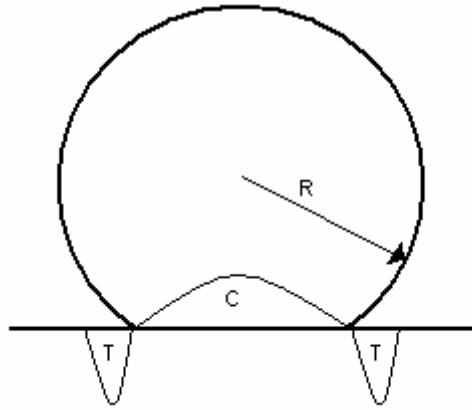


Figure 1.8. Diagram showing the regions of compression (C) and tension (T) according to the DMT theory.

ring shaped zone of the adhesion contact: it predicts that the two surfaces will part only when the contact area is equal to zero and that the adhesion force will be defined by the equation –

$$F_{ad} = 2\pi\gamma_{ad}R \quad (\text{Eq 1.10})$$

While this model has been used (Burnham *et al.*, 1990), it has not been as popular as the JKR theory, and is better suited to hard, non-deforming contacts of low surface energy (Muller *et al.*, 1980).

The JKR and DMT theories are not opposing theories, but instead should be considered as opposite ends of the same scale. In order to decide which equation would best suit a particular situation, the Tabor equation can be used.

1.4.4. Tabor Equation

The Tabor equation (Tabor, 1977) assumes that the attractive forces between a particle and surface are only found in the first few atomic layers of the contacting area whilst outside of this zone the forces are negligible, as shown in figure 1.9. If z_0 is the equilibrium distance of separation between atoms in contact, as soon as this value is exceeded the surfaces will pull apart (Tabor, 1977). Outside this zone of contact there is a neck of height h , whose height is approximated by –

$$h \approx \left(\frac{R\gamma^2}{E^{*2}} \right)^{1/3} \quad (\text{Eq 1.11})$$

where E^* is the reduced Young's modulus. If h becomes comparable with z_0 then any forces present outside the contact zone can no longer be ignored

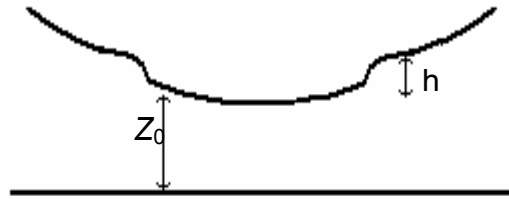


Figure 1.9. The dimensions of the neck formed when a particle comes into contact with a surface. When the equilibrium distance of separation between the atoms in contact (z_0) becomes comparable with the neck height (h), forces outside the contact zone can no longer be ignored, meaning that the DMT theory must be used to describe the adhesion force.

(Tabor, 1977). This can be described using the dimensionless parameter ϕ_0 , which is defined by the equation –

$$\phi_0 = \left(\frac{\gamma_{ad}^2 R}{E^* z_0^3} \right)^{1/3} \quad (\text{Eq 1.12})$$

If the equation is followed strictly, then any value above 0 would require the use of the JKR theory, although the value of 0.3 is more commonly used (Podczech *et al.*, 1996).

These theories of adhesion have been tested using different methods to measure the adhesion forces. These will be discussed below.

1.5. Methods of Measuring Forces

1.5.1. Surface Force Apparatus

This was originally developed by Tabor and Winterton (1969) for measuring van der Waals forces between mica sheets in air in order to test Lifshitz theory. The surface force apparatus (SFA) consists of two curved mica surfaces, which are in a crossed cylinder configuration. This has the same geometry of two spheres close together or a sphere near a flat surface (as this is a special case of two spheres close together, where one sphere is much larger than the other) (Israelachvili, 1991). The two mica surfaces are coated before use with a semi-reflecting layer of silver, before being positioned in the apparatus: one in a fixed position, the other mounted onto a spring. Once mounted in the apparatus, the distance between the two surfaces is controlled by the expansion or contraction of a piezoelectric tube, and the resulting movement of the two surfaces is measured by the use of an interferometric technique. The force can then be calculated by multiplication of the distance moved, by the spring constant of the spring the mica sheet is placed on (Capella and Dietler, 1999; Israelachvili, 1991).

While this apparatus has proved useful in understanding the fundamental forces involved in adhesion, it is not suitable for acquiring particle-particle force data. This is because the equipment requires molecularly smooth samples, which must be transparent for the interferometric technique to be employed.

1.5.2. Impaction Methods

These methods are characterised by the use of impaction on the opposite side of the substrate to which the particles are adhered. The method of impaction can be achieved by many methods, for example the impact of a bullet, or by the dropping of a hammer from a fixed height onto the disk. This has the advantage that it can be easily coupled to equipment that may provide further analysis of the particles removed, for example the electric charge present (Derjaguin *et al.*, 1968).

1.5.3. Centrifuge Technique

This is a method of examining forces between particles and flat surfaces. It consists of a centrifuge, which has been modified by the introduction of specially manufactured adapters, in which disks of material, with particles added onto the top, can be placed. A typical centrifuge experiment begins with the disks being placed inside the adapters, with the particles placed facing the centre of the centrifuge rotor. This allows a press-on force to be applied. Following this, the number of particles on the disk are counted and the disk is then placed in the centrifuge again, although this time the disk is facing outwards. The removal force is then applied (Podczeck and Newton, 1995). The detachment force (F_{det}) applied is directed through the centre of gravity of the particle, outwards from the centre of rotation (Kulvanich and Stewart, 1987), and is given by –

$$F_{\text{det}} = M_p r \omega^2 \quad (\text{Eq 1.13})$$

where M_p is the particle's mass, r is the distance from the axis of rotation to the particle and ω is the angular velocity (Booth and Newton, 1987).

The centrifuge system has been used to study a number of different pharmaceutical systems. For example, Lam and Newton (1993) used it to examine the effect of time on the press-on force of particles of PEG 4000 and Starch 1500 against a steel surface, whereas Podczech *et al.*, (1997) used it to compare the effects of particle on compressed disk of material to particle-on-particle experiments.

The centrifuge and impaction approaches to particle measurements have many advantages. They provide data regarding the bulk, integrated effects of physical and environmental variation of particle adhesion, are of low cost, and are simple and accessible. However, the main disadvantage is that due to the large scale nature of the measurements, it provides limited information on individual particle interaction (Price *et al.*, 2000; Podczech *et al.*, 1995). However, the ability to generate data regarding single particle events has been facilitated by the introduction of scanning probe microscopy, particularly the atomic force microscope.

1.6. Scanning Probe Microscopy

Scanning probe microscopy (SPM) is the name given to a range of recent techniques which involves the formation of images and acquisition of surface property data from a range of physical, optical and chemical interactions between a sharp proximal probe and a surface (Vansteenkiste *et al.*, 1998; Shao *et al.*, 1996).

The first such instrument was the Scanning Tunnelling Microscope (STM), invented by Binnig and Rohrer (1982). This consisted of a conducting tip

passing a few angstroms over a surface, while a voltage was applied across the gap. This led to a tunnelling current that is detected and used to form an image (Binnig *et al.*, 1982). Detection of this current and its changes due to surface features was then used to form an image.

Due a number of limitations of this technique (most importantly the presence of a conducting surface of very low contamination), this technique underwent extensive modification to allow for a variety of different properties and materials to be studied. One such modification led to the invention in 1986 of the Atomic Force Microscope (AFM) (Binnig *et al.*, 1986).

1.6.1. Atomic Force Microscopy

A schematic diagram of an AFM is shown in figure 1.10. The AFM consists of a flexible cantilever with a probe at the end, which is in close proximity to a sample mounted onto a substrate (eg mica), on top of a piezoelectric xyz-scanner. A piezoelectric material will change its dimensions in response to an applied voltage, in this case in the x, y and z directions. A laser is aimed onto the back of the cantilever tip, and reflected via a mirror onto a position-sensitive photodiode, which is incorporated into a feedback loop to the piezo to allow for detection of cantilever deflection.

When the probe is in close proximity to or in contact with the sample the tip undergoes deflection due to the nano-newton forces that will exist between sample and probe. The probe is then raster-scanned across the sample, where detection of cantilever deflection by the photodiode allows for subsequent adjustment of the piezo, maintaining a constant deflection. The change in height of the piezo is monitored by a PC based controlled feedback system and used to acquire topographic information (Shao *et al.*, 1996; Roberts *et al.*, 1994).

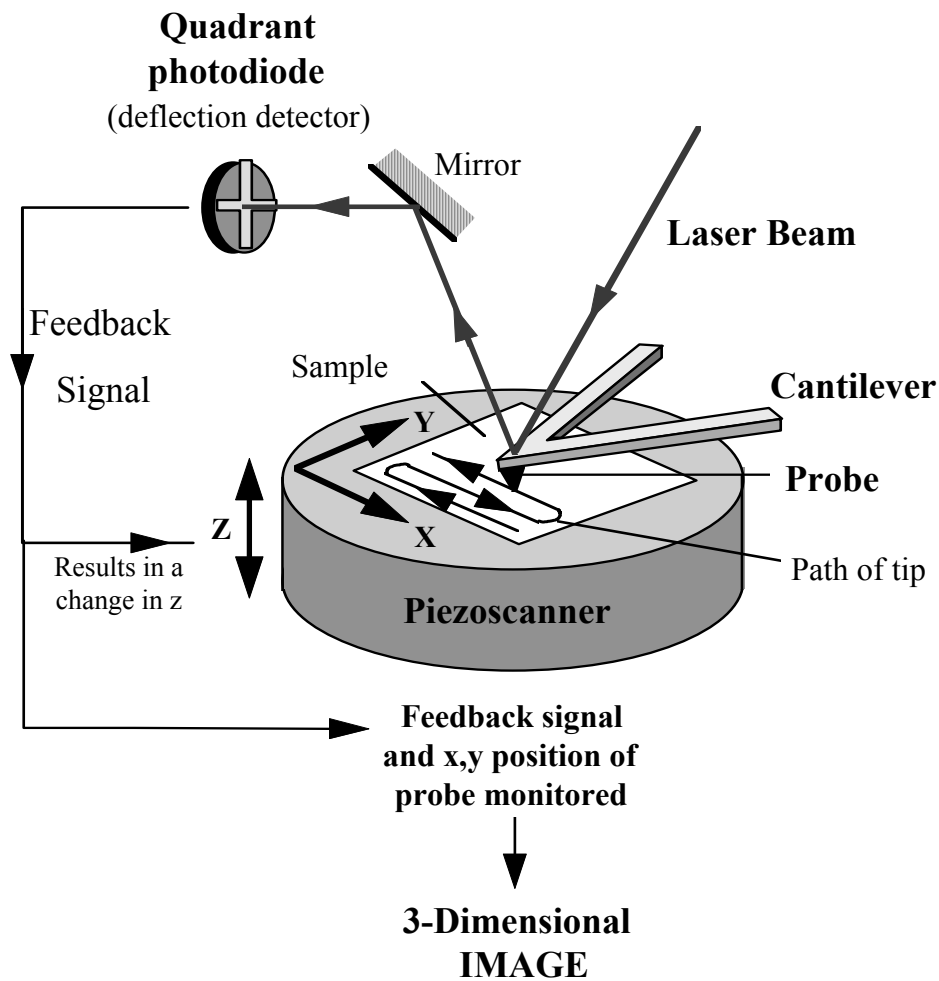


Figure 1.10. Schematic diagram of an AFM (Allen *et al.*, 1997). A probe which comes into contact with the substrate is mounted onto the end of the cantilever. This probe is then raster scanned across the sample, causing changes in the deflection of a laser which is reflected off the back of the cantilever. These changes are detected by a photodiode, and relayed to a computer which then makes the appropriate alterations to the piezoscanner upon which the sample is mounted. The computer is able to record these changes to create an image of the sample.

1.6.2. Modes of Operation

1.6.2.1. Imaging Modes

There are two main methods of detecting changes in the sample, contact mode and tapping mode.

In contact mode, the probe is in constant contact with the sample surface as it is raster scanned across. This is shown schematically in figure 1.11 (a). While this mode has the advantage of giving the highest resolution, it also causes the most sample deformation due to the lateral shear force that results from raster scanning. In addition to deformation, if the sample is not strongly adhered to a surface, the raster scanning pattern can cause the sample to be 'swept' aside by the probe movements as shown in figure 1.12. In 1.12 (a), the particles are securely adhered to the substrate, leading to an image of the particles, however in (b) there are only weak interactions, leading to the sample being moved aside, and an image of the substrate only being formed.

Tapping mode differs from contact mode in that the probe is vibrated at its resonant frequency as it is raster scanned across the sample. This is shown schematically in figure 1.11 (b). The oscillation means the probe only makes intermittent contact with the sample surface during scanning. When the probe is in contact with the sample at these points, the changes in its oscillating amplitude or phase are detected and used to form an image. This is useful as it not only reduces the total tip-sample contact time, but it also brings about a reduction in the lateral force that a sample may experience in contact mode, leading to a reduction in deformation and sweeping of the sample. (Ikai, 1996; Lal *et al.*, 1994).

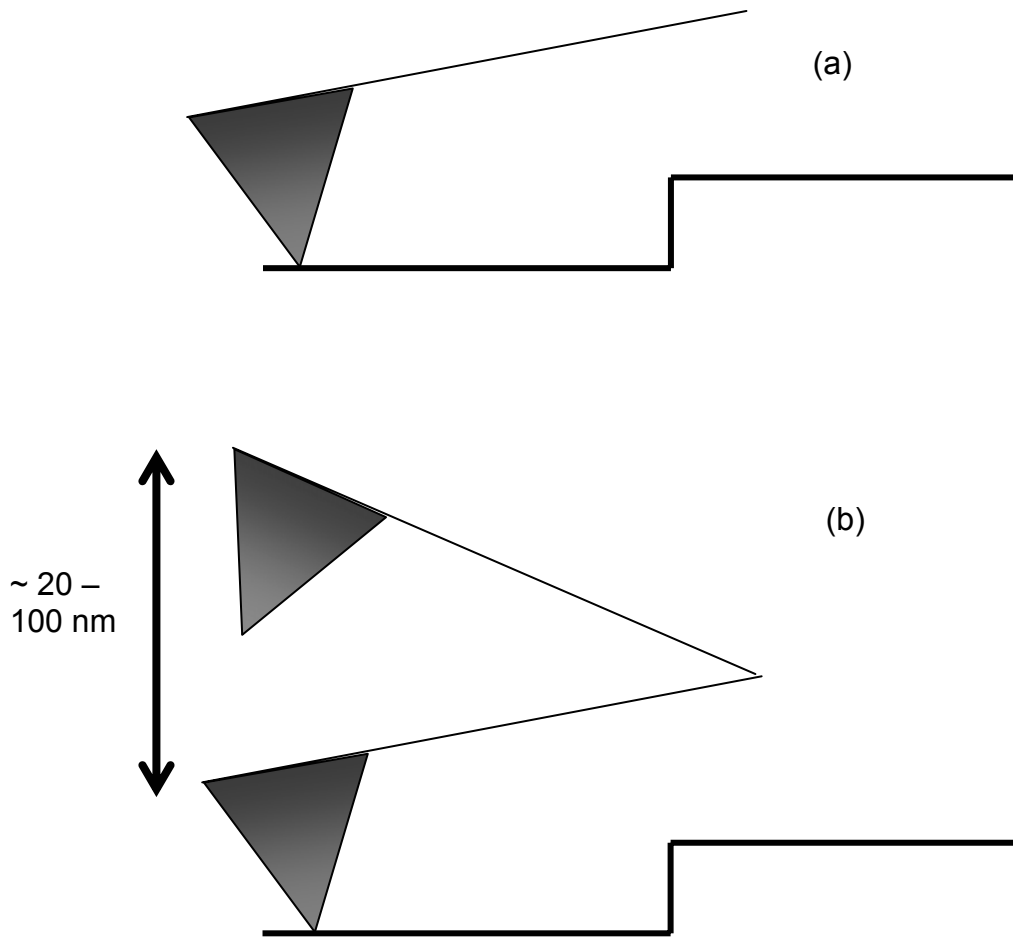


Figure 1.11. AFM imaging modes.

- (a) Contact mode. In this mode, the probe is in constant contact with the sample surface, leading to high resolution images. However, this may also cause significant deformation of the sample.
- (b) Tapping mode. Here, the probe is oscillated at its resonant frequency, causing intermittent contact with the sample surface, leading to a lower level of sample deformation.

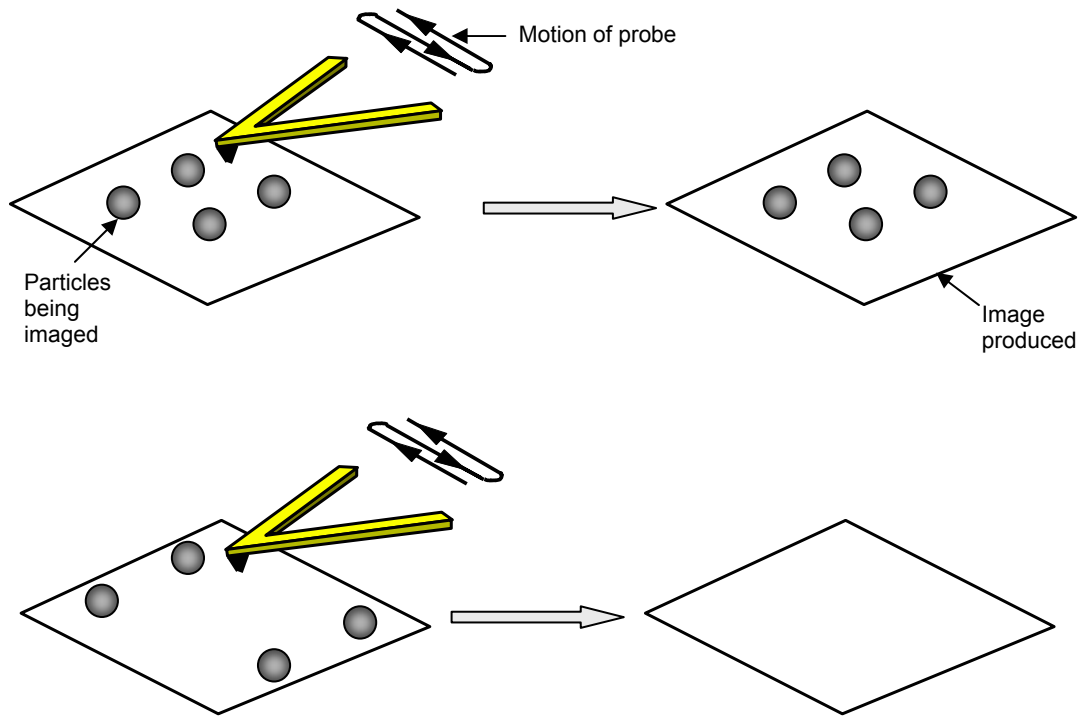


Figure 1.12. AFM artefact of sweeping.

- (a) The particles are firmly adhered to the substrate, allowing for a image of the particles to be produced.
- (b) The particles are weakly adhered to the substrate, meaning they are swept aside and not imaged, leading to an image of the substrate only.

1.6.2.2. Force Measurements

The ability to acquire localized force measurements between the AFM probe and a substrate was realised soon after the invention of AFM, with force measurements being undertaken to examine surface forces on graphite and lithium-fluoride (Meyer *et al.*, 1989). The introduction of the colloid probe technique by Ducker *et al.*, (1991), greatly increased the importance of AFM for the collection of information about single particle events. In this work, an AFM probe was modified by the addition of a silica sphere of radius 3.5 μm to allow the measurement of colloidal forces between the particle and a planar surface in sodium chloride solution. Since then the method has been used in a wide variety of systems, for example measuring electrostatic, van der Waals and hydration forces and oil-mediated adhesion (Butt, 1991; Rabinovich *et al.*, 2002). It has also found increasing importance in the pharmaceutical industry. For example, in relation to interactions between particles and gelatine capsule surfaces, the effect of roughness on adhesion and the interaction of particles with pharmaceutically relevant substrates (Beach *et al.*, 2002; Ibrahim *et al.*, 2000; Eve *et al.*, 2002).

1.7. Aims of the Project

The overall aim of this project is to use the AFM to characterise particles produced using the SEDSTM technique in order to aid understanding as to why they display differing and often superior properties over those made using more traditional techniques. Work will focus on structure, surface properties and inter-particulate interactions compared with particles produced by standard micronisation approaches.

For this work, a method has been devised to image the contacting asperities of particles and calculations have been performed to extract the work of adhesion and surface energy that they possess. This was done for both SEDSTM and conventionally produced particles so that comparisons could be made between the differing processes.

In addition, work has been undertaken within the project to investigate how the differing processing conditions affect the performance of particles under conditions of controlled humidity. This work has generated a model of adhesion to illustrate how the surface features change the observed behaviour of adhesion with humidity.

Finally, work has also been done to examine how co-processing two different materials affects the distribution of both components and alters the surface structure.

Chapter 2

Materials and Methods

2.1 Imaging of Samples

2.1.1. Scanning Electron Microscopy (SEM)

SEM images were acquired of the raw samples using a SEM 505 (Philips, Holland). A small quantity of each sample was sprinkled on to stubs freshly coated with carbon glue. The glue was allowed to dry, and following this the stubs were then gold coated by placing in a SCD 030 gold coater (Balzers Union, FL9496) for 4 minutes at 30 mA. The samples were then imaged under an accelerating voltage of 25 kV.

2.1.2. Atomic Force Microscopy (AFM)

Samples were mounted for AFM imaging by either using double-sided adhesive tape or thermosetting glue (Agar Scientific, Essex, UK). When using adhesive tape, tape was fixed on to a metal stub, and then a small quantity of sample was sprinkled over. Excess powder was removed by blowing nitrogen over the stub for about 1 minute. When using thermosetting glue, a metal stub was placed on a glass slide that was then placed on a hotplate. The stub was allowed to heat up, before a thin layer of

thermosetting glue was melted on the top. The sample was then sprinkled over the stub, and both were allowed to cool. Once the glue had set, any excess sample was removed, as for the adhesive tape.

Images were obtained using a Nanoscope IIIa MultiMode AFM with a 'E' type scanner (Digital Instruments, Santa Barbara USA). Once the sample was mounted onto the scanner, a suitable area was located using a video camera. Tapping mode imaging of the sample was undertaken using silicon TESP probes of 300 kHz resonant frequency and a nominal spring constant of 50 N/m (Veeco, Bicester, UK). Because the samples often had a small degree of lateral movement with either sample fixation method, images were obtained using a relatively slow scan rate of ~ 1 Hz to reduce the problems of sweeping artefacts.

2.2 Force Measurements and Tip Characterisation

2.2.1. Addition of Particles onto Tips

Addition of particles on to tips is shown schematically in figure 2.1. Silicon nitride v-shaped cantilevers of approximate spring constant 0.58 nNm^{-2} were plasma etched with oxygen at 10W for 30 seconds (RF plasma barrel etcher PT7100, Bio-Rad). Because the spring constants of tips can vary greatly from the approximate value, the exact spring constant was determined using the thermal method (Hutter and Bechhoefer, 1993). Particles of the drug under examination were then mounted onto the cantilever apex using a Nanoscope IIIa MultiMode AFM (Digital Instruments, Santa Barbara, USA). A clean metal stub was prepared with glue (Loctite, UK) on one half and particles of drug on the other. An old tip was then used to draw out a thin line of glue on the substrate. This tip was then replaced with the plasma

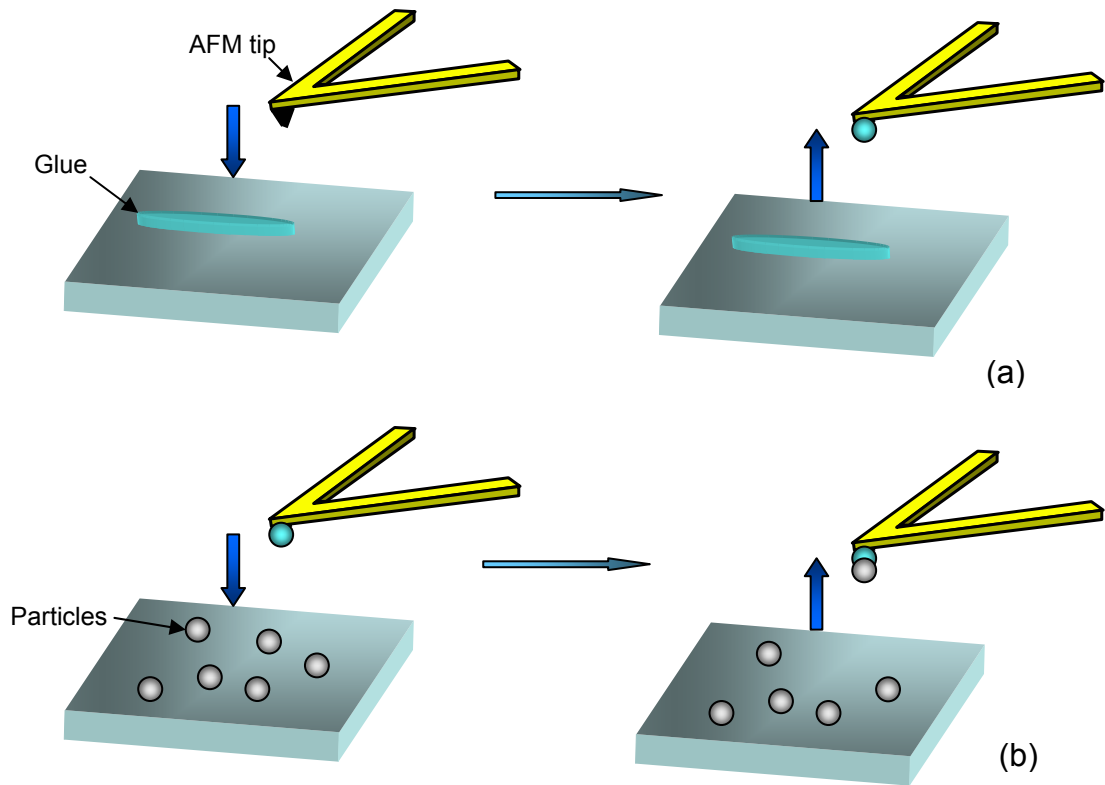


Figure 2.1. The addition of particles onto tips.

- (a) Tip is brought into contact with the glue, and retracted leaving glue on the probe.
- (b) Tip is then positioned over particles and brought into contact leading to particle addition.

etched tip to which the particle was to be added. The tip was first placed over the glue, and then brought into contact ((a) in figure 2.1). The tip was then repositioned over an individual particle before being brought into contact with it ((b) in figure 2.1). The tip with the particle now added was then retracted and left for 24 hours to allow the glue to dry.

To check that particles had been successfully added onto the cantilevers, the tips were examined by SEM. The tips were mounted on to metal stubs using carbon tape before imaging using an accelerating voltage of approximately 12 kV. A SEM image of a particle added on to a tip is shown in figure 2.2. In order to ensure that no glue was present on the particle, a control experiment was undertaken in which a particle was imaged before and after the addition of glue on to the particle. Figure 2.3 (a) shows the initial image of the particle before glue was added. Following this the particle was then dipped in glue and re-imaged with the SEM. It can be seen in figure 2.3 (b) that the presence of glue gives the particle a smooth, shiny appearance that differs from when no glue is added.

Two control cantilevers were prepared for each experimental sequence to show that the particle was coming into contact with the sample surface and not the cantilever tip. This consisted of a cantilever that was plasma etched only, and a further plasma etched cantilever that was dipped in glue, but had no particle added.

2.2.2. Force Measurements

Force measurements were performed using a Topometrix Explorer AFM (Veeco, USA). Following successful addition of particles on to the tip apex, the prepared tips were mounted on to half moon metal stubs using epoxy adhesive (Araldite, UK), and allowed to dry overnight. Force measurements were undertaken in one of two environments. For work undertaken in a liquid environment of model propellant, the mounted tips were placed on a liquid scanner with a Z range of 12 μm (Veeco, USA). The scanner was then

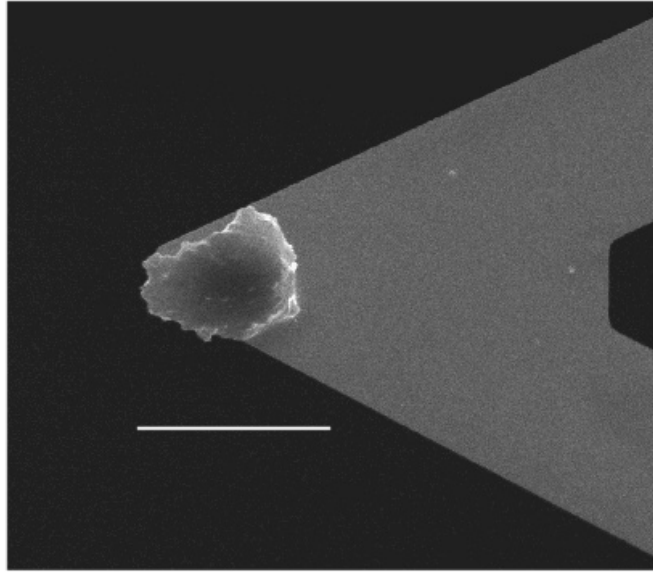


Figure 2.2. Tip with particle added onto end. It can be seen that the probe at the end of the tip is fully covered by the particle, bar size 20 μm .

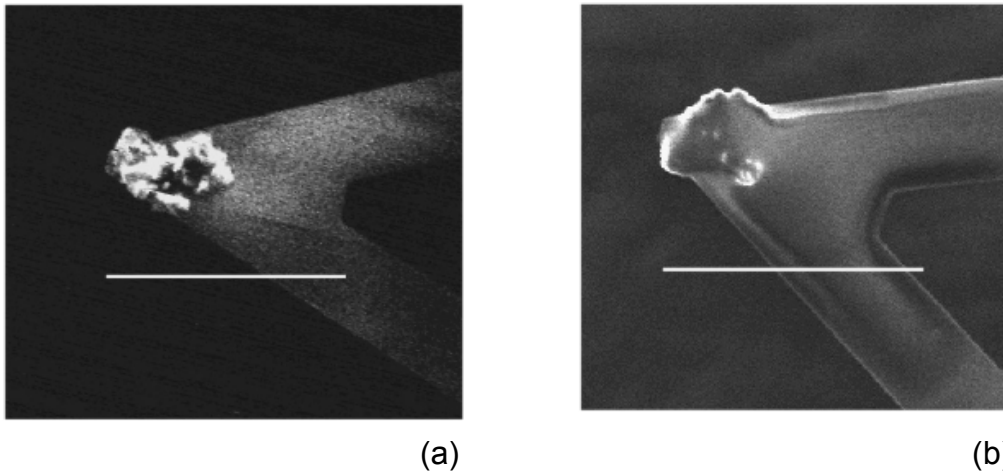


Figure 2.3. SEM images of before and after glue added onto particle. Bar size in both images is 50 μm .

- (a) Before glue is added.
- (b) After glue is added it can be seen that the particle morphology becomes smoother, and of more shiny appearance.

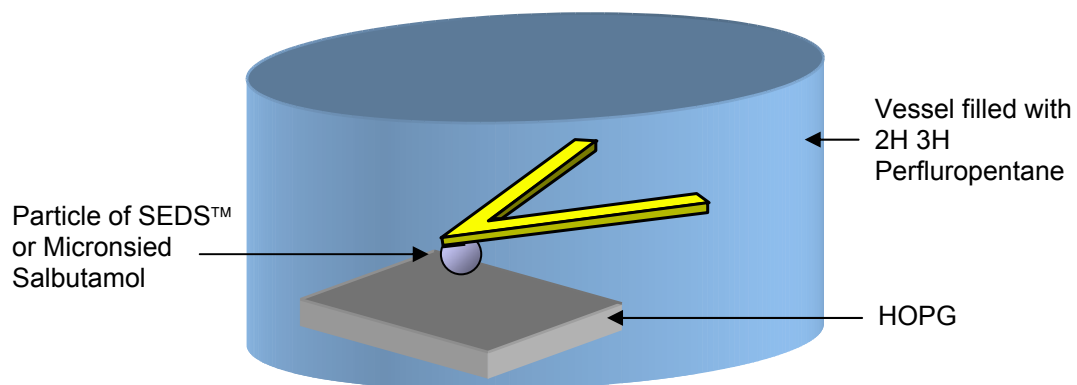


Figure 2.4. AFM set-up in liquid. The modified AFM cantilever and substrate are enclosed in a vessel containing the model propellant.

lowered into a sample chamber as shown in figure 2.4, which contained approximately 5 ml of 2H 3H perfluoropentane (Apollo Scientific Limited, Derbyshire, UK).

For work undertaken in an air environment, the AFM tip was placed on an air scanner with a Z range of 10 μm (Veeco, USA) before being lowered on to the substrate. The AFM was placed in a sealed container where humidity was controlled by one of two methods.

2.2.3. Control of Humidity

The first method was the use of desiccants. The desiccants used were silica gel (Fisher Scientific, UK) for <10% RH, and the saturated salts of potassium acetate (Fisher Scientific, UK) for 22% RH, potassium carbonate for 44% RH (Fluke, UK) and sodium chloride for 65% RH (Aldrich, UK). These humidity values are correct for 20°C, and the temperature of the room was controlled to 20°C \pm 1°C via the use of air conditioning. It is noted that sodium chloride usually has a saturated RH of 75% RH (Podczeck *et al.*, 1996 a). However a stable value of 65% RH was continually reached for all experiments. This indicates that either the probe was incorrectly calibrated or that the sealed environment was not at steady state. However, the humidity meter was compared against another meter and showed no differences in %RH recorded, and when the humidity was recorded for the enclosed system, the value had stayed steady for at least 15 minutes prior to the reading. The dessicant was placed into a petri disk, which was then placed in the AFM container which was then sealed.

The second method was the use of dry nitrogen gas, which is shown schematically in figure 2.6. The dry nitrogen was generated in an air compressor (Comp Air, UK), and following this, was split into two separate feeds. The first feed was passed through a series of three flasks of distilled water to produce saturation of the gas. The second feed was not passed through any flasks and remained dry. The two nitrogen pipes were then

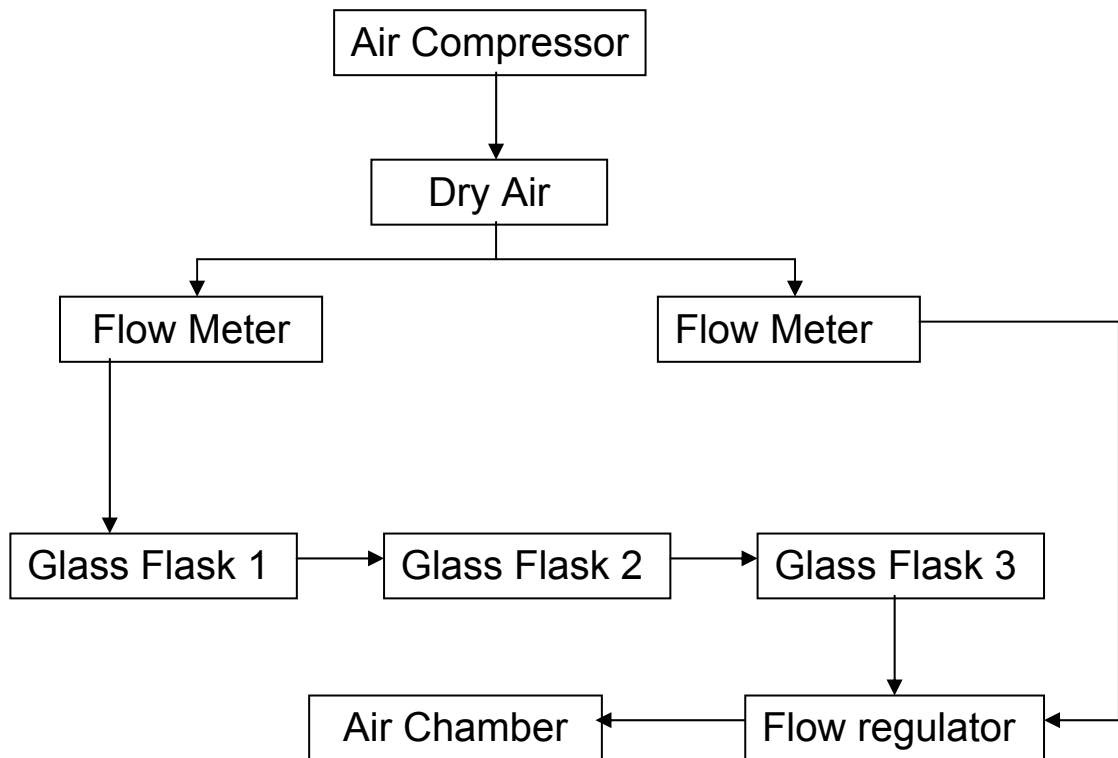


Figure 2.5. Humidity control equipment schematic. Dry nitrogen is pumped through a series of three flasks containing distilled water. This is then recombined with a separate flow of dry gas before passing to the humidity chamber.

recombined into a single feed which was connected to the container containing the AFM. By altering the flow rates through both of the pipes, it was possible to control the level of humidity of the nitrogen reaching the chamber, and therefore the environmental humidity.

Following enclosure, the apparatus was left for 2 hours for the conditions to equilibrate. In order to ensure the required humidity had been attained, a humidity probe (Testo 608-H2, UK) was also enclosed inside the container to allow constant reading of humidity. Humidity control was achieved to $\pm 2\%$ RH.

2.2.4. Force Measurement Substrates

Force measurements were performed against either freshly cleaved atomically flat highly orientated pyrolytic graphite (HOPG) (Agar Scientific, Essex, UK), a compressed disk of the drug, or particles of the drug affixed to a stub using the method described in the imaging section earlier. For measurements against HOPG, approximately 70 force curves ($n = 70$) were taken. For the measurements undertaken against particles, $n = 50$ for the point measurements, and $n = 70$ for the measurements taken over a $10\ \mu\text{m} \times 10\ \mu\text{m}$ area.

ANOVA analysis was performed using Minitab (Minitab Inc., PA) software on the force data acquired. ANOVA was used as it a parametric test appropriate for analysis of data sets in which there is only one variable. In addition, Fisher's analysis was undertaken in order to provide confidence intervals ($P < 0.05$) for the differences between means of data pairs.

The AFM can be used to perform force measurements by bringing the tip in and out of contact with a substrate, to produce a force curve, a typical example of which is shown in figure 2.6. In this diagram, the probe is initially a large distance from the surface in the rest position, but is then brought towards the sample at a constant velocity in the approach trace. The

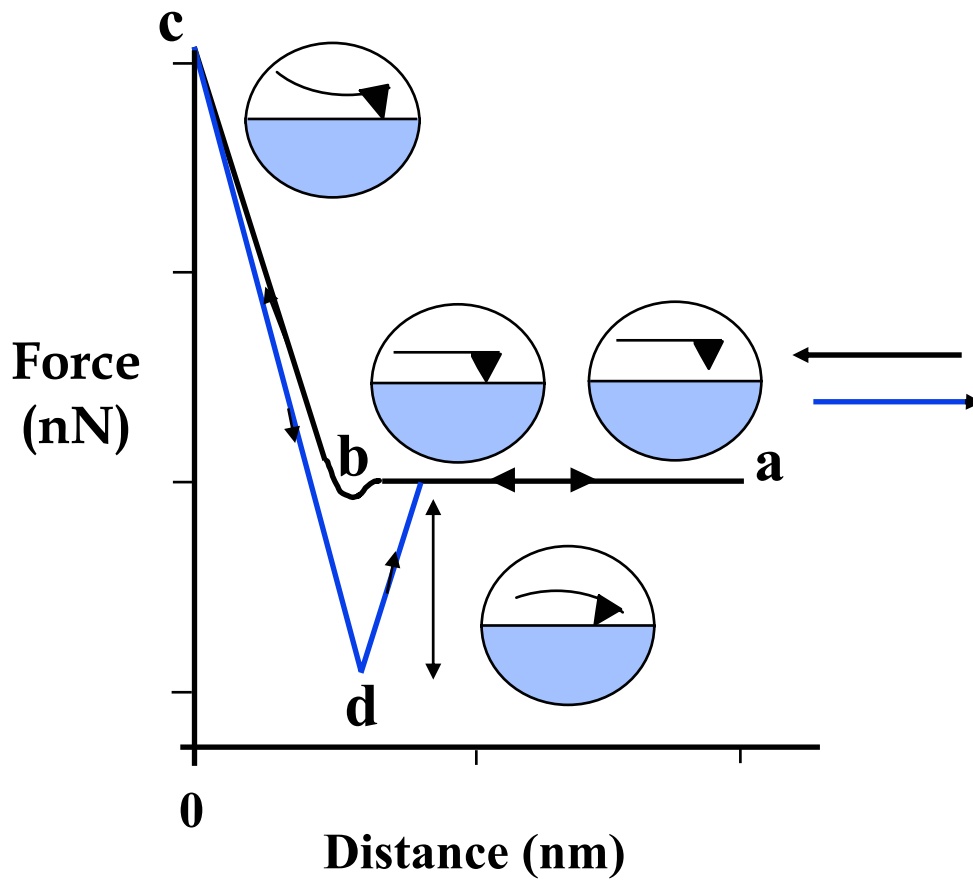


Figure 2.6. A force measurement curve (Allen *et al* 1997). The probe is moved towards the surface, and makes contact at (b). This motion is continued until a point of maximum load (c) is reached. The probe is then retracted, and the maximum adhesion force is calculated by measuring the distance from when the probe loses contact (d) and the starting position of the cantilever (a).

cantilever is subjected to many forces of attraction (e.g. van der Waals) and repulsion (e.g. electrostatic) which deflects the cantilever away from the surface.

At point (b) a small dip is typically seen in the approach curve. This is when the attractive force gradient on the probe exceeds the spring constant of the free cantilever. This is known as the jump-to-contact.

Once the probe is in contact any further reduction in distance will either force the probe into the surface of the sample or cause the cantilever to bend, depending on the mechanical properties of the surface. The forward motion is continued until the probe reaches a set point of pre-defined force between probe and sample, seen at point (c).

Once this point has been reached the probe motion is reversed for the retract trace. As the probe is retracted a minimum is observed at (d). It is noted that there is a difference between approach and retract traces known as the force-distance curve hysteresis (Cappella *et al.*, 1997). This is due to interactions between the surface and the probe, causing the probe to adhere to the surface. This feature can hence appear due to,

- Adhesive bonds formed during contact
- Increase in adhesion due to deformation of sample causing it to engulf the tip and increase contact area
- Hysteresis of the force curve
- A layer of liquid leading to a meniscus force

The pull-off force is equal to the adhesion force, and is the product of the cantilever deflection during jump-off contact and the spring constant of the cantilever (Cappella *et al.*, 1997). Hence, by assessing the distance of the trough to the rest position, the maximum adhesion force can be calculated by considering Hookes Law, which is –

$$F = -kd$$

(Eq 2.1)

where k is the spring constant of the cantilever and d is the distance of deflection of the cantilever from its rest position (Kappl and Butt, 2002). The adhesion forces calculated can then be used to form a force histogram, to show the distribution of forces.

It should be noted that this distance recorded in the raw data is not the real tip-sample distance, but a distance between the rest position of the cantilever and the sample surface. This difference is due to the presence of cantilever deflection and sample deformation. This means that the force-distance curve does not reproduce tip-sample interactions, but is instead a convolution of tip-sample interaction and elastic force of the cantilever (Cappella *et al.*, 1997). Although this can be corrected for by consideration of the Hooke's elastic potential of the cantilever and the sample deformation, due to the complexity of the analysis required it was not undertaken in this work (Cappella and Dieler, 1999).

Chapter 3

Characterization and Quantification of Particle Contact Area

3.1. Introduction

3.1.1. Contact Area

As discussed in the introduction, van der Waals forces and surface energy are of great importance in particle adhesion, and the magnitude of such forces are also dependent on contact area. For van der Waals forces, an increase in the contact area will lead to an increase in the area over which the short range forces can act. Surface free energy is calculated for a unit area of a solid, and is related to the work of adhesion that must be done to separate two surfaces. Therefore, in order to calculate the work of adhesion and relate this to particle-particle contact, the contact area must be calculated.

A limitation of AFM-based force measurements of individual particulate interactions is that it has not been possible to fully estimate the area of interaction. This has limited the ability of experimenters to undertake

quantitative comparisons of forces between different particles. Several methods have been used previously with varying degrees of success to attempt to characterise the contact area, including the use of SEM observations, nanoindentation of the contacting asperity into soft polymeric films, and calculation of theoretical contact areas (Bowen et al., 1995; Beach et al., 2002; Podczeczek et al., 1996). Without knowledge of contact area, large numbers of individual particle measurements would be required in order to make valid comparisons between different types of particles. This is impractical due to the large amount of time this would take and also negates the advantages of undertaking single particle measurements.

3.1.2. Pressurised Metered Dose Inhalers

Salbutamol sulphate is a short acting selective β_2 agonist used for the treatment of asthma and chronic obstructive airway disease. Its action is due to the chemical structure shown in figure 3.1, which is similar to that of adrenaline. It may be administered by injection, the oral route as tablets, or more commonly by inhalation. The two most common types of device used, in order to deliver the drug by inhalation, are the dry power inhaler (DPI), which is discussed in chapter 4, and the pressurised metered dose inhaler (pMDI). In pMDI's, the drug is dispersed in a pressurised canister containing propellant. Following activation of the canister, a unit amount of the drug in propellant is emitted. The propellant then evaporates rapidly leading to particles of the drug being released.

3.1.3. Aim

In this study, particles of salbutamol sulphate produced using both the SEDSTM technique and micronisation were mounted on to AFM probes and force data was acquired in a liquid environment in order to remove the effect of capillary forces between particles. The liquid chosen was 2H 3H perfluoropentane as it has industrial applications as a model propellant system

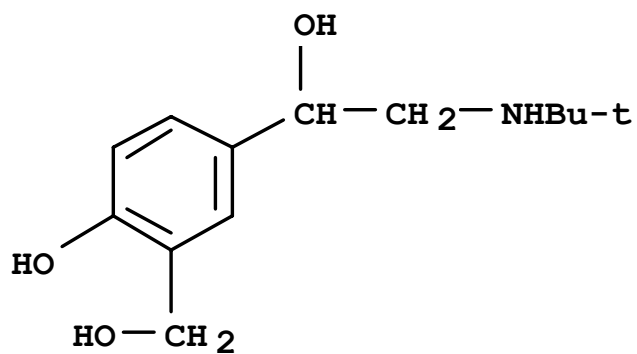


Figure 3.1. Chemical structure of salbutamol.

for simulation of environments in pressurized inhaler systems (Bosewell et al., 1998). The contact area involved in the interaction was then assessed by using a method first suggested by Neto and Craig (2001) using tip characterisation gratings to characterise colloidal probe particles. This method has been adapted to estimate the contact area of pharmaceutical particles involved in AFM force distance measurements. By relating this to the force measurements, a quantitative comparison in terms of force of interaction per unit area and work of adhesion was made between micronised and SEDS™ salbutamol.

3.2. Methods

Samples of micronised salbutamol (Nektar sample no 020/99-03) and SEDS™ salbutamol (Nektar sample no 0141025) were obtained from Nektar. Particle size data was acquired using the aerosizer technique (Aerosizer Tsi Inc., USA), and showed that the d_{50} particle size of the micronised salbutamol was 1.46 μm , with d_{10} and d_{90} values of 0.75 μm and 3.45 μm respectively, and that the d_{50} particle size of the SEDS™ material was 4.62 μm with d_{10} and d_{90} values of 1.07 μm and 12.33 μm respectively. The methods used for particle and substrate imaging with AFM and SEM, along with particle addition to AFM tips and force measurements were conducted as described in the materials and methods section.

In order to demonstrate the difference between the two samples of salbutamol, two tips were prepared initially, one with micronised salbutamol and one with SEDS™ salbutamol. These tips were then compared to the controls of a blank, plasma etched AFM tip and an AFM tip dipped in glue to ensure it was the particle interacting with the surface.

3.2.1. Tip Imaging

The 'particle' tips were imaged using a tip characterisation grating (TGT01, NT-MDT, Moscow) which consists of an array of inverted sharp tips as

shown in figure 3.2. As the cantilevers were scanned across the grid, the particles on the tips were imaged due to an artefact of AFM known as tip imaging (Kitching et al., 1999; Villarrubia, 1997). This occurs when the dimensions of features on a sample surface are sharper than that of the imaging probe. This is illustrated in figure 3.3 (a) and (b). In figure 3 (a), the usual situation that occurs in AFM is seen, whereby the tip is sharper than the asperities of the sample, leading to an image largely due to the sample morphology. However in (b), the sample has features that are sharper than that of the tip, which causes changes in cantilever deflection, due to the surface features of the tip and not the sample surface. This effectively creates an image of the probe and not the sample surface, as shown in figure 3.4. The image produced is a convolution of the features of the tip and the sample. However, this effect was not considered to be critical because the cone angle of the characteriser tip is 20° , compared to 70° for the contact tips employed in this study.

A $10\ \mu\text{m} \times 10\ \mu\text{m}$ image was acquired of each tip using a scan rate of approximately $0.5\ \mu\text{m/s}$. To show that the particles were being imaged, a plasma etched cantilever with no particle added was imaged using the same conditions as a control. Following imaging of the particle-coated tips, they were then re-examined under the SEM to ensure that the particles were still present and had not been removed by imaging, and that no changes in the structure of the particle had occurred.

3.2.2. Image Analysis

Images were analysed using SPIP software (Image Metrology ApS, Denmark). The images were first passed through a median filter in order to reduce the image noise. Because the tip characterisation grating caused the particle to be imaged repeatedly, three such repeats of the particle were chosen, and cross-sections of each were obtained in both the orthogonal X and Y directions. From these, the radius of a sphere that would fit these cross sections was calculated for both the X and Y direction. Small changes

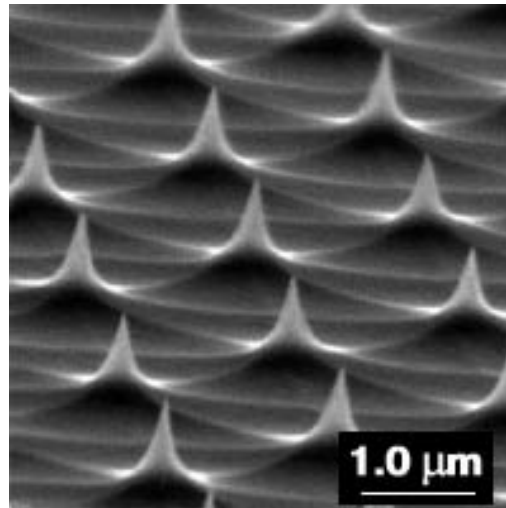


Figure 3.2. Tip imaging grid (taken from www.nanoandmore.com). It can be seen that the grid consists of a series of sharp asperities, which will cause the artefact of tip imaging.

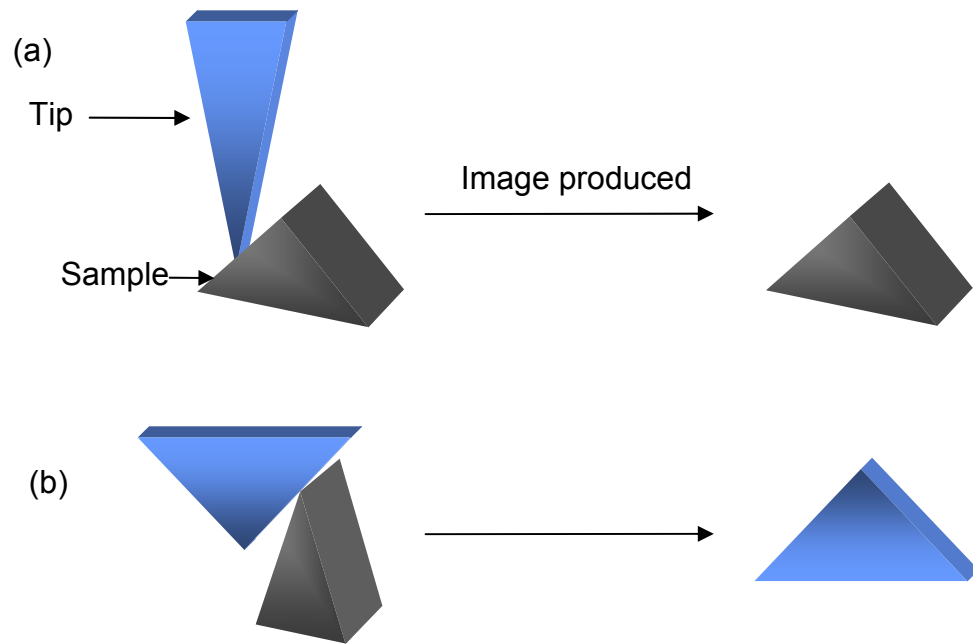


Figure 3.3. The AFM artefact of tip imaging.

- (a) The normal situation where the tip images the sample, causing an image of the sample.
- (b) Tip imaging where the asperity is sharper than the tip, leading to an image of the tip.

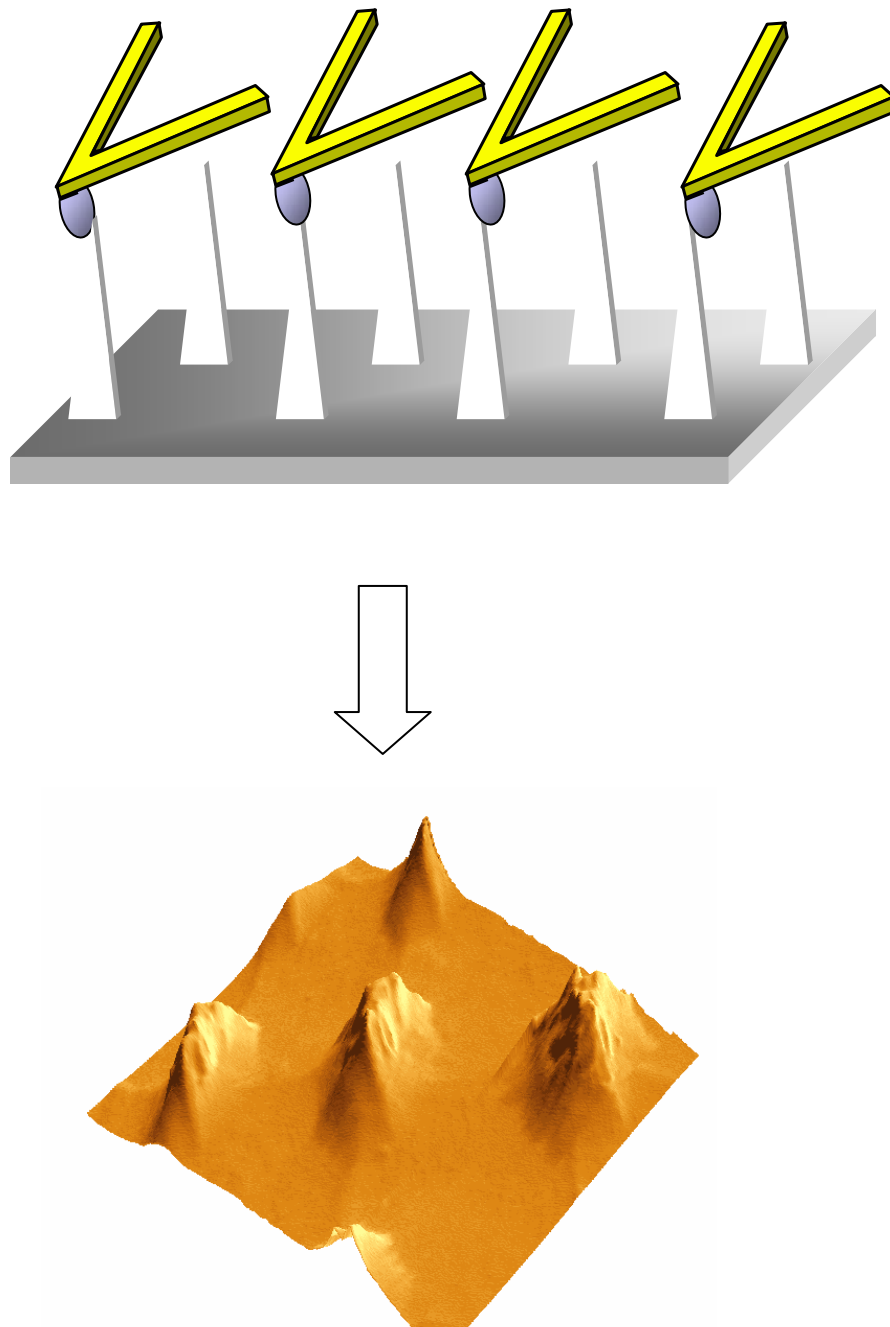


Figure 3.4. Tip imaging of particle on the end of an AFM cantilever. The resulting 3D image shows the image of a single asperity repeated.

were seen in the cross sectional data for each of the three repeats taken from the images. Such variations may have been due to environmental noise, but also possibly due to variation in the sharp features of the imaging grid causing small changes in the surface area. The average fitted sphere was then used to calculate the work and force per unit area.

3.2.3. Force Per Unit Area

Force per unit area was calculated using two methods. The first was an approximation of the contact area by using the radius of the asperity to calculate the area of a half sphere, and then dividing the force data by this value. The second involved a determination of contact area based on the mechanics of the particle and substrate, as described below.

3.2.4. Contact Mechanics Calculation of Particle Against Surface

The calculation of contact area using mechanics is shown schematically in figure 3.5. When a particle comes into contact with a surface, changes in the contact area will occur due to deformation, which will be related to the Young's modulus (E) of the surfaces in contact. If the Young's modulus of the particle (E_1) is greater than that of the surface (E_2), then the particle will deform the surface. However, some particle deformation may also occur meaning that a contact radius (R_C), that is a combination of both the surface and particle deformation, will result (Zimon, 1982; Tabor, 1948). This is defined by the equation –

$$\frac{1}{R_C} = \frac{1}{R_1} + \frac{1}{R_2}$$

(Eq 3.1)

where R_1 is the radius of the particle and R_2 is the radius of the indent in the substrate (Podczeck et al., 1996).

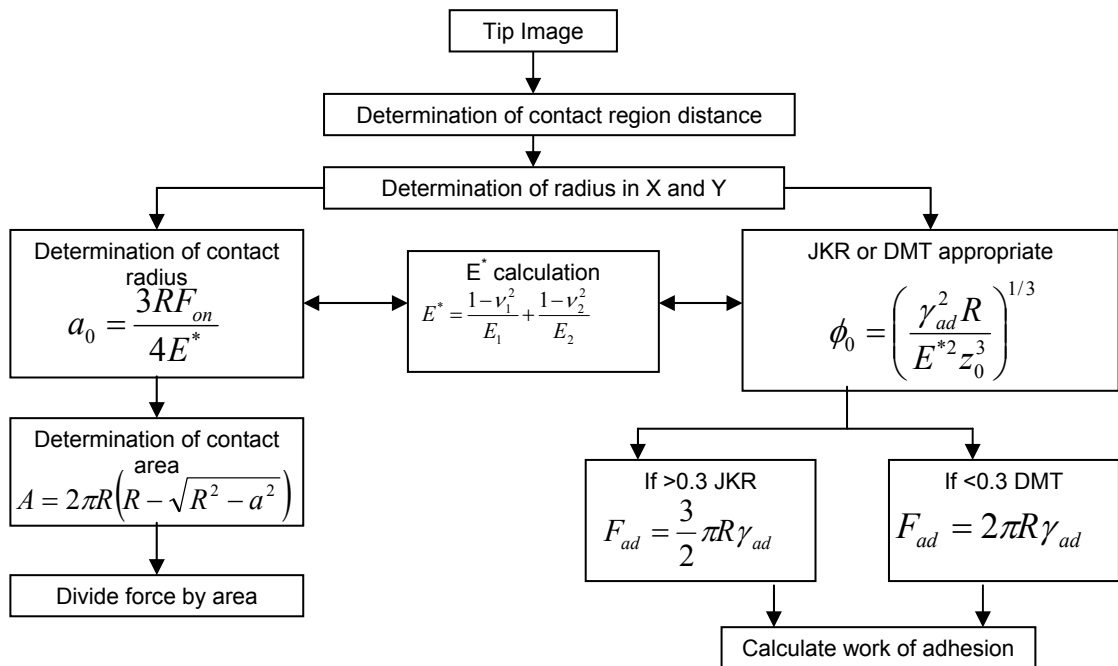


Figure 3.5. Schematic representation of the calculations undertaken to calculate contact area by consideration of mechanical properties and work of adhesion.

In order to determine the contact radius, contact mode imaging of the HOPG surface was undertaken before and after force measurements were undertaken with both a blank tip and a tip with a particle added. No changes were seen in the surface structure following the measurements, which showed that the HOPG was deforming elastically and the tips left no indent. Because of this, the radius of the asperity was taken as the contact radius, and the Hertz equation (Eq 1.5) was used to calculate contact radius a_0 . The value of ν for the HOPG and salbutamol was 0.3 (Burnham and Colton, 1989; Roberts et al., 1991). The Young's modulus of HOPG was taken to be 225 MPa (Burnham and Colton, 1989). The Young's modulus of salbutamol was not determined, however most crystalline drug compounds have a value in the range of 5 – 10 GPa (Duncan-Hewitt and Weatherly, 1989; Roberts and Rowe, 1987; Roberts et al., 1991). From this, the Young's modulus of both the micronised and SEDSTM salbutamol was taken as being 10 GPa. Calculations were performed using a value of 5 GPa in order to see the effect this change would have on the values obtained for the Young's modulus and contact area. The reduced Young's modulus was calculated by using equation 1.6, as shown below -

$$\frac{1}{E^*} = \left(\frac{1-\nu_1^2}{E_1} \right) + \left(\frac{1-\nu_2^2}{E_2} \right)$$

(Eq 1.6)

$$\frac{1}{E^*} = \left(\frac{1-0.3^2}{5^9} \right) + \left(\frac{1-0.3^2}{225^6} \right)$$

E^* was found to decrease to 236.8 MPa. From this, Hertz theory (equation 1.5) was used to calculate the contact radius of each particle. If the SEDSTM particle is used as an example, and F_{on} is 15 nN, then -

$$a_0^3 = \frac{3F_{on}R}{4E^*}$$

(Eq 1.5)

$$a_0 = \sqrt[3]{\frac{3 \times 15^{-9} \times 0.223^{-6}}{4 \times 236.8^6}}$$

The a_0 value was calculated as 0.022 μm , which was the same as the value for the SEDSTM particle calculated using the higher Young's modulus. A similar result was also found for the micronised particle.

Using the calculated values of a_0 and R , the area of contact (A) of the particle on the surface was calculated using the equation –

$$A = 2\pi R(R - \sqrt{R^2 - a_0^2})$$

(Eq 3.2)

The contact area was then related to force data obtained for each of the particles by division of the force data by the surface area. The force distributions were then re-plotted using this corrected data.

3.2.5. Work of Adhesion

The calculation of work of adhesion is shown schematically in figure 3.5. In order to investigate the work of adhesion, the Tabor equation was used, as discussed in chapter 1. To define ϕ_0 , the particle and the surface were assumed to come into atomic contact, so the value of z_0 was taken to be the average atomic diameter of carbon (0.154 nm). The value of γ_{ad} was calculated from the surface free energy values determined using inverse gas chromatography (Feeley et al., 1998). For both sets of data the value of ϕ_0 was found to be above 0.3, indicating that the JKR model was more appropriate.

3.2.6. Reproducibility

In order to demonstrate reproducibility, two additional tips with SEDS™ material were made, and used to perform force measurements and tip imaging as described above. Following this, the contact areas were characterised using the contact mechanics approach, and the pre and post correction force results of these tips and the initial SEDS™ tip were examined.

3.3. Results

3.3.1. Images

The SEM images of the micronised salbutamol are shown in figure 3.6. This shows the presence of several large structures approximately 100 μm in diameter. By zooming in on the structures it can be seen that they are formed by aggregation of smaller particles, the smaller particles varying in size from 0.5 μm to 3 μm . The SEDS™ SEM images are shown in figure 3.7. These show the presence of particles ranging in size from 1 μm to 5 μm , and are not as aggregated as the micronised material.

The AFM images of the micronised salbutamol are shown in figure 3.8 (a) – (d), and consist of a high resolution image of a particle of micronised salbutamol. It appears to contain a number of small domains. From observing a larger scan area, there appear to be numerous small particles in the image similar in dimensions to the small areas evident on the circled large particle. This, and the marked demarcation present on the large particle, make it likely that the particle examined is composed of smaller fragments.

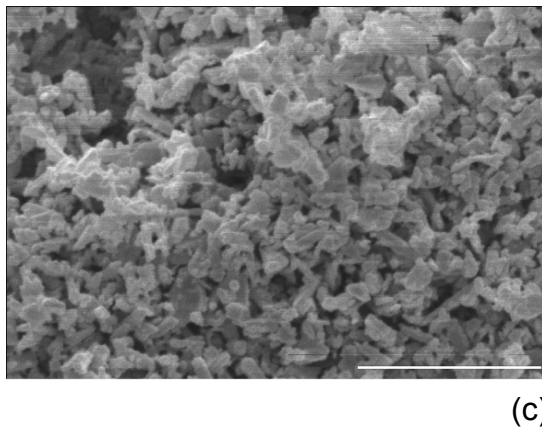
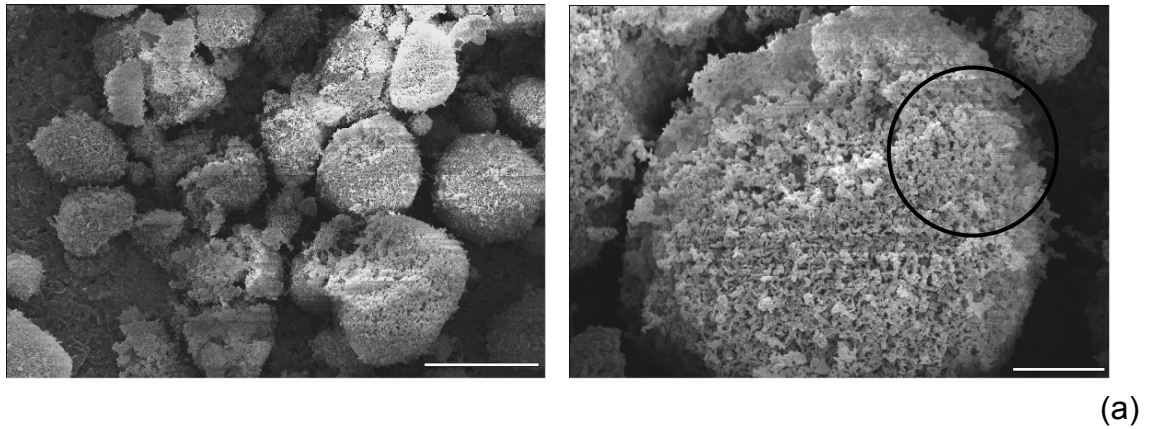


Figure 3.6. SEM images of micronised salbutamol.

- (a) Overview SEM image, bar length 100 μm .
- (b) Zoom in of circled particle, bar length 20 μm .
- (c) Zoom in on centre of particle, bar length 10 μm .

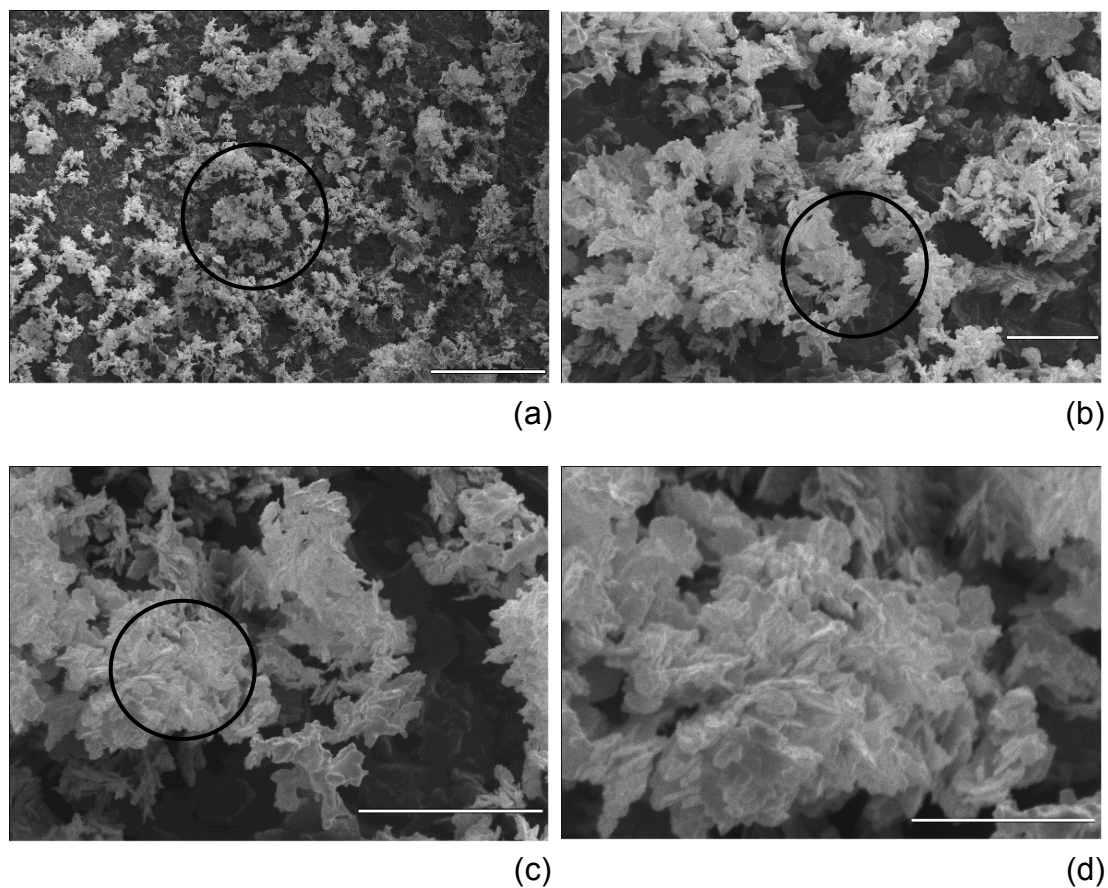


Figure 3.7. SEM images of SEDS™ salbutamol.

- (a) Overview SEM image, bar length 100 μm .
- (b) Zoom in on circled area, bar length 20 μm .
- (c) Zoom in on circled area, bar length 20 μm .
- (d) Zoom in on circled area, bar length 10 μm .

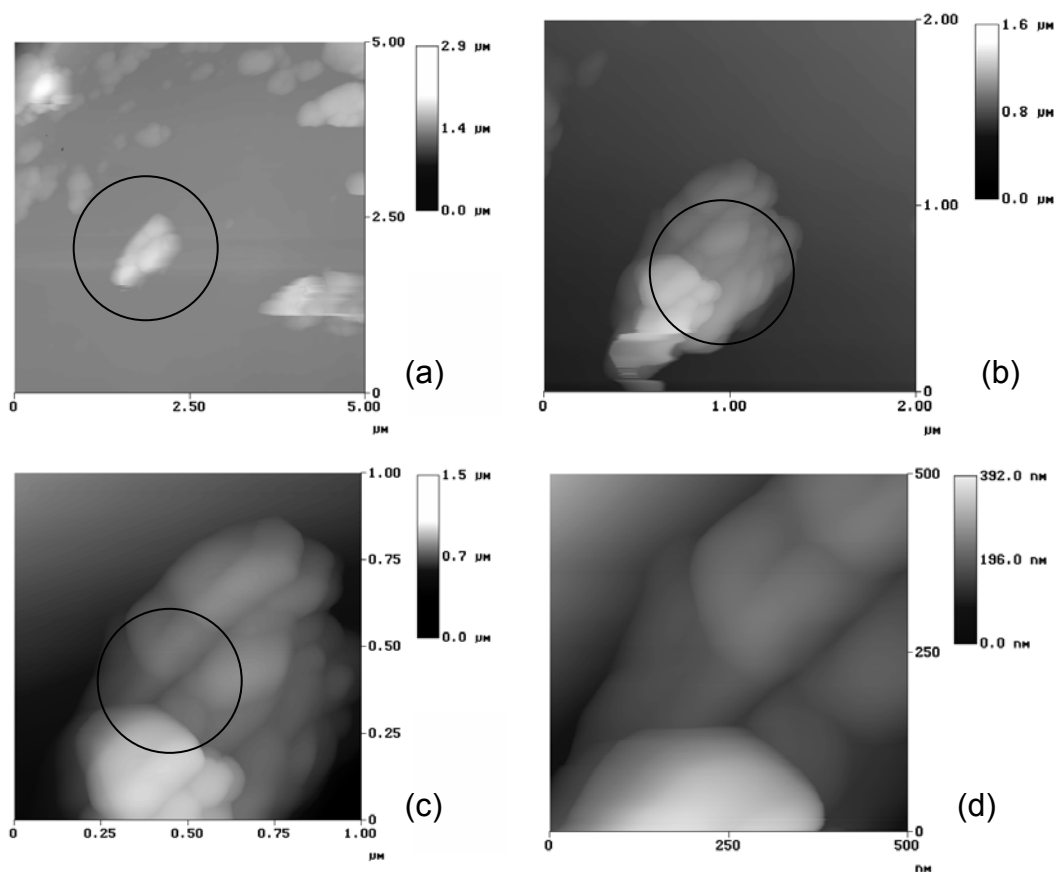


Figure 3.8. AFM images of micronised salbutamol.

- (a) Large area showing a number of small particles.
- (b) Zoom in on the particle circled in figure (a).
- (c) Zoom in on the particle area circled in figure (b).
- (d) Zoom in on the particle area circled in figure (c).

A cross section of the data in figure 3.8 (d) is shown in figure 3.9. The ridges were found to vary from 5.7 nm to 61.1 nm. The cross section showed the particle to have a rough surface, which could be due to morphology of single particles as the size of section is smaller than the d_{10} value.

The AFM images of the SEDSTM material are shown in figure 3.10 (a) to (c), and show difference in microstructure compared to micronised salbutamol. The SEDSTM material appears to be composed of globular domains that form from one particle as opposed to agglomerated smaller particles. This conclusion was drawn because of the low level of distinction between each of the globular units, as well as the reproducibility of this result.

A cross section of 3.10 (b) is shown in figure 3.11. Here the steps were found to vary from 15.3 nm to 510 nm. The cross section image shows the surface to be of smooth texture, and also shows that the particle is unlikely to be composed of smaller units due to the size of the image.

An image of the HOPG is shown in figure 3.12. This image demonstrates the expected smoothness of the surface. The roughness (R_q) was determined to be 0.207 nm. The observed steps were also measured and were found to vary from 0.22 nm to 2.55 nm in height. The carbon-carbon bond length in graphite layers is 0.142 nm, with layers being spaced 0.34 nm apart (Daintith, 1996). Hence the HOPG steps observed here are approximately 2 to 8 molecular layers thick.

The SEM images of the drug particles on the tips are shown in figure 3.13. These images show that particles had been successfully added on to the tips. In this example the micronised salbutamol tip (figure 3.13 (a)) showed that one elongated particle expressing an irregular morphology with a diameter of approximately 10 μm had been adhered to the tip. The SEDSTM tip (figure 3.13 (b)) also appeared to consist of one particle, again approximately 10 μm in diameter.

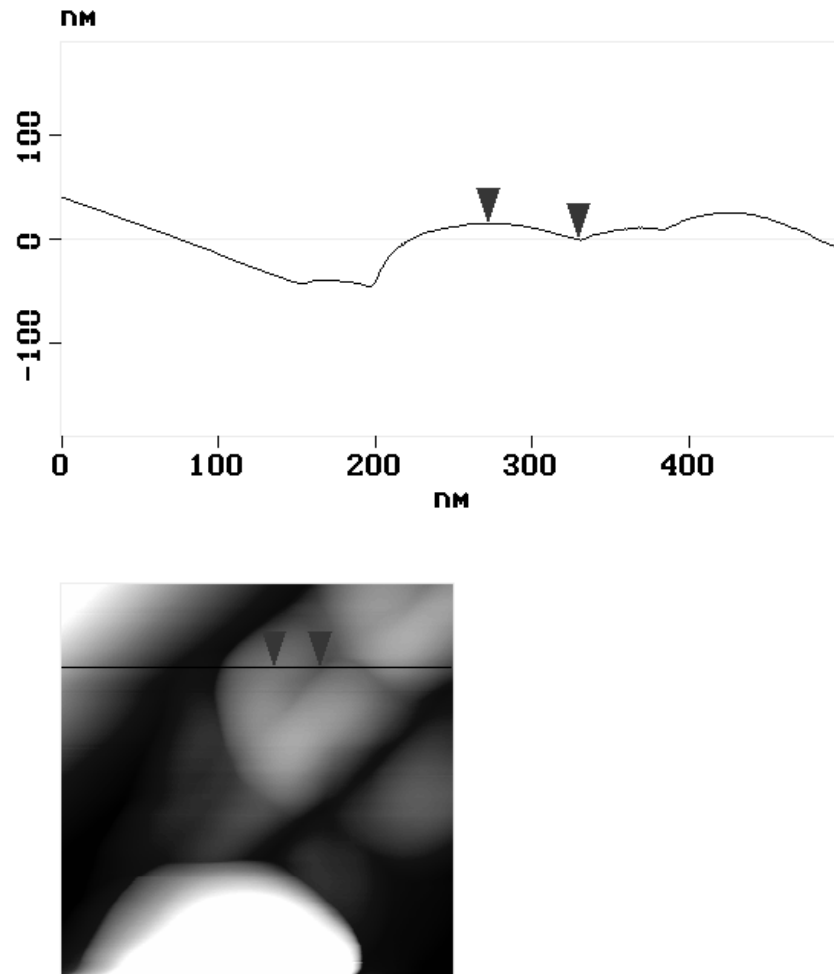


Figure 3.9. Cross section of micronised salbutamol showing ridges in a particle.

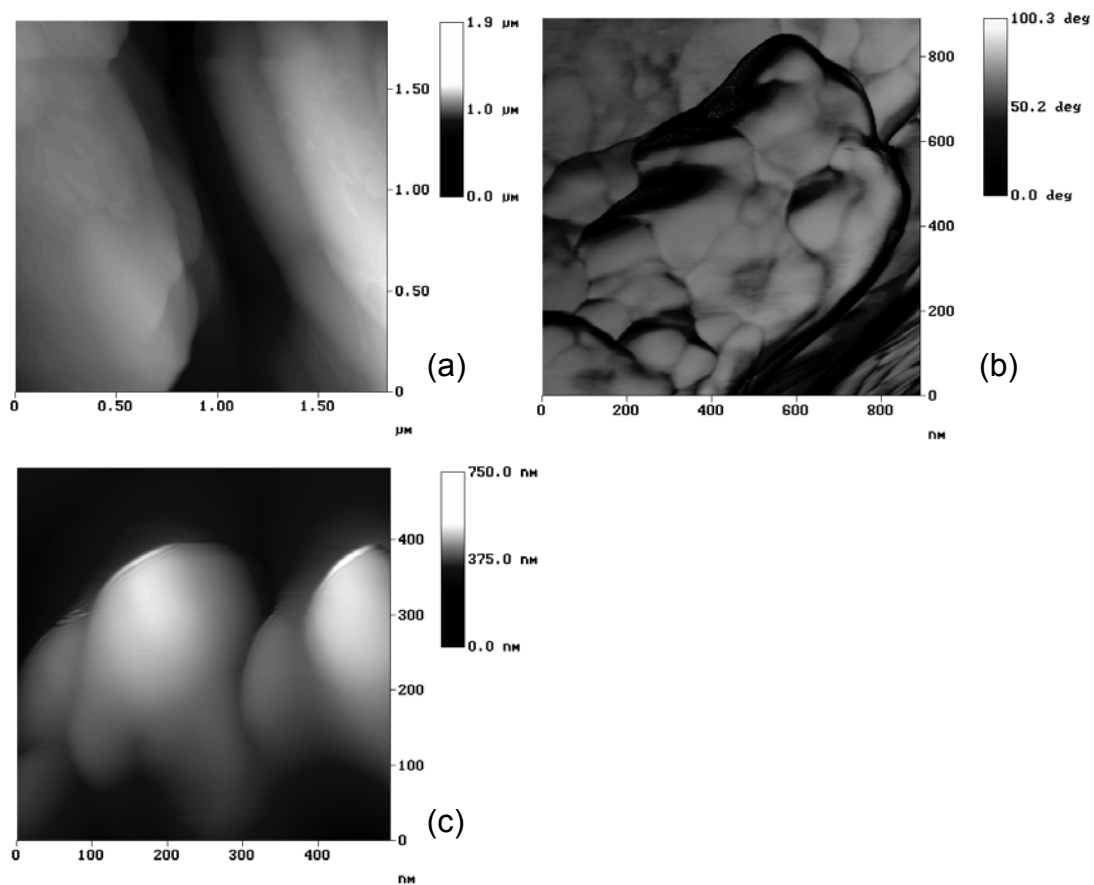


Figure 3.10. AFM height and phase images of SEDSTM processed salbutamol.

- (a) Height image of two particles.
- (b) Phase image of a different SEDSTM particle.
- (c) Height image of a different particle.

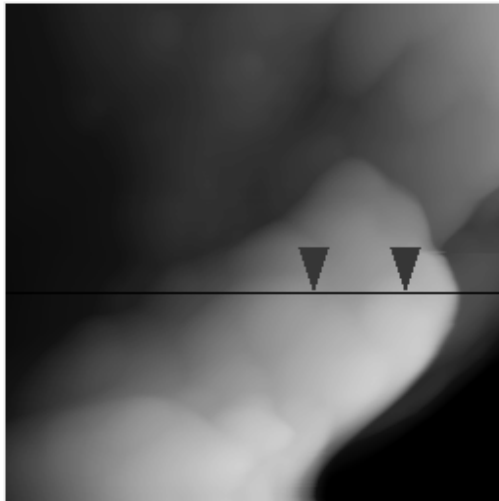
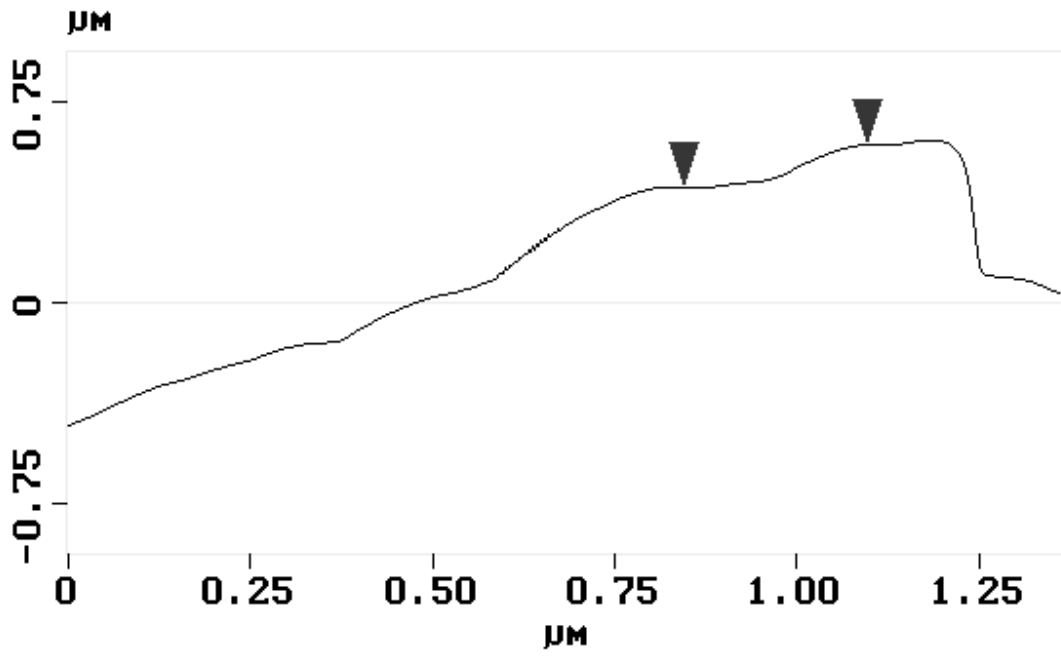


Figure 3.11. Cross-section of SEDS™ particle in figure 3.10 (b).

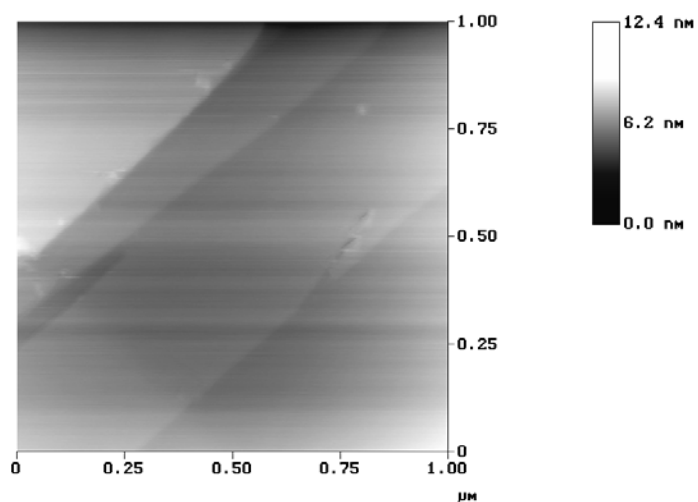


Figure 3.12. Image of HOPG substrate. The substrate was found to be flat with steps present that are 2 to 8 molecular layers thick.

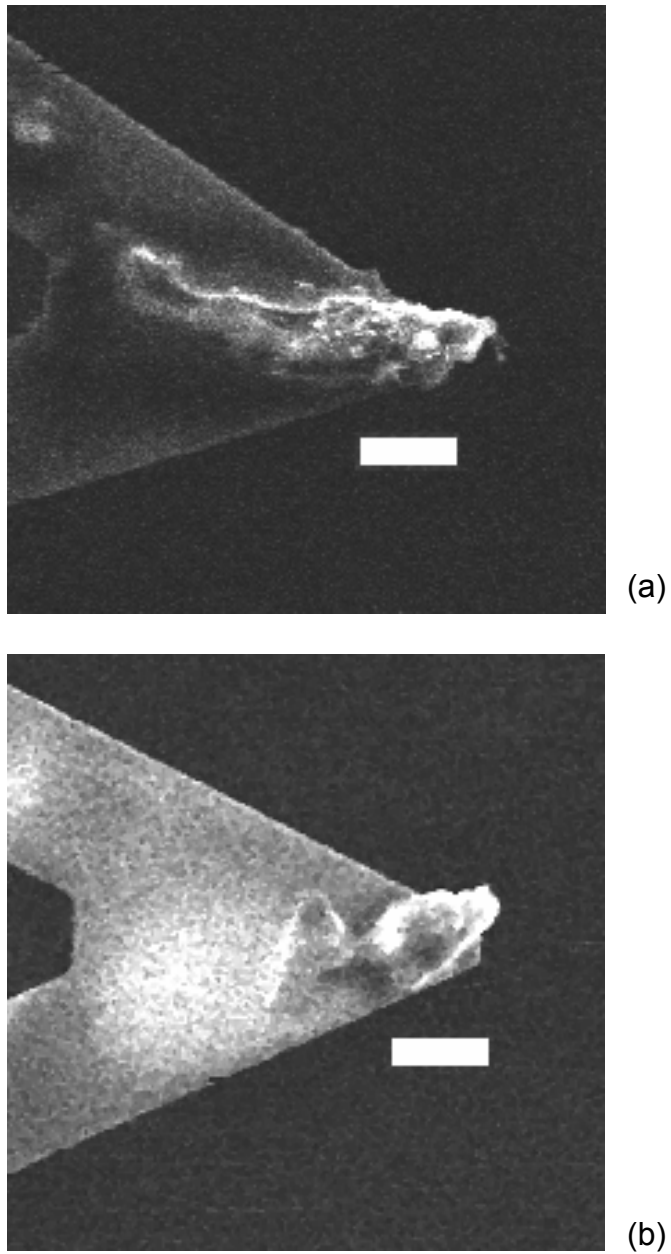


Figure 3.13. SEM images of tips with (a) micronised and (b) SEDS™ salbutamol added onto tips (bar length in both images is 10 μm).

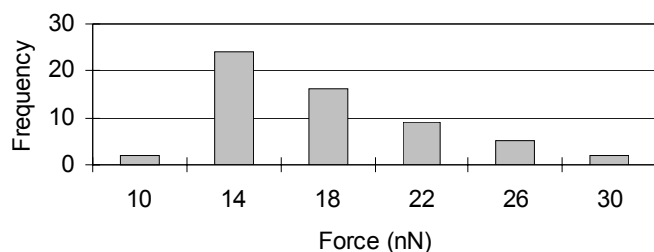
3.3.2. Force Distance Data

Force data for the different particles and controls are displayed in figure 3.14. Regression coefficients were calculated for each set of data, and indicated that, although the frequency distribution appeared skewed, there was still a normal distribution present for all the observed interactions. This means that the distribution can be characterised by the geometric mean and standard deviation. The mean force for the SEDSTM material is 4.2 nN (SD 0.8 nN) which is lower than that observed for the micronised material at 14.1 nN (SD 2.5 nN). The plasma etched tip however, had an average force of 0.4 nN (SD 0.1 nN) and the tip in glue had a corresponding average of 10.2 nN (SD 2.1 nN).

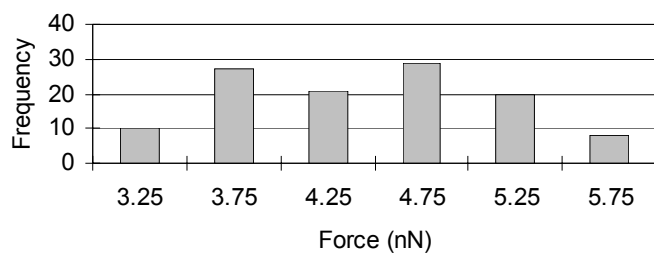
3.3.3. Tip Imaging

The tip images of the particles and the control are displayed in figure 3.15. The tip image for the micronised particle in figure 3.15 (a) shows there were two asperities of sufficient height to be imaged by the grid. The larger asperity was approximately 1 μm wide, 0.5 μm long and 0.35 μm high, while the smaller asperity was 0.6 μm wide, 0.35 μm long and 0.15 μm high. The difference in height between the two was approximately 0.2 μm . Using the contact region distance (region (b) to (c) in figure 2.6) it was established that the smaller asperity would not be involved in the interaction.

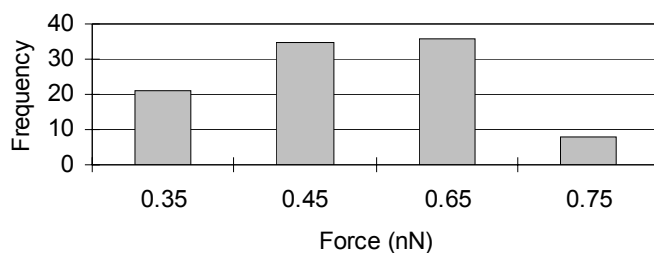
An AFM image of the SEDSTM salbutamol is shown in figure 3.15 (b). This image shows the presence of an asperity that is approximately 1.5 μm wide, 1.2 μm long and 0.45 μm high. The AFM image is also different from the micronised salbutamol image, in that the asperity appears to be more spherical in shape with a flatter edge at the top.



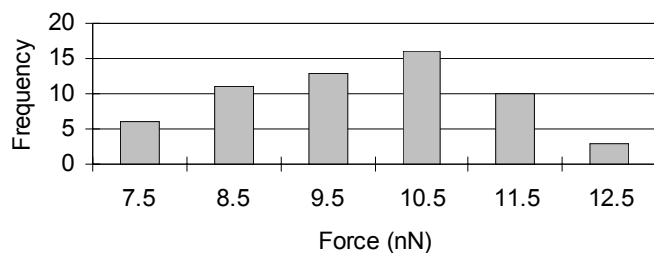
(a)



(b)



(c)



(d)

Figure 3.14. Frequency distributions for salbutamol particles and control tips. The X-axis values refer to the forces where x nN means greater than x but less than the next force value.

(a) Micronised salbutamol.

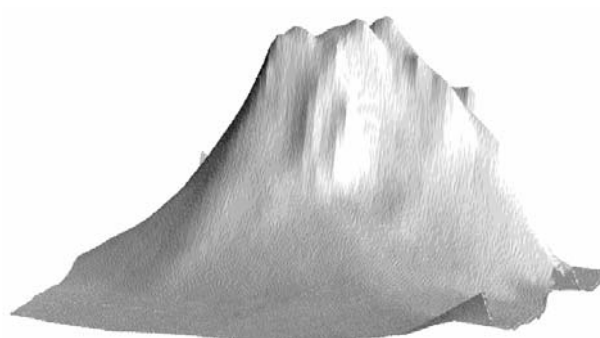
(b) SEDS™ salbutamol.

(c) Blank AFM tip.

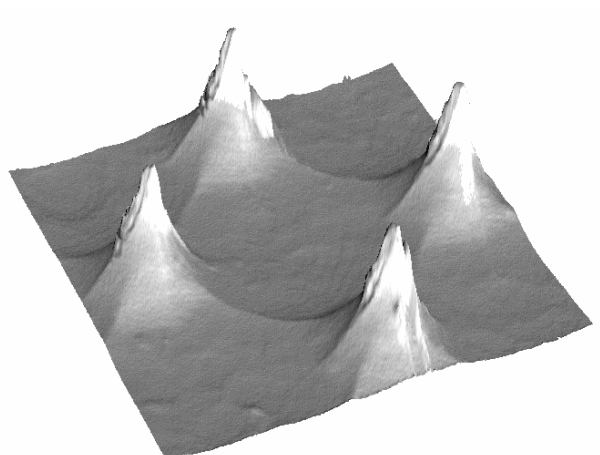
(d) AFM tip dipped in glue.



(a)



(b)



(c)

Figure 3.15. Tip images of contacting asperities.

(a) Micronised salbutamol ($XY = 1.3 \mu\text{m}$, $Z = 500 \text{ nm}$).

(b) SEDSTM salbutamol ($XY = 1.5 \mu\text{m}$, $Z = 380 \text{ nm}$).

(c) Blank AFM tip ($XY = 4 \mu\text{m}$, $Z = 400 \text{ nm}$).

The AFM image of the control tip (figure 3.15 (c)) shows a series of peaks of a more regular cone like structure of approximate height $0.35\ \mu\text{m}$ and a width of $1.5\ \mu\text{m}$. This is very different to the images seen with the particles on the end of the tip, and consistent with the expected structure for an AFM tip.

The tips were re-examined under the SEM following the experiment (images not shown). The particles were still present on the tips with no obvious change in the shape of the particle compared to the initial SEM images.

3.3.4. Half Sphere Approximation

The surface area calculated for the micronised, SEDSTM and control tips, using the half sphere approach, are shown in table 3.1. It can be seen that each area is different. The radius of the micronised particle was $0.158\ \mu\text{m}$, and the calculated area is $156 \times 10^{-3}\ \mu\text{m}^2$. This is smaller than that seen for the SEDSTM material which had a particle radius of $0.223\ \mu\text{m}$ and an area of $312 \times 10^{-3}\ \mu\text{m}^2$.

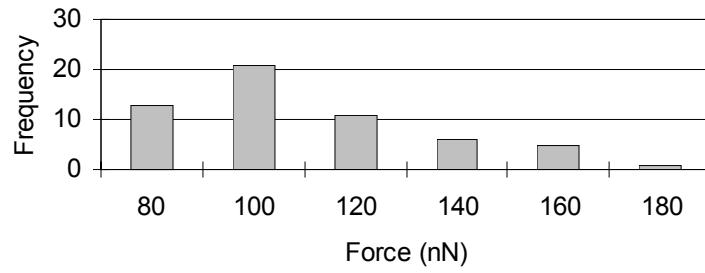
The force data following correction for half sphere surface area are presented in figure 3.16. The average force per unit area of the micronised particle is $100.9\ \text{nN}/\mu\text{m}^2$ (SD $9.2\ \text{nN}/\mu\text{m}^2$). This is in comparison with the SEDSTM tip where the average force per unit area is $13.5\ \text{nN}/\mu\text{m}^2$ (SD $2.3\ \text{nN}/\mu\text{m}^2$).

3.3.5. Contact Mechanics Approach

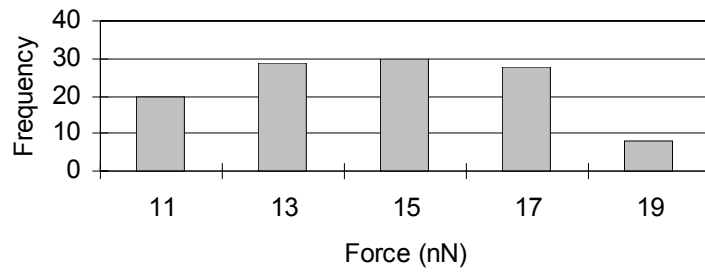
The surface area calculated for the micronised and SEDSTM salbutamol considering the contact mechanical properties are shown in Table 3.1. The area of the micronised particle is $1.1 \times 10^{-3}\ \mu\text{m}^2$ and is smaller than that seen for the SEDSTM material of $1.4 \times 10^{-3}\ \mu\text{m}^2$.

Particle	Half sphere area (μm^2)	Contact mechanics area (μm^2)
Micronised salbutamol	156×10^{-3}	1.1×10^{-3}
SEDS TM salbutamol	312×10^{-3}	1.4×10^{-3}

Table 3.1. Areas for micronised salbutamol and SEDSTM salbutamol calculated using half sphere and contact mechanics approaches.



(a)



(b)

Figure 3.16. Data corrected for half sphere area.

(a) Micronised salbutamol.

(b) SEDS™ salbutamol.

The force data following correction for mechanical calculated surface area are presented in Figure 3.17. The average force per unit area of the micronised particle is 13.0 mN/ μm^2 (SD 2.3 mN/ μm^2). This is in comparison with the SEDSTM tip where the average force per unit area is 3.0 mN/ μm^2 (SD 0.6 mN/ μm^2).

3.3.6. Work of Adhesion

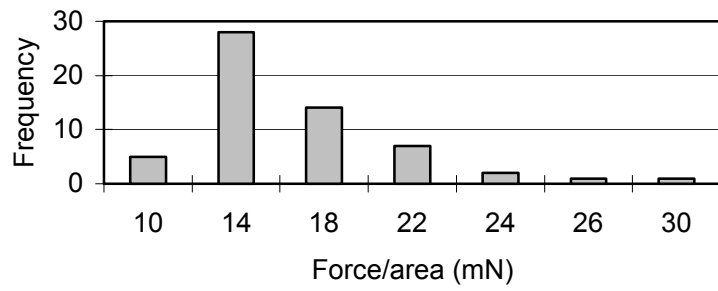
The average work of adhesion to the HOPG of the particles calculated, using the JKR theory described above, is shown in figure 3.18. The average work of adhesion per unit area for the micronised particle was 19.0 mJm⁻² (SD 3.4 mJm⁻²). This is compared to an average value of 4.0 mJm⁻² (SD 0.8 mJm⁻²) for the SEDSTM tip.

3.3.7. Reproduceability

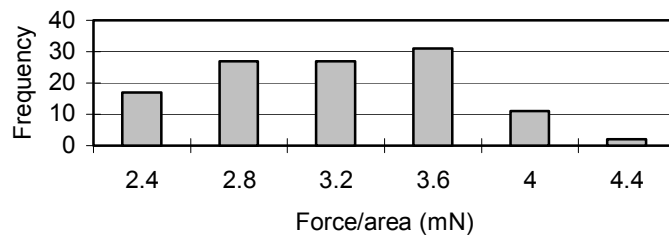
Before correction, the average adhesion force of the three SEDSTM salbutamol tips averaged out is 6.5 nN (SD 3.5 nN), and following correction the force becomes 3.4 mN/ μm^2 (SD 1.3 mN/ μm^2). In order to illustrate the reduction in variation between the different tips, the coefficient of variation (CV) was used, which is calculated by –

$$CV = \frac{SD}{Averageforce} \times 100 \quad (\text{Eq 3.3})$$

The CV before correction is 54%, and following correction drops to a value of 39%.



(a)

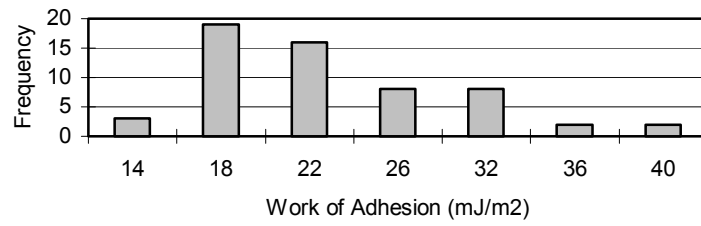


(b)

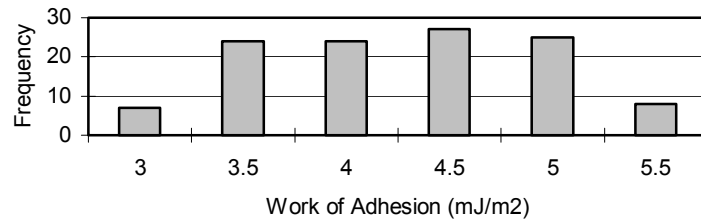
Figure 3.17. Force corrected for area calculated using the contact mechanics approach.

(a) Micronised salbutamol.

(b) SEDS™ salbutamol.



(a)



(b)

Figure 3.18. Work of adhesion calculated for micronised and SEDSTM salbutamol.

(a) Micronised salbutamol.

(b) SEDSTM salbutamol.

3.4. Discussion

3.4.1. Images

The SEM and AFM images (figures 3.6, 3.8 and 3.9) of the micronised salbutamol showed that the particles were highly aggregated. This is attributed to the high surface energy associated with the large surface area created from milling. In an attempt to reduce energy, grouping occurs.

The salbutamol particles were also of a smaller size and possessed a coarser morphology compared to the SEDSTM processed material, which was evident on the cross section taken. The unit cell dimensions have been given as $a=21.654$, $b=8.798$, $c=14.565$ Å (Beale and Grainger, 1972). This did not appear to correlate with the ridges measured for the sample in figure 3.9, which indicated they are due to the fracturing process inherent in micronisation.

The SEM of the SEDSTM material (figure 3.7) showed the presence of more dispersed smoother, flatter particles of larger size than the micronised material. AFM (figures 3.10 and 3.11) showed the presence of smooth globular domains on the particle surface that were not evident in micronised samples and are not consistent with normal crystallization, indicating they were a result of SEDSTM processing. A cross section showed the particles to be smoother than the micronised material with larger distances between globular domains. The heights between the various globular regions were measured and showed little similarity to the unit cell data.

The SEM images of the AFM cantilever (figure 3.13) showed that both tips were completely covered by the drug particles. Consequently, it was unlikely that it was the AFM tip contacting the sample surface during subsequent force measurements.

3.4.2. Force Data

The uncorrected force data for the salbutamol particles showed that there was a difference between the mean values of control data (figure 3.14 (c) and (d)) and the data for the particles (figure 3.14 (a) and (b)). The force measurements of the tip in glue do overlap slightly with those obtained for the micronised particle. Although, when this data is examined in combination with the images, it is unlikely that the cantilever tip is responsible for the interaction observed with the 'particle' tips.

3.4.3. Tip Imaging Data

Both the micronised and SEDS™ salbutamol tip images (figures 3.15 (a) and (b)) showed distinct differences between the SEM and AFM data. This indicates that there is an area of both of the salbutamol particles which protrudes from the surface, and is responsible for the observed interaction. In consequence, if the SEM data had been used alone for contact area estimation, it would have lead to an over estimation of surface area.

The structure of the blank AFM tip control image shown in figure 3.15 (c), differs to that obtained for the particle tips shown in figures 3.15 (a) and (b). This provides further evidence that it is the particles interacting and not the substrate surface.

3.4.4. Corrected Data

The data corrected for the force per unit area (figures 3.16 and 3.17) calculated using both methods, shows in each case that the SEDS™ material has lower adhesion than the micronised. This trend is also seen for the work of adhesion calculated for each tip (figure 3.18). Materials with a high surface free energy have high adhesive forces (Zeng et al., 2001), and this result can be explained by examining the surface energy of both materials.

Previous inverse gas chromatography studies have showed that the SEDS™ salbutamol sulphate has a lower surface free energy than the micronised material (38.45 mJm^{-2} compared to 58.57 mJm^{-2}), and additionally displays lower cohesion (17.0% w/w compared to 73.6% w/w) ((Feeley et al., 1998; Feeley et al., 2001).

Because the work of adhesion is related to the surface energy of the particle, this indicates that the surface energy of the SEDS™ material is lower, as the higher surface energy of the micronised material would account for the higher adhesion observed compared to the SEDS™ material. The higher surface energy of the micronised salbutamol is also indicated in the SEM and AFM data, where these particles were found to be more aggregated than the SEDS™ counterpart, a common consequence at elevated surface energy.

3.4.5. Reproducibility

One additional rational for using the SEDS™ processed material is that the more common micronisation process leads to the generation of amorphous regions, which can, in turn lead to large variations in the properties of a drug material. Gilbert et al. (2000) showed that for salbutamol, SEDS™ material has an amorphous content of 0.13% compared to micronised material, which demonstrates a 6.2% amorphous content. As the SEDS™ has the lower level of amorphous content, it was felt that this was the better material to demonstrate reproducibility, that is there would be a lower level of variation between the individual powder particles.

The correction for surface area reduced the CV value by 28% for the SEDS™ material. Some variation is still to be expected due to a number of reasons, as illustrated in figure 3.19. There are three main reasons, the first of which is error in the imaging process, due to reasons such as noise, the AFM gain controls not responding fast enough to the changes in topography, and the tip imaging grid not being sharp enough to image all of the surface features. The second cause of error is due to the macro used to calculate

the radius. Here, difficulties in determining how far the particle is indenting into the surface and small features that are not accounted for in the radius calculation are a source of error. The final reason is due to errors in determination of the deformation of the particle and substrate. The contact radius should be calculated from the common radius of curvature. However, without an exact knowledge of how the HOPG is deforming, it is not possible to calculate this accurately.

It should also be remembered that this is a small sample size. If a larger one was used then variability would be expected to decrease further. There will also be an intrinsic variability between individual particles, as well difference due to the presence of different crystalline faces as it is not possible to preferentially orientate particles when attaching to the AFM tip.

3.5. Conclusions

In this chapter, a method of determining the contact area of asperities has been proposed in which the artefact of tip imaging has been used to produce 3D images of the contacting asperities. Following this, calculations were performed to determine the contact area so that observed contact forces could be normalized to account for differences between particles. Following correction for contact area using both a half-sphere approximation and a contact mechanics approach, the micronised particles were found to have a higher adhesion force per unit area than the SEDSTM particles. In addition, the work of adhesion was calculated using the JKR theory, as for pharmaceutical materials particle adhesion can be a critical factor during drug manufacture, processing and delivery. Individual particles of micronised and SEDSTM processed salbutamol were used to perform force measurements against a model substrate. For the micronised material the work of adhesion to HOPG was 19 mJm^{-2} (SD 3.4 mJm^{-2}). This is compared to an average value of $4.0 \text{ mJ}^{-2}\text{m}$ (SD 0.8 mJm^{-2}) for the SEDSTM material. These data are consistent with the results of previous macroscopic inverse gas chromatography studies (Feeley et al., 1998; Feeley et al., 2000).

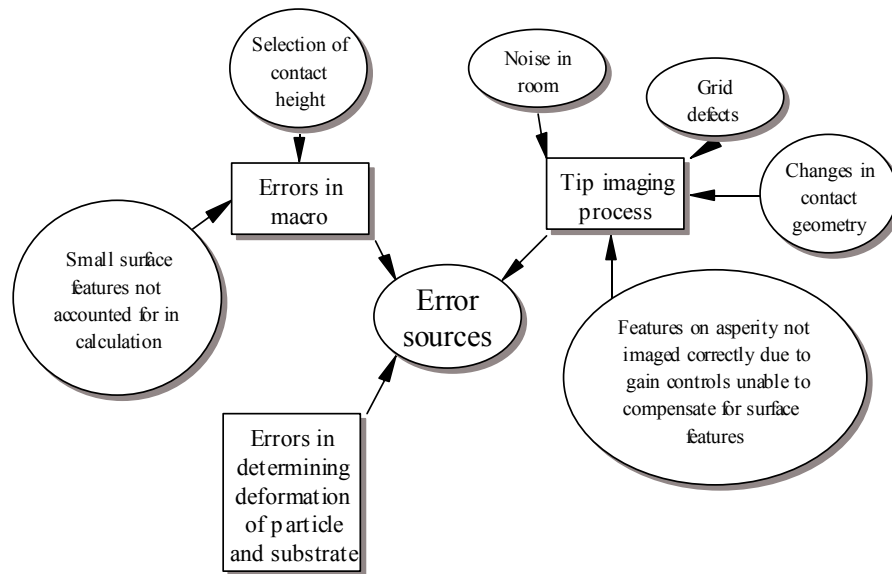


Figure 3.19. Sources of error in determination of radius of asperities.

The use of a half sphere approximation and a contact mechanics approach produce different results for the force per unit area. Because the contact mechanics approach takes into account the properties of the surfaces and press on force, this is a better method of comparing particles made from different substances. However, due to the lesser time involved in completing the calculations, the half sphere approach is still useful in providing a quick comparison between particles of the same drug.

It has also been shown that these results are reproducible, with correction for different contact areas producing similar results. However, as discussed there is still variation present due to a number of factors. It is anticipated that further research in this area will reduce the extent of such variation.

In conclusion, using an AFM-based approach it has been shown that it is possible to make direct quantitative comparisons of particulate adhesion forces in a relevant model environment between particles produced using different manufacturing techniques. This would overcome one of the key limitations frequently noted for AFM force distance data acquisition on complex pharmaceutical materials.

Chapter 4

Effect of Humidity and Contact Geometry on Adhesion

4.1. Introduction

4.1.1. Dry Powder Inhalers

The interaction between particles is fundamental for the functioning of dry powder inhalers (DPI's) used in, for example, the treatment of asthma. In the majority of these devices, small particles of a drug are adhered onto larger carrier particles (usually lactose), to allow efficient aerosolisation of the active ingredient (Podczeck *et al.*, 1996 a; Berard *et al.*, 2002). Once the particles are in the air stream, the smaller drug particles separate from the carrier and are carried into the lung. The carrier particles are too large ($>10\ \mu\text{m}$) to make the turn into the lungs and usually impact onto the back of the throat where they are swallowed. Most aerosol systems will deliver less than 10% of the administered dose to the lung, and this will be strongly affected by the surface properties of the drug and carrier particle (Buckton, 1995), but by understanding this interaction the delivered dose can be improved. While numerous inter-particulate forces are important such as the van der Waals

and electrostatic forces as discussed in chapter 1, the most dominant force is usually that of capillary interaction.

4.1.2. Capillary Forces

Capillary forces are created by the formation of liquid bridges via capillary condensation around the contact site between two surfaces as shown in figure 4.1. These forces are highly dependent on the relative humidity (RH) of the environment and have two main sources (Podczeck, 1998) -

- Hydrophilic, porous materials that trap moisture in the surface pores which can build up to form bridges
- Moisture that condenses in gaps between contiguous bodies

If a liquid has a small contact angle on a particular surface, then the vapour will spontaneously condense in cracks and pores to form bulk liquid. Because the liquid pressure is less than the air pressure, a concave meniscus will result where curvature ($1/r_1 + 1/r_2$) is related to RH by the *Kelvin equation* –

$$\left(\frac{1}{r_1} + \frac{1}{r_2}\right)^{-1} = r_K = \frac{\gamma_L V}{R_g T_p \log(p/p_s)}$$

(Eq 4.1)

where r_1 is the concave radius, r_2 is the contact radius of the meniscus (See figure 4.1), r_K is the Kelvin radius, V is the molar volume, R_g is the gas constant, T_p is the temperature and (p/p_s) is the RH (Israelachvili, 1991).

In order to show the effect of a liquid condensate on the adhesion force between a macroscopic sphere and a surface, the *Laplace pressure* (P) can be calculated –

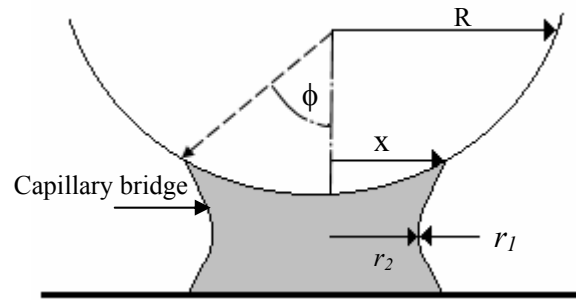


Figure 4.1. Formation of a capillary bridge between a particle and substrate, where R is the radius of the particle, r_1 is the concave radius, r_2 is the contact radius of the meniscus, Φ is the angle between the centre of gravity of the particle and the outer surface of the meniscus and x is the distance between the centre of gravity and the top of the meniscus.

$$P = \gamma_L \left(\frac{1}{r_1} + \frac{1}{r_2} \right) \approx \frac{\gamma_L}{r_1} \quad (\text{Eq 4.2})$$

where γ_L is the surface tension of the liquid (Jones *et al.*, 2002; Israelachvili, 1991).

The Laplace pressure will act to pull two surfaces together over an area πx^2 (where x is the radius from the centre of the meniscus to the top of the meniscus curve), which approximates to $2\pi R d_m$. This means that the adhesion force will be approximated by –

$$F_{ad} \approx 2\pi R d_m \left(\frac{\gamma_L}{r_1} \right) \quad (\text{Eq 4.3})$$

where R is the radius of the particle and d_m is the distance from the top of the meniscus to the base of the particle. If the angle between the centre of gravity of the particle and the outer surface of the meniscus (ϕ) is small, then –

$$d_m \approx 2r_1 \cos \theta \quad (\text{Eq 4.4})$$

From this the Laplace contribution of a spherical particle against a flat surface can be calculated by (Mc Farlane and Tabor, 1950) –

$$F_{ad} = 4\pi R \gamma_L \cos \theta \quad (\text{Eq 4.5})$$

This equation is only valid, however, if the gap between the contiguous bodies contains only very small amounts of moisture and if the adhesion is

between dissimilar materials with similar contact angles. In addition, if the surface is rough, the amount of condensed moisture needs to exceed the asperity size.

If the solid-solid contact contribution inside the liquid meniscus is added to the adhesion force, then adhesion force can be calculated using the equation –

$$F_{ad} = 4\pi R(\gamma_L \cos \theta + \gamma_{SL}) = 4\pi R\gamma_{SV} \quad (\text{Eq 4.6})$$

where γ_{SV} is the surface energy of the surface in vapour.

If the contact angles for the two materials differ, then adhesion can be calculated by –

$$F_{ad} = 2\pi R\gamma_L (\cos \theta_1 + \cos \theta_2) \quad (\text{Eq 4.7})$$

where θ_1 and θ_2 are the contact angles between the contacting surfaces and the liquid (O'Brien and Hermann, 1973).

Equations 4.5 and 4.7 are limited as there is no allowance for adjustment in the menisci and hence contact area between liquid and particle, which will vary with the liquid vapour pressure (Podczeck *et al.*, 1996 a). The equations also ignore the effect of the circumference surface tension forces ($F_{c,1}$) on the adhesion (Jones *et al.*, 2002), which is calculated by (Podczeck, 1998) -

$$F_{c,1} = 2\pi r_2 \gamma_L \quad (\text{Eq 4.8})$$

The presence of a meniscus will also reduce the liquid pressure due to its concave shape (Zimon, 1982). The liquid pressure ($F_{c,2}$) -

$$F_{c,2} = \pi r_2^2 P_{cap} \quad (\text{Eq 4.9})$$

where P_{cap} is the capillary pressure. The capillary pressure is an indication of the pressure difference between two bulk phases (liquid and gas) that are separated by a curved surface and are in a state of equilibrium (Zimon, 1982). This is calculated differently for adhesion and autoadhesion (Podczeck, 1998).

If the particle and plane surfaces have different wetting properties then the equation for capillary pressure is –

$$P_{cap} = \frac{\gamma_L}{R} \left(\frac{\cos(2 + \theta_1) + \cos \theta_2}{1 - \cos \phi} \right) \quad (\text{Eq 4.10})$$

where θ_1 and θ_2 is the contact angle for the particle and substrate surface respectively (Podczeck, 1998). However if $\theta_1 = \theta_2$, then the equation becomes (Zimon, 1982) -

$$P_{cap} = \frac{\gamma_L}{R} \left(\frac{R}{r_2} - \frac{\cos(\theta + \phi)}{1 - \cos \phi} \right) \quad (\text{Eq 4.11})$$

Therefore, the capillary force (F_c) can be calculated as

$$F_c = F_{c,1} - F_{c,2} = 2\pi r_2 \gamma_L - \pi r_2^2 P_{cap} \quad (\text{Eq 4.12})$$

In order to determine which equation is valid in which situation the interplay between all of the factors discussed above must be understood. RH changes are most significant for small contacts, where the values of r_1 and r_2 are comparable in magnitude (Xu *et al.*, 1998; Jones *et al.*, 2002). This is seen at small values of R (~100 nm, similar to the dimensions of an AFM tip) where the Laplace pressure (Eq 4.2) is predicted to decrease at high RH while the surface tension (Eq 4.8) should increase. The sum of these two opposing contributions should then lead to a decrease in adhesion at high RH (Jones *et al.*, 2002).

However, when R increases to the size of a silica bead (20 μm), the adhesion force is predicted to be constant and independent of RH, and equal to the MacFarlane and Tabor equation (Eq 4.5) because r_1 is now small compared with the other dimensions (Xu *et al.*, 1998; Jones *et al.*, 2002). Between these two extremes of R , there is a transition between the two behaviours that will depend upon not only R , but also the geometry of contact as well.

It should also be noted that direct comparisons between calculated and experimental force is often not possible because at high RH, water will fill the gap between the surfaces in contact. This gap has the equilibrium value (T), which is equivalent to the liquid film thickness. This will cause the two surfaces to separate due to the generation of a disjoining pressure (F_{disj}), leading to a decrease in the adhesion force given by (Podczeck, 1998) –

$$F_{ad} = F_c - F_{disj} \quad (\text{Eq 4.13})$$

4.1.3. Aim of Work

In chapter 3, it was shown that it was possible to calculate the contact area between a flat substrate and a particle, and relate this to adhesion force measurements. While data obtained against model substrates such as

HOPG is valuable, in order to be useful for actual problems it must be applicable to real life systems. In this chapter, the work of chapter 3 is further developed by examining how the adhesion of particles varies with humidity, for both model and particle systems.

In this work, particles of SEDSTM and micronised salbutamol were again used to perform force measurements against both HOPG and compressed disks of the pharmaceutical materials at controlled humidity. From this, humidity profiles were generated for the particles, and the work of adhesion and surface energies were calculated.

4.2. Methods

4.2.1. Force Measurements

Particle addition onto the tip apexes, and force measurements were performed as described in chapter 2. Force measurements were also undertaken using blank AFM contact and tapping tips against compressed disks of micronised and SEDSTM salbutamol. The same contact and tapping tips were applied to both compressed disks, and the results shown are the averages of three point measurements taken for each humidity.

Compressed disks were produced by compressing approximately 100 mg of powder under vacuum at a pressure of 10 tons for 5 minutes in a 10 mm diameter die. The disks were then mounted onto magnetic studs using adhesive tape. Force measurements were also performed against HOPG and the compressed disks of the micronised and SEDSTM salbutamol using particles of both materials added onto AFM tips, with humidity control via the use of dessicants as discussed in chapter 2. Separate tips were used for the measurements against HOPG and compressed disks. It was not possible to perform direct single particle-particle measurements, as it could not be determined if the measurement was being performed against a specific particle or substrate because of the small size of the particles.

Additional force measurements were performed using a blank, plasma etched contact tip and a contact tip with glue added against the HOPG at 22% RH only. This was in order to act as a control, demonstrating that the AFM tip alone was not responsible for the observed interaction.

4.2.2. Work of Adhesion, Surface Energy and Predicted Force Values

The work of adhesion and was calculated using the JKR theory as discussed in chapter 3. Only the data acquired at <10% RH was used for the calculation, as higher humidities would increase the contribution of capillary forces, which are not accounted for by the JKR theory.

The surface energy of both the micronised and SEDSTM salbutamol was calculated using the adhesion measurements acquired using the particle tips against HOPG and against compressed disks of materials. For the HOPG, the surface energy was calculated from the work of adhesion by the equation –

$$\gamma_{ad} = \gamma_1 + \gamma_2 - \gamma_{12} \quad (\text{Eq 4.14})$$

where γ_{ad} is the work of adhesion, γ_1 is the surface energy of the HOPG (taken to be 100 mJm^{-2} taken from Shaefer *et al.*, (1995)), γ_2 is the surface energy of the particle and γ_{12} is the interfacial energy between the particle and the substrate (Israelachvili, 1991). The interfacial energy can be calculated from the equation –

$$\gamma_{12} = \gamma_1 + \gamma_2 - 2\sqrt{\gamma_1\gamma_2} \quad (\text{Eq 4.15})$$

These equations can then be rearranged, so that when force measurements are obtained against HOPG, the surface energy of the particle is given by -

$$\gamma_2 = \frac{\gamma_{ad}^2}{4\gamma_1}$$

(Eq 4.16)

For measurements taken between the particles on AFM tips and the compressed disks of material, the work of adhesion is simply the separation of two identical surfaces (Israelachvili, 1991). This means the surface energy is calculated by -

$$\gamma_2 = \frac{\gamma_{ad}}{2}$$

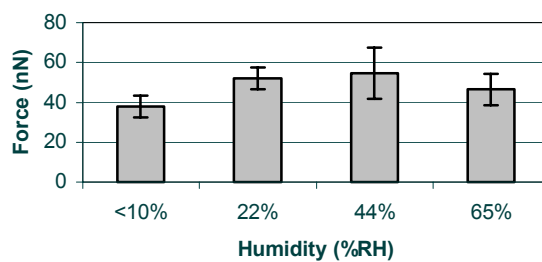
(Eq 4.17)

Once the surface energy values were calculated for each of the three tips of both materials used on each of the two substrates, the values were averaged to provide the work of adhesion and surface energy. In addition, the predicted forces of adhesion were also calculated using the JKR and DMT theories. In order to make comparisons of the predicted forces easier, the JKR forces were divided by the actual forces to create a ratio, ν_0 .

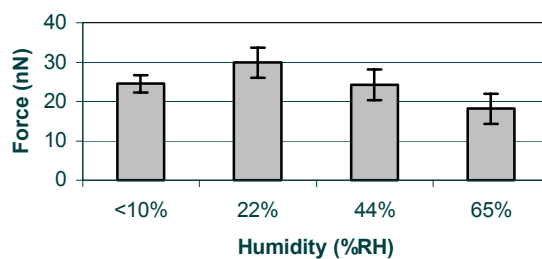
4.3. Results

4.3.1. Blank Tip Against Compressed Disks

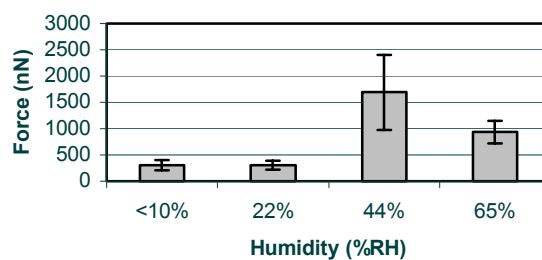
The average forces measured for the tapping and contact tip against the compressed disk of material are shown in figure 4.2 (a) to (d). It can be seen that both the flexible contact tips and stiffer tapping tips show peaks at 22% RH and 44% RH for the SEDSTM and micronised salbutamol respectively. However, for the more flexible contact tips there is a much larger standard deviation, due to the presence of long range attractive forces to which these tips are sensitive. These caused the cantilever to bend before contact was made with the substrate, although this was not observed when the stiffer



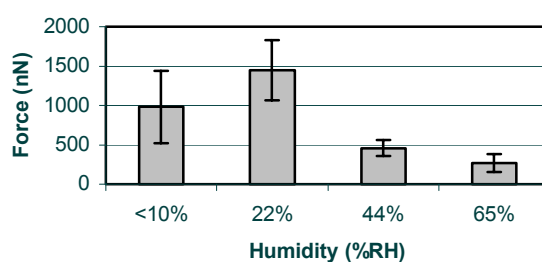
(a)



(b)



(c)



(d)

Figure 4.2. Force measurements using blank AFM tips against compressed disks of material ($n = 3$). Error bars show the SD.

- (a) Blank contact tip against compressed disk of micronised salbutamol.
- (b) Blank contact tip against compressed disk of SEDSTM salbutamol.
- (c) Blank tapping tip against compressed disk of micronised salbutamol.
- (d) Blank tapping tip against compressed disk of SEDSTM salbutamol.

tapping cantilever was used due to the greater spring constant which made it less sensitive to these forces. The surface roughness of each of the two disks is shown in figure 4.3. The maximum R_q of the micronised material was 12.8 nm, while for the SEDSTM material it was 21.8 nm. However, on a sample size of less than 2 μm x 2 μm there were no significant differences between the two roughness values, meaning that the contact geometry of the tip on the disk would not have varied greatly between the two samples.

4.3.2. Particles and Blank Tips Against HOPG

The tip images of the asperities and adhesion data generated at each humidity are shown in figures 4.4 to 4.9. These figures show that two of the three tips of both the micronised and SEDSTM salbutamol have similar behaviour to the sharp AFM tip on the compressed material.

If the micronised particles are examined first, tip A is shown in figure 4.4 (a). This consists of a single asperity 340 nm high, 846 nm wide and 1.042 μm in breadth. The force versus humidity profile is shown in figure 4.4 (b) and has a clear peak effect at 44% RH ($P < 0.05$).

Tip B is shown in figure 4.5 (a). This consists of a large single asperity that has numerous peaks and regions present. The highest point is 610 nm high, with the next highest point being separated by a distance of only 4 nm. The actual width and breadth were difficult to measure, but were approximately 2.3 μm wide and 2 μm in breadth. The humidity profile is shown in figure 4.5 (b). While this shows a peak effect at 44% RH, there is a much larger SD (CV ranging from 20% to 54%) than is seen for tip A, leading to a masking of the peak effect, however significant differences are observed between each increasing humidity force value ($P < 0.05$).

Tip C is shown in figure 4.6 (a). This consists of a single peak 304 nm high, 754 nm wide and 981 nm in breadth. The humidity profile in figure 4.6 (b) shows a significant increase in adhesion force with humidity ($P < 0.05$).

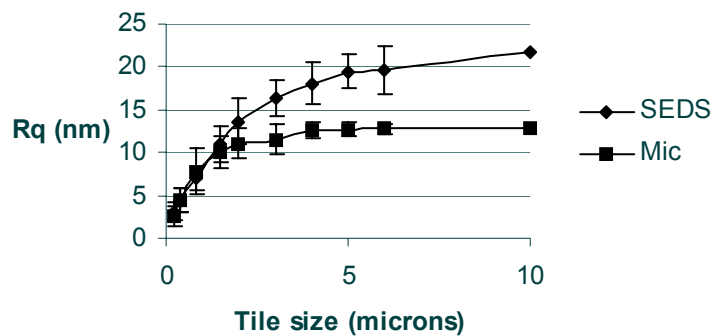


Figure 4.3. Surface roughness measurements of SEDSTM and micronised salbutamol. Measurements were taken using increasing size of sample square.

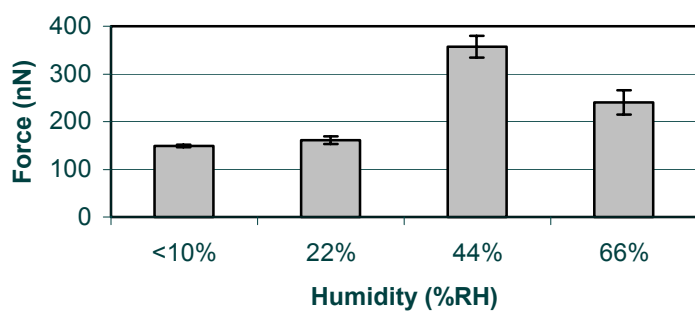
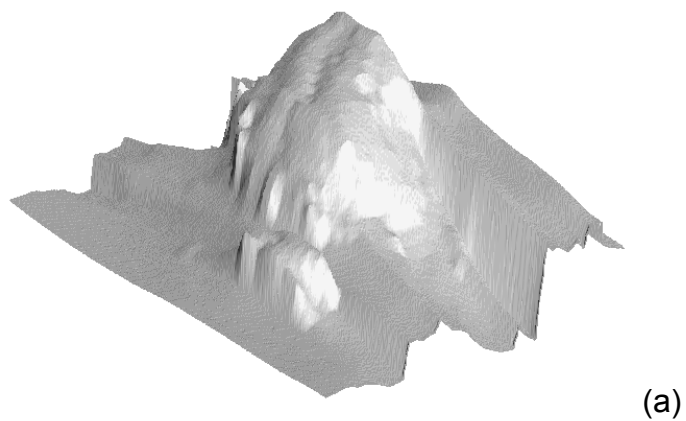


Figure 4.4. Image and force data for micronised salbutamol tip A. Error bars show the SD.

(a) Image of asperity ($XY = 1.3 \mu\text{m}$, $Z = 333 \text{ nm}$).

(b) Force measurements against HOPG.

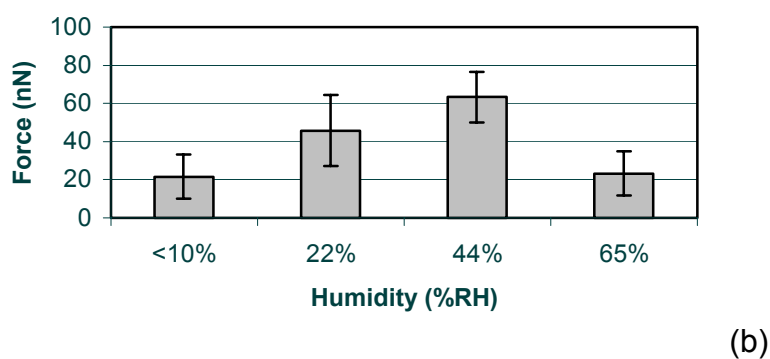
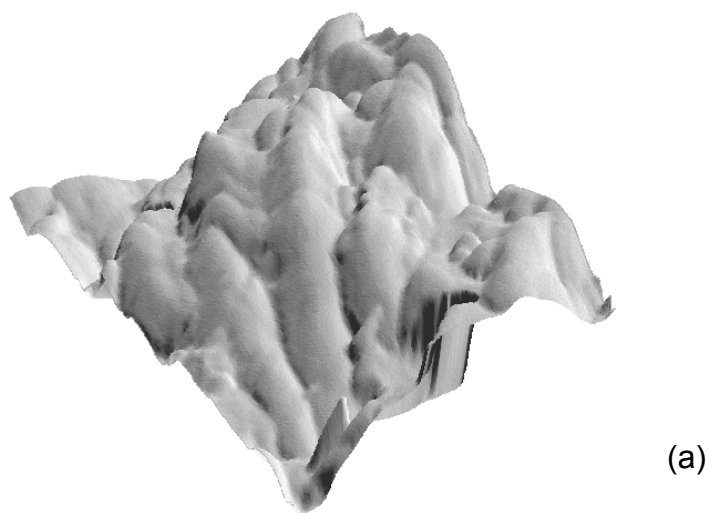


Figure 4.5. Image and force data for micronised salbutamol tip B. Error bars show the SD.

- (a) Image of asperity ($XY = 2.51 \mu\text{m}$, $Z = 559 \text{ nm}$).
- (b) Force measurements against HOPG.

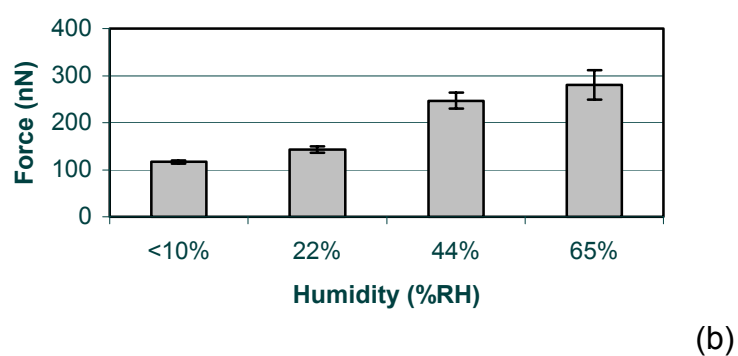
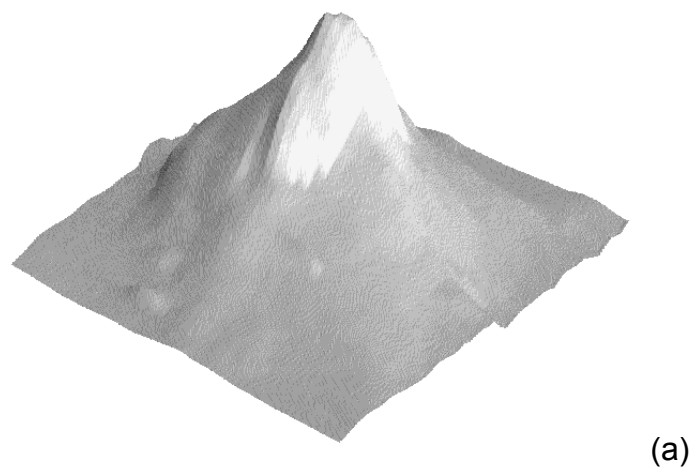


Figure 4.6. Image and force data for micronised salbutamol tip C. Error bars show the SD.

(a) Image of asperity ($XY = 1.2 \mu\text{m}$, $Z = 314 \text{ nm}$).

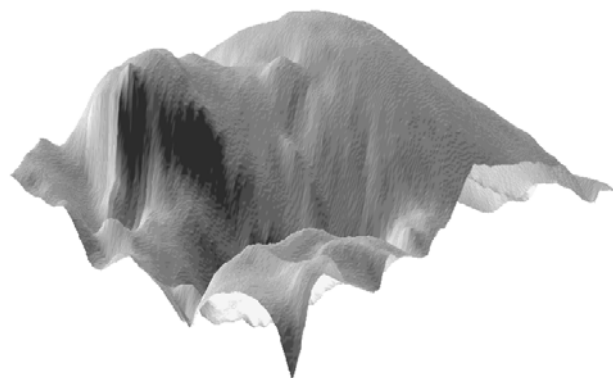
(b) Force measurements against HOPG.

If the SEDS™ tips are considered, tip D is shown in figure 4.7 (a). This consists of one main asperity formed from three sections and a number of smaller surrounding asperities. The largest section was 446 nm high, 934 nm wide and 2.029 μm in breadth. The next largest section was 332 nm high, and 528 nm wide and 679 nm in breadth. The smallest section was only 280 nm high, 763 nm wide and 619 nm in breadth. Of the smaller surrounding asperities, the second highest was separated from the highest by 211 nm and was not deemed to have been involved in the interaction. The humidity profile is shown in figure 4.7 (b). This shows an increase in adhesion force at 22% RH, before decreasing at 44% RH, although these changes are not significant ($P > 0.05$). The force then significantly increases at 65% RH ($P < 0.05$), with a large accompanying increase in standard deviation.

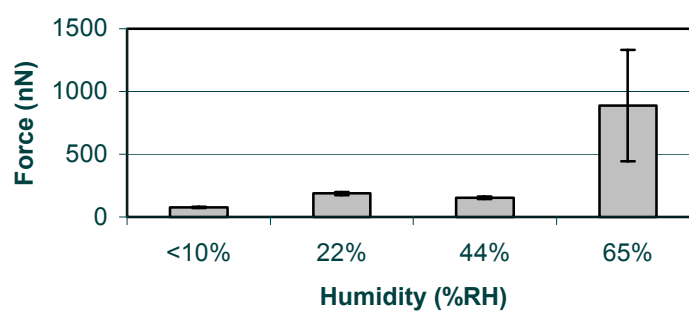
Tip E is shown in figure 4.8 (a). This consists of a single asperity 279 nm high, 899 nm wide and 984 nm in breadth. The humidity profile is shown in figure 4.8 (b). It can be seen that there is a significant peak in adhesion ($P < 0.05$) at 22% RH, followed by a gradual decrease in the adhesion force with increasing humidity.

Tip F is shown in figure 4.9 (a). This consists of a single asperity 306 nm high, 400 nm wide and 644 nm in breadth. There was a smaller section of the main asperity that was 88 nm below the top section. The humidity profile is shown in figure 4.9 (b), which illustrates a statistically significant ($P < 0.05$) increase in the adhesion force with increasing humidity.

The data acquired for the control AFM tips is shown in figure 4.10 (a) and (b). The plasma etched tip had an average force of 0.62 nN (SD 0.06 nN), whilst the tip in glue had an average of 4.46 nN (SD 4.61 nN). These values are much lower than those seen for the particle tips and indicate that it is unlikely that the AFM tip is responsible for the interaction.



(a)

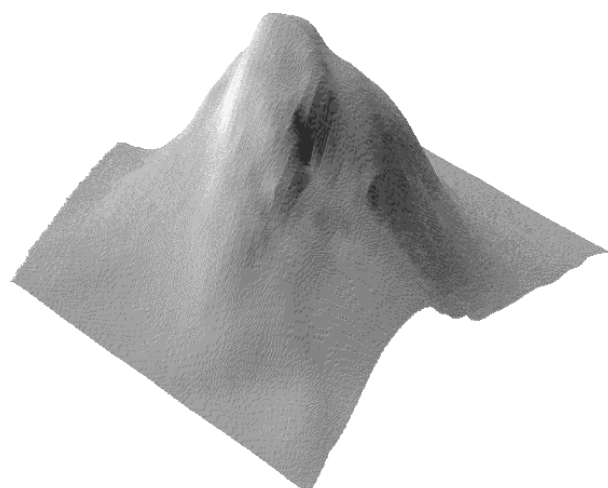


(b)

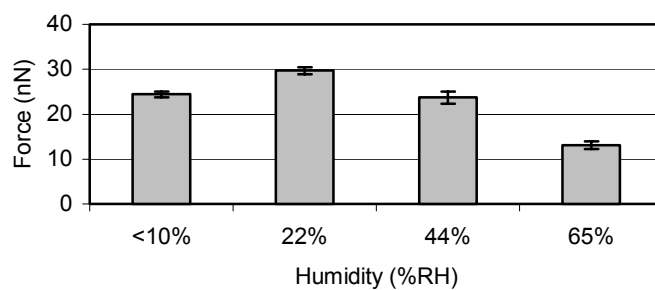
Figure 4.7. Image and force data for SEDSTM salbutamol tip D. Error bars show the SD.

(a) Image of asperity ($XY = 1.45 \mu\text{m}$, $Z = 409 \text{ nm}$).

(b) Force measurements against HOPG.



(a)



(b)

Figure 4.8. Image and force data for SEDSTM salbutamol tip E. Error bars show the SD.

(a) Image of asperity ($XY = 1.25 \mu\text{m}$, $Z = 407 \text{ nm}$).

(b) Force measurements against HOPG.

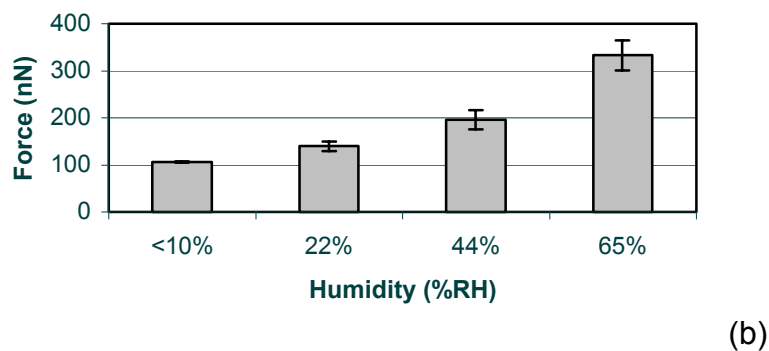
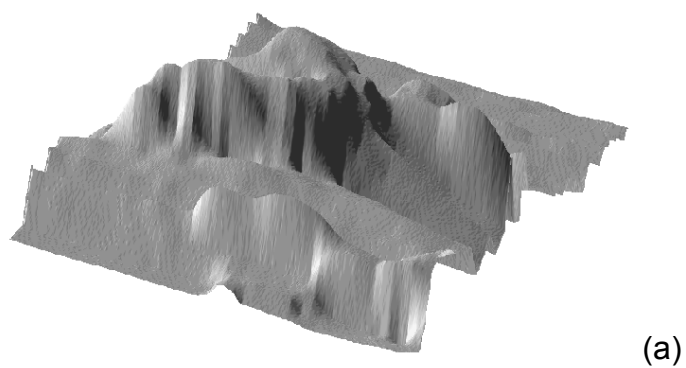


Figure 4.9. Image and force data for SEDSTM salbutamol tip F. Error bars show the SD.

(a) Image of asperity ($XY = 1.2 \mu\text{m}$, $Z = 396 \text{ nm}$).

(b) Force measurements against HOPG.

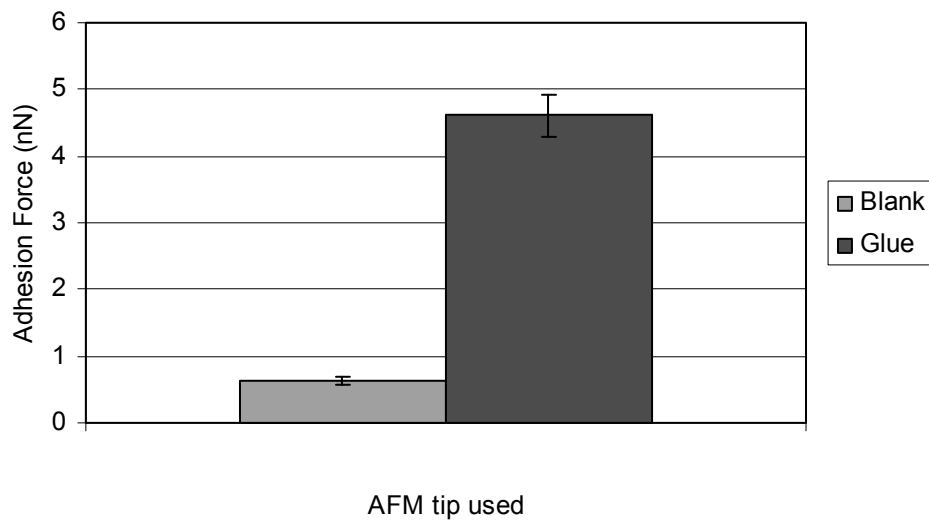


Figure 4.10. Adhesion force measurements of plasma etched and glue added AFM tips against HOPG at 22% RH (n = 1). Error bars show the SD.

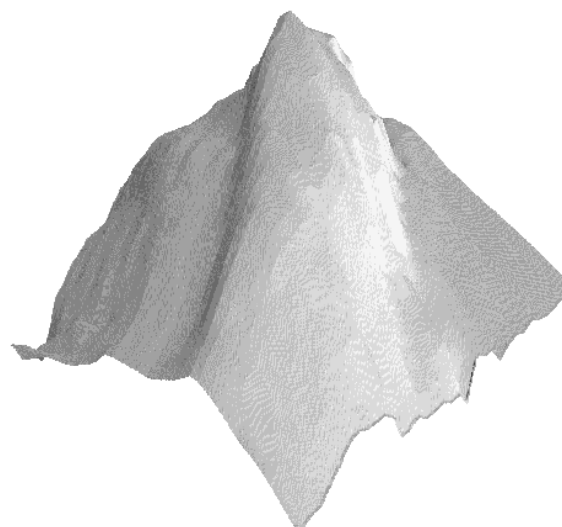
4.3.3. Particles Against Compressed Disks

4.3.3.1. Micronised Salbutamol

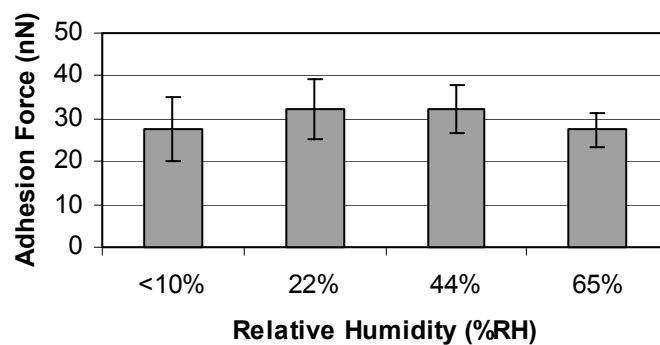
The force measurements of micronised salbutamol particles against compressed disks are shown in figures 4.11 to 4.13. All three tips displayed different behaviours with humidity. Tip G is shown in figure 4.11 (a), and consists of a single peak of height 317 nm, width 669 nm and breadth 777 nm. The adhesion force measurements are shown in figure 4.11 (b), and illustrates an increase ($P < 0.05$) from $< 10\%$ RH to 22% RH, followed by no significant change ($P > 0.05$) at 44% RH, and then a decrease ($P < 0.05$) at 65% RH.

Tip H is shown in figure 4.12 (a). The image shows the presence of three asperities. The main one is 208 nm high, 390 nm wide and 817 nm in breadth. Of the smaller two peaks, the first is 67 nm in height, 242 nm wide and 492 nm in breadth. The second smaller peak is 113 nm high, 422 nm wide and 565 nm in breadth. The adhesion force measurements are shown in figure 4.12 (b). It can be observed that a significant increase ($P < 0.05$) is seen at 22% RH. However, following this, insignificant differences ($P > 0.05$) consisting of a slight decrease at 44% RH and increase at 65% RH are seen. It is also seen that the SD were typically large.

Tip I is shown in figure 4.13 (a). The image consists of a single asperity that has three smaller asperities protruding from the top. The main base structure is 1.914 μm in width and 1.776 μm in breadth. Of the three smaller asperities on the top the tallest is 463 nm high, the next is 345 nm high and the smallest is 146 nm high. Between the highest and middle peak, a trough of 120 nm depth is reached, however if the trough between the smallest peak and the highest is measured it is only 25 nm from the smallest peak. The adhesion force measurements are shown in figure 4.13 (b), and these show a significant increase ($P < 0.05$) in adhesion force with humidity.



(a)

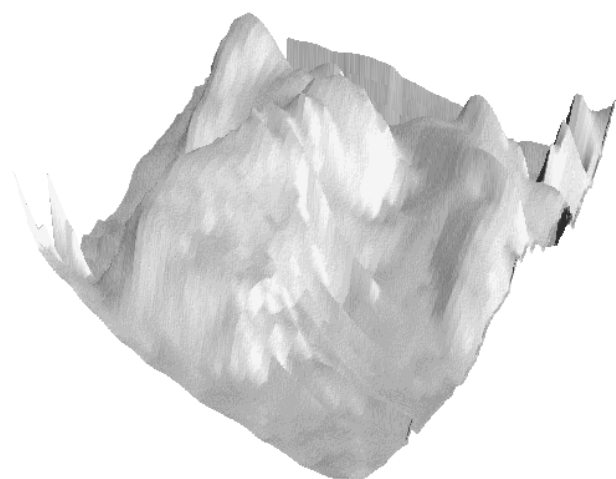


(b)

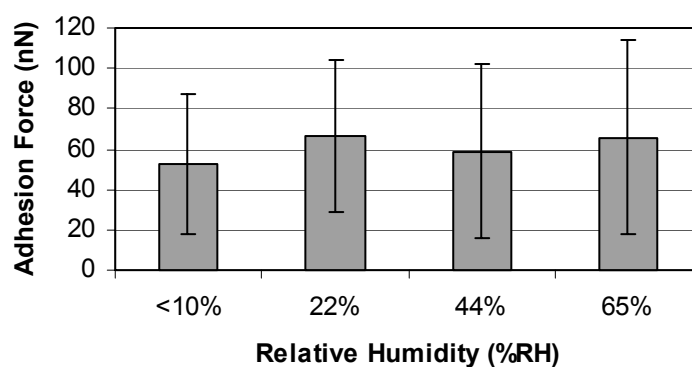
Figure 4.11. Image and force data for micronised salbutamol tip G. Error bars show the SD.

(a) Image of asperity ($XY = 0.85 \mu\text{m}$, $Z = 357 \text{ nm}$).

(b) Force measurements against compressed disk of micronised salbutamol.



(a)



(b)

Figure 4.12. Image and force data of micronised salbutamol tip H. Error bars show the SD.

(a) Image of asperities ($XY = 1.3 \mu\text{m}$, $Z = 534 \text{ nm}$).

(b) Force measurements against compressed disk of micronised salbutamol.

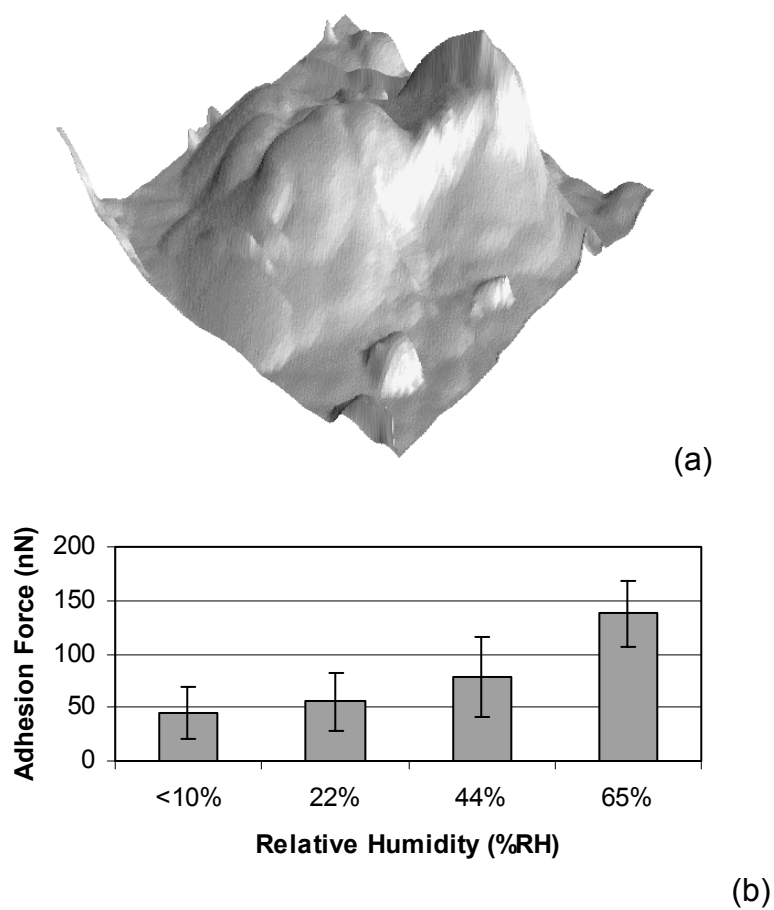


Figure 4.13. Image and force data of micronised salbutamol tip I. Error bars show the SD.

(a) Image of asperity ($XY = 2.1 \mu\text{m}$, $Z = 547 \text{ nm}$).

(b) Force measurements against compressed disk of micronised salbutamol.

4.3.3.2. SEDS™ Salbutamol

The particle measurements for SEDS™ salbutamol particles against a SEDS™ salbutamol compressed disk are shown in figures 4.14 to 4.16. It is seen that the tips show a more regular behaviour than that seen for the micronised salbutamol.

Tip J is shown in figure 4.14 (a). This consists of a single asperity that has a shoulder present. The height of the main asperity is 340 nm and is separated from the shoulder by a distance of 100 nm. The base measures 769 nm wide and 714 nm in breadth. The force measurements can be seen in figure 4.14 (b), which shows that as the humidity increases there is a statistically significant increase ($P < 0.05$) in adhesion force.

Tip K is shown in figure 4.15 (a). This consists of one large asperity surrounded by a number of smaller ones. The tallest asperity is 329 nm high, 763 nm wide and 840 nm in breadth. The next highest asperity is 214 nm high, 754 nm wide and 1.763 μm in breadth. Between these two, there is a trough of 166 nm depth when measured from the highest asperity. Following this, the next highest asperity was separated from the highest asperity by a distance of 1.286 μm . Because this distance was large, no other asperities were measured as it was unlikely they were involved in the interaction. The force measurements can be seen in figure 4.15 (b), which again shows a significant increase ($P < 0.05$) in adhesion force with humidity.

Tip L is shown in figure 4.16 (a). This consists of two asperities: the larger of the two is 257 nm high, 834 nm wide and breadth 1.23 μm , whilst the smaller one is 163 nm high, 954 nm in width, and 600 nm in breadth. When measured from the highest asperity, the trough has a maximum depth of 198 nm. The force measurements for this tip against the compressed disk are shown in figure 4.16 (b), and were found to differ from the other tips in that the forces showed a significant decrease ($P > 0.05$) with increasing humidity.

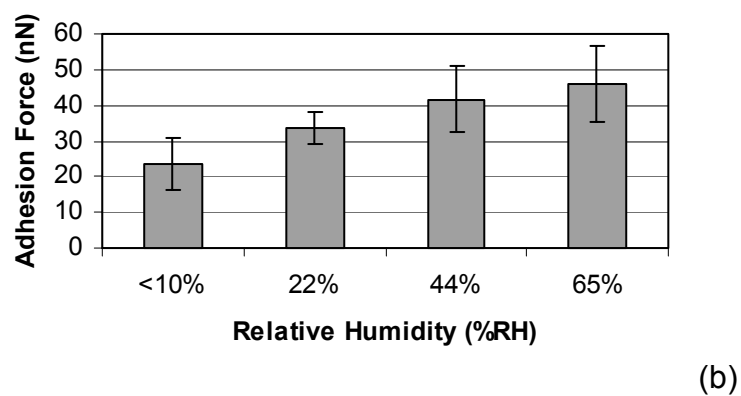
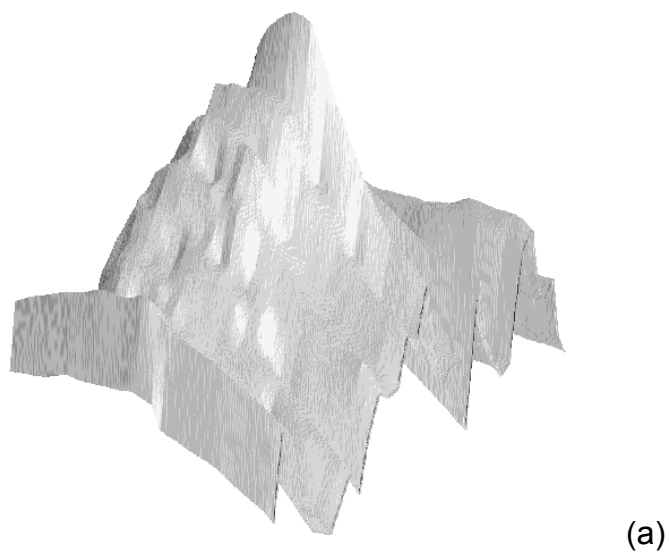


Figure 4.14. Image and force data for SEDSTM particle tip J. Error bars show the SD.

(a) Image of asperity ($XY = 0.85 \mu\text{m}$, $Z = 367 \text{ nm}$).

(b) Force measurements against compressed disk of SEDSTM salbutamol.

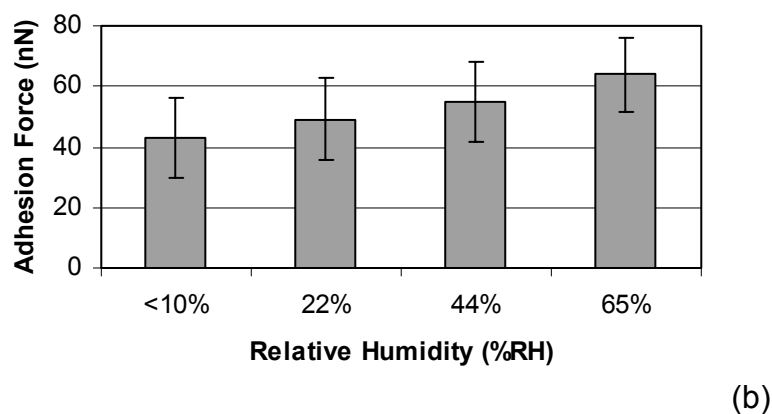
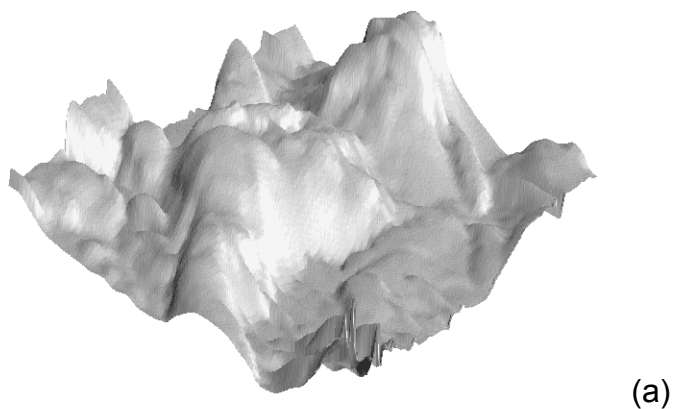


Figure 4.15. Image and force data for SEDSTM tip K. Error bars show the SD.

(a) Image of asperities ($XY = 2.1 \mu\text{m}$, $Z = 391 \text{ nm}$).

(b) Force measurements against compressed disk of SEDSTM salbutamol.

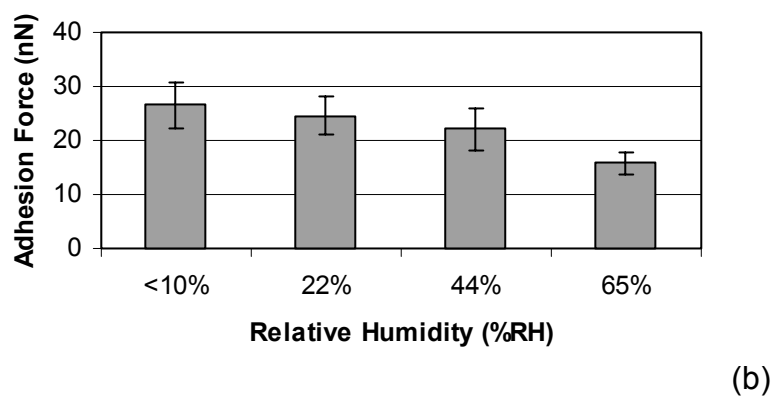
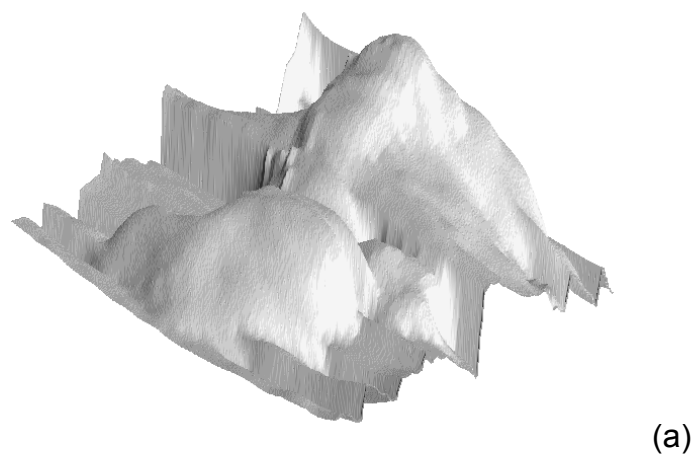


Figure 4.16. Image and force data for SEDS™ tip L. Error bars show the SD.

(a) Image of asperities ($XY = 1.55 \mu\text{m}$, $Z = 405 \text{ nm}$).

(b) Force measurements against compressed disk of SEDS™ salbutamol.

4.3.4. JKR/Actual Forces

The forces predicted by JKR theory divided by the actual forces for the HOPG for the micronised and SEDSTM salbutamol data acquired at <10% RH are shown in tables 4.1 and 4.2. It is seen that the JKR forces are closer to the experimentally observed values than the DMT values. This is what would be expected, as DMT is considered more suitable for hard, non-deforming contacts, while the JKR is more appropriate for contact where elastic deformation occurs, which is what would be expected for the HOPG and the pharmaceutical particles. Table 4.2 shows that the SEDSTM observed forces are often considerably lower than the calculated values, as shown by two ν_0 values of 7. This is in comparison with the micronised material where the actual forces are closer to the predicted forces as shown by ν_0 values that are nearer to 1, as shown in table 4.1.

The forces for the particle against particle measurements are shown in tables 4.3 and 4.4. Only the JKR theory was used to calculate the force of adhesion as it was the closer for the HOPG measurements. Results showed that while all of the micronised particles have ν_0 values greater than one, the SEDSTM displayed two of the three values less than 1.

4.3.5. Surface Energy Measurements

The work of adhesion and surface energy measurements against HOPG and compressed disks are shown in figure 4.17 (a) and (b) respectively. Against HOPG, the micronised particles displays a greater work of adhesion and surface energy than the SEDSTM. However when particle-particle measurements are taken, the situation is reversed in that the SEDSTM has an apparent higher work of adhesion and calculated surface energy than that of the micronised.

Tip	Actual force (nN)	JKR prediction (nN)	DMT prediction (nN)	ν_0 (Actual/predicted force)
Tip A	148.98	274	365	1.84
Tip B	21.49	129	172	6.14
Tip C	116.50	144	192	1.24

Table 4.1. Table of actual forces obtained at <10% RH, forces calculated using the JKR and DMT theories and ν_0 value for micronised salbutamol tips against HOPG.

Tip	Actual force (nN)	JKR prediction (nN)	DMT prediction (nN)	ν_0 (Actual/predicted force)
Tip D	78.43	587.5	783.67	7.52
Tip E	24.47	170	226.7	7.08
Tip F	106.39	128	170.6	1.20

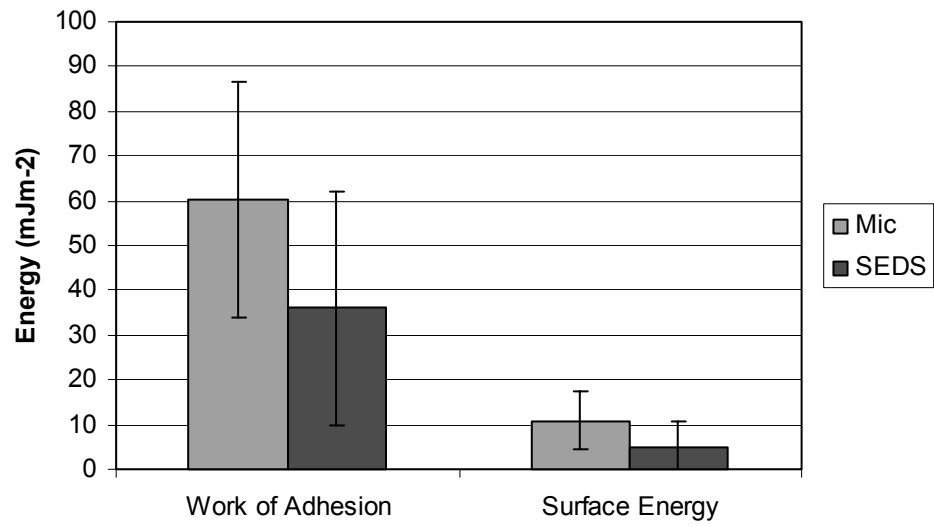
Table 4.2. Table of actual forces obtained at <10% RH, forces calculated using the JKR and DMT theories and ν_0 value for SEDSTM salbutamol tips against HOPG.

Tip	Actual force (nN)	JKR prediction (nN)	ν_0 (Actual/predicted force)
Tip G	27.5	47.7	1.7
Tip H	52.8	59.3	1.1
Tip I	43.9	52.7	1.2

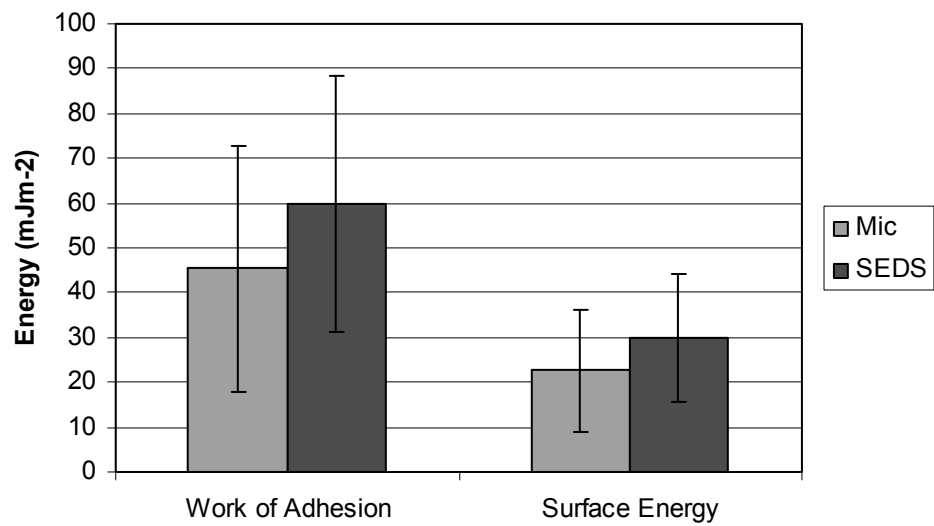
Table 4.3. Table of actual obtained at <10% RH, forces calculated using the JKR and ν_0 values for micronised salbutamol particle against particle measurements.

Tip	Actual force (nN)	JKR prediction (nN)	ν_0 (Actual/predicted force)
Tip J	23.5	11.9	0.5
Tip K	42.8	22.6	0.5
Tip L	26.5	34.9	1.3

Table 4.4. Table of actual obtained at <10% RH, forces calculated using the JKR and ν_0 values for SEDS™ particle against particle measurements.



(a)



(b)

Figure 4.17. Work of adhesion and surface energy of micronised and SEDSTM salbutamol particles. Error bars show the SD.

(a) Against HOPG.

(b) Against particles.

4.4. Discussion

4.4.1. Blank Tips on Compressed Disks

Previous work has been undertaken using blank AFM tips to perform force measurements against substrates at increasing humidity (He *et al.*, 2001, Xu *et al.*, 1998), and it was observed that at low humidity the adhesion data showed a flat region due to the presence of van der Waals forces only. However, when a mid-range humidity was reached (40% RH for silicon, 20%RH for mica) a second region is seen where a critical humidity is reached and adhesion forces increases due to the domination of capillary forces.

Following the increases observed in the second region, both He *et al.* (2001) and Xu *et al.*, (1998) observed a third region whereby the adhesion forces began to decrease. This was attributed to a mixture of attractive and repulsive forces. The reason for the repulsive forces has been discussed in terms of Laplace pressure (Eq 4.2) and chemical potential, which are related by the Kelvin equation (Eq 4.1).

For the McFarlane and Tabor equation (Eq 4.5) (which relates Laplace pressure to adhesion) to be valid, one requirement is that $r_2 \gg r_1$. However, as discussed in the introduction, if a nano-contact is responsible for the interaction then this condition may not be fulfilled, and hence the Laplace pressure will decrease, leading to a decrease with increasing humidity in adhesion forces (Xu *et al.*, 1998).

The second potential explanation of the results describes the decrease in adhesion in relation to the chemical potential of the liquid in the gap (μ_1) (Binggeli and Mate, 1994). The chemical potential generates an attractive force on the tip, which will decrease with an increase in humidity as described by the equation –

$$F = \frac{\delta G}{\delta z} = -\frac{a_c}{V} \mu_1 = -\frac{a_c}{V} kT \ln\left(\frac{p}{p_s}\right)$$

(Eq 4.18)

where G is the Gibb's free energy, V is the molar volume, a_c is the area of the liquid and k is the Boltzmann constant.

It is proposed that the above observations and theories form a framework by which we can understand the peaks in adhesion seen with humidity when using blank AFM tips on compressed disks. When the change in adhesion force as a function of humidity is observed (figure 4.2), the micronised material shows a flat region between <10% RH and 22% RH, before a second region is observed that shows an increase in adhesion at 44% RH. Following this increase a third region is seen where adhesion begins to decrease. When the measurements are performed against the SEDS™ material, there is a region of low adhesion at <10% RH before an increase is seen at 22% RH. However after this the adhesion forces decrease at 44% and 65% RH. It is therefore suggested that this peak effect is occurring due to the nanoscale geometry of the contacting asperities of the tip creating a decrease in adhesion at high humidities due to either a decrease in the Laplace pressure, or a decrease in chemical potential in the gap. However, it should be noted though, that the data did show large variations and that these conclusions are based on two repeats.

The generation of this peak effect is dependant upon the ability of capillary forces to form, which in turn is related to the ability of water to form a liquid layer upon a surface, which must be occurring at a lower humidity level with the SEDS™ material due to the early onset of capillary forces as demonstrated by the peak effect at 22% RH. A possible explanation of this may be found with the different surfaces which both materials possess. SEDS™ and micronised materials will have different surface chemistry and energies, which may affect the spreading of water over the surfaces. The micronised salbutamol has more amorphous regions than the SEDS™,

meaning it will absorb more water, so that a higher humidity is required before a water film is formed. In addition, both samples will have different functional groups present on the surface, which may facilitate spreading in the case of the hydrophilic groups, or hinder spreading in the case of the hydrophobic groups.

This data suggests that the SEDSTM salbutamol facilitates the spreading of water over the surface, which may be hydrophilic and is likely to be crystalline in nature. The minimum height of water required for spreading across a surface (e) is given by the equation –

$$e = a_{mol} \left(\frac{\gamma}{S} \right)^{\frac{1}{2}}$$

(Eq 4.19)

where γ is the liquid surface tension, S is the spreading coefficient, and a_{mol} is the molecular length, which is defined by the equation -

$$a_{mol} = \left(\frac{A_H}{6\pi\gamma} \right)^{\frac{1}{2}}$$

(Eq 4.20)

where A_H is the Hamaker constant. S must be zero or positive in order for spreading to occur, and is defined using the equation -

$$S = \gamma_{SO} - \gamma_{SL} - \gamma$$

(Eq 4.21)

where γ_{SO} is the solid-vacuum interfacial energy, and γ_{SL} the solid-liquid interfacial energy (He *et al.*, 2001). These equations imply that a lower surface energy will lead to a higher minimum spreading thickness. In previous work it has been shown that SEDSTM salbutamol has a lower surface energy than micronised salbutamol (Feeley *et al.*, 1998, Hooton *et al.*, 2003), but because the capillary forces are formed at a lower humidity,

this must mean that the surface chemistry of the SEDS™ causes the spreading thickness to be reached at a lower humidity, causing the adhesion to the SEDS™ disk to peak at a lower value of humidity than that of the micronised disk.

As mentioned in the results section, the maximum roughness of the SEDS™ disk was approximately twice that of the micronised disk. According to Coelho and Harnby (1978), the thickness of the adsorbed water layer on the surface of the disk would hence decrease by an amount equal to half the average peak to trough height. This would mean that the increased roughness of the SEDS™ disk would hinder the formation of the water layer. However, because wetting occurred at a lower level, there is a further indication that the SEDS™ material is more hydrophilic, and thus promotes earlier wetting of the disk surface.

4.4.2. Particles on the HOPG Surface

The previous arguments are extrapolated in order to explain the behaviour observed against the HOPG surface, allowing for a model of adhesion to be developed that encompasses the different contacting geometries. This model has three scenarios.

The first scenario (scenario one) is shown in figure 4.18 (a). Here, there is only a single point of nano-contact adhesion and the profile is similar to that seen for a blank tip against a compressed disk, meaning that the contact geometry and surface chemistry for the tip on compressed disk, as discussed above, will be valid here, leading to the clearly defined peak in the humidity profile. This scenario one profile is seen in three tips: the micronised tip A (figure 4.4), and SEDS™ tips D and E (figures 4.7 and 4.8 respectively).

If we examine the micronised tip first (figure 4.4), it is seen that there is a peak at 44% RH, which is the same humidity as the peak seen for the blank

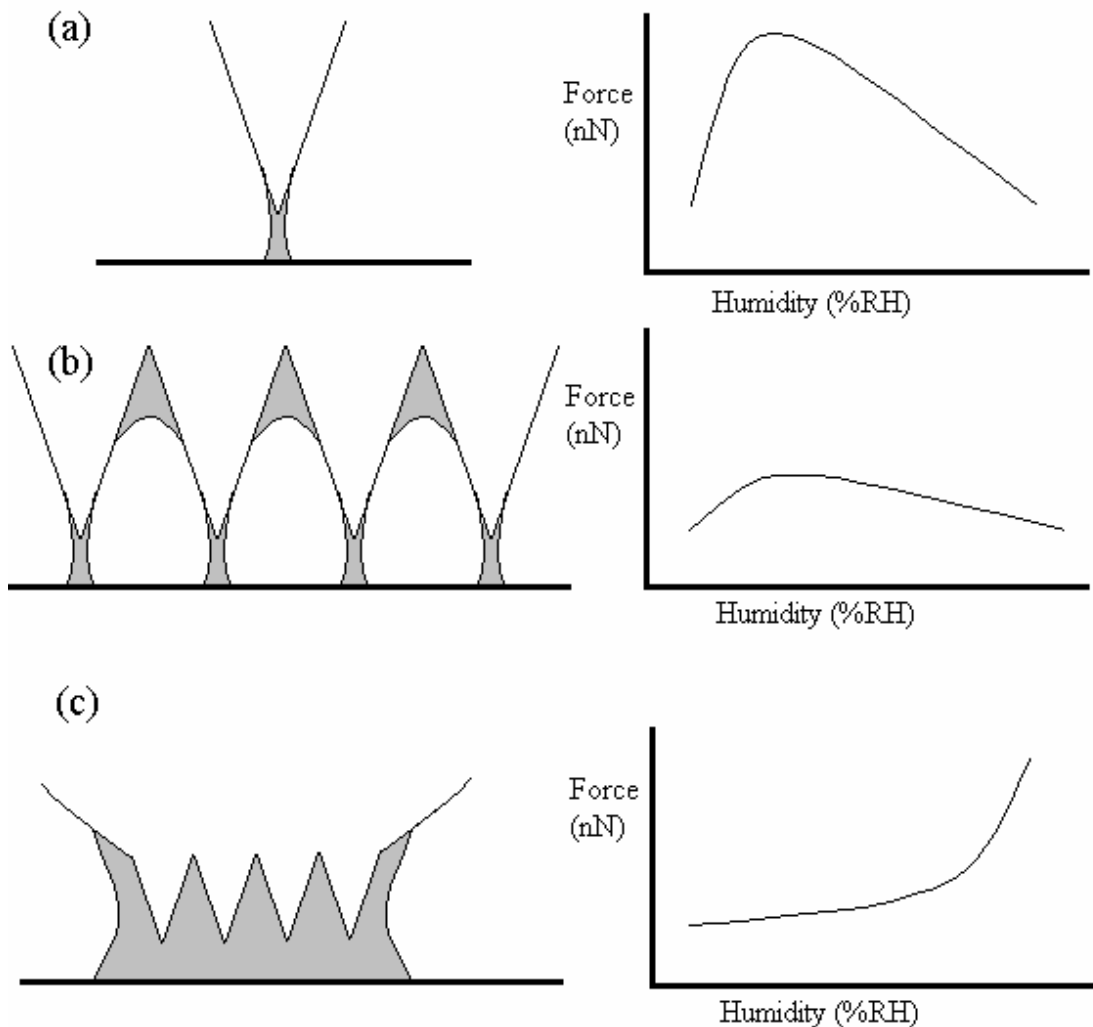


Figure 4.18. The three scenarios of adhesion and how they correspond to behaviour.

- (a) **Scenario one** - a single asperity is in contact with the surface leading to a clearly defined peak in adhesion force.
- (b) **Scenario two** - Multiple nano scale asperities contacting the surface. Moisture begins to condense between the gaps, but is not sufficient to saturate the individual asperities. This lead to a peak effect, however it is more depressed than that seen for scenario one.
- (c) **Scenario three** – Saturation of asperities leading to larger contact area creating a gradual increase in adhesion force with humidity.

tip on micronised compressed disk. This provides an indication that the surface chemistry of the micronised material may be dominating the interaction. The contacting asperity of this tip consists only of a single point, as expected for scenario one.

If we examine the SEDS™ tips, it is seen that there is a gradual increase in adhesion force up to 22% RH, before a decrease at 44% RH. This is similar to the behaviour observed for the blank tip on the SEDS™ compressed disk, meaning that the surface chemistry is again involved. If we look at the force measurements at 65% RH, we see that for tip E (figure 4.8) the decrease continues at 65% RH, whereas for tip D (figure 4.7) there is a large rise in force.

The reason for this large rise in force with tip D can be explained by a sudden change in contact geometry leading to a massive increase in the capillary force present. As observed earlier, there are two distinct asperities present on tip D, differing in height by 59 nm. At the lower humidity, only the larger asperity is involved, although once 65% RH is reached the thickness of the HOPG water layer will be ~34 nm thick (Freund *et al.*, 1999). When combined with the water layer on the particle it will allow the second peak to become involved in the interaction. In addition, the gap between the two asperities was found to have a maximum depth of 94 nm and could have become filled with liquid due to spontaneous condensation, leading to an increase in capillary force.

Scenario two behaviour was only seen with tip B (figure 4.5), and is shown schematically in figure 4.18 (b). In this scenario, there are multiple nanoscale contact points. These will produce a peak effect, however they will trap more moisture in the gaps between the asperities and substrate at lower humidity, leading to a greater disjoining effect as discussed in the introduction. This disjoining effect will cause the peak effect to be depressed and less distinct than seen for scenario 1. On tip B, the highest of the multiple asperities are separated by only 4 nm, with a trough depth of 115

nm. It is possible that both asperities were involved in the interaction leading to the scenario observed.

For tip B, when the force recorded is examined taking into account measurement order, it is seen that at 44% RH there is a gradual decrease in forces as the measurements progress. Podczeck *et al.* (1996 and 1997) have observed that at humidity levels below 55% RH plasticizing of the surfaces may occur due to absorbed moisture. This could imply that humidity-dependent plastic changes in the sample were occurring at 44% RH.

The final scenario is shown in figure 4.18 (c). In this scenario, the asperities are of much smaller dimensions, meaning that the gaps between them become saturated before a peak is seen in the humidity profile. This eliminates single nano contacts at a much lower humidity, leaving only one large area involved in the interaction. This means that the discussion for the tip on compressed disks no longer becomes valid, and is replaced by Eq 4.5, since the contact has changed from a nano scale to a macro scale contact, where the adhesion forces increase with humidity and no peak effect is seen.

This behaviour is seen with two tips, the first being tip C (figure 4.6). While there is a continual increase in adhesion force with humidity with this tip, there is a much bigger increase at 44% RH than is seen between <10% RH and 22% RH. This could be due to surface chemistry. At 65% RH the force increases again instead of decreasing, as previously explained by the geometry and height of the tip. The tip is of much narrower geometry and of lower height than the other micronised tips, meaning that it may have been saturated by surface water and therefore a larger contact area is involved, thus increasing the force.

This behaviour is also seen with tip F (figure 4.9). Here, the main asperity consists of numerous smaller asperities, separated from the highest asperity by distances of between 50 and 56 nm. The troughs in between vary from 50 to 72 nm in depth. Once 44% RH is reached, there is a gradual increase

in the adhesion force with the number of measurements taken. It may be possible that some plastic deformation may have occurred, leading to either an increase in the number of asperities coming into contact, or deformation of smaller asperities to become larger asperities. In addition, the small gaps between the asperities could easily have become filled with moisture, increasing the capillary force and leading to a masking of the peak effect at 22% RH.

Previous work has been undertaken which involved force measurements being performed with salbutamol modified probes against a range of substrates, including atomically flat lactose (Price *et al.*, 2002) and compacts of drug (Young *et al.*, 2002). In this work, no peaks in adhesion were reported, and instead, adhesion was found to increase with increasing humidity. While this trend is expected with the model compact surfaces due to the surface roughness effects discussed earlier, this is not expected with the work performed using the atomically flat lactose. However, it should be noted that in this work no attempt was made to characterise the contacting surface of the drug probes which were used to perform the measurements. Without an understanding of the geometry of the probe at the point of contact, and the resulting contacting area, it would not be possible to make comparisons to the data presented in this chapter.

4.4.3. Particle Against Particle Force Measurements

With the particle on particle measurements, the scenario models developed so far can again be fitted for most of the force profiles seen. However, while the measurements against HOPG showed mainly scenario 1 type behaviour, the predominant behaviour observed here has shifted towards scenario 3. This is expected as the previous particle measurements were performed against a flat substrate, whereas these are against a rougher substrate. This will lead to an unpredictable contact geometry where interlocking effects will also be seen, meaning that a single nano contact is not likely.

With micronised salbutamol tip G (figure 4.11), there was a slight peak effect, although this was masked by the SD of the data, as demonstrated by the CV ranging from 14% to 27%. This is similar to scenario 2 behaviour, where a peak effect would be expected due to the sharp features of the asperity. However, due to the rough nature of the substrate surface the peak is beginning to be masked.

Micronised tip H (figure 4.12) also showed scenario 2 behaviour in that there was a slight peak effect at 22% RH, however this was again heavily masked by a large SD (CV ranged from 56% to 73%). There were three asperities imaged, the two highest being separated by 170 nm, meaning that only the highest was involved in the interaction. The main asperity was of much broader morphology than that of tip G, meaning that the increase in contact area, combined with the unknown geometry of the substrate surface, created a much larger contact region which would have led to the increase in standard deviation.

Scenario 3 was seen with three tips, the first being the micronised tip I (figure 4.13). The two highest asperities are closer in height than those of tip H and may have become gradually more and more involved in the interaction, leading to an increase in the contact radius and hence an increase in adhesion force due to Eq 4.5.

If the SEDSTM tips are examined, it is noticeable that for the first two tips (J and K, figures 4.14 and 4.15 respectively) there is an increase in the adhesion force with an increase of humidity. Both CV are in the range of 20% – 30%, meaning there was less deviation than that seen for the micronised. The increase would be related to both of the asperity peaks becoming gradually filled with water in scenario three type behaviour.

The final SEDSTM tip L (figure 4.16) showed different behaviour in that there was a decrease in adhesion with increasing humidity. This behaviour cannot, as yet be explained by the scenarios highlighted.

4.4.4. JKR Forces

When the ν_0 value of the SEDSTM material against HOPG are examined in table 4.2, it is noted that tips D and E, where a peak is seen at 22% RH, have a larger ν_0 value than that of tip F where no peak was seen. This may be due to one of two reasons. The first explanation is that there are surface features that are too fine to be imaged by the tip characteriser, meaning that at lower humidity levels the contact region is smaller than that calculated using the images.

The second possibility is that surface chemistry may also be involved. Schaefer *et al.*, (1995) performed similar calculations between HOPG surfaces and glass, tin and polystyrene surfaces. They found that the predicted JKR forces were 40 to 68 times higher than the observed values, which was mainly attributed to surface roughness effects. Following an allowance for this, predicted forces were still three times greater than observed. This was accounted for by small layers of moisture that could not be removed by vacuum, and variations in the interfacial energies. However, in this study the tip on compressed disk work showed that the SEDSTM material is more sensitive to moisture at a lower humidity than the micronised. This may mean that a water layer was present on the SEDSTM material even at low humidity, which could lead to the generation of a disjoining pressure by the water in the meniscus as discussed in the introduction. This would also assist in keeping the asperities away from the surface and create a deviation from predicted values. Tip F had a lower ν_0 value, however we believe plastic deformation has occurred in this case, which would have led to an incorrect estimation of the contact area and hence an incorrect calculation of the predicted JKR force.

When the ν_0 values for the micronised salbutamol against HOPG in table 4.1 are examined, it is seen that for tips A and C there is a lower ν_0 value. This could be due to a better characterisation of the asperity coming into contact with the surface, as well as the fact that at lower humidity levels the

micronised salbutamol was less sensitive to moisture, meaning that there was a lower disjoining pressure present. For tip B it is observed that there is a larger ν_0 value. This could be due to the difficulty in predicting which asperities would be coming into contact with the substrate surface, inconsistent interfacial energy and plastic deformation leading to an incorrect prediction of contact area and thus JKR calculation.

When the measurements against particles are examined (tables 4.3 and 4.4), it is seen that all of the micronised salbutamol tips and tip L of the SEDSTM material have ν_0 values that are close to 1. However, the other two SEDSTM tips had ν_0 values that were lower than 1. This is due to the particle asperities adhering in the troughs of the rough substrate surface, which will increase the contact as shown in chapter 1 (figure 1.5 (a)). This increasing in the contact area will result in a higher adhesion force, making the ν_0 value closer to 1. Because the adhesion forces of SEDSTM tips J and K are higher than the predicted value, there must be much greater contact than that predicted from the calculated contact area, which will affect the surface energy measurements recorded.

4.4.5. Surface Energy Measurements

The surface energy measurements (figure 4.17) differed for both the HOPG and the particle measurements. Against HOPG, the surface energy measurements were as expected, in that the SEDSTM material was lower than the micronised (5 mJm^{-2} compared to 10.8 mJm^{-2}), although this lower value may in part be due to the presence of a disjoining pressure as discussed in the previous section. It was also noted that the surface energies were of a similar magnitude and in proportion to those observed previously (Feeley *et al.*, 1998 and Hooton *et al.*, 2003). There was a large SD observed with both results (117% for the SEDSTM and 60% for the micronised). This was because even though a low humidity was used (<10% RH) some moisture would still have been present that could have affected

the results as discussed for the differences in actual and predicted JKR forces.

Against compressed disks of materials, a different trend was seen. The micronised particles had a slightly lower surface energy than that of the SEDSTM (22.6 mJm⁻² compared to 29.9 mJm⁻²). This slight increase is likely to be due to the increase in surface roughness of the SEDSTM disks as discussed in the JKR section above.

4.5. Conclusion

In this chapter, a comparison has been made between the adhesion behaviour and surface energy of SEDSTM and micronised salbutamol.

When force measurements were performed using blank AFM tips against compressed disks of both materials, the different surface chemistries led to different wetting effects, which created differing peaks in the adhesion profile with humidity. For SEDSTM salbutamol this peak is seen at 22% RH, and at 44% RH for micronised salbutamol.

When particles of both materials are mounted onto AFM tips and measurements performed against a flat HOPG substrate, a mixture of behaviours is seen which is attributed to a three scenario model ranging from single nano-scale contacts to macro contacts. When measurements were done using particles against similar particles in the form of compressed disks the model could be applied to certain situations but not all, due to the uncertain morphological nature of the contacting surface. It should be noted however, that this model is based upon a small sample (n=3) of each of the two materials. This means that further work would be required to be undertaken in order to develop this model to produce statistically significant results with a variety of samples.

When the v_0 values were calculated using the HOPG measurements, it was seen that the SEDSTM material had a higher deviation from predictions based upon JKR model than the micronised. However, this could be explained by the SEDSTM material being more sensitive to lower humidity levels than the micronised material. However against compressed disks the trend was reversed. This was due to the rough surface of the SEDSTM increasing the contact area in a manner which could not be accounted for.

This work has shown that differences in surface chemistry and asperity geometry can lead to changes in adhesion with different humidity conditions. The work against a flat substrate has shown that at high humidity levels, the adhesion properties of materials may be reduced by the use of particles with numerous, well-defined asperities in a system similar to that seen in scenario two. This will lead to the avoidance of sharp peaks in adhesion with humidity, and depressed forces through the humidity range. However, when measurements were performed against a surface made of the same material, similar peaks were not seen due to the differences in surface roughness. This shows that while model systems provide fundamental understanding of the principles involved in adhesion, further work is required to properly apply model systems to those found in real life.

Chapter 5

Comparison of Polymorphs

5.1. Introduction

5.1.1. Polymorphism

The ability of a compound to crystallize into more than one crystal species, where each differs in the 3D arrangement of atoms is known as *polymorphism*. Whilst having the same chemical composition, different polymorphic forms of the same substance may show differences in surface structure and bulk properties, such as melting point and solubility, however once in the liquid or gaseous state they will behave identically (Haleblian and McCrone, 1969). A well known example of polymorphism is seen in carbon, where two such polymorphs are graphite and diamond. The physical properties of both substances vary dramatically, for example, whilst graphite is a soft substance that breaks easily, diamonds are the hardest natural substance known and are used in such applications as making drill bits (Haleblian and McCrone, 1969).

Because of the differences in properties that can result, the ability to control the polymorph formed is of vital interest to the pharmaceutical industry as changes can affect the stability, bioavailability and elegance of

pharmaceutical dosage forms (Haleblian, 1975; Yu *et al.*, 2003). An example of this was seen in 1998, where the presence of an unwanted polymorph led to major delays in the manufacturing of the anti-HIV drug Ritonavir (Pharm. J., 1998). Many drug substances are able to exhibit polymorphism, for example carbamazepine and cimetidine (Roberts and Rowe, 1996, Hegedus and Gorog, 1985). In this AFM force study, the polymorphs of sulphathiazole have been characterised.

5.1.2. Sulphathiazole

Sulphathiazole is an antibiotic of the sulphonamide family. It has 5 known polymorphic forms, although form V has only been seen with solid state NMR (Apperley *et al.*, 1999). The chemical structure and some physical properties of some of the polymorphs are shown in figure 5.1 and table 5.1.

5.1.3. Formation of Sulphathiazole Polymorphs

Sulphathiazole polymorphs have traditionally been prepared by crystallization from different solvents, for example acetone will crystallise forms I and IV and the use of water will result in forms II and III (Khoshkhoo and Anwar, 1993). Recently the use of supercritical fluids has been employed. Kitamura *et al.* (1997) used a gas antisolvent method (GAS) to make crystals of polymorphs I and III. The SEDSTM technique has also been used, where it was found that by changing the process solvent, amorphous forms and pure crystalline samples of polymorphs I, III and IV could be produced (Kordikowski *et al.*, 2001). It is the SEDSTM technique that has been employed to make the particles used for this work.

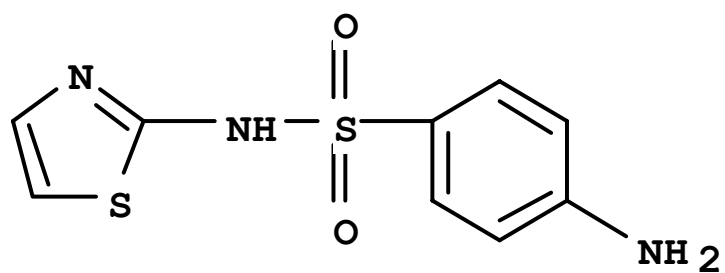


Figure 5.1. Chemical structure of sulphathiazole.

Polymorph	Density (g cm ³)	Transition Temperature (°C)	Melting Point (°C)	Young's Modulus (GPa)
I	1.7		201	10.55
III	1.57	140 – 170 (I > III)	201	14.59

Table 5.1. Physical properties of Sulphathiazole polymorphs I and III (Taken from Roberts and Rowe, 1996).

5.1.4. Aim of Work

The aim of this work is to compare the surface structure and adhesive properties of three polymorphs of sulphathiazole, forms I, III and IV. In addition, form I has been crystallised using two different solvents, methanol (polymorph I-Met) and acetone (polymorph I-Ace) as it was noted that the solvent used could change the method by which polymorph formation was controlled. Methanol was found to show thermodynamically controlled crystallization, while crystallisation from acetone was kinetically controlled (Kordikowski *et al.*, 2001). Each of the 4 samples were imaged using SEM and AFM. AFM force measurements were performed for each form against HOPG and their corresponding particle surfaces. From this the work of adhesion and surface energy were calculated for each polymorph. These data are then related to the known polymorphs properties.

5.2. Methods

5.2.1. Formation of Particles

Particles were supplied by Nektar, and were formed using the SEDS™ technique as described in Kordikowski *et al.* (2001). Two solvents were used, methanol to produce forms I, III and IV, and acetone to make polymorph I. The presence of each of the polymorphs was confirmed by the use of differential scanning calorimetry (DSC) by Nektar.

5.2.2. Acquisition of Force Measurements

The addition of particles on to AFM tips, the preparation particle substrates and control of humidity by saturated nitrogen gas were performed using the techniques described in chapter 2.

Force measurements against the particle substrates were acquired for individual points as well as across a 10 µm x 10 µm area as shown in figure

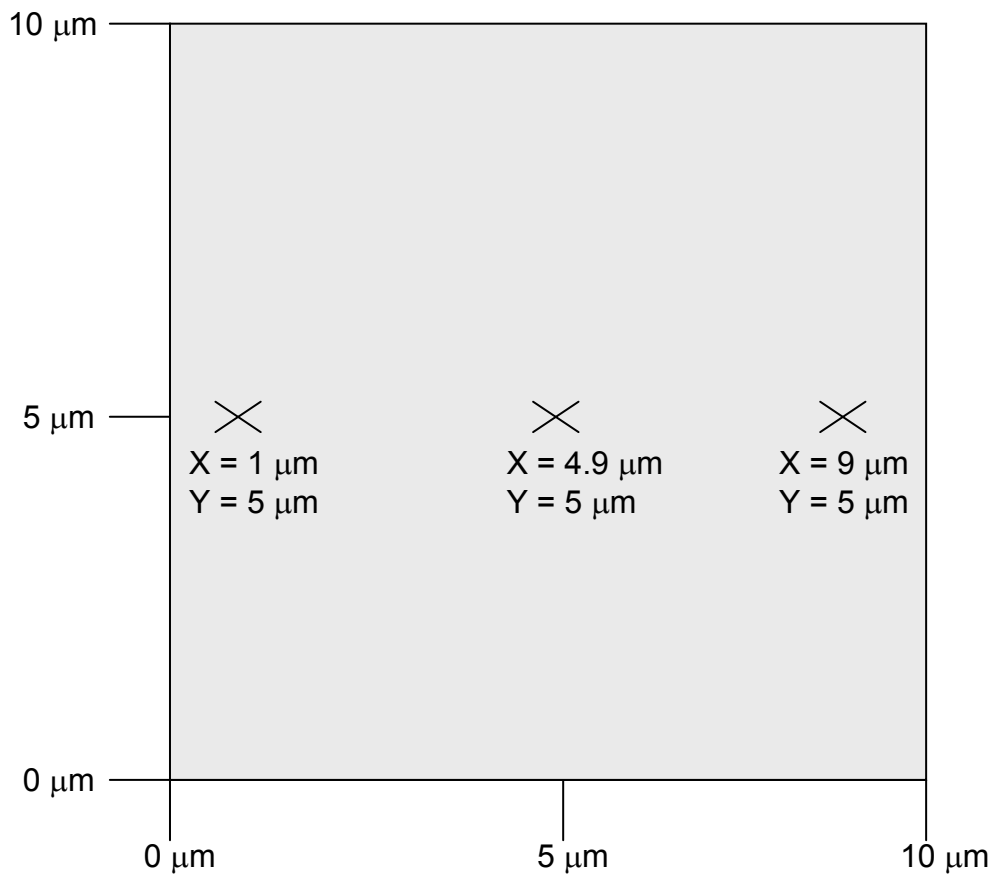


Figure 5.2. Position of point measurements for particle-particle measurements. The point measurements were undertaken at $Y = 5 \mu\text{m}$, and $X = 1 \mu\text{m}$, $4.9 \mu\text{m}$ and $9 \mu\text{m}$.

5.2. For point measurements, 50 force measurements were carried out at each of three points, where $Y = 5 \mu\text{m}$ and $X = 1 \mu\text{m}$, $4.9 \mu\text{m}$ and $9 \mu\text{m}$. For the whole area approximately 70 measurements were taken across a $10 \mu\text{m} \times 10 \mu\text{m}$ area.

Following measurements against particles, force measurements were performed using the same tip against HOPG, again using the methods described in chapter 2. Once these results were obtained, the tip was characterised, to determine the particle contact area as previously described in chapter 3. This was repeated using three tips of each of the four polymorph samples.

The work of adhesion and surface energy was calculated using the JKR theory for the particle and HOPG data acquired at $<10\%$ RH as seen in chapter 4. Once the values were calculated for each of the three tips used for each of the polymorphs, the values were then averaged to provide the work of adhesion and surface energy.

Conformation of the polymorphs was not undertaken following completion of the experiments. However, samples of forms I and IV take several months to transform (Anwar *et al.*, 1989), which is longer than the time period in which the experiments were undertaken.

5.3. Results

5.3.1. Images of Polymorphs

SEM images of polymorph I-Met are shown in figure 5.3. The images showed two types of regions, which were observed in differing proportions. The first type of region, which was in the minority, consisted of large plate like structures $20 \mu\text{m}$ to $50 \mu\text{m}$ long. The second region dominated the sample, and consisted of small aggregated particles varying in size from $0.5 \mu\text{m}$ to $1 \mu\text{m}$ long. The AFM images of polymorph I-Met are shown in figure

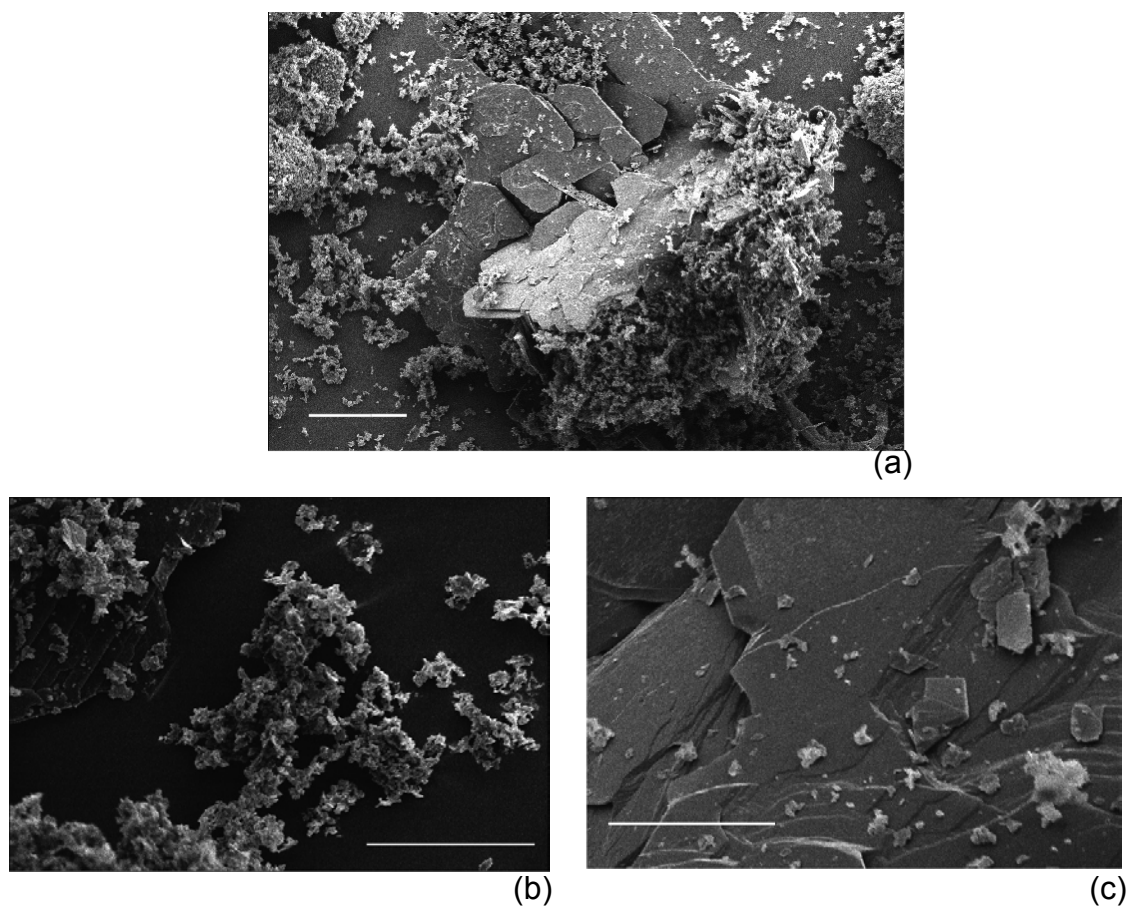


Figure 5.3. SEM images of polymorph I-met.

(a) Image of plate and aggregated region, bar length 20 μm .

(b) Zoom in of aggregated region, bar length 10 μm .

(c) Zoom in of plate like region, bar length 5 μm .

5.4. The images show a series of crystal planes separated by step heights varying from 47 nm to 416 nm.

The SEM images of polymorph I-Ace are shown in figure 5.5. The images showed a large number of small plate like structures ranging in size from 5 μm to 10 μm . AFM images of polymorph I-Ace are shown in figure 5.6. It was seen that the surface demonstrated nano-scale roughness, with a R_q maximum value of 26 nm. In all the images only one step was seen, which had a height of 1.08 μm .

The SEM images of polymorph III are shown in figure 5.7. The images showed a large number of elongated needle-like structures ranging in length from 20 μm to 70 μm . High magnification images showed what appears to be a large number of crystal growth planes. The AFM images of polymorph III are shown in figure 5.8. Polymorph III consisted of large plate like regions with steps present. The heights of the steps were found to vary in height from a minimum of 16 nm, to a maximum of 280 nm. A single region of spherical particles was also seen that may indicate the presence of an amorphous region.

The SEM images of polymorph IV are shown in figure 5.9. The images showed plate-like structures, some of which were elongated and sizes ranged from 30 μm to 70 μm long. Higher magnification images showed crystal plane structures present. AFM images of polymorph IV are shown in figure 5.10. It is seen that the structure is similar to that of polymorph I-Ace in that it consists of large areas of nano roughness. Some steps were seen in images not shown, and were found to vary from 103 nm to 244 nm in height.

5.3.2. Surface Roughness

The surface roughness of all the polymorphs is shown in figure 5.11. The figure shows that as expected for this type of measurement, the roughness

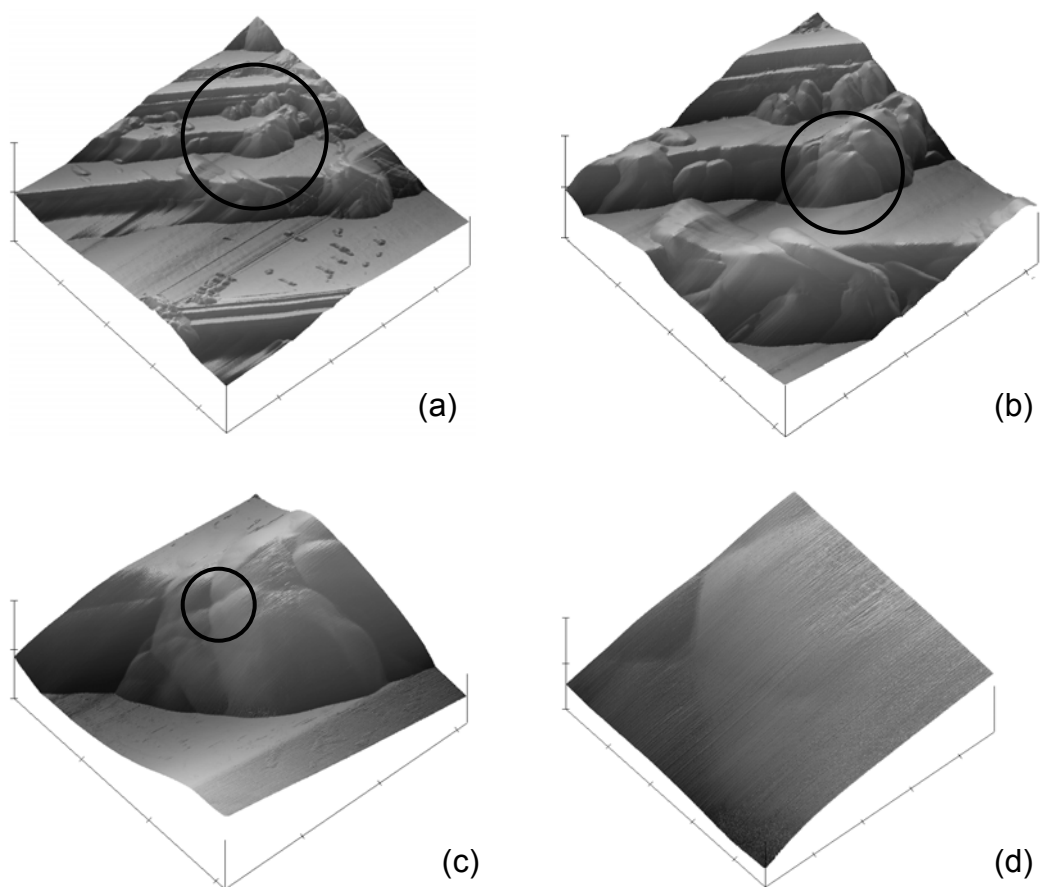


Figure 5.4. AFM images of polymorph I-Met.

(a) Initial area ($XY = 2 \mu\text{m}/\text{div}$, $Z = 2.75 \mu\text{m}/\text{div}$).

(b) Zoom in of the circled area ($XY = 1 \mu\text{m}/\text{div}$, $Z = 900 \text{ nm}/\text{div}$).

(c) Zoom in of the circled area ($XY = 500 \text{ nm}/\text{div}$, $Z = 484 \text{ nm}/\text{div}$).

(d) Zoom in of the circled area ($XY = 100 \text{ nm}/\text{div}$, $Z = 265 \text{ nm}/\text{div}$).

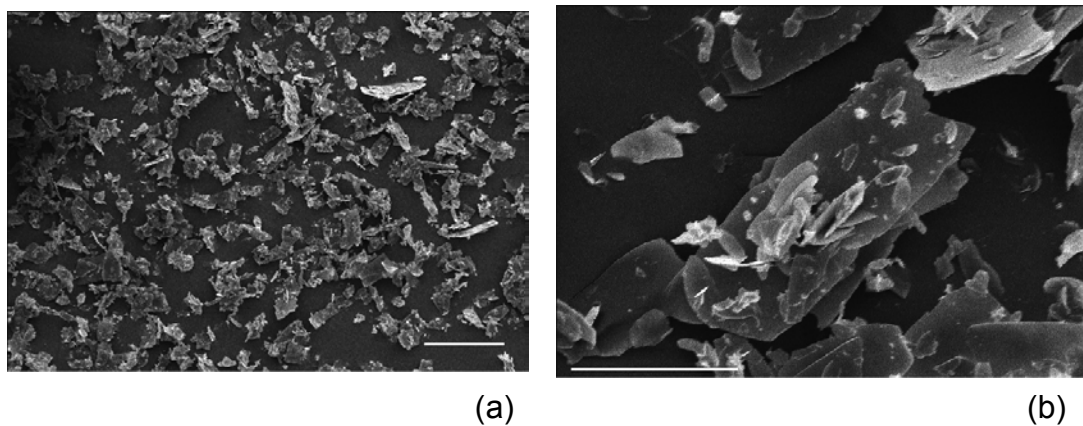


Figure 5.5. SEM Images of polymorph I-Ace.

(a) Large area, bar length 20 μm .

(b) Zoom in of the plate region, bar length 5 μm .

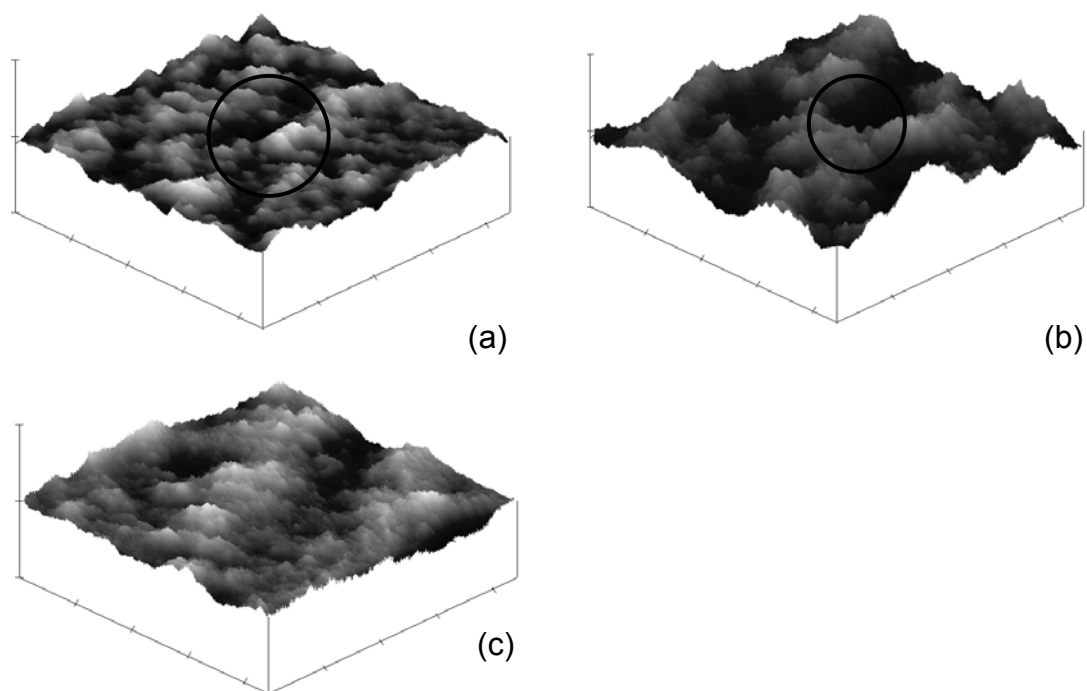


Figure 5.6. AFM images of polymorph I-Ace.

(a) Initial area ($XY = 1\mu\text{m}/\text{div}$, $Z = 87\text{ nm}/\text{div}$).

(b) Zoom in of the circled area ($XY = 350\text{ nm}/\text{div}$, $Z = 18\text{ nm}/\text{div}$).

(c) Zoom in of the circled area ($XY = 200\text{ nm}/\text{div}$, $Z = 16\text{ nm}/\text{div}$).

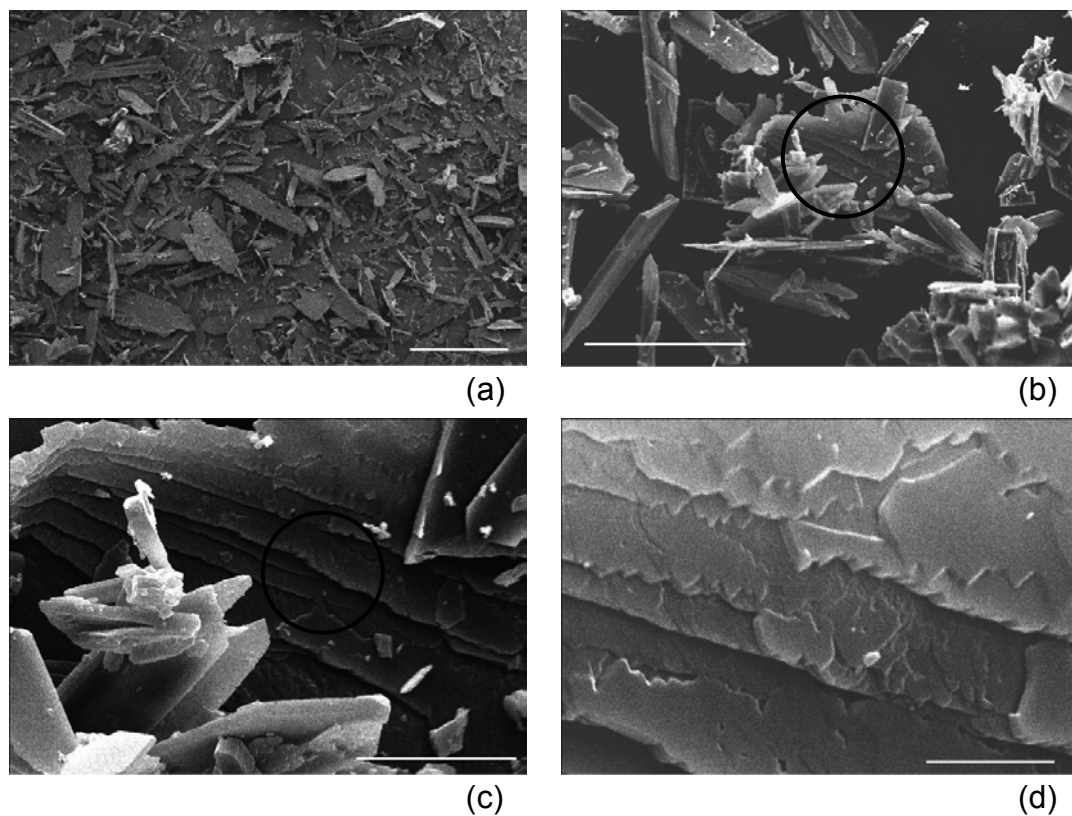


Figure 5.7. SEM images of Polymorph III.

- (a) Overview of general particle structure, bar length 50 μm .
- (b) Higher magnification image of needle like structures, bar length 20 μm .
- (c) Zoom in of circled area, bar length 5 μm .
- (d) Zoom in of circled area, bar length 1 μm .

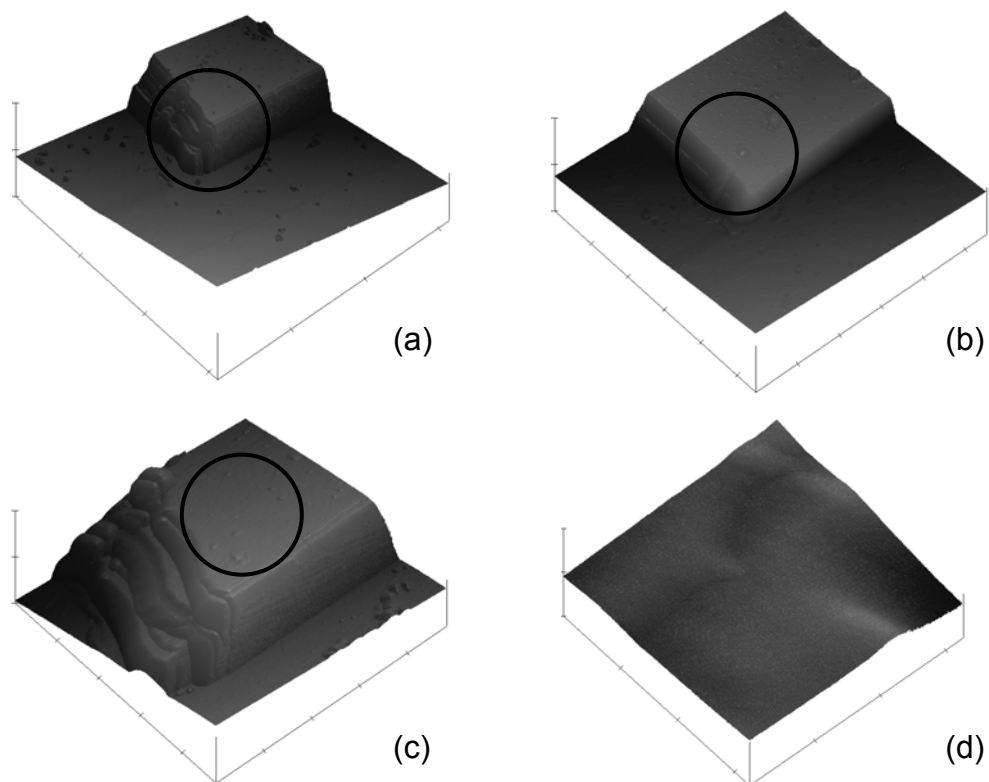


Figure 5.8. AFM images of polymorph III.

- (a) Initial image ($XY = 1 \mu\text{m}/\text{div}$, $Z = 705 \text{ nm}/\text{div}$).
- (b) Zoom in of the circled area ($XY = 1 \mu\text{m}/\text{div}$, $Z = 372 \text{ nm}/\text{div}$).
- (c) Zoom in of the circled area ($XY = 200 \text{ nm}/\text{div}$, $Z = 330 \text{ nm}/\text{div}$).
- (d) Zoom in of the circled area ($XY = 50 \text{ nm}/\text{div}$, $Z = 42 \text{ nm}/\text{div}$).

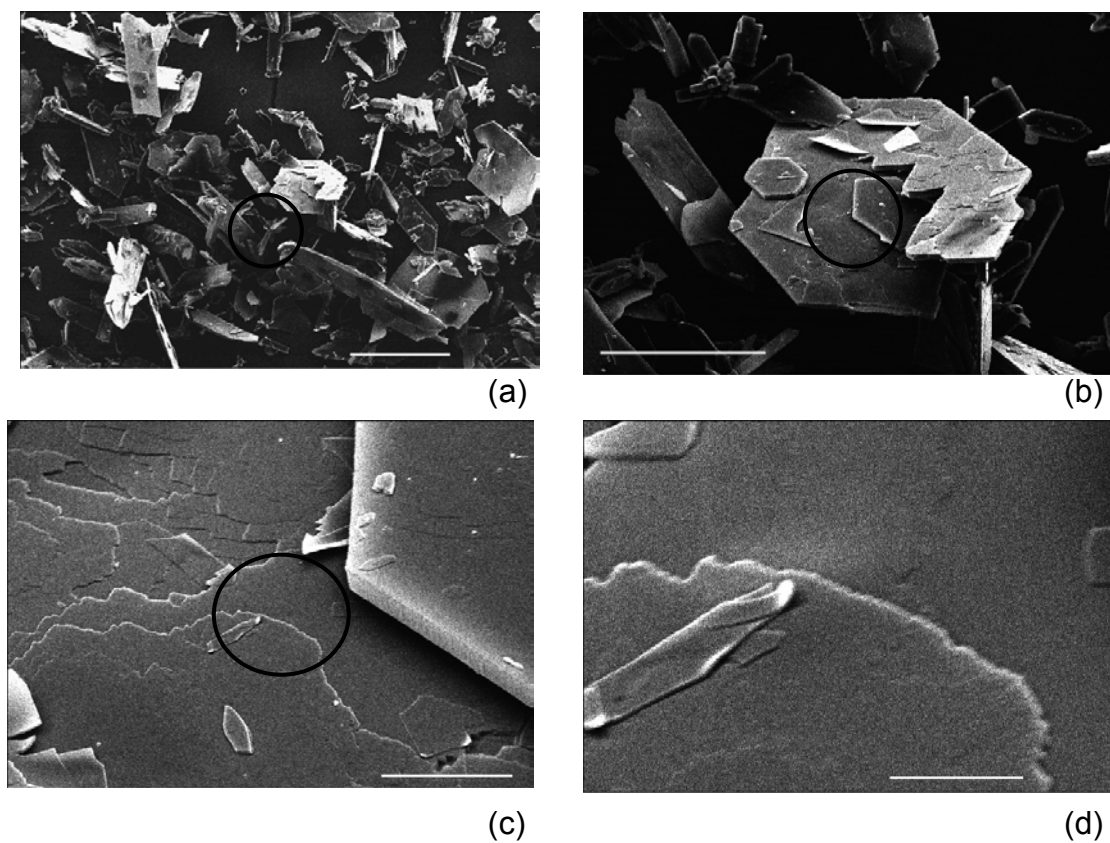


Figure 5.9. SEM images of polymorph IV.

- (a) Large area, bar length 50 μm .
- (b) Zoom in of circled crystal, bar length 20 μm .
- (c) Zoom in of circled area, bar length 2 μm .
- (d) Zoom in of circled area, bar length 500 nm.

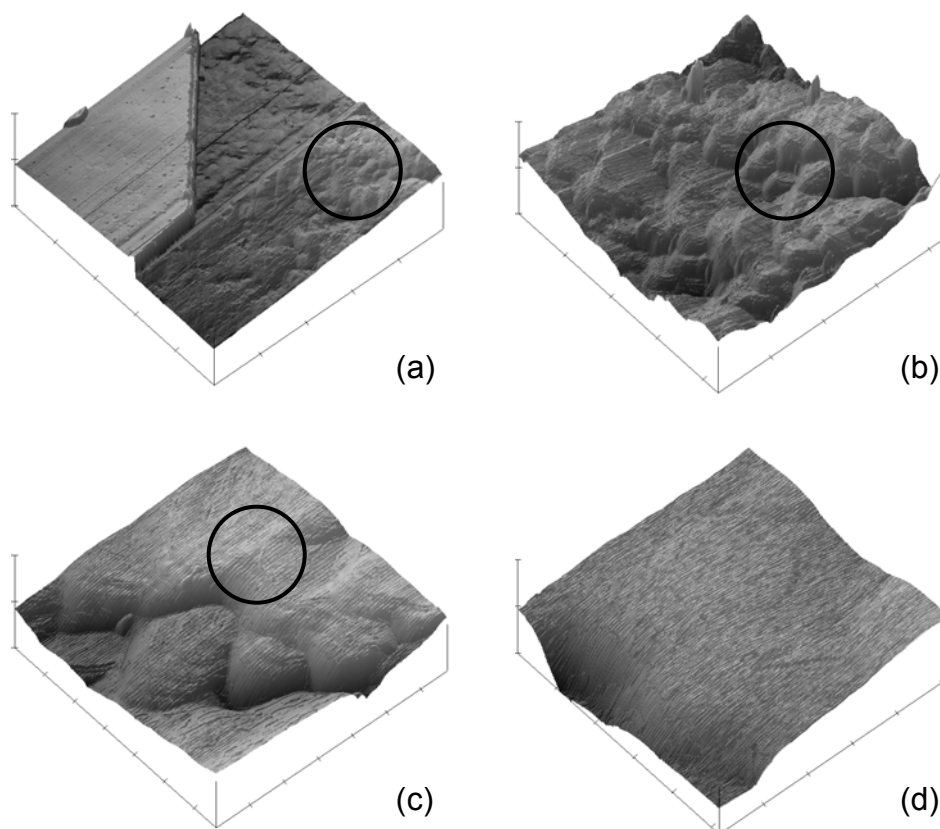


Figure 5.10. AFM images of polymorph IV.

(a) Initial area ($XY = 2 \mu\text{m/div}$, $Z = 799 \text{ nm/div}$).

(b) Zoom in on circled area ($XY = 1 \mu\text{m/div}$, $Z = 80 \text{ nm/div}$).

(c) Zoom in on right corner ($XY = 200 \text{ nm/div}$, $Z = 80 \text{ nm/div}$).

(d) Zoom in on centre ($XY = 100 \text{ nm/div}$, $Z = 28 \text{ nm/div}$).

varies with the scale of the sample box size used (Kiely and Bonnell, 1997). When a size of less than $1\ \mu\text{m} \times 1\ \mu\text{m}$ was used the order of roughness was I-Met>IV>I-Ace>III. However for sample sizes of greater than $4\ \mu\text{m} \times 4\ \mu\text{m}$ the order of roughness changed to I-Met>III>I-Ace>IV. This may be related to the images used to take the roughness measurements. For Polymorphs IV and I-Ace the images had no steps present. However for polymorph III, where steps were present, it was seen that the roughness was found to vary sharply depending on the sample box size used. When box sizes of $<1\ \mu\text{m}$ were used the roughness increased at a uniform rate, however when a box size of $\geq 2\ \mu\text{m}$ was used, it began to encompass the step region of the image so that the roughness increased more markedly.

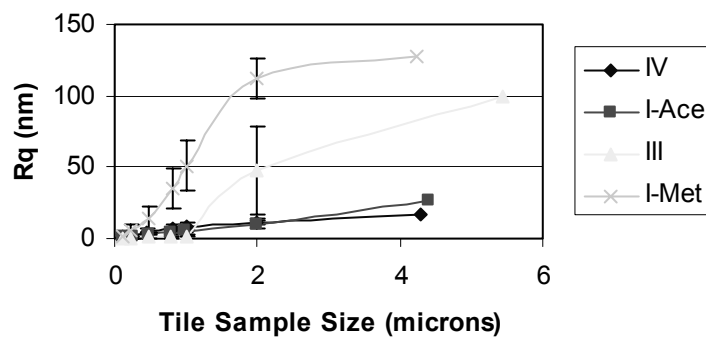
5.3.3. Force Measurements and Surface Energy Calculations

5.3.3.1. Polymorph I-Met

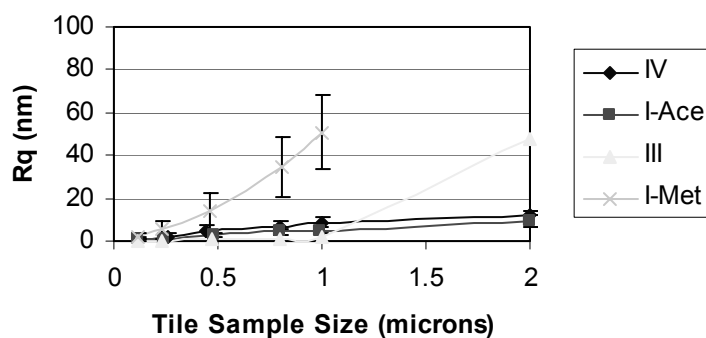
The tip image of polymorph I-Met tip A is shown in figure 5.12 (a). It can be seen that the asperity morphology consisted of a single broad particle of height 297 nm, breadth 703 nm and width $1.6\ \mu\text{m}$.

The tip A adhesion force measurements against HOPG are shown in figure 5.12 (b). The measurements showed a maximum at 22% RH, followed by a decrease at 44% RH. Following this there was a large increase observed at 72% RH. Significant differences ($P<0.05$) were observed between all forces.

Tip A force measurements against individual particles of polymorph I-Met are seen in figure 5.12 (c). The behaviour of the inter-particulate interaction varied depending on if it was a point or a general area measurement. It is seen that the $1\ \mu\text{m}$ and $9\ \mu\text{m}$ point measurements showed decreasing adhesion force with increasing humidity. For both results the decrease was significant ($P<0.05$) except between the 22% RH and 44% RH forces. The $4.9\ \mu\text{m}$ point adhesion force decreased from $<10\%$ RH to 22% RH, but then increased at 44% RH before decreasing again at 72% RH. The individual



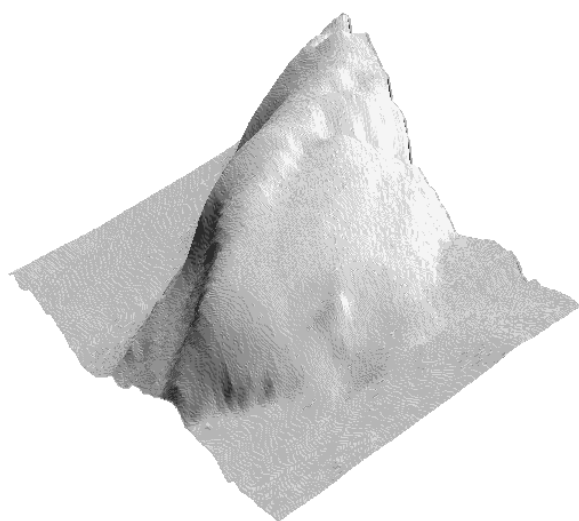
(a)



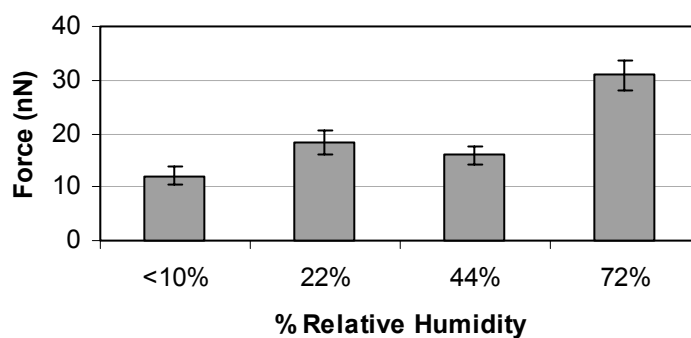
(b)

Figure 5.11. Roughness of polymorphs. Error bars show the SD.

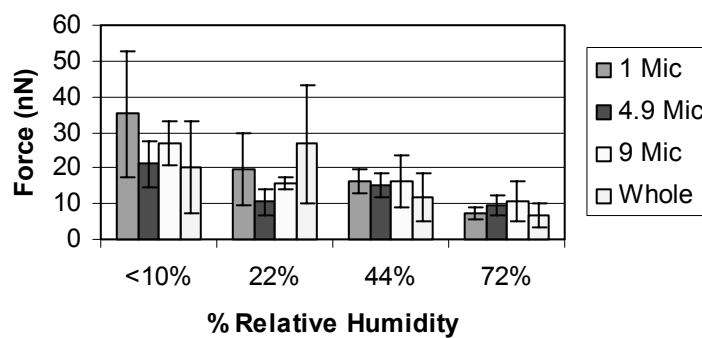
- (a) Roughness measurements taken using increasing sample sizes up to maximum image size.
- (b) Roughness measurements from (a) showing the data obtained sample sizes up to a maximum of $2\mu\text{m} \times 2\mu\text{m}$ on a larger scale.



(a)



(b)



(c)

Figure 5.12. Image and force data for polymorph I-Met Tip A. Error bars show the SD.

- (a) Image of asperity ($XY = 1.2 \mu\text{m}$, $Z = 326 \text{ nm}$).
- (b) Force measurements against HOPG.
- (c) Force measurements against particles.

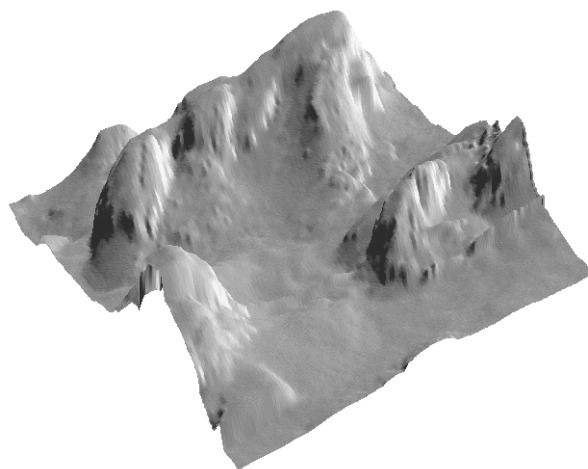
measurements taken over the 10 μm x 10 μm area showed a peak in adhesion at 22% RH, but with a large SD. However, there was a significant difference observed between results ($P < 0.05$).

Polymorph I-Met tip B is seen in figure 5.13 (a), and consists of a single asperity. The dimensions of the asperity were height 480 nm, breadth 330 nm and width 2 μm . It is seen that the asperity has a shoulder, the edge of which is separated from the top of the asperity by a height of 78 nm and horizontal distance of 1.146 μm .

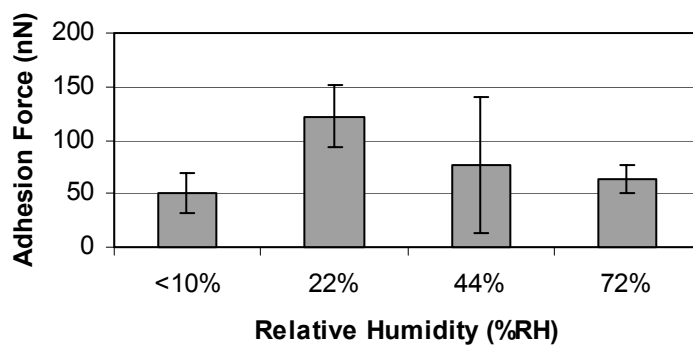
The force measurements of tip B against HOPG are shown in figure 5.13 (b). These showed a similar increase at 22% RH to that seen for tip A, however following this the force decreases until a minimum is reached at 72% RH. It is also of note that a large SD is observed at 44% RH, as the CV was 83% compared to the values of 21% to 36% seen with the other humidity measurements, although there was a significant difference between the results ($P < 0.05$).

Tip B force measurements against particles of I-Met are shown in figure 5.13 (c). A mixture of adhesion behaviours was again observed. The 1 μm point measurements showed no difference ($P > 0.05$) between <10% RH and 22% RH, before reaching a peak at 44% RH. The 4.9 μm measurements showed a significant decrease ($P < 0.05$) in force between <10% RH and 22% RH, before gradually increasing. The 9 μm and whole area measurements showed peaks in adhesion at 22% RH, however the whole area measurements peak was smaller and again masked by large SD. The 9 μm measurement showed significant differences ($P < 0.05$) between adjacent humidity values, while the whole area measurements only showed a significant difference ($P < 0.05$) between <10% and 22% RH.

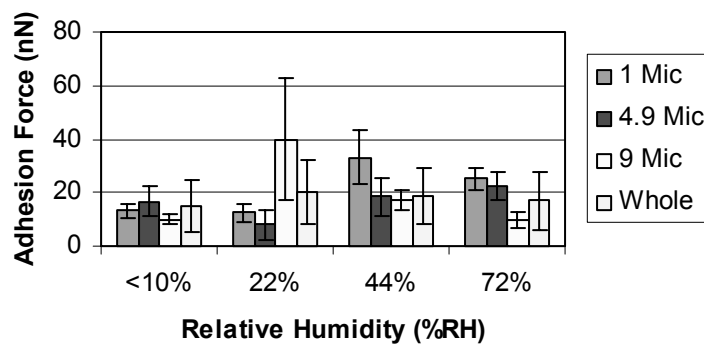
Polymorph I-Met tip C is shown in figure 5.14 (a). The asperity consisted of a single structure of height 336 nm, width 1.37 μm and breadth 817 nm.



(a)



(b)



(c)

Figure 5.13. Image and force data for polymorph I-Met tip B. Error bars show the SD.

- (a) Image of asperity ($XY = 2.6 \mu\text{m}$, $Z = 561 \text{ nm}$).
- (b) Force measurements against HOPG.
- (c) Force measurements against particles.

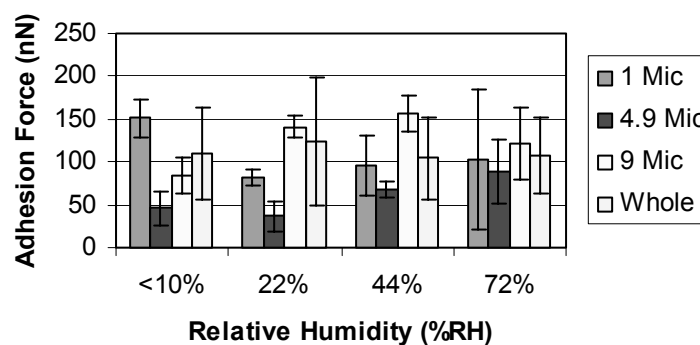
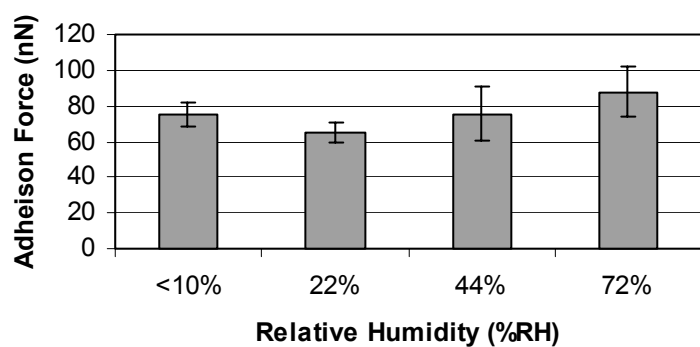
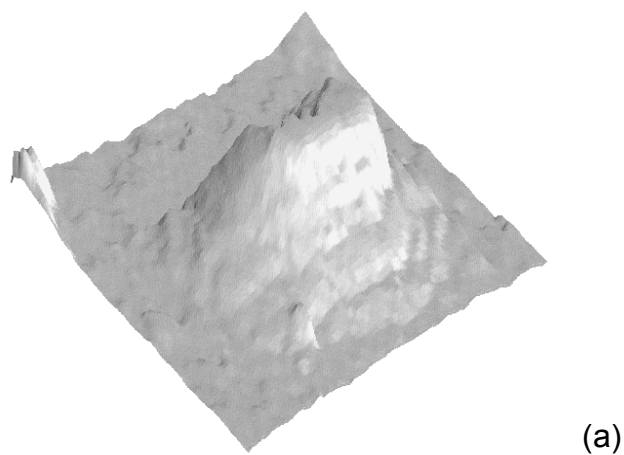


Figure 5.14. Image and force data of polymorph I-Met Tip C. Error bars show the SD.

- (a) Image of asperity ($XY = 1.8 \mu\text{m}$, $Z = 412 \text{ nm}$).
- (b) Force measurements against HOPG.
- (c) Force measurements against particle.

However accurate height measurements are not possible due to the surface structure of the top of the asperity not being very well defined.

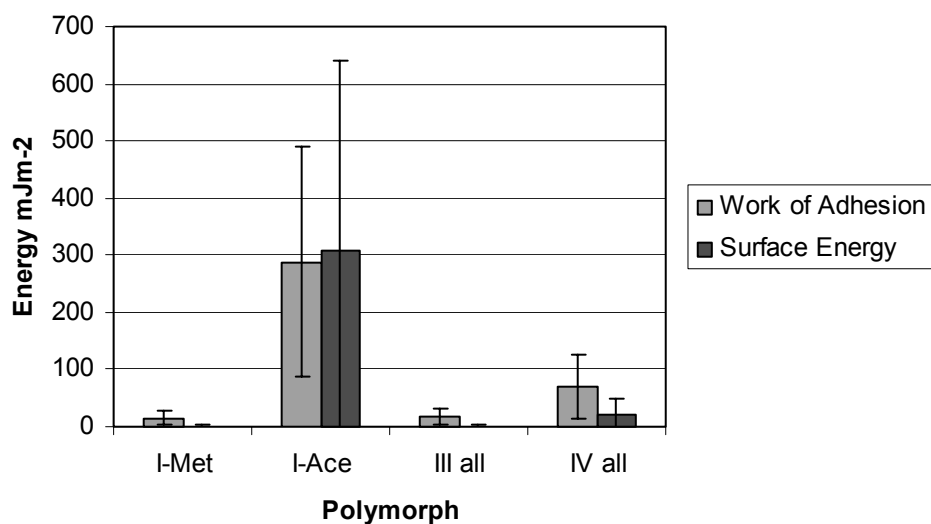
The adhesion force measurements of tip C against HOPG are shown in figure 5.14 (b). These showed significant differences ($P < 0.05$) in behaviour between sequential humidity changes, in that there was a slight decrease from $< 10\%$ RH to 22% RH, followed by an increase in force.

Tip C particle force measurements against polymorph I-Met are shown in figure 5.14 (c). The $1\ \mu\text{m}$ and $4.9\ \mu\text{m}$ measurements show a decrease in adhesion force from $< 10\%$ RH to 22% RH, before increasing. The $1\ \mu\text{m}$ measurements showed no significant differences ($P > 0.05$) between 22% and 72% RH, while the $4.9\ \mu\text{m}$ point showed significant differences ($P < 0.05$) between all humidity values. The $9\ \mu\text{m}$ point shows significant differences ($P < 0.05$) between the different humidity values, with a peak in adhesion force at 44% RH, while the whole area shows a peak effect at 22% RH, although there was no significant difference ($P > 0.05$) between the forces.

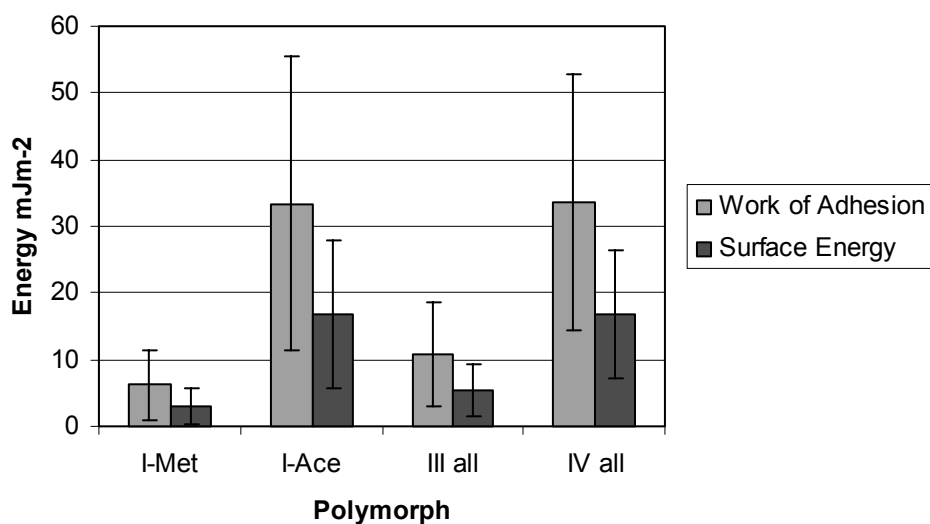
The work of adhesion of all of the polymorphs is shown in figure 5.15 (a). Against HOPG, the average work of adhesion of polymorph I-Met was found to be $15\ \text{mJm}^{-2}$ (SD $13\ \text{mJm}^{-2}$), and against particles was $6.17\ \text{mJm}^{-2}$ (SD $6\ \text{mJm}^{-2}$). The surface energy of polymorph I-Met is shown in figure 5.15 (b). Against HOPG this was found to be $0.99\ \text{mJm}^{-2}$ (SD $1.25\ \text{mJm}^{-2}$), and when using the particle measurements was $3.09\ \text{mJm}^{-2}$ (SD $2.67\ \text{mJm}^{-2}$).

5.3.3.2. Polymorph I-Ace

The tip image of polymorph I-Ace tip D is shown in figure 5.16 (a). This consisted of a single asperity of triangular shape approximately $217\ \text{nm}$ high, $600\ \text{nm}$ wide and breadth $233\ \text{nm}$. The force measurements against HOPG are shown in figure 5.16 (b). It was seen that the adhesion forces showed significant changes ($P < 0.05$) with each humidity, with a decrease between $< 10\%$ RH to 44% RH, before increasing at 72% RH.



(a)

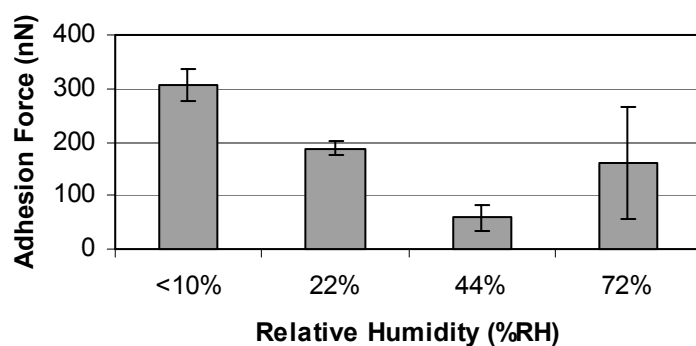
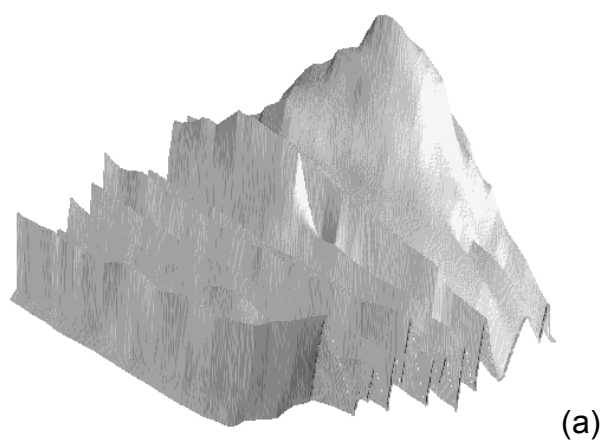


(b)

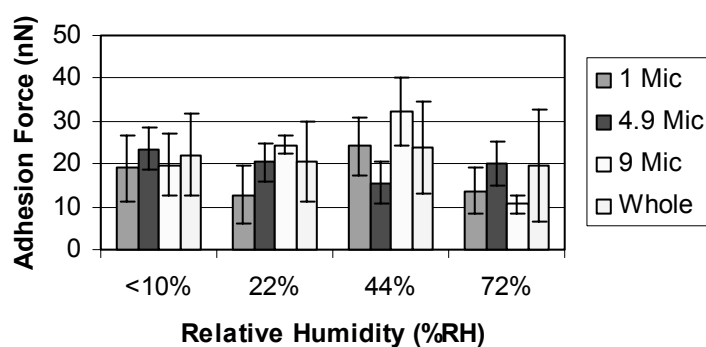
Figure 5.15. Work of adhesion and surface energy measurements of polymorph particles. Error bars show the SD.

(a) Against HOPG.

(b) Against particles of the same polymorph.



(b)



(c)

Figure 5.16. Image and force data for polymorph I-Ace Tip D. Error bars show the SD.

(a) Image of asperity ($XY = 1 \mu\text{m}$, $Z = 402 \text{ nm}$).

(b) Force measurements against HOPG.

(c) Force measurements against particles.

Tip D adhesion force measurements against particles of polymorph I-Ace are seen in figure 5.16 (c). It is seen that only the 4.9 μm point showed significant differences ($P < 0.05$) between the forces, and resembled the HOPG measurements in terms of trend. The 9 μm point shows significant differences ($P < 0.05$) between the forces, and a peak in adhesion at 44% RH, while the 1 μm point and whole area measurements show similar behaviour with decreasing adhesion force between <10% RH and 22% RH, before peaking at 44% RH. The whole area measurements are masked by a large SD, and show no significant difference ($P > 0.05$) between <10% and 44% RH, while the 1 μm measurements show significant differences ($P < 0.05$) between sequential humidity readings.

Polymorph I-Ace tip E is shown in figure 5.17 (a). This consisted of two asperities, the largest one being of irregular shape and height 225 nm, width 1.8 μm and breadth 654 nm. The next highest point from the main asperity was separated by 130 nm. The smaller asperity was of flat morphology, and its dimensions were 489 nm breadth, 1.175 μm width and 287 nm high. Both asperities were deemed to have been involved in the interaction.

The force measurements of tip E against HOPG are shown in figure 5.17 (b). It can be noted that the forces increase with humidity, with only the 22% to 44% RH change showing no significant change ($P > 0.05$) in adhesion. Because of the irregular appearance of the particle the increase could be due to the crevices present on the surface of the asperity filling up with moisture with increasing humidity.

Tip E adhesion measurements against particles of polymorph I-Ace are shown in figure 5.17 (c). These again show a mixture of behaviours. The 1 μm point adhesion measurements showed significant differences ($P < 0.05$), with a peak observed at 22% RH, before decreasing at 44% RH and then further increasing at 72% RH. Point 4.9 μm and the whole area adhesion measurements show the opposite to the 1 μm point behaviour by showing a

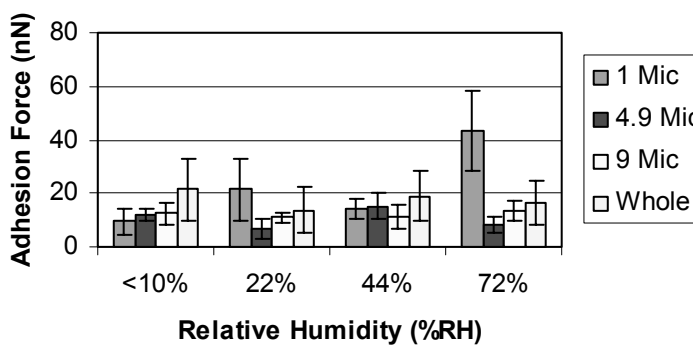
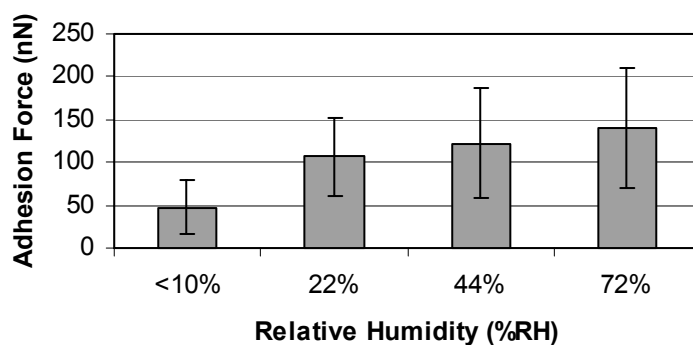
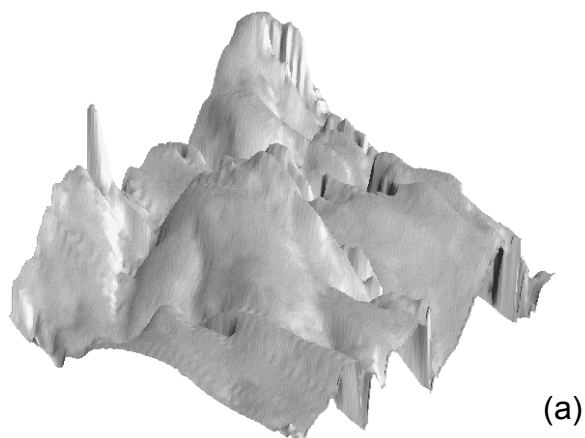


Figure 5.17. Image and force data of polymorph I-Ace tip E. Error bars show the SD.

- (a) Image of asperities ($XY = 2.05 \mu\text{m}$, $Z = 534 \text{ nm}$).
- (b) Force measurements against HOPG.
- (c) Force measurements against particles.

drop at 22% RH, before peaking at 44% RH. The 1 μm point showed significant differences ($P < 0.05$) between sequential humidity values, while the whole area measurements only showed significant differences between the <10% and 44% values. The 9 μm point shows a peak in adhesion at 44% RH, although no significant difference ($P > 0.05$) is observed between the 44% and 72% RH values.

Polymorph I-Ace tip F is shown in figure 5.18 (a). This demonstrated a very irregular morphology, with a main asperity of length 2.44 μm and width 865 nm. The main asperity had a number of sharp features on the surface meaning that accurate determination of the height was not possible. However heights were found to range from 192 nm to 277 nm.

Against HOPG (figure 5.18 (b)), the tip F adhesion forces measured showed similar behaviour to tip E in that the force increased with humidity. There was a large SD present (CV varied from 35 to 65%), but the only non-significant difference ($P > 0.05$) was observed between 44% and 72% RH. This could be due to the smaller asperities filling with moisture increasing the pull off force.

Tip F adhesion measurements against polymorph I-Ace are shown in figure 5.18 (c). Point 1 μm showed significant increases ($P < 0.05$) in adhesion force with humidity. Point 9 μm showed a peak in adhesion at 22% RH, although there was no significant difference ($P > 0.05$) in adhesion between 22% and 44% RH, while point 4.9 μm and the whole area measurements showed a decrease at 22% RH, followed by a peak at 44% RH, with significant differences ($P < 0.05$) between sequential humidity measurements.

A typical force curve for polymorph I-Ace is shown in figure 5.19. This is different to force curves that are normally seen for AFM measurements (for example figure 2.6). Force curves obtained for this polymorph often had a saw edge appearance that is consistent with either multiple contact points or a polymer like substance on the surface being stretched.

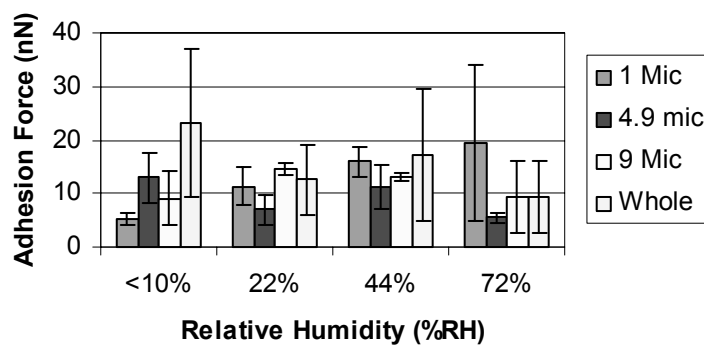
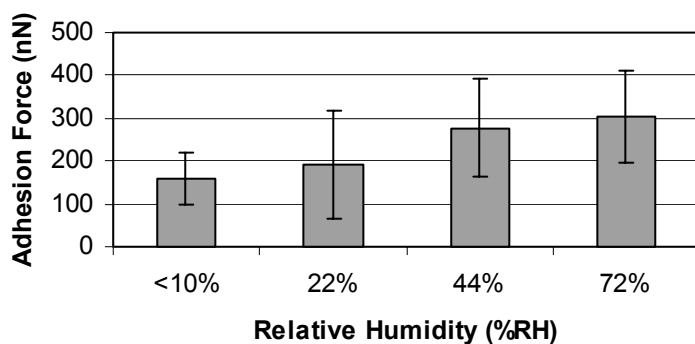
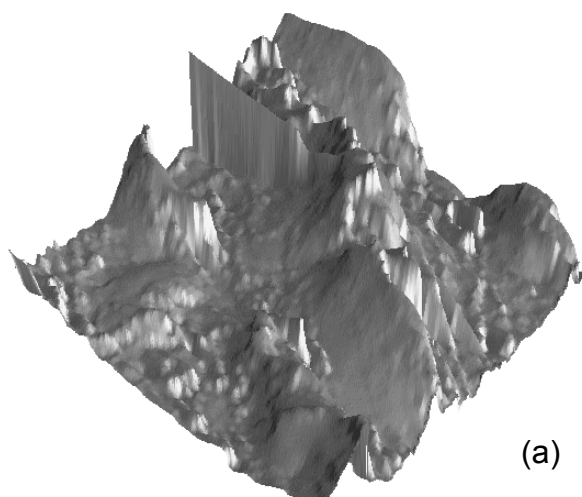


Figure 5.18. Image and force data of polymorph I-Ace tip F. Error bars show the SD.

- (a) Image of asperity ($XY = 2.2 \mu\text{m}$, $Z = 514 \text{ nm}$).
- (b) Force measurements against HOPG.
- (c) Force measurements against particles.

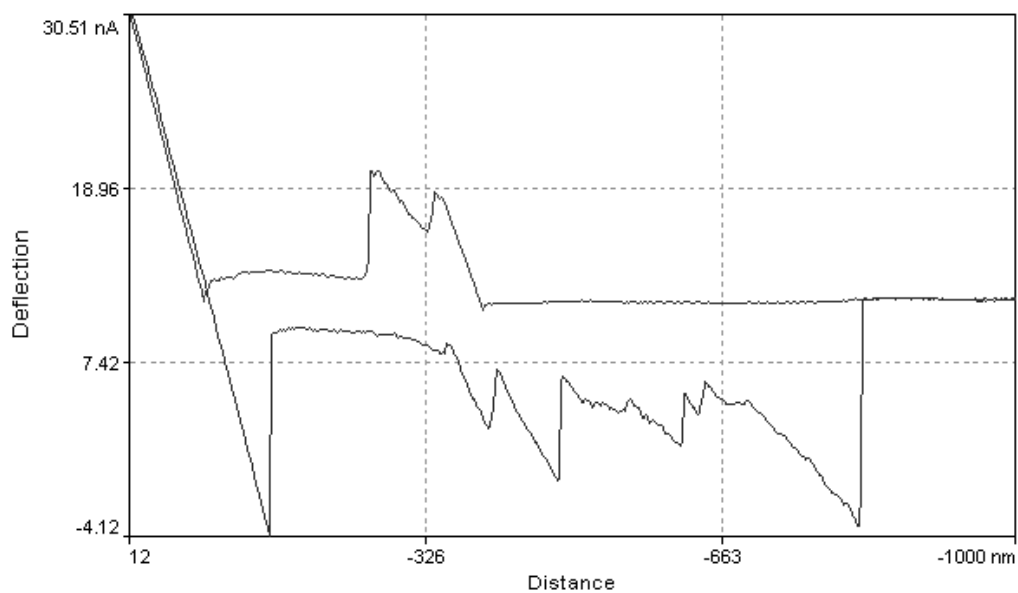


Figure 5.19. Typical force curve seen for polymorph I-Ace. The approach curve shows an increase in deflection at ~ 320 nm, which could be due to the collapse of asperities. The retract curve shows multiple pull-off events, consistent with the presence of a polymer on the surface or multiple adhesion events.

The work of adhesion and surface energy measurements against HOPG and particles are shown in figure 5.15 (a) and (b). Against HOPG, the work of adhesion was found to be 288 mJm^{-2} (SD 202 mJm^{-2}) and the surface energy of polymorph I-Ace was 309 mJm^{-2} (SD 329 mJm^{-2}). Against particles the work of adhesion was found to be 33 mJm^{-2} (SD 22 mJm^{-2}) and the surface energy was 16 mJm^{-2} (SD 11 mJm^{-2}).

5.3.3.3. Polymorph III

The tip image of polymorph III tip G is shown in figure 5.20 (a). This consisted of a flat triangular structure with a small raised area in one corner. The main structure had a height of 580 nm, width $1.9 \mu\text{m}$ and breadth $1.9 \mu\text{m}$. The smaller raised area was separated from the tip of the main structure by a height of 103 nm, and had dimensions of 613 nm by 753 nm.

The force measurements of tip G against HOPG are shown in figure 5.20 (b). The force measurements showed significant differences ($P < 0.05$) between sequential humidity measurements, and showed a peak at 22% RH, followed by a drop at 44% RH, and then a further increase at 72% RH.

The force measurements of tip G against particles are seen in figure 5.20 (c). These measurements show a strong resemblance to that of the HOPG results. The $1 \mu\text{m}$ and $9 \mu\text{m}$ points showed significant ($P < 0.05$) sequential changes in adhesion force, with an increase at 22% RH before decreasing at 44% RH, and then increasing again at 72% RH. The remaining point and whole area measurements show an increase in force at 22% RH, which then remains constant before undergoing a large increase at 72% RH. However, for the $4.9 \mu\text{m}$ point there is a significant difference ($P < 0.05$) between measurements, whereas the only significant difference ($P < 0.05$) for the $9 \mu\text{m}$ point is seen between the 44% and 72% RH measurements. There is an accompanying large increase in SD for the whole area measurements at 72% RH (CV of 50% compared to 6.2 to 23% for the other humidity measurements).

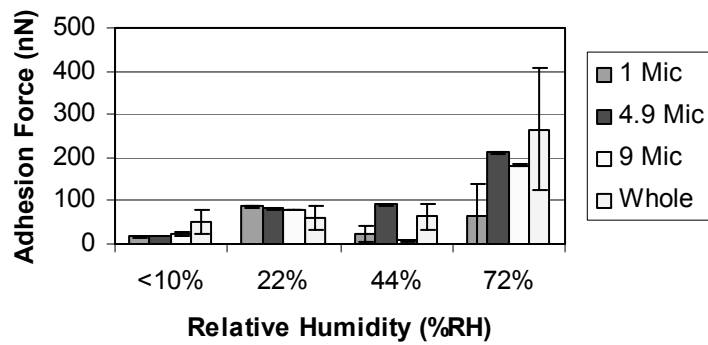
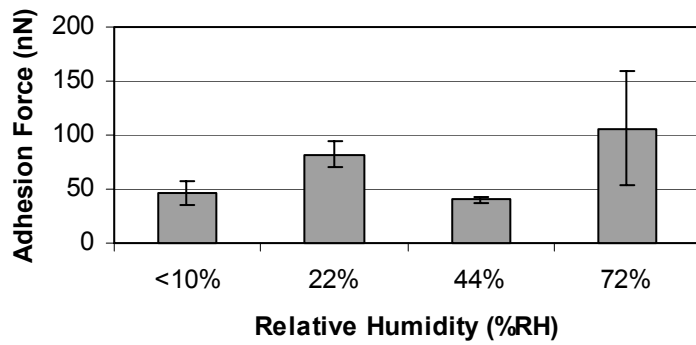
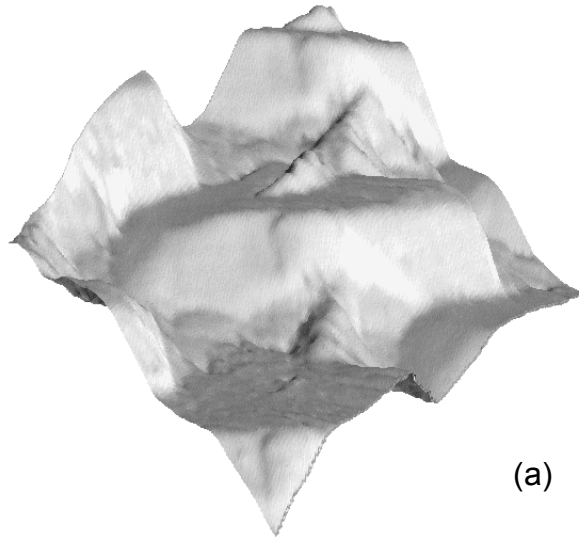


Figure 5.20. Image and force data of polymorph III Tip G. Error bars show the SD.

- (a) Image of asperity ($XY = 2.75 \mu\text{m}$, $Z = 513 \text{ nm}$).
- (b) Force measurements against HOPG.
- (c) Force measurements against particles.

The tip H asperity of polymorph III is shown in figure 5.21 (a). This asperity consisted of a single long structure. While it was not possible to determine actual heights of the structure, the minimum difference in height between repeats of the structure was 72 nm, and the maximum distance was 119 nm. The length of the asperity was 5.4 μm long and 856 nm wide.

The forces against HOPG are shown in figure 5.21 (b), and showed no significant difference ($P>0.05$) between <10% RH and 44% RH. However once 72% RH was reached there was a significant increase ($P<0.05$) in adhesion force.

Tip H adhesion force measurements against particles are shown in figure 5.21 (c). All of the points and the whole areas show the same adhesion behaviour from <10% RH to 44% RH in that they decrease at 22% RH before increasing at 44% RH. However at 72% RH the behaviour changes, as points 1 μm and 9 μm decrease again, point 4.9 μm increases and the whole area measurements remains the same. With the exception of the 1 μm point between 22% and 44% RH, and the whole area measurements between 44% and 72% RH, all data series showed significant differences ($P<0.05$) between sequential humidity readings.

The contacting asperities of polymorph III tip I is shown in figure 5.22 (a), and consist of a raised triangular structure with smaller protrusions on the top. The base of the asperity was 263 nm high, 2.3 μm wide and was of breadth 1.5 μm . The largest of the smaller asperities on the top of the structure was 455 nm wide and 101 nm high. The height difference between this asperity and the next largest asperity was 72 nm.

The force measurements of tip I against HOPG are shown in figure 5.22 (b). It is seen that there is a insignificant ($P>0.05$) increase in adhesion force between <10% RH and 22% RH. This is then followed by a significant decrease ($P<0.05$) at 44% RH before increasing significantly ($P<0.05$) at

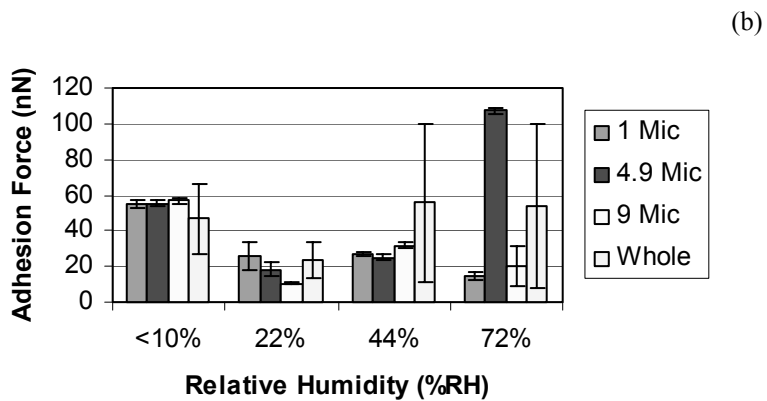
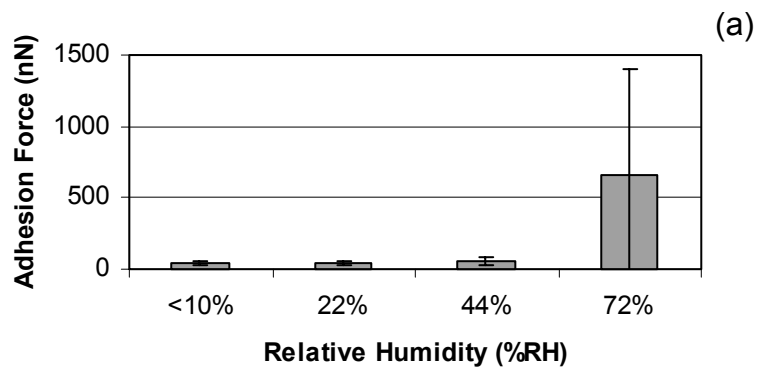
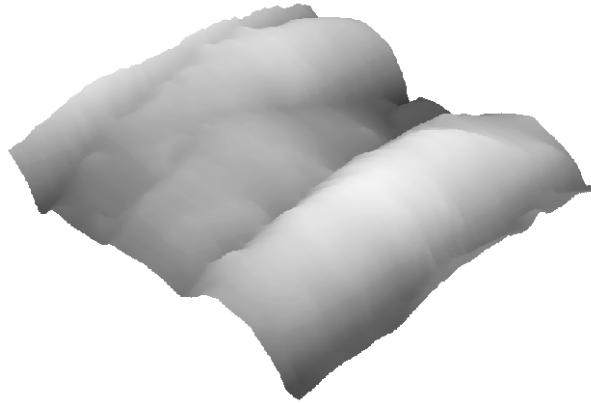


Figure 5.21. Image and force data of polymorph III tip H. Error bars show the SD.

(a) Image of asperity (XY = 2 μ m, Z = 215 nm).

(b) Force measurements against HOPG.

(c) Force measurements against particles.

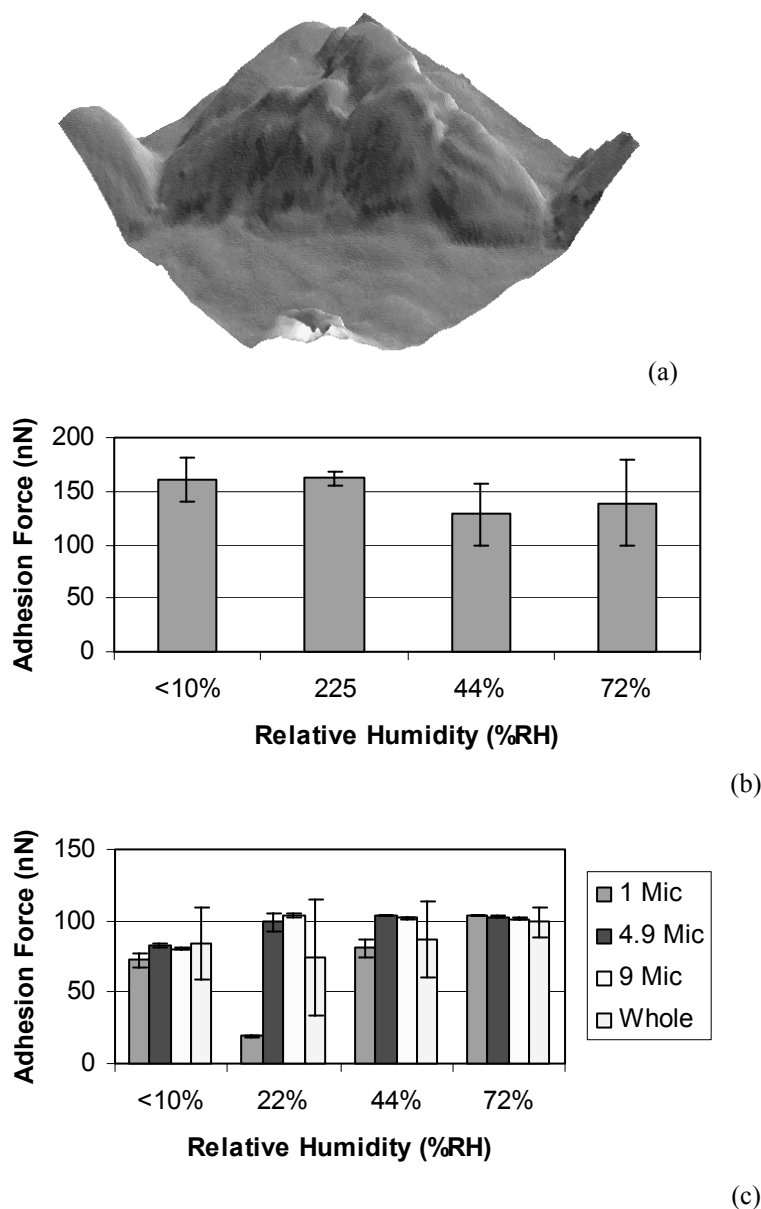


Figure 5.22. Image and force data for polymorph III tip I. Error bars show the SD.

(a) Image of asperity ($XY = 2.25 \mu\text{m}$, $Z = 430 \text{ nm}$).

(b) Force measurements against HOPG.

(c) Force measurements against particles.

72% RH. It is also seen that all of the forces had overlapping SD meaning that the subtle changes in forces were masked.

The tip I forces measured against polymorph III particles are shown in figure 5.22 (c). This showed different behaviour in that the measurements at points 4.9 μm and 9 μm showed an increase in adhesion at 22% RH and then remained constant. However, at 1 μm and the whole area measurements, there was a slight decrease in adhesion force at 22% RH, followed by an increase as humidity increased. Significant differences ($P < 0.05$) were observed between all of the data points. It was also observed that as the humidity increased, the SD of the whole area measurements decreased.

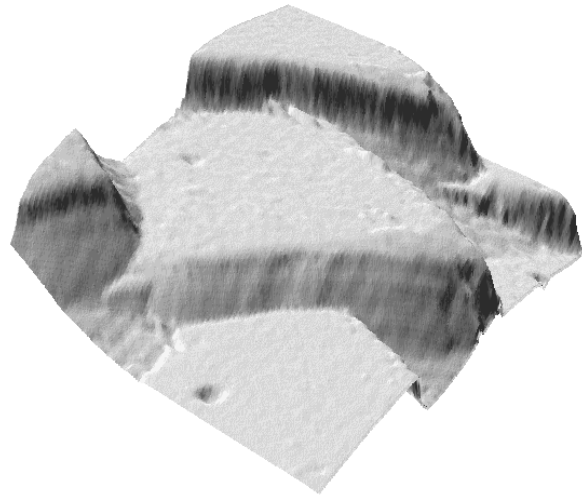
Against HOPG, the work of adhesion of polymorph III was found to be 16.2 mJm^{-2} (SD 14.4 mJm^{-2}), and the surface energy was 1.17 mJm^{-2} (SD 1.5 mJm^{-2}). Against particles of polymorph III, the work of adhesion was found to be 10.78 mJm^{-2} (SD 7.9 mJm^{-2}) and the surface energy was 5.4 mJm^{-2} (SD 3.9 mJm^{-2}).

5.3.3.4. Polymorph IV

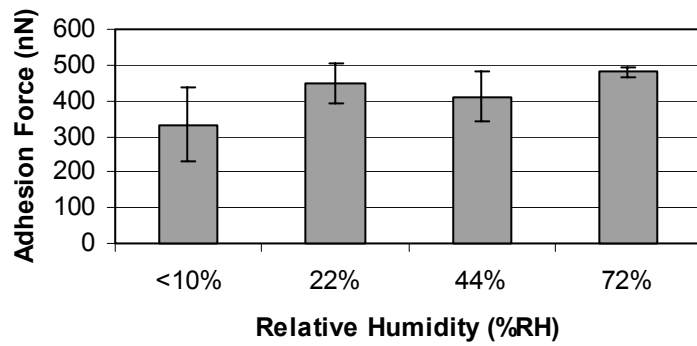
The tip image of polymorph IV tip J is shown in figure 5.23 (a). The asperity consisted of a triangular structure of length 3.2 μm , width 1.6 μm and height 254 nm.

The force measurements of tip J against HOPG are shown in figure 5.23 (b). It is seen that there is a slight increase in adhesion at 22% RH, before decreasing at 44% RH, then an increasing at 72% RH. However, while all measurements have overlapping SD, meaning that the peaks are masked, there is a significant difference ($P < 0.05$) between the sequential measurements.

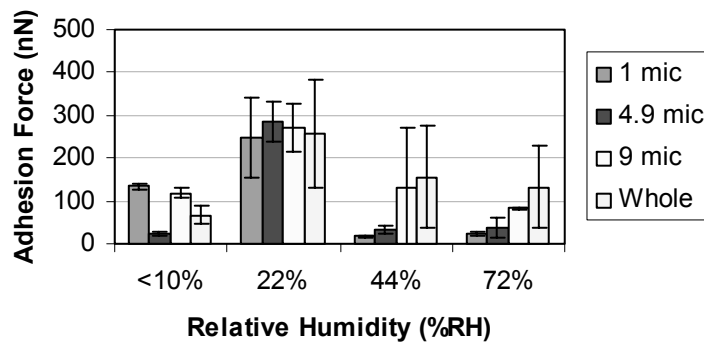
The force measurements of tip J against particles are illustrated in figure 5.23 (c). All of the points as well as the whole area measurements showed



(a)



(b)



(c)

Figure 5.23. Image and force data for polymorph IV tip J. Error bars show the SD.

(a) Image of asperity ($XY = 2.5 \mu\text{m}$, $Z = 482 \text{ nm}$).

(b) Force measurements against HOPG.

(c) Force measurements against Particles.

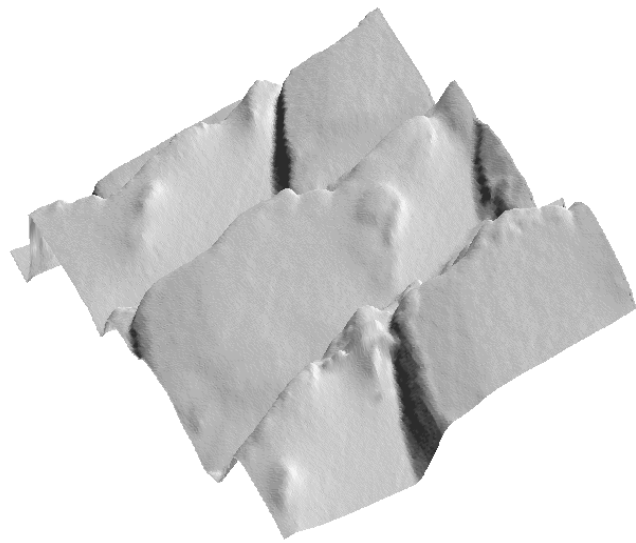
the same behaviour in that a peak in adhesion force could be observed at 22% RH. However it is noted that from 22% RH to 72% RH the SD of the whole area measurements was large, as was the SD of the 9 μm point at 44% RH. The only non-significant differences ($P>0.05$) between the data were seen with the 1 μm , 4.9 μm and whole area measurements between 44% and 72% RH.

The tip image of polymorph IV tip K is shown in figure 5.24 (a). This consisted of a single structure of height 365 nm, breadth 1.1 μm and width 2.6 μm . There were two points of contact separated by 85 nm and a trough with a maximum depth of 100 nm.

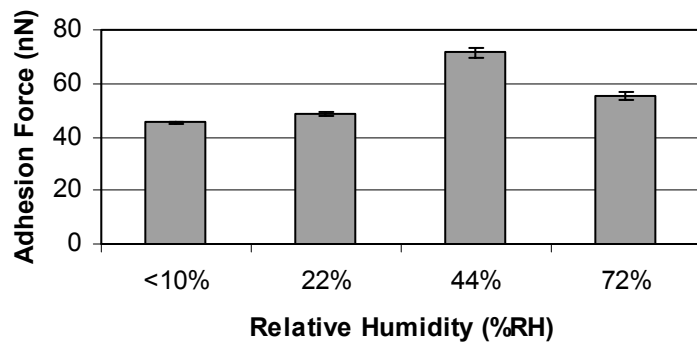
The force measurements of tip K against HOPG are shown in figure 5.24 (b). It is seen that there is significant difference ($P<0.05$) between all the forces recorded with changing humidity. The data shows a peak in adhesion at 44% RH, before decreasing at 72% RH. There is also a very low SD (CV of 1% to 2.5%).

Tip K particle-particle adhesion force measurements are shown in figure 5.24 (c). All of the point measurements show significant differences ($P<0.05$) between forces recorded at different humidity, as well as differences in the adhesion pattern observed, with the 1 μm point showing a peak in adhesion at 44% RH, while the 4.9 μm shows a peak at 22% RH, before decreasing at 44% RH and then increasing again at 72% RH. The 9 μm point shows a decrease at 22% RH, followed by an increase. The whole area measurements show a slight increase at 22% RH before decreasing, although no significant differences ($P>0.05$) are observed between the data obtained at changing humidity.

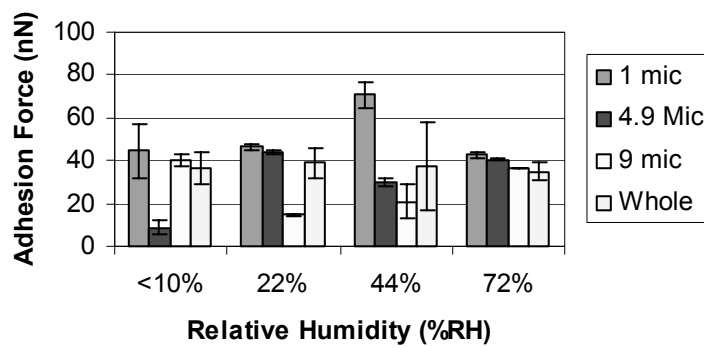
The polymorph IV tip L tip image is shown in figure 5.25 (a). The asperity consisted of a large irregular structure with length 2.1 μm and breadth 2 μm . The height was 311 nm, with smaller peaks separated by a minimum of 93 nm.



(a)



(b)



(c)

Figure 5.24. Image and force measurements of polymorph IV tip K. Error bars show the SD.

(a) Image of asperity (XY = 3 μ m, Z = 438 nm).

(b) Force measurements against HOPG.

(c) Force measurements against particles.

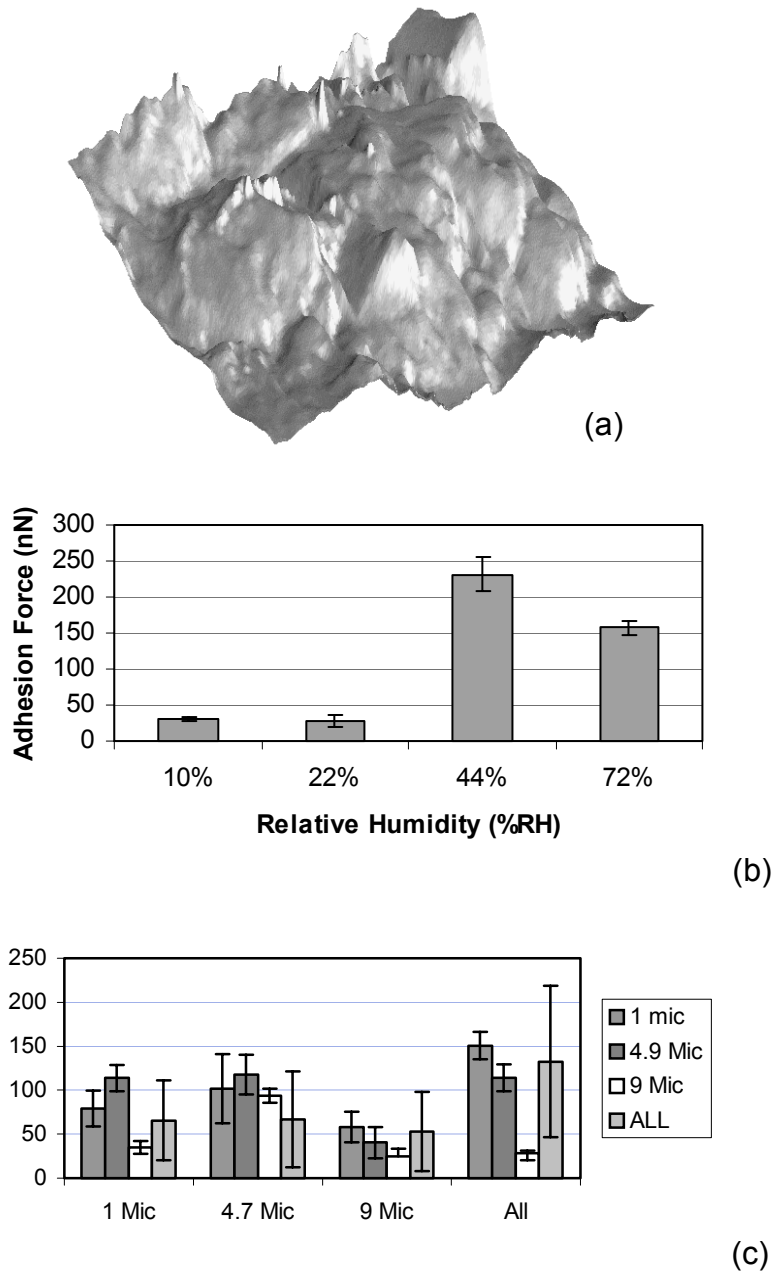


Figure 5.25. Image and force data for polymorph IV tip L. Error bars show the SD.

- (a) Image of asperity (XY = 2.4 μm , Z = 375 nm).
- (b) Force measurements against HOPG.
- (c) Force measurements against particles.

The force measurements of tip L against HOPG are shown in figure 5.25 (b). Again, there is a peak at 44% RH before decreasing at 72% RH, It is seen that the deviation is much larger than that of tip K (CV ranged from 6.5% to 29%), however the only non significant differences ($P>0.05$) in data were seen between <10% and 22% RH.

Tip L against particle-particle adhesion force measurements are shown in figure 5.25 (c). All of the point measurements and the whole area adhesion measurements show the same behaviour from <10% RH to 44% RH, in that they show a peak at 22% RH. However, once 72% RH is reached, the 1 μm point, 4.9 μm point and the whole area measurements show an increase in adhesion force, whereas the 9 μm point remains approximately the same. The measurements acquired at each point showed significant differences ($P<0.05$) with each rise in humidity, except for the 4.9 μm measurements, which showed no significant difference between <10 and 22% RH, and the whole area measurements which showed no difference between <10% and 44% RH.

Against HOPG, the work of adhesion of polymorph IV was found to be 70.1 mJm^{-2} (SD 56.9 mJm^{-2}), and the surface energy was 20.35 mJm^{-2} (SD 28.5 mJm^{-2}). Against particles the work of adhesion was found to be 33.5 mJm^{-2} (SD 19.3 mJm^{-2}) and the surface energy was 16.8 mJm^{-2} (SD 9.6 mJm^{-2}).

5.3.4. Change of Maximum Contact Force and Rate of Tip-Sample Approach

No significant changes were seen for alterations in press-on force and measurement rate for polymorphs I-Met, III and IV (data not shown). The only significant changes seen were for polymorph I-Ace which is discussed below.

5.3.4.1. Polymorph I-Ace

The changes in adhesion force as a function of press-on force and rate for I-Ace are seen in figure 5.26 and 5.27 (a) to (d). At <10% RH, 22% RH and 72% RH (figure 5.26 (a), (b) and (d)), it is seen that an increase in press on force decreases the adhesion force. These decreases were significant ($P<0.05$) except for the decrease in force between 25 nN and 35 nN at 22% RH, and between 23 nN and 35 nN at 72% RH. However, at 44% RH (figure 5.26 (c)), a significant increase ($P<0.05$) in adhesion force is seen between 15 nN and 25 nN before remaining constant for the subsequent press-on forces.

When the rate measurements are examined, significant differences ($P<0.05$) in adhesion are seen between 0.5 Hz and 2 Hz, but not between the 2 Hz and 4 Hz forces at 10% RH (figure 5.27 (a)). At this humidity, the increase in rate causes the adhesion to peak at 1 Hz before decreasing. At 22% RH (figure 5.27 (b)), the only significant difference ($P<0.05$) is between the measurements taken at 0.5 Hz and 1 Hz, and this is shown by the adhesion force decreasing at 1 Hz, before remaining constant for the other measurements. At 44% RH (figure 5.27 (c)), the increase in rate causes a significant increase ($P<0.05$) in the adhesion force across the range of rate measurements. At 72% RH (figure 5.27 (d)), we see the opposite to that seen for <10% RH in that a dip occurs at 1 Hz before the increase at higher rates. The changes in rate at 72% RH are significant ($P<0.05$) with the exception of the change between the measurements undertaken at 2 Hz and 4 Hz,

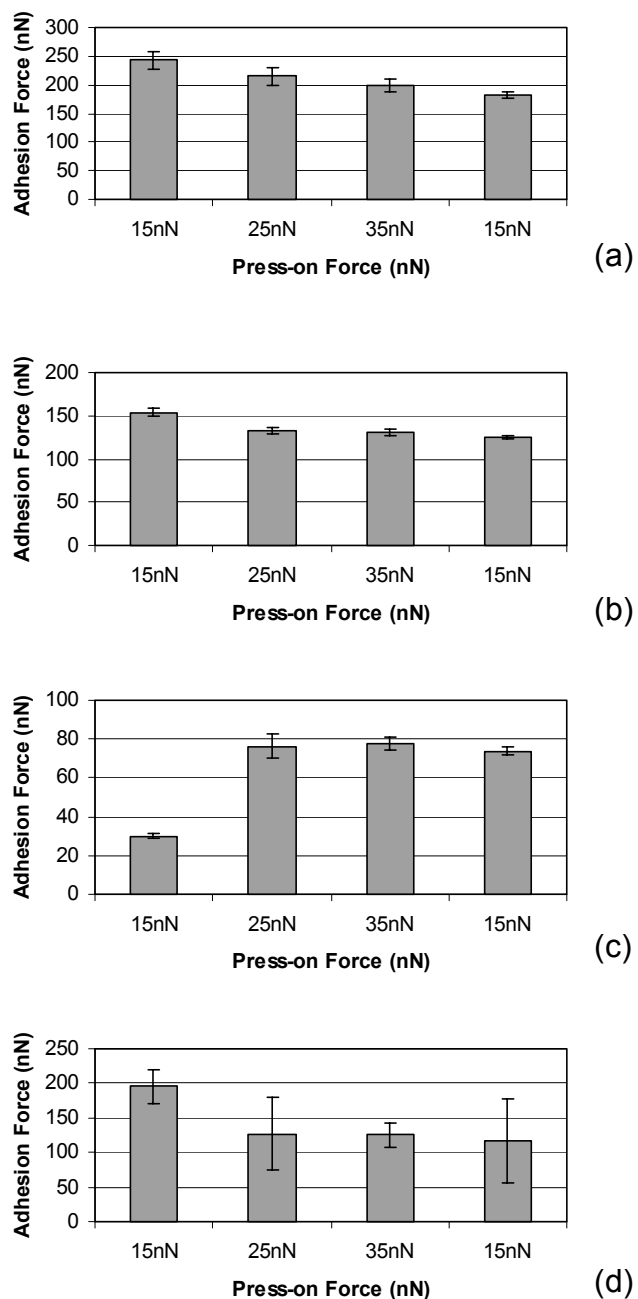


Figure 5.26. Effect of change in press on force on polymorph I-Ace. Error bars show the SD.

- (a) Effect of change of press-on force at <math><10\%</math> RH.
- (b) Effect of change of press-on force at 22% RH.
- (c) Effect of change of press-on force at 44% RH.
- (d) Effect of change of press-on force at 72% RH.

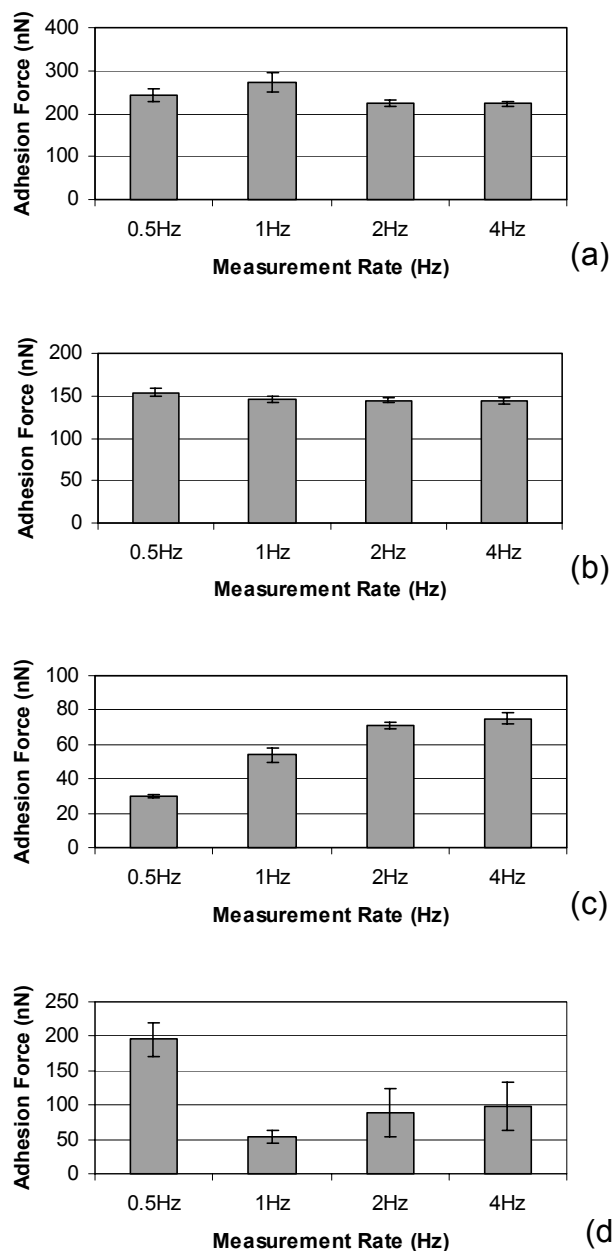


Figure 5.27. Effect of change in measurement rate on polymorph I-Ace. Error bars show the SD.

- (a) Effect of change of measurement rate at <10% RH.
- (b) Effect of change of measurement rate at 22% RH.
- (c) Effect of change of measurement rate at 44% RH.
- (d) Effect of change of measurement rate at 72% RH.

5.4. Discussion

5.4.1. Polymorph I-Met

The SEM images of polymorph I-Met (figure 5.3) show there is a mixture of two types of structures. Crystal habit is a term used to describe the different shapes of crystals of the same polymorph (Haleblian, 1975). Changes in crystal habit can occur for a number of reasons, including growth inhibition by adjacent crystals or vessel walls, changes in the supersaturation of the solvent or changes in the rate of cooling of the solvent (Haleblian, 1975). The literature states that polymorph I generally expresses a needle shaped morphology (Anwar *et al.*, 1989), which is not seen in these images. However, previous work has shown that the small aggregated regions which form the majority of the sample are consistent with the normally observed structure of SEDSTM I-Met (Kordikowski *et al.*, 2001). The larger plate-like crystal structures have not been previously reported, although changes in crystal habit may have occurred due to the nature of the crystallizing vessel size. The AFM images (figure 5.4) show the surface structure to be dominated by tightly packed step features. This presence of such a high density of features explains why it was shown to be the roughest polymorph of all the samples by AFM.

The behaviour of polymorph I-Met against HOPG shows strong correlation with the scenario model proposed in the previous chapter. Tips A and B (figures 5.12 and 5.13 respectively) are both showing scenario one behaviour. However when 44% RH is reached, the peak effect in both is beginning to be masked. For tip A this is due to the broad nature of the asperity, however for tip B it is due to the shoulder of the asperity becoming involved in the interaction. This shoulder is significantly flatter than the asperity on the top, meaning it would be more sensitive to small changes in the meniscus that will occur, leading to drastic changes in the adhesion force for small changes in humidity and, hence the increased SD recorded.

Once 72% RH is reached, the behaviour of both tips changes slightly. Tip A begins to emulate SEDS™ tip D discussed in chapter 4 (section 4.4.2). This is due to asperity saturation, leading to a big increase in adhesion. However, once 72% RH is reached for tip B, the meniscus has passed the shoulder region and is encompassing only the base of the asperity and not saturating it. Because the base of the asperity has no shoulder, the force is more regular than is seen at 44% RH. The reason it is unlikely that the whole of the asperity has been saturated is because the height of the asperity is greater than that of tip A by nearly 200 nm.

Tip C (figure 5.14) does not appear to fit in with the scenarios discussed so far. However, from the 2D images of the asperities it was obvious that the top of the asperity was not well characterised; it is possible that this flat, ill-defined smooth region was composed of surface features which the gain controls on the AFM were unable to compensate for. In consequence, it would not be possible to make a detailed comparison of behaviours.

When looking at the particle-particle measurements for all three tips (figures 5.12 (c), 5.13 (c) and 5.14 (c)), the measurements over the whole 10 μm particle area showed a similar trend to that seen with the HOPG in that there was a peak at 22% RH. In addition, it was also observed that for tip A (figure 5.12) the particle-particle adhesion force is at its lowest for 72% RH, while for the HOPG this gave the largest force. However there was also a very large standard deviation seen with these measurements, which would be related to the variation in surface features, and would lead to different contact area and also local changes in water layer coverage.

The point measurements undertaken with all three tips showed vastly differing behaviour. It is postulated that occasions where behaviour was similar to that seen for the HOPG, the local area must have been of flat morphology, and deviation from this behaviour was due to local changes in the surface morphology. The alteration in pull-off forces with surface roughness has been documented in previous work (Beach *et al.*, 2002).

The surface energy in figure 5.15 was determined to be the lowest of all the polymorphs from both the HOPG and particle measurements. While the lower surface energy recorded from the particle interaction could be due to the rough nature of the particle surface, the flat nature of the HOPG means measurements would not be affected in the same manner. In addition, the behaviour observed is consistent with work in the previous chapter, in which the lower surface energy polymorph showed a peak in adhesion at a lower humidity.

5.4.2. Polymorph I-Ace

The SEM images (figure 5.5) showed that the particles consisted of small aggregates of plate like structures. This again deviates from the literature description of conventionally crystallised polymorph I, but is similar to that previously seen for the SEDSTM material (Anwar *et al.*, 1989, Kordikowski *et al.*, 2001). The AFM images (figure 5.6) showed considerable differences from the same polymorph crystallised from methanol, in that far fewer step features were observed and a lower roughness was recorded. This was the only sample that was crystallized from a solvent other than methanol, meaning that a different reaction mechanism may have occurred leading to the observed differences in surface structure (Kordikowski *et al.*, 2001).

Against HOPG, tip D (figure 5.16) would be expected to show scenario one type behaviour, but this was not the case as the profile did not fit with any of the models. The mostly common reason for the observed decrease in adhesion force with humidity is that the particle is electrostatically charged and the decrease is due to gradual leaking of the charge, and hence reduction in electrostatic attractive forces (Kulvanich and Steward, 1988). However, this was deemed unlikely because the HOPG measurements were taken after the particle measurements, which would have caused any charge present to leak away. Another potential explanation is that there was some local change in the surface chemistry of the asperities that caused repulsion

with increasing humidity, but when 72% RH was reached the asperity was overcome leading to the increase in adhesion.

Both Tips E and F (figures 5.17 and 5.18) showed scenario three behaviour with a large SD. This would be related to the irregular surface structures that would have undergone gradual saturation.

The behaviour against particles was mixed (figures 5.16 (c), 5.17 (c) and 5.18 (c)). When examining the 10 μm x 10 μm area measurements of all tips it is seen that there is a decrease between <10% RH and 22% RH, before a slight peak is observed at 44% RH. Some of the point measurements also show this behaviour, although many showed peak effects at a single humidity. Polymorph I-Ace was, for both sample sizes, the second smoothest polymorph. The peak effects seen may be related to local changes in the surface energy of the polymorph, and when this was not seen may be related to changes in the surface roughness of the polymorph.

The change in press-on force and rate of measurements (figures 5.26 and 5.27) was shown to have a profound effect on the adhesion forces measured for this polymorph. The large alterations in adhesion observed for a 20 nN change in press-on force may also have been a reason for the differences in behaviour observed for tip D. At <10% RH and 22% RH the decrease could have been due to changes in the press-on force (as seen in figure 5. 26) leading to the decrease seen against HOPG. However this would not explain the further decrease seen at 44% RH nor the increase seen at 72% RH. This polymorph would be expected to display the same behaviour as polymorph I-Met. However, Kordikowski *et al.*, (2001) did note that some amorphous material was formed if a lower mole fraction was used, which may account for the different mechanical properties.

The surface energy of I-Ace was found to be the highest of all the polymorphs when using HOPG (figure 5.15 (a)), and the joint highest when considering the particle interaction data (figure 5.15 (b)). Because the peak

effect is seen at higher humidities with higher calculated surface energies, this may mean that since no peak was seen with any of the tips against HOPG, a high enough humidity may not have been reached for the peak to occur. Peak effects were seen with some of the point measurements, and a number of these were at 44% RH, which is what is expected for a higher surface energy material.

5.4.3. Polymorph III

The literature states the equilibrium morphology of polymorph III crystals to be small hexagonal platelets (Anwar *et al.*, 1989). This is different to that seen in the SEM images in figure 5.7, although there is some similarity to the images taken by Kordikowski *et al.*, (2001). The AFM images (figure 5.8) showed the particle to consist of many steps, however these were of lower density than those of I-Met. The roughness of polymorph III was found to depend on sample size, as discussed for polymorph I-Met. A small sample size showed it had the lowest roughness, whereas the larger sample sizes meant it was the second roughest polymorph.

Against HOPG, tip G (figure 5.20) showed a mixture of scenario one and three behaviour. Scenario one type behaviour is dominant at low humidities as only the point of the triangular asperity is involved. However, once 72% RH is reached scenario 3 behaviour dominates because the smaller asperity becomes involved, leading to the increase in force. Tip H (figure 5.21) also displays scenario three behaviour against the HOPG substrate, due to the presence of a single flattened asperity.

Tip I (figure 5.22) shows scenario two behaviour with HOPG as there is a slight peak at 22% RH masked by a large SD. The tip image shows a large asperity with a number of smaller features on the top, the larger of which would dominate the adhesion at low RH. However as humidity increased to 44% RH the smaller ones would have become involved, leading to the

increased SD. Once 72% RH was reached an increasing number of asperities would have become involved leading to the increase in force.

For the particle measurements (figures 5.20 (c), 5.21 (c) and 5.22 (c)), the only similarity to the HOPG measurements was seen with tip G, whilst there was very little similarity for the other tips. This may be because although polymorph III has the lowest level of roughness for small sample sizes, at larger sizes it has the second roughest surface. Only tip G had a single well defined point involved in the interaction, whereas tips H and I had a broad peak and multiple peaks respectively, meaning that a much larger, and more unpredictable contact area would be involved leading to the changes in adhesion measured.

The surface energy of polymorph III was the second lowest of all the polymorphs, and the values were of a similar order of magnitude to those of polymorph I-Met (figure 5.15). This is of note because both displayed peak behaviour at 22% RH, providing further indication that the peak effect is related to low surface energy.

The similarity between the adhesion behaviour and surface energy of polymorphs I and III may be related to similarities present in the surface structure. Forms I and III are monoclinic forms with eight molecules in the unit cell which are similar in conformation, but differ only in hydrogen bonding patterns. Despite the different hydrogen bonding motifs, both forms have the same number of hydrogen bonds per molecule with similar strengths, giving rise to similar mechanical properties (Roberts and Rowe, 1996). If this similarity between polymorphs gives rise to similar bonding, then it is feasible that similar surface chemistry may result as well.

Muster and Prestidge (2002) examined the adhesive forces and wetting properties of sulphathiazole polymorphs I and III. When forces of adhesion were determined using a hydrophobic silica probe it was found that the forces for form I, (23 nN) were higher than those of form III, which varied from 4 nN to 16 nN. The JKR theory can be applied to this data to calculate

surface energy, and it is noted that the values obtained are a similar order of magnitude to the results presented here in figure 5.15.

5.4.4. Polymorph IV

The SEM images (figure 5.9) showed the presence of plate-like crystals. This is similar to the literature, which describes the morphology of polymorph IV to be of small platelets of undefined profile (Anwar *et al.*, 1989). The AFM images (figure 5.10) consisted of step structures similar to polymorph III, although the plane areas were rougher.

Tips K and L (figures 5.24 and 5.25) both show scenario one type behaviour as a clearly defined peak is seen at 44% RH. Compared to tip L, K has a greater asperity height, which means that only the sharp edges of the asperity were involved. This is also supported by the SD of forces of tip L, which is much greater than that of tip K (CV varied from 6.5 to 29% compared to 1.1% to 2.5% for tip K). Tip L consisted of a single large asperity with numerous smaller ones on top, so the increased SD at 44% RH is related to the asperities of the smaller surfaces coming into contact with the surface.

Tip J (figure 5.23) differs from tips K and L in that it shows a slight peak at 22% RH, and not 44% RH, although this is heavily masked by a large SD. Under standard room condition, polymorph IV is known to readily transform into form III (Anwar *et al.*, 1989), which showed a peak at 22% RH, meaning that an interplay of forces may be resulting due to a change in crystal form from IV to III. At 72% RH there is an increase in adhesion force with a slight decrease in SD, which could be due to the saturation of the peak.

The tip-particle force measurements (figures 5.23 (c), 5.24 (c) and 5.25 (c)) again showed considerable variation. Only tip J showed correlation to the HOPG measurements. For the other two tips, a variety of behaviours was seen for both the whole area and point force measurements. Tip K

measurements tended to show a lower SD than tip L, which had a larger contact area meaning it would have interacted over the larger, rougher area.

The behaviour of polymorph IV differed from the other polymorphs because of the presence of clear peaks at 44% RH instead of 22% RH. This is of interest because, as stated in chapter 4, micronised salbutamol also showed a peak at 44% RH against HOPG. As polymorph IV is known to transform and micronised materials have large proportions of amorphous regions, this may mean that less stable materials have a decreased wetting effect. The surface energy measurements showed that polymorph IV had the second highest surface energy of all the polymorphs against both HOPG and particles. This indicated that the high surface energy causes the peak in adhesion measurements to occur at 44% RH.

5.5. Conclusions

This chapter has examined the effect of different polymorphs of a drug on the adhesion phenomena. These differences are related to many factors, including the nano-structure and surface energy.

It has been shown again that higher surface energies and differences in surface chemistry can lead to a shift towards peaks in the adhesion force at higher humidities. This was seen with polymorphs of I-Met and III which had peaks at 22% RH, similar crystal structures and lower surface energies than that of polymorph IV, which peaked at 44% RH.

Performing measurements against HOPG and particles has shown to supply useful complimentary information, although as discussed in chapter 4, the low sample number (n=3) of each polymorph used means that further work must be undertaken to generate statistically significant results. It is possible to calculate the surface energy of the material using both sets of results, although differences are seen. This is due to changes in the surface chemistry and roughness of both samples, but it is seen that results obtained

with both methods tend to be of a similar order of magnitude, and that trends seen are the same for both of the substrates used. Similar findings have been reported by Podczeck *et al.* (1997) using a centrifuge technique, when comparing particle-particle measurements performed against compressed, smoother disks of material to particles.

When examining particle-particle adhesion measurements, individual point measurements have limited use in comparison to measurements over larger areas. This is due to the variations in surface structure, as a single point will be of unknown geometry. However performing measurements over larger areas will lead to an averaging out of such unknown geometries.

In conclusion, we have demonstrated using AFM that different polymorphs of the same drug can exhibit different adhesion properties. In addition, understanding of particle adhesion can be enhanced by examination of measurements against more than one type of substrate. It has been shown that data obtained from different systems can be complementary and provides a useful source of additional information.

Chapter 6

Force Measurements Using Biological Materials

6.1. Introduction

6.1.1. Supercritical Processing of Biological Material

Supercritical fluids have been used for processing many types of biological material. For example, Winters *et al.* (1996) used the SAS anti-solvent technique to form protein particles of trypsin and lysozyme, and Yeo *et al.* (1993) used the GAS anti-solvent technique to form insulin particles. While both of these processes produced biologically active particles with a small size distribution, long drying times (2 hours) were required in order to ensure all the solvent was removed.

SEDS™ has also been used for biological material. Tservistas *et al.* (2001) were able to produce plasmid DNA-loaded particles of mannitol, with an 80% recovery of the supercoiled DNA, with much shorter drying times required (typically 20 minutes). Recently, SEDS™ has also been used to process insulin.

6.1.2. Insulin

Insulin is a 6-kD protein that consists of two peptide chains connected by two disulphide bridges. A schematic of its structure is shown in figure 6.1. It is produced by the body in the β -cells of the islets of Langerhans in the pancreas, or it can be manufactured from recombinant DNA technology or chemical modification of porcine insulin (Rang *et al.*, 1995).

The main role of insulin is to control intermediary metabolism in order to conserve body fuel. This is achieved by reducing the blood sugar levels in the body by increasing the uptake, utilisation and storage of glucose after a meal (Rang *et al.*, 1995). Lack of insulin or insulin resistance in the tissues leads to an increased blood glucose concentration, a condition known as diabetes mellitus. As a consequence of the poor control of glucose in the body, complications may arise over a period of many years including cardiovascular disease, nerve and renal damage, and eye disorders (Walker and Edwards, 1999). There are two main forms of diabetes

- Non-insulin-dependent diabetes mellitus (NIDDM)
- Insulin-dependent diabetes mellitus (IDDM)

In NIDDM there is impaired insulin secretion and insulin resistance, and can usually be treated via dietary modification and oral hypoglycaemic drugs. However in IDDM there is an absolute deficiency of insulin, meaning that if insulin is not administered, the patient will die.

6.1.3. Insulin Administration

Because insulin is a protein, it cannot be administered directly via the oral route as it will be denatured and broken down by the digestive system into smaller peptides. Currently, the only way of administering insulin is via injection. This can lead to further complications such as low compliance, irritation and infection of the injection site, and it also has the disadvantage of

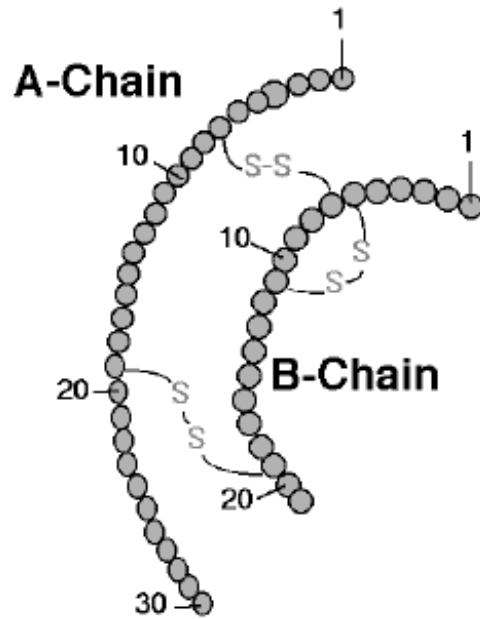


Figure 6.1. Structure of insulin (taken from www.blc.arizona.edu/.../rick/biomolecules/protein.html). Insulin consists of an A and B chain joined at the 7th and 19th amino acids by two disulphide bonds.

being absorbed too slowly to properly mimic the action of the pancreas (Kumar and Clark, 1994). Because of these issues, other methods have been examined to deliver the drug, including nasal and oral delivery using specially developed coatings (Ghilzai, 2003). While these have not as yet proved successful (Patton *et al.*, 1999), the inhalation route has shown more promise, and has recently been shown to provide blood sugar level control in IDDM (Skyler *et al.*, 2001).

6.1.4. Aim of this Work

It has been documented that the flow properties of SEDSTM materials are better than those prepared using traditional techniques (York, 1999). However, when using the SEDSTM process to manufacture insulin, it was noted that the particles produced demonstrated poorer flow properties and more agglomeration than the unprocessed material. The aim of this work is to use the methods of surface energy calculation and models of adhesion behaviour developed in the previous chapters to aid in the understanding of why the performance of this material is inferior to that of unprocessed insulin.

Batches of unprocessed and SEDSTM processed insulin were imaged using SEM and AFM in order to compare morphological characteristics. Following this, particles of both samples were mounted onto AFM tips, and force measurements were performed against HOPG and particles of the same materials in order to observe adhesion changes with humidity, and to calculate the work of adhesion and surface energy of the particles.

6.2. Methods

Two samples of insulin were supplied from Nektar, unprocessed insulin (Nektar sample no 001/98-04) and SEDSTM processed insulin (Nektar sample no 0401103). Particle imaging by SEM and AFM techniques as well as force measurements and humidity generation by nitrogen gas were performed using the methods discussed in chapter 2. Three tips were

prepared for each of the two insulin samples, and measurements were performed against 10 μm x 10 μm areas of HOPG, and particles of the same materials at individual points and over 10 μm x 10 μm areas as discussed in the methods section of chapter 5.

The work of adhesion was calculated using each of the three tips of unprocessed and SEDSTM processed insulin, using the methods described in chapter 4.

6.3. Results

6.3.1. Images

The SEM images of the unprocessed insulin are shown in figure 6.2. These show the presence of large crystals of mixed morphology, some of which are narrow and elongated, while others are of broader, flatter shape. The larger crystals are 30 μm to 50 μm long. By zooming in it can be seen that there are a large number of smaller, finer crystals present with an approximate length range of 1 μm to 10 μm .

The SEM images of the SEDSTM insulin are shown in figure 6.3. These show the presence of much larger particles, which could not be measured using the SEM, but were found to be 3 mm to 4 mm in diameter by visual techniques. Upon zooming in on the images it can be seen that these larger particles are composed of much smaller, smoother particles, ranging in size from 1 μm to 10 μm in diameter. By examining the higher magnification images, it can be seen that some of the smaller particles appear to be fused together.

The AFM images of the unprocessed insulin are shown in figure 6.4. These show a mixed morphology. A mixture of globular regions, ridges, and smoother areas were seen. The diameters of the globular regions varied between 10 nm and 90 nm, and the heights between 10 nm and 110 nm,

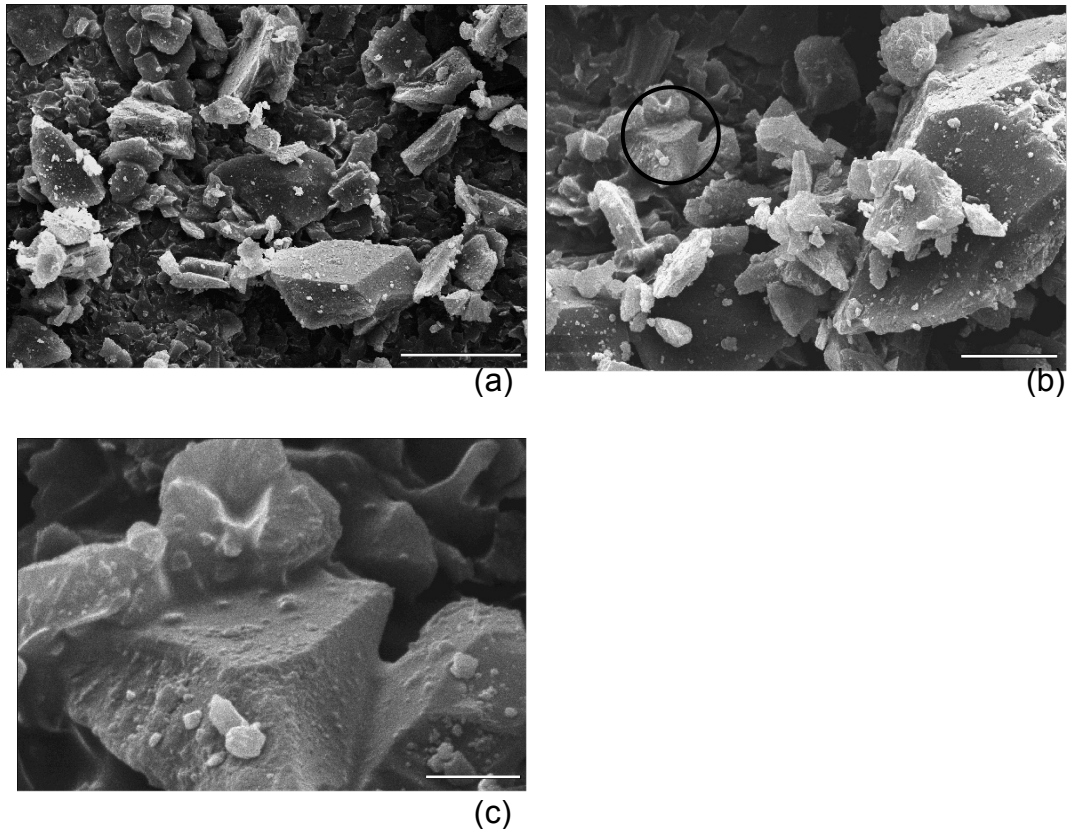


Figure 6.2. SEM images of unprocessed insulin.

(a) Overview image, bar length 50 μm .

(b) New area at higher magnification, bar length 20 μm .

(c) Zoom in on circled area, bar length 5 μm .

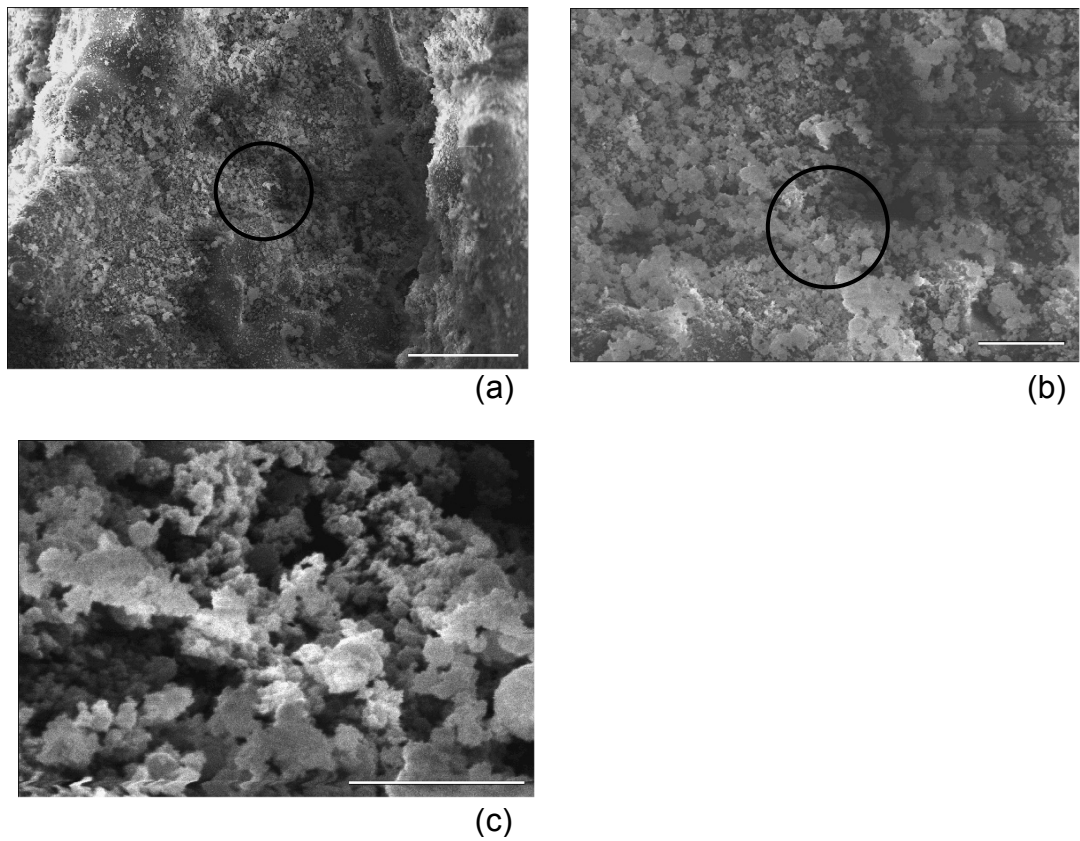


Figure 6.3. SEM images of SEDS™ insulin.

(a) Overview image, bar length 100 μm .

(b) Zoom in on circled area in (a), bar length 20 μm .

(c) Zoom in on circled area in (b), bar length 10 μm .

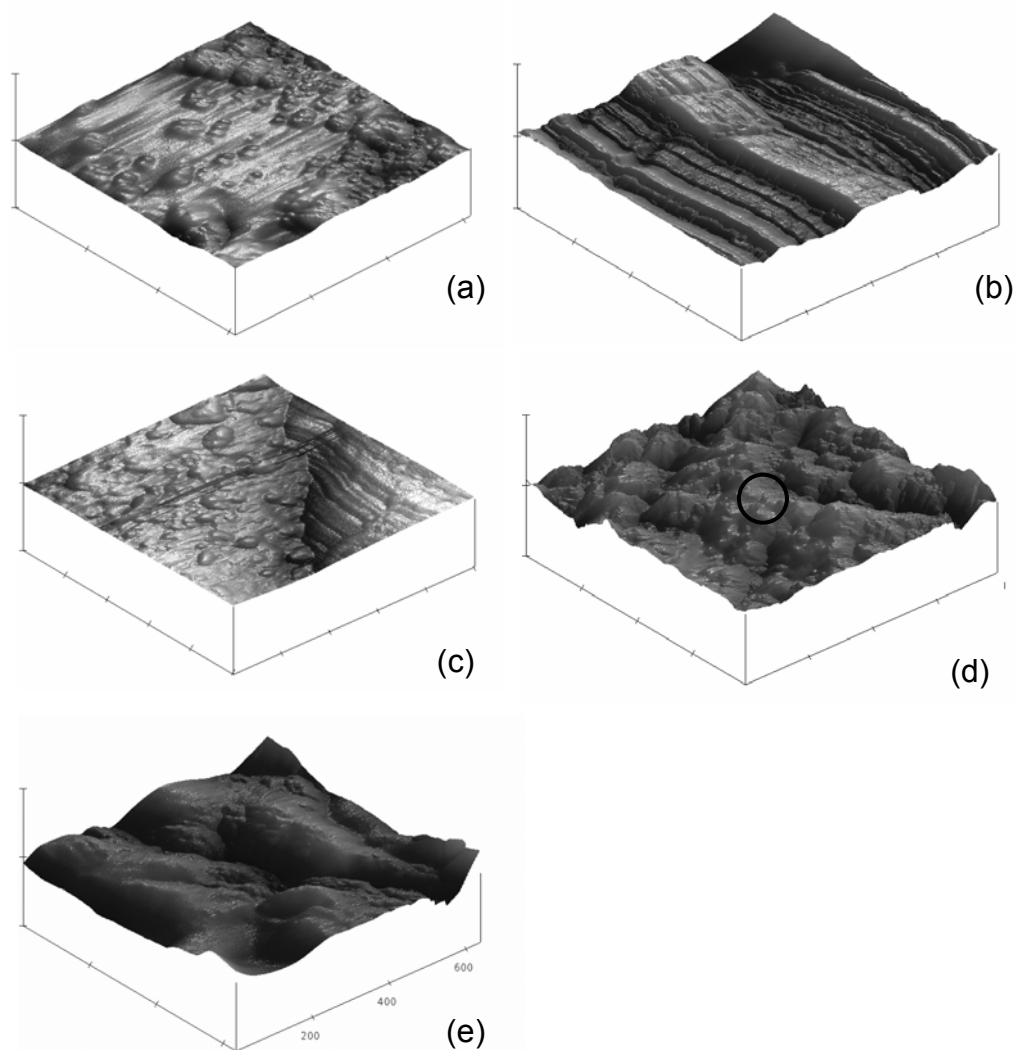


Figure 6.4. AFM images of unprocessed insulin.

- (a) New Area ($XY = 1 \mu\text{m}/\text{div}$, $Z = 2.3 \mu\text{m}/\text{div}$).
- (b) New area ($XY = 1 \mu\text{m}/\text{div}$, $Z = 1.7 \mu\text{m}/\text{div}$).
- (c) New area ($XY = 200 \text{ nm}/\text{div}$, $Z = 3 \mu\text{m}/\text{div}$).
- (d) New Area ($XY = 500 \text{ nm}/\text{div}$, $Z = 1 \mu\text{m}/\text{div}$).
- (e) Zoom in on centre of (d) ($XY = 200 \text{ nm}/\text{div}$, $Z = 270 \text{ nm}/\text{div}$).

although determining the heights of individual aggregates was difficult. The ridges varied in height from 10 nm to 300 nm. The roughness (R_q) of the smooth areas was found to be 16.8 nm over a $3\ \mu\text{m} \times 3\ \mu\text{m}$ area.

The AFM images of the SEDSTM insulin are shown in figure 6.5. The SEDSTM material consists mainly of smooth globular regions that were of a larger and smoother morphology than the unprocessed material, and ranged in diameter from 180 nm to 280 nm, and with heights from 10 nm to 150 nm. Some areas of ridges were also seen that were similar to those in the unprocessed insulin, with heights varying between 30 nm and 60 nm.

6.3.2. Force Measurements

The tip images and force measurements for the unprocessed insulin are shown in figures 6.6 to 6.8. The tip image of unprocessed insulin tip A is shown in figure 6.6 (a). This consists of a single broad lozenge shaped asperity $2.2\ \mu\text{m}$ wide, $2.3\ \mu\text{m}$ long and of height 311 nm.

The tip A force measurements against HOPG are shown in figure 6.6 (b). There is no change between <10% RH and 22% RH, however at 44% RH and 65% RH a significant increase ($P < 0.05$) in adhesion with humidity is seen.

The tip A force measurements against particles of unprocessed insulin are shown in figure 6.6 (c). For all three point measurements, a significant peak ($P < 0.05$) in adhesion is seen at 44% RH, however when the measurements taken over a whole area are examined then a gradual increase in adhesion with humidity is seen as well as increasing SD, although between sequential humidities this increase is not significant ($P > 0.05$).

The tip image of unprocessed insulin tip B is shown in figure 6.7 (a). This shows that two asperities are present. The tallest one is 317 nm in height, $1.49\ \mu\text{m}$ in length and 763 nm in width. The shorter one is only 176 nm in

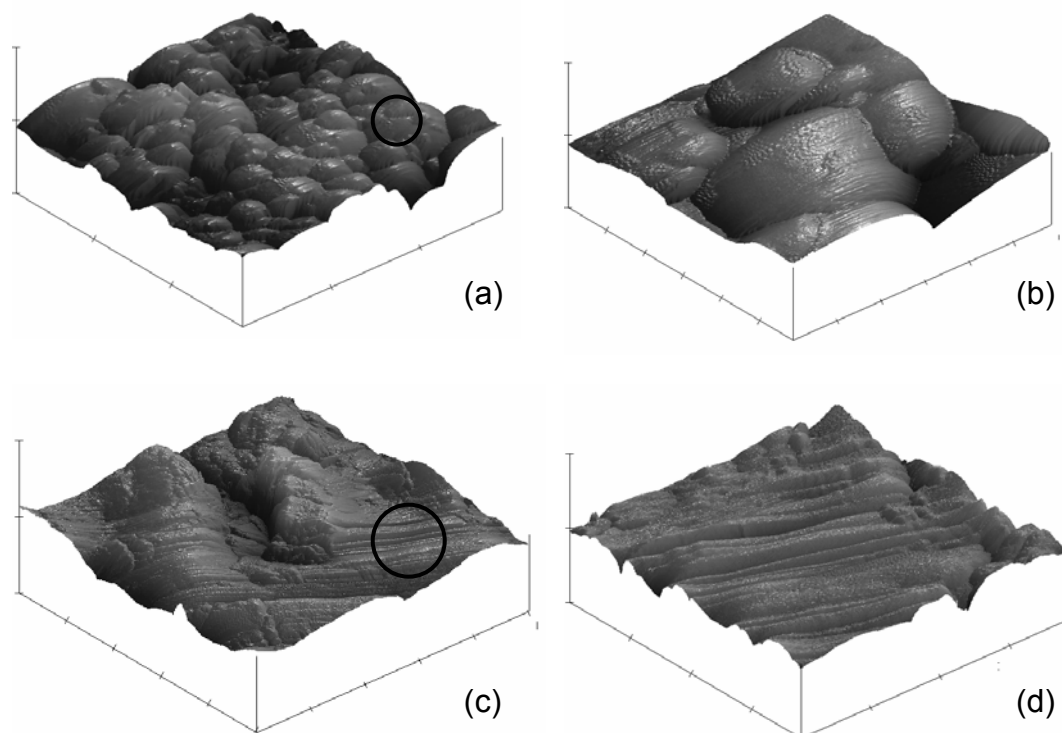


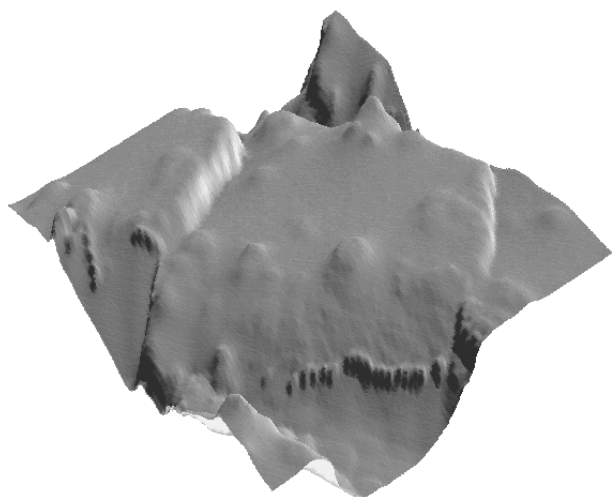
Figure 6.5. AFM images of SEDS™ insulin.

(a) New area ($XY = 500 \text{ nm/div}$, $Z = 1.5 \text{ }\mu\text{m/div}$).

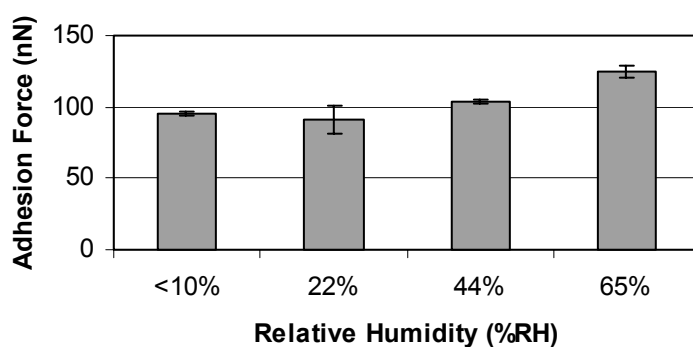
(b) Zoom in on circled area of image ($XY = 60 \text{ nm/div}$, $Z = 350 \text{ nm/div}$).

(c) New area ($XY = 1 \text{ }\mu\text{m/div}$, $Z = 1.8 \text{ }\mu\text{m/div}$).

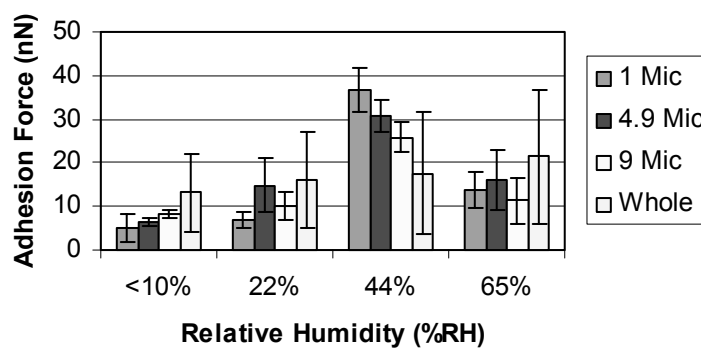
(d) Zoom in on circled area of image ($XY = 500 \text{ nm/div}$, $Z = 370 \text{ nm/div}$).



(a)



(b)



(c)

Figure 6.6. Image and force data of unprocessed insulin tip A. Error bars show the SD.

(a) Image of asperity (XY = 2.4 μm , Z = 501 nm).

(b) Force measurements against HOPG.

(c) Force measurements against unprocessed insulin particles.

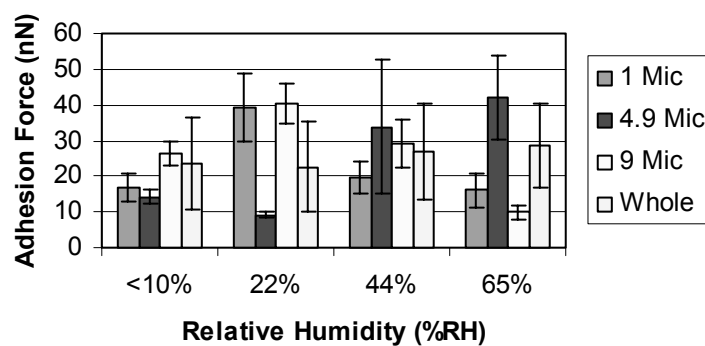
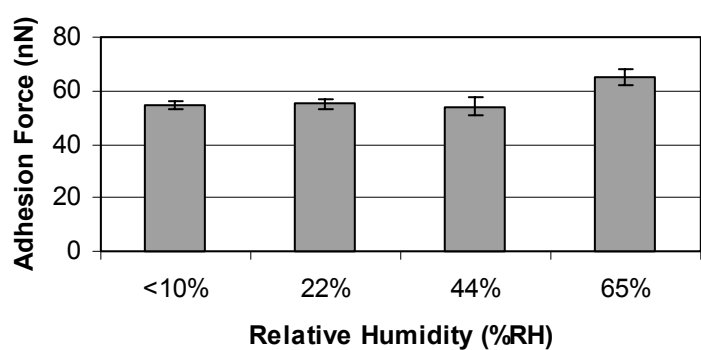
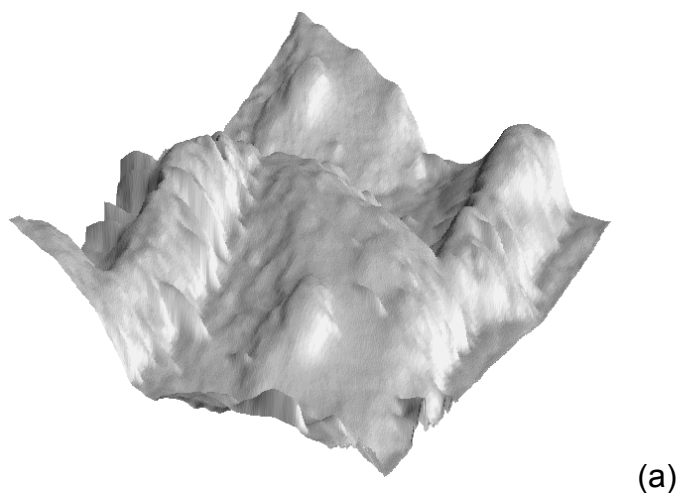


Figure 6.7. Image and force data for unprocessed insulin tip B. Error bars show the SD.

- (a) Image of asperities ($XY = 2.7 \mu\text{m}$, $Z = 445 \text{ nm}$).
- (b) Force measurements against HOPG.
- (c) Force measurements against unprocessed insulin particles.

height, but has a length of 1.36 μm and width of 1.60 μm .

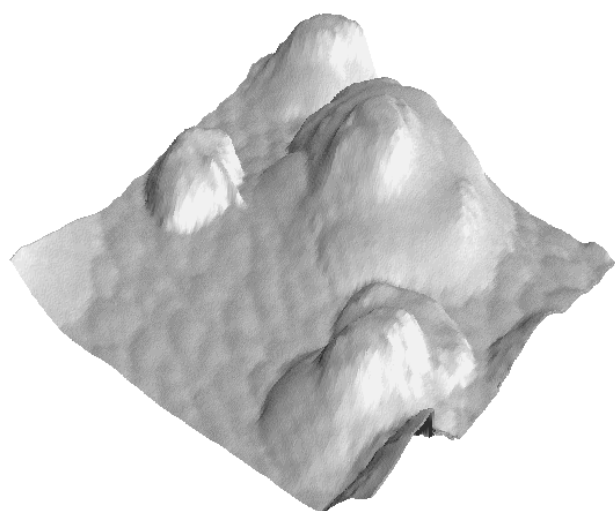
The force measurements of tip B against HOPG are shown in figure 6.7 (b). These show a very limited change in adhesion with humidity until 65% RH is reached, when there is a significant increase ($P < 0.05$) in adhesion.

The force measurements of tip B against particles showed significant differences ($P < 0.05$), and are shown in figure 6.7 (c). These show more mixed behaviour than tip A. Two of the point measurements show peak effects at 22% RH, the other point measurement resembles the measurements taken over the 10 μm x 10 μm area in that there is little change between the adhesion forces at <10% RH and 22% RH, but they start to increase at 44% RH.

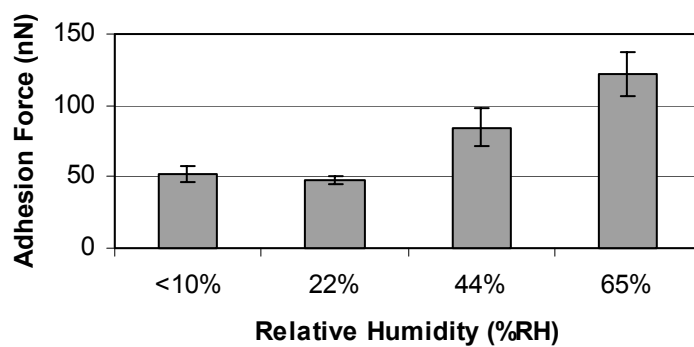
The tip image of unprocessed insulin tip C is shown in figure 6.8 (a). This shows the presence of four asperities. The largest is 430 nm high, 1.3 μm wide and 1.3 μm long. The second largest is 376 nm high, 1.82 μm long and 845 nm wide. The third asperity is 255 nm high, 688 nm wide and 644 nm long, and the final asperity is 123 nm high, 418 nm wide and 530 nm long.

The force measurements of tip C against HOPG are shown in figure 6.8 (b). This shows a similar pattern to that of tip A, in that there is little change between <10% RH and 22% RH, but at 44% RH the adhesion force starts to significantly increase ($P < 0.05$).

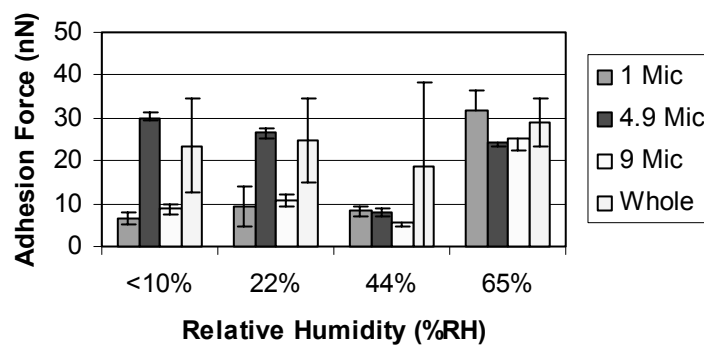
The force measurements of tip C against unprocessed insulin particles showed significant sequential differences ($P < 0.05$) and are shown in figure 6.8 (c). Two of the point measurements show similar behaviour in that there is a slight peak in adhesion at 22% RH before decreasing at 44% RH, however, once 65% RH is reached there is a large increase in force. The third point measurements shows a decrease in force from <10% RH to 44% RH, but the force increases at 65% RH. The measurements taken over the whole area show a slight peak effect at 22% RH, before decreasing at



(a)



(b)



(c)

Figure 6.8. Image and force data for unprocessed insulin tip C. Error bars show the SD.

(a) Image of asperities (XY = 2.1 μm , Z = 481 nm).

(b) Force measurements against HOPG.

(c) Force measurements against unprocessed insulin particles.

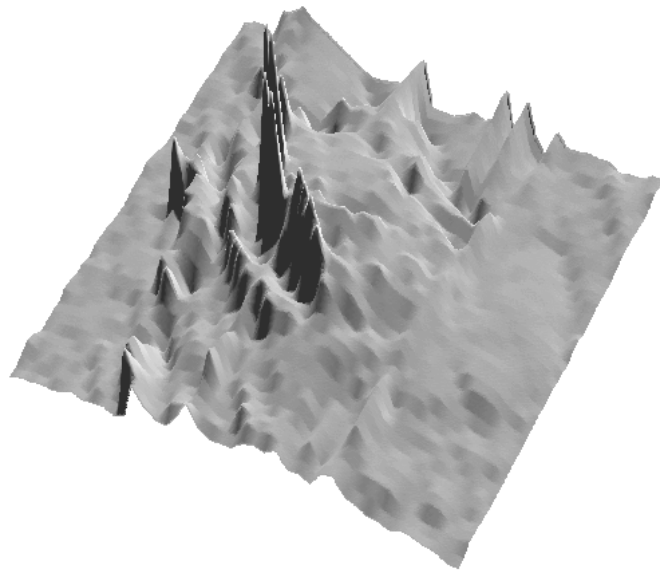
44% RH and then increasing again at 65% RH. However, there is a large SD associated with this profile.

The measurements taken using the tips with SEDSTM insulin added onto the tip apexes are shown in figures 6.9 to 6.11. The tip image of SEDSTM insulin tip D is shown in figure 6.9 (a). This shows a single particle with a series of sharp features on top that were approximately 500 nm high. The features were seen on each repeat of the tip image, meaning such reproducibility would be due to the particle surface features imaging the tip characterisation grid, and not noise. The base of the particle was 615 nm high, 729 nm wide and 958 nm long.

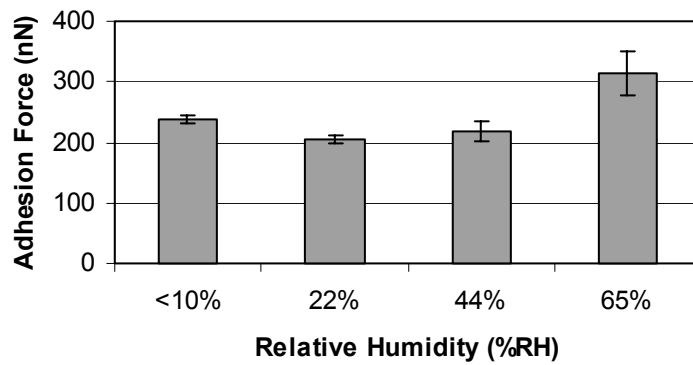
The force measurements of tip D against HOPG were significantly different ($P < 0.05$) and are shown in figure 6.9 (b). This shows a slight drop in adhesion force between <10% RH and 22% RH, before increasing at 44% RH.

The force measurements of tip D against SEDSTM insulin particles are shown in figure 6.9 (c). Significant differences ($P < 0.05$) were seen between sequential measurements, except for the 1 μm point measurement. The force measurements show a mixture of behaviours as at one of the point measurements there is an increase in adhesion force with humidity, while the other points and whole area measurements show peaks in the adhesion. The position of these peaks varied, for one point measurement it was at 44% RH, while for the other point and the whole area measurements it was at 22% RH. However, it should be noted that the SD for the whole area measurements was large enough to mask the peak effects seen.

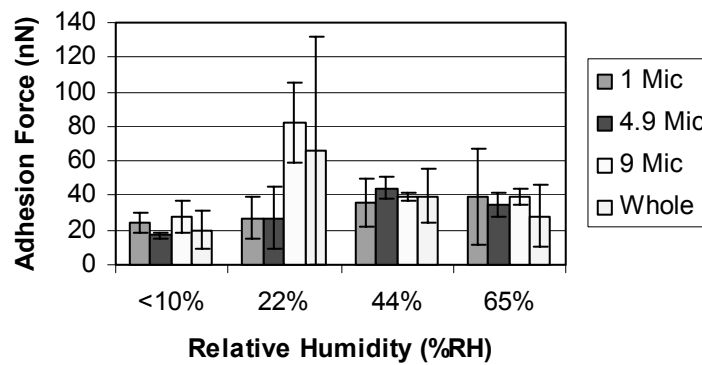
The tip image of SEDSTM insulin tip E is shown in figure 6.10 (a). This shows two asperities, the largest being 283 nm high, 534 nm wide and 979 nm long. The smaller is 119 nm high, 495 nm wide and 291 nm long.



(a)



(b)



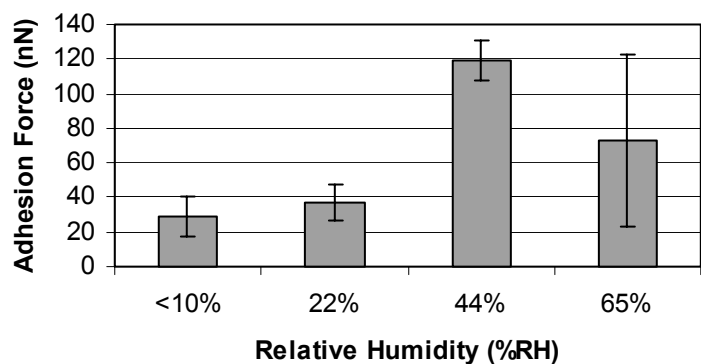
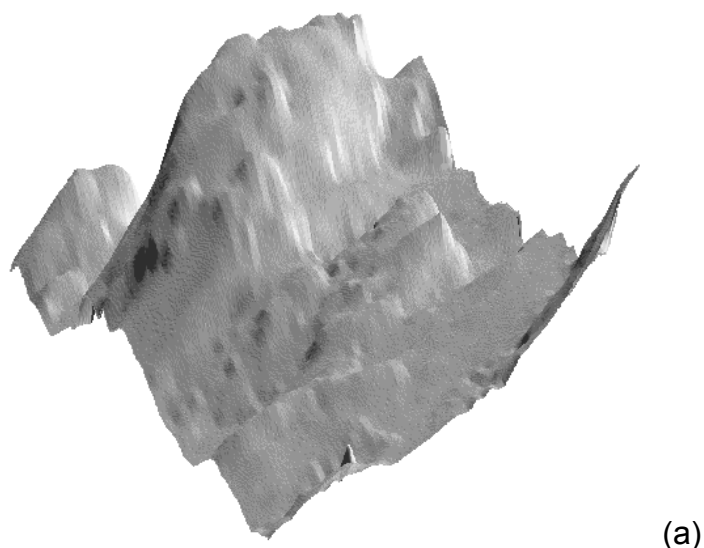
(c)

Figure 6.9. Image and force data for SEDS™ processed insulin tip D. Error bars show the SD.

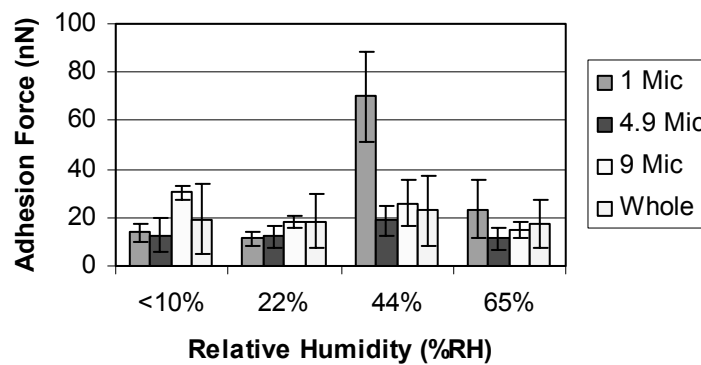
(a) Image of asperity ($XY = 1.05 \mu\text{m}$, $Z = 1.49 \mu\text{m}$).

(b) Force measurements against HOPG.

(c) Force measurements against SEDS™ insulin particles.



(b)



(c)

Figure 6.10. Image and force data for SEDS™ processed insulin tip E. Error bars show the SD.

(a) Image of asperity ($XY = 1.25 \mu\text{m}$, $Z = 465 \text{ nm}$).

(b) Force measurements against HOPG.

(c) Force measurements against SEDS™ insulin particles.

The force measurements of tip E against HOPG are shown in figure 6.10 (b). This shows a significant peak ($P < 0.05$) in adhesion at 44% RH, however at 65% RH there is an increased SD which masks the peak seen. Similar significant ($P < 0.05$) effects are seen for the force measurements of tip E against particles of SEDS™ insulin, which are shown in figure 6.10 (c). For all of these measurements, peak effects can be seen at 44% RH.

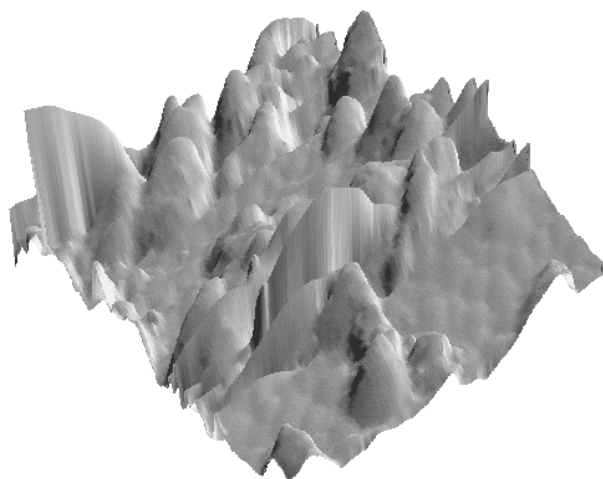
The tip image of the final SEDS™ insulin tip F is shown in figure 6.11 (a). This shows a number of smaller peaks ranging in height from 421 nm to 208 nm. The difference in height between the largest and next largest was only 10 nm.

The force measurements of tip F against HOPG are shown in figure 6.11 (b). It is seen that there is a significant increase ($P < 0.05$) in adhesion with humidity.

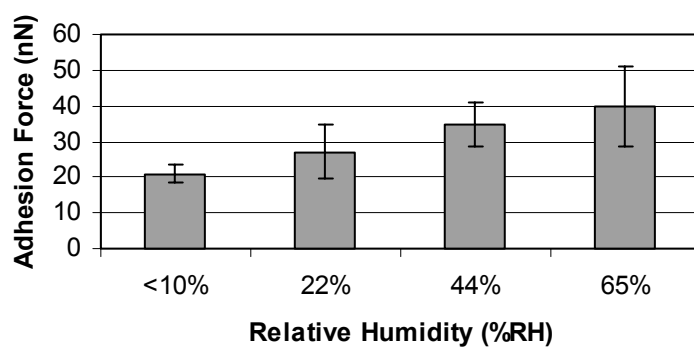
The force measurements of tip F against insulin particles are shown in figure 6.11 (c). The point measurements show a mixture of behaviours. The 1 μm point shows no significant change ($P < 0.05$), the 9 μm point shows a significant decrease ($P < 0.05$) with increasing humidity and the 4 μm point significantly decreases ($P < 0.05$) from <10% RH to 22% RH, before significantly increasing ($P < 0.054$) at 44% RH. The measurements taken over the 10 μm x 10 μm area show an increasing adhesion force with increasing humidity, although the increase was not significant ($P > 0.05$).

6.3.3. Work of Adhesion and Surface Energy Measurements

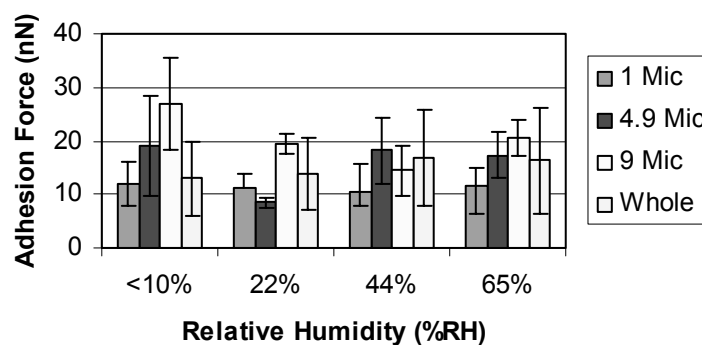
The work of adhesion and surface energy of the unprocessed and SEDS™ insulin against HOPG are shown in figure 6.12. Against HOPG, the SEDS™ materials was found to have an average work of adhesion and surface energy of 104.5 mJm^{-2} (SD 141.9 mJm^{-2}) and 77.5 mJm^{-2} (SD 118.3 mJm^{-2}) respectively, and the unprocessed insulin had values of 27.8 mJm^{-2} (SD 12.2 mJm^{-2}) and 2.4 mJm^{-2} (SD 1.5 mJm^{-2}).



(a)



(b)



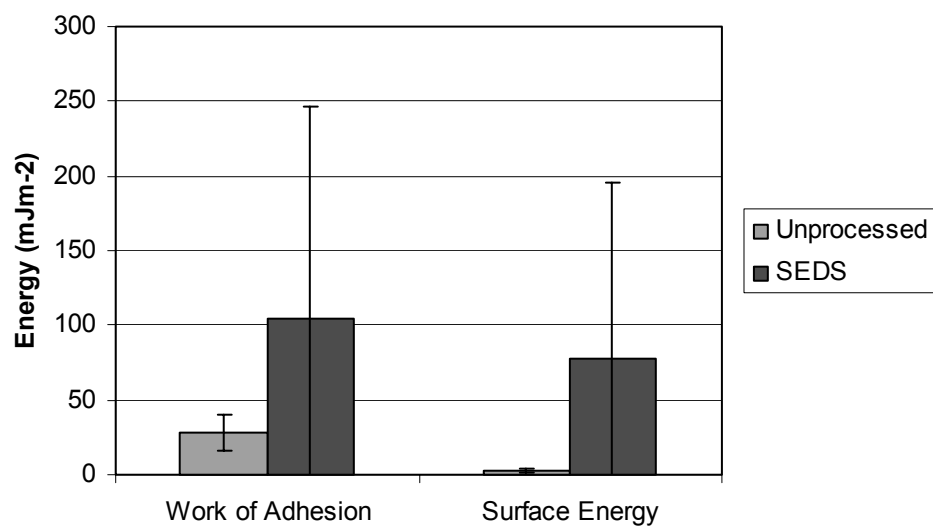
(c)

Figure 6.11. Image and force data for SEDS™ processed insulin tip F. Error bars show the SD.

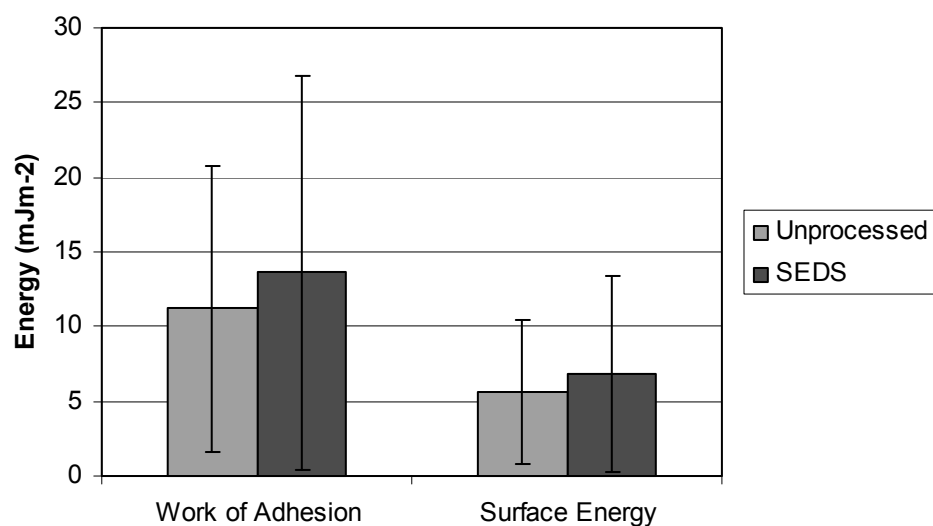
(a) Image of asperities ($XY = 2.3 \mu\text{m}$, $Z = 736 \text{ nm}$).

(b) Force measurements against HOPG.

(c) Force measurements against SEDS™ insulin particles.



(a)



(b)

Figure 6.12. Work of adhesion and surface energy of unprocessed and SEDSTM processed Insulin. Error bars show the SD.

(a) Calculated from measurements against HOPG.

(b) Calculated from measurements against particles of the same material.

The work of adhesion and surface energy calculated using the particle-particle measurements are shown in figure 6.12 (b). The SEDSTM had an average work of adhesion of 13.6 mJm⁻² (SD 13.2 mJm⁻²) and surface energy of 6.8 mJm⁻² (SD 6.6 mJm⁻²), while the unprocessed had a work of adhesion of 11.2 mJm⁻² (SD 9.6 mJm⁻²) and surface energy of 5.6 mJm⁻² (SD 4.8 mJm⁻²).

6.4. Discussion

6.4.1. Images

The SEM images (figures 6.2 and 6.3) showed that the unprocessed insulin and SEDSTM insulin have different structures. The unprocessed insulin has a more crystalline morphology compared to the SEDSTM insulin, which showed the presence of large numbers of smaller, more regular particles, although some of these appeared to have fused together.

The AFM images (figures 6.4 and 6.5) showed two differing structures, the SEDSTM with mainly globular and ridge structures, and the unprocessed with its mixed features. Both samples of insulin had a high amorphous content (unpublished data). When these images are compared to the work of Yip and Ward (1996), who imaged crystals of bovine insulin, it is seen that the unprocessed insulin showed a strong resemblance to their images, in that it also possesses rounded aggregates on the terraces. Yip and Ward found these aggregates to be ~ 60 nm in diameter, while for the unprocessed insulin in this work found them to vary between 10 nm and 90 nm. The SEDSTM insulin showed no similarity to this, in that the spherical regions were 180 nm to 280 nm in diameter. It is possible that there is a mixture of strong and weak adhesion occurring between these individual regions. During imaging, the presence of sweeping, as discussed in chapter 1, was a problem. In the image shown, there was strong adhesion leading to clearly defined features, however in many images that were taken, sweeping meant no structure could be seen.

6.4.2. Force Measurements

All of the unprocessed insulin tips (figures 6.6, 6.7 and 6.8) used for force measurements against HOPG showed scenario three type behaviour as discussed in chapter 4. For the SEDSTM process insulin, two of the tips (D and F, figures 6.9 and 6.11 respectively) showed type three behaviour, while the final tip (E, figure 6.10) showed scenario one behaviour.

The dominance of scenario three behaviour may be related to the amorphous nature of both insulin samples, and the problems that can arise due to humidity. Because amorphous materials are able to absorb large quantities of water vapour (Aulton, 1998), moisture sorption analysis was undertaken to assess differences between the two samples (unpublished data). Both the unprocessed and SEDSTM insulin showed similar high levels of moisture uptake. At 70% RH the moisture uptake of unprocessed insulin was 10.66%, and the SEDSTM value was 10.43%. Because water may act as a plasticizer (Podczeck *et al.*, 1996), this may have contributed to the dominance of scenario three behaviour, as this may have caused the surface to deform leading to the flat structures observed which possessed an increased contact area, and hence caused an increase in adhesion force with increasing humidity.

To understand deformation as a function of humidity, measurements were undertaken to assess the effect of the change in rate and press-on force on the adhesion forces recorded (data not shown). When the press-on force was increased from 15 nN to 35 nN, no significant change ($P > 0.05$) was seen between measurements taken at <10% RH, 22% RH and 44% RH for both the unprocessed and SEDSTM processed insulin. However, at 65% RH, a significant ($P < 0.05$) non-recoverable increase in adhesion force was seen for both samples with the increase in press-on force, the effect being more marked for the SEDSTM insulin. There was no significant change ($P < 0.05$) in adhesion force with changes in rate of measurements for the unprocessed insulin, however for the SEDSTM insulin changes in rate from 0.5 Hz to 4 Hz at 65% RH lead to large changes in the adhesion force. This suggests that

while a plasticizing effect is seen for both samples, which causes the scenario three behaviour observed, the effect is greatest for the SEDSTM insulin surface at 65% RH.

For unprocessed insulin tip C (figure 6.8) and SEDSTM insulin tip F (figure 6.11), the adhesion force started to increase at 44% RH. Both of these have tip images that show the presence of contacting areas formed from multiple asperities. Because of the number of small asperities in close proximity, the humidity effect may have started earlier due to moisture condensing in the gaps between the asperities. In addition, deformation of both particles may have occurred at the higher %RH, leading to an increase in contact area of the particles.

SEDSTM processed insulin tip E (figure 6.10) was the only tip to display peak behaviour, although the large standard deviation present at 65% RH masks this. The peak is due to the large asperity being responsible for the interaction, however once 65% RH is reached a smaller asperity is beginning to become involved, leading to the unpredictable nature of the forces at 65% RH. It is of interest to note that this peak was seen at 44% RH, which is the same humidity peaks as were seen for the micronised salbutamol in chapter 4, and sulphathiazole polymorph IV in chapter 5. Both of these samples possessed the most variation in surface properties – micronised salbutamol contained amorphous regions and polymorph IV was able to transform into polymorph III, giving further indication that the amorphous nature of the insulin is playing an important role in the adhesion process.

The force measurements against particles (figures 6.6 (c) – 6.11 (c)) showed a range of behaviours for both materials. These included peaks at 22% RH and 44% RH, as well as gradual increases in adhesion with humidity. As discussed in chapter 5, the surface roughness would have played an important part in the effect of humidity at each individual point. The measurements taken over the 10 μm x 10 μm area with unprocessed insulin showed increases at 65% RH which would be consistent with the increase

seen against HOPG. The SEDSTM processed insulin force measurements over the 10 μ m x 10 μ m area showed a mixture of behaviours, two of which (tips E and F) showed profiles which were consistent with the HOPG measurements. The exception was tip D, which showed a peak at 22% RH, although this was accompanied by a large SD. This difference could be due to local changes in the surface roughness and chemistry.

6.4.3. Work of Adhesion and Surface Energy Measurements

The work of adhesion and surface energy of the SEDSTM processed insulin was slightly higher than that of the unprocessed insulin (figure 6.12). The higher SEDSTM insulin value was seen in both the measurements against HOPG and against particles of the same material, although the SEDSTM had a large SD associated with the measurements. Because both of the insulin samples were amorphous, a high variation would be expected in surface energy due to the disordered nature of the surfaces.

The high work of adhesion and surface energy of the SEDSTM insulin will be a contributing factor to the poor flow properties of the powders recorded, as small particles of high surface energy agglomerate in order to confer an energetic advantage (Podczec, 1998).

6.5. Conclusions

This work has shown that it is possible to apply AFM imaging, force measurements and surface energy calculations to address real manufacturing problems, in this case to investigate the differences in performance between unprocessed and SEDSTM processed insulin. The poor flow performance of the SEDSTM materials has been attributed to three reasons, although the low sample number of both materials used (n=3) should be remembered.

The first reason is the presence of particles that have agglomerated together to form larger entities. This was evident in the SEM image where fused particles could be seen. In addition, the AFM images showed a large number of small, spherical regions present which were firmly bound together. This agglomeration is related to the second reason, which is that SEDS™ insulin has a higher work of adhesion and surface energy compared to the unprocessed insulin. This was more marked against the flat HOPG substrate, although it was also seen against the particles

The final reason is due to the amorphous nature of the particles. Amorphous particles adsorb moisture leading to plasticizing effects. This means that at higher humidity the surfaces will be able to deform more easily, leading to increased contact between particles. This was observed with both the unprocessed and SEDS™ processed insulin.

Chapter 7

The Co-Formulation of a Drug Using the SEDSTM Technique

7.1. Introduction

7.1.1. Co-Formulation

The ability to co-formulate drugs with excipients from solutions containing two components has been shown to be a further advantage of the use of supercritical fluids. For example, Kim *et al.* (1996) showed that a RESS process could be used to co-formulate naproxen with poly (L-lactic acid) to allow for controlled release of the drug, while Godinas *et al.* (1998) showed that RESS could be used to co-formulate a water insoluble drug with a modifier to produce a stable aqueous suspension.

As well as the previously discussed functions, the SEDSTM process has also been used as a co-formulation technique, for example Ghaderi *et al.* (2000) co-precipitated hydrocortisone with poly(DL-lactide-co-glycolide). This process produced microparticles of more irregular morphology than those of made from pure polymer. SEDSTM has also been used to co-formulate a model drug with different carriers in order to increase solubility (Juppo *et al.*,

2003). In the work discussed in this chapter, SEDS™ has been used to co-formulate the drug pregabalin with a lipid in order to allow for taste masking.

7.1.2. Pregabalin

Pregabalin is used for the treatment of epilepsy, anxiety and chronic pain. The molecular structure of pregabalin is shown in figure 7.1 (a). It is an analogue of γ -Aminobutyric acid (GABA), an inhibitory neurotransmitter found in the brain that is important in regulating neural function (Nogrody, 1988). One of the limitations of this drug is the unpleasant taste, which may reduce patient compliance. In order to overcome this, the drug has been co-formulated using the SEDS™ process with the lipid DL- α -Phosphotidylcholine Dipalmitoyl (DPPC), the chemical structure of which is shown in figure 7.1 (b).

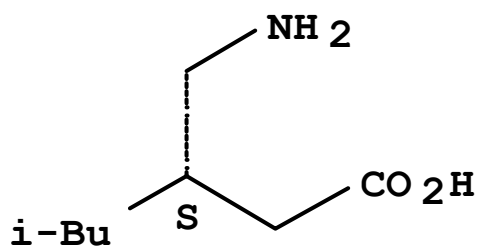
7.1.3. X-ray Photoelectron Spectrometry (XPS)

In XPS, the sample is irradiated using a low-energy X-ray source under ultra-high vacuum conditions, which causes electrons to be emitted from atoms in a process known as *photoionisation*. The electrons (or *photoelectrons*) that are emitted will not only consist of the valence electrons, which are involved in the binding of the atoms together, but also the core electrons, which are not involved in the bonding. The 'binding energy' (BE) of each core electron is a characteristic of the individual atom to which it is bound (Walls, 1988). When a photoelectron is emitted it will have a kinetic energy (KE) which is related to the X-ray energy ($h\nu$) and the BE of the electron emitted by the Einstein relation -

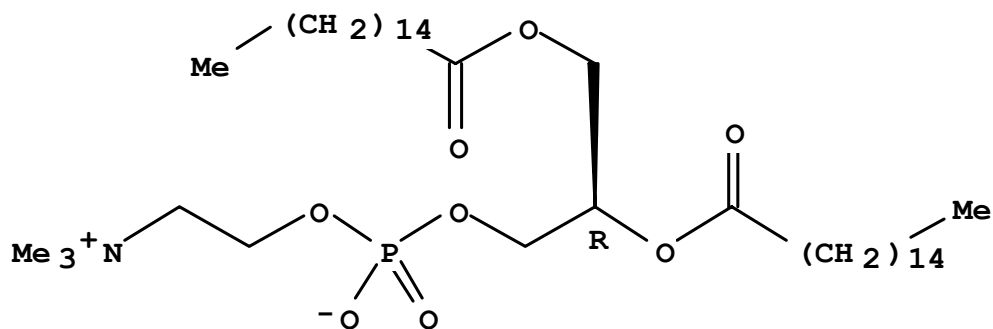
$$KE = h\nu - BE$$

(Eq 7.1)

Photoemission will have occurred if the photoelectrons have sufficient KE to



(a)



(b)

Figure 7.1. Chemical structures of pregabalin and DPPC.

- (a) Pregabalin.
- (b) DPPC Lipid.

overcome the work function of the specimen and escape from the surface. The name given to the whole process is the *photoelectric effect*. By measuring this kinetic energy it is possible to characterise the surface layer composition (Rubinson and Rubinson, 1998). The photoelectrons emitted have a kinetic energy distribution, $N(E)$, that consists of a series of bands that reflect the 'shell' form of electronic structure of the atoms in the sample, with the low BE electrons having higher kinetic energy than those that are strongly bonded. By experimentally determining $N(E)$, XPS spectra are produced.

The chemical environments in which the core electrons are found will affect the BE, leading to a chemical shift in the measured photoelectron energy (ranging from 0.1 to 10 eV in magnitude). This is due to the variation of electrostatic screening experienced by core electrons as valence electrons are drawn towards or away from the atom of interest (Walls, 1988).

Even though the X-rays involved may penetrate several microns into the surface, XPS is a surface technique. This is because before the energy of the photoelectron can be analysed, they must travel through the solid and escape into the vacuum without energy loss. The solid's stopping power for electrons is much higher than for X-rays, so that electrons in the energy range 50 eV to 1000 eV will only be able to move across 2 to 10 atomic layers before they lose energy by inelastic scattering events with other electrons. As a result of these factors only the surface atoms will be involved (Walls, 1988).

7.1.4. Time of Flight Secondary Ion Mass spectrometry (ToF-SIMS)

In SIMS, a surface is bombarded by high energy primary particles, that impart their energy to the sample via collision with the surface atoms. Following this, the atoms of the solid undergo a cascade process of collisions, in which some of the collisions cause emission of atoms or atom

clusters, which may become ionised (Vickerman and Briggs, 2001). Following ionisation, the atoms enter the time of flight (ToF) mass spectrometer. This works on the principle that singly charged species, subjected to the same potential difference, will achieve the same kinetic energy (Briggs, 1998). Because -

$$KE = \frac{1}{2} M_p V_s^2$$

(Eq 7.2)

where M_p is the mass of the particle and V_s is the velocity, lighter particles will possess faster velocities than heavier ones, so they will have a shorter time of flight over a particular distance. This means that particles can be analysed by their arrival time at the detector, and as a result spectra can be produced showing the component atoms and molecules present (Harwood and Claridge, 1997).

The main advantage of ToF-SIMS is that by using a low dose of primary ions most of the secondary ions will desorb from only the top two molecular layers of the surface (the approximate thickness of the layer is 1 nm) (Vickerman And Briggs, 2001; Briggs, 1998). There is also an additional advantage in that secondary ions generated by ToF-SIMS will only arise from a small area (10 nm^2) that has received only one primary ion strike, and which is independent from the next sample area. This means that the rest of the surface will be unaffected and as a result spectra obtained are from undamaged surfaces.

The techniques of ToF-SIMS and XPS can be used to identify the differences between the components, which arise from the differences present in the chemical structure of the drug and the lipid. By observing the chemical structures shown in figure 7.1, it can be seen that the lipid has a phosphorous group, which is not present in the drug structure. By looking for the presence or absence of this atom it is hoped that an understanding of the drug coating can be gained.

7.1.5. Aims

The aim of the work presented in this chapter is to determine the nature of the lipid coating on the drug, as to whether it is a uniform coating or if it is present in patches across the drug surface. In order to examine this, the two complimentary surface techniques of XPS and SIMS have been used in parallel with AFM and SEM imaging of three samples - pure lipid, SEDS™ processed pure drug and SEDS™ processed 50:50 lipid:pregabalin.

7.2. Methods

7.2.1. Samples

Samples of SEDS™ processed pregabalin (Nektar sample no 3401029) and pregabalin that was co-processed via the SEDS™ technique with lipid (50:50 lipid:pregabalin) (Nektar sample no 3401021) were obtained from Nektar. The lipid used was DL- α -Phosphotidylcholine Dipalmitoyl (DPPC). Samples were prepared and imaged by SEM and AFM using the methods discussed in chapter 2.

7.2.2. XPS

XPS analysis was undertaken using a VG Escalab Mark I X-ray photoelectron spectrometer. Non-monochromated Al Ka X-rays were used at an anode potential of 10 kV and a filament emission current of 20 mA. The specimen take-off angle used was 90 degrees and the area analysed was approximately 1cm x 1 cm.

Data generated was analysed using CasaXPS software. The C1s peak at 285 eV, attributed to the C-C/C-H bonds, was used as an internal standard to correct the binding energy shift due to charging. This correction was applied to all element peaks following background subtraction/peak deconvolution to give 'true' binding energy values.

7.2.3. SIMS

Samples were prepared by mounting particles on to small squares of silica of approximately 1 cm² in size. In order to add particles to the substrate, chloroform was used to dissolve the glue of adhesive tape to form a solution. This solution was then dropped onto the silica square and particles of powder were added once it dried. SIMS analysis was undertaken using a SIMS IV (Ion-ToF GmbH, Muenster, Germany). Spectra were obtained using positive and negative ion sources, at accelerating voltages of 5 kV over areas between 75 x 75 µm and 100 x 100 µm for 200 seconds. In addition to the pregabalin and lipid samples, a spectra of the glue, used to adhere the particles to the silica substrate, was also undertaken to act as a control.

7.3. Results

7.3.1. Imaging

The SEM images of the SEDSTM samples are shown in figures 7.2 and 7.3. Neither SEM or AFM imaging was attempted with the DPPC due to its low melting point, which meant that surface changes would have occurred before imaging could be undertaken, reducing the value of data produced. Figure 7.2 shows 100% SEDSTM pregabalin. These particles are highly aggregated, but possess a uniform size distribution, with a particle size of 1 µm to 2 µm.

The 50:50 lipid:pregabalin particles are shown in figure 7.3. These are of different morphology to those of the 100% pregabalin in that they have a more elongated appearance, and a larger size (lengths range from 5 µm to 15 µm).

AFM images of the SEDSTM samples are shown in figures 7.4 and 7.5. Figure 7.4 shows 100% SEDSTM pregabalin. This consisted of globular regions ranging in length from 220 nm to 1.36 µm in diameter.

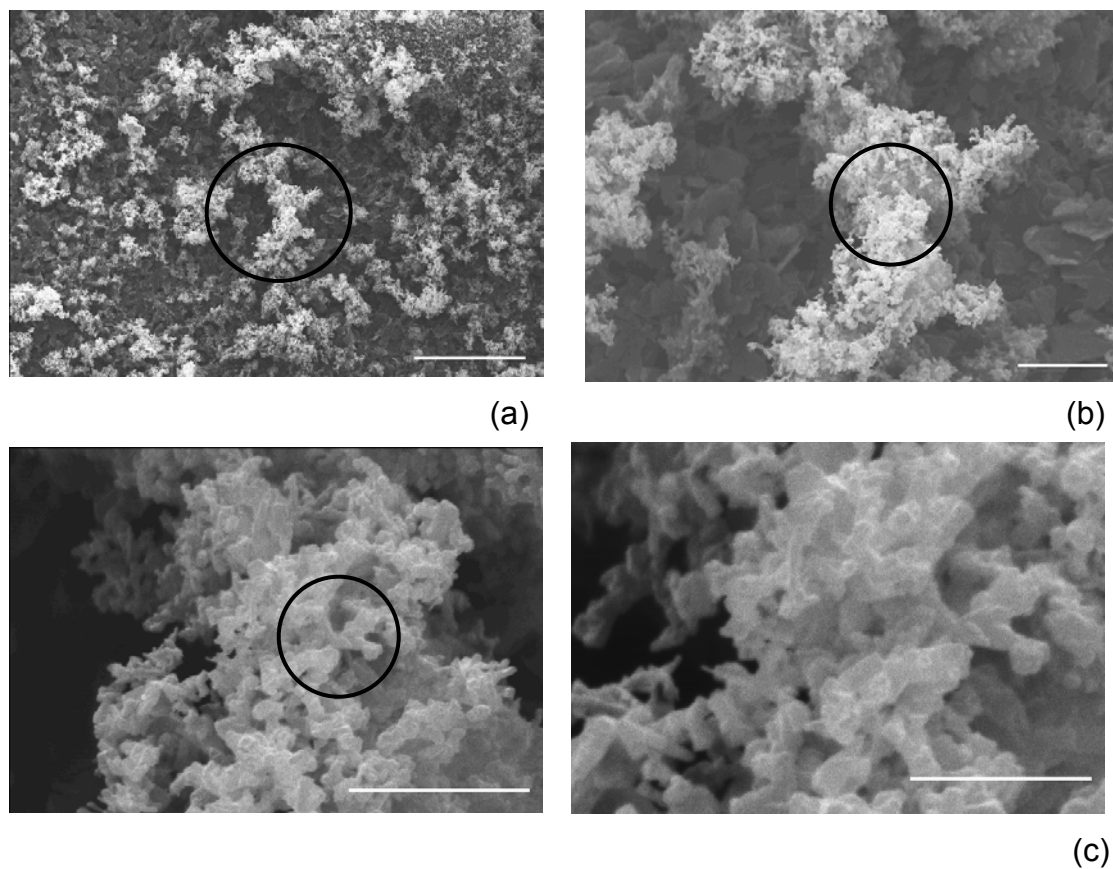


Figure 7.2. SEM images of 100% SEDSTM pregabalin.

- (a) Large area, bar length 100 μm .
- (b) Zoom in of the centre of (a), bar length 20 μm .
- (c) Zoom in of the centre of (b), bar length 10 μm .
- (d) Zoom in of the centre of (c), bar length 5 μm .

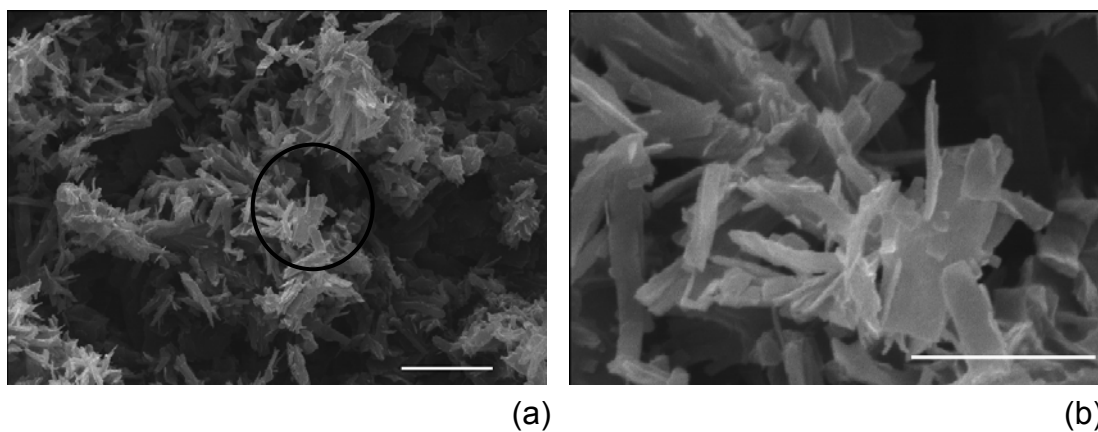


Figure 7.3. SEM images of 50:50 Lipid:pregabalin SEDSTM processed material.

(a) Large area, bar length 20 μm .

(b) Zoom in on centre of (a), bar length 10 μm .

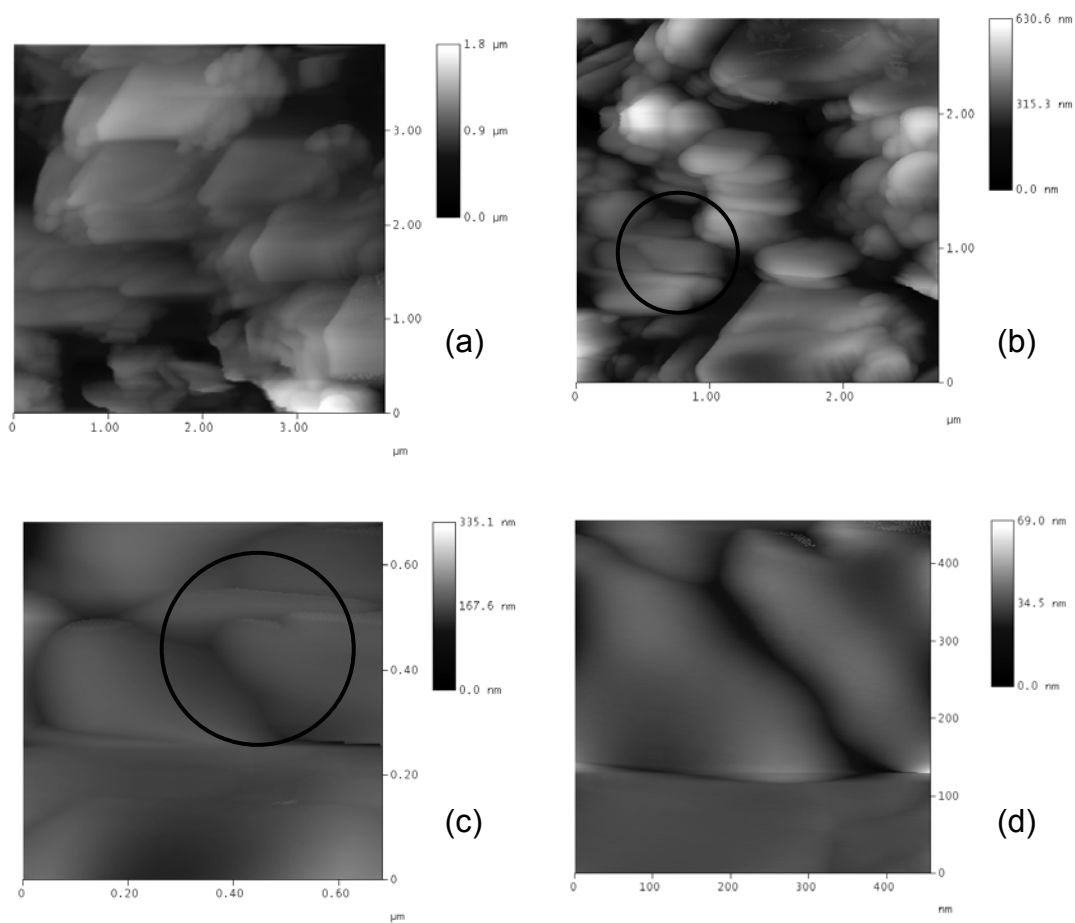


Figure 7.4. AFM images of 100% SEDS™ pregabalin.

- (a) Large area of surface.
- (b) New area of surface showing similar features to those seen in (a).
- (c) Zoom in on circled area in (b).
- (d) Zoom in on circled area in (c).

Figure 7.5 shows 50:50 lipid:pregabalin. This shows a series of step like structures ranging in height from 30 nm to 208 nm. These steps lacked the uniformity seen in the non-co-formulated pregabalin images.

Tapping mode AFM imaging was used for all the images, but no non-topographic changes in phase were observed in any of the images (phase images not shown).

7.3.2. XPS Data

The XPS overview spectra for all three samples are shown in figure 7.6 (a) to (c). These show that both the lipid and 50:50 lipid:pregabalin samples have phosphorous peaks present, which are not seen in the pure pregabalin spectra.

The carbon spectra for all three samples are shown in figure 7.7 (a) to (c). The lipid (figure 7.7 (a)) showed the presence of a main peak of C-C/C-H at 285 eV, as well as peaks due to C-O at 286.5 eV and COOH at 289 eV. The presence of an increased C-O content was shown by a broadening of the peak on the left side of the spectra. The pure drug is shown in figure 7.7 (b). Again, the main peak at 285 eV is due to the presence of C-C/C-H. There is also a smaller peak at 286.5 eV, which may be due to C-N=, although this is not a good fit. Alternatively, the smaller peak may also be due to C-N \equiv ⁺, which is a better fit and is also possible due to the chemical structure of the drug. The final peak at 288 eV is due to the presence of COOH. The 50:50 lipid:pregabalin spectra is shown in figure 7.7 (c). This again consists of a main peak at 285 eV due to C-C. There are also peaks at 286.5 eV and 289 eV due to C-O and COOH, respectively.

The oxygen spectra are shown in figure 7.8 (a) to (c). The lipid spectra, figure 7.8 (a), shows that C=O, C-O and P-O/P=O are present at 531 eV, 532 eV and 534 eV, respectively. For the pure pregabalin it is seen that there is again C=O and C-O present at 531 eV and 532 eV, but they are

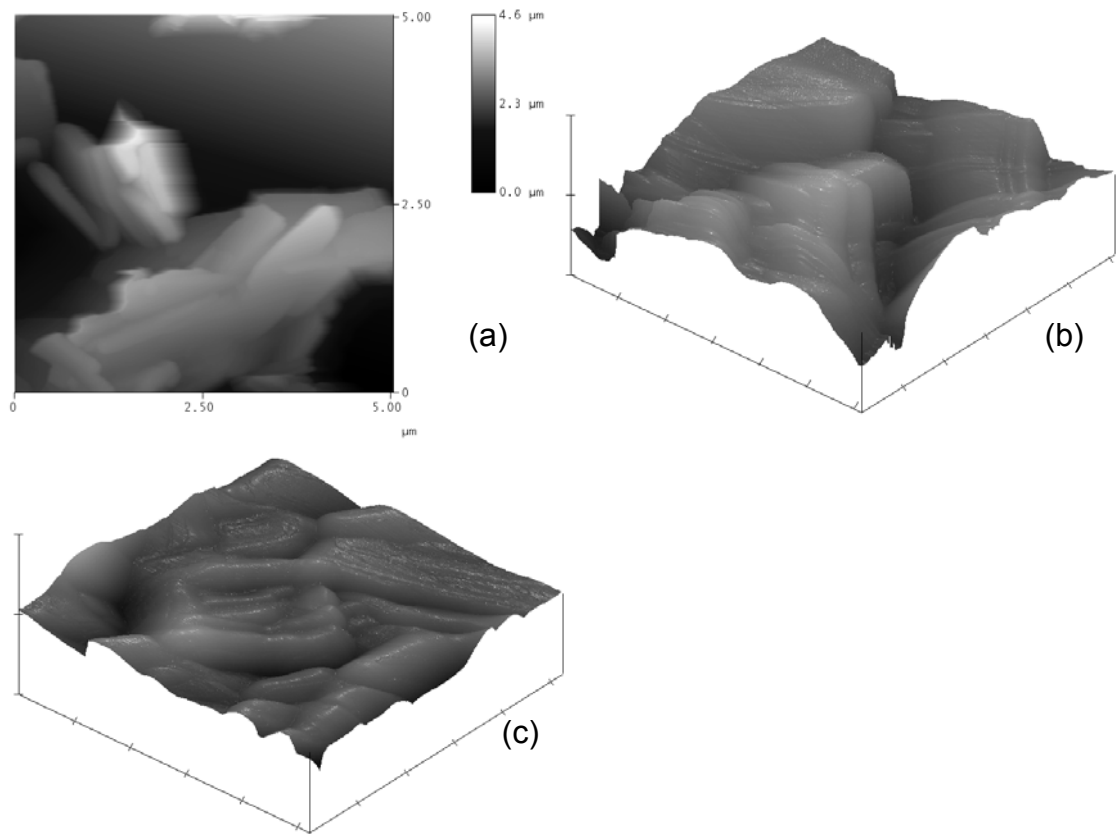


Figure 7.5. AFM images of 50:50 lipid pregabalin.

(a) Large image.

(b) Zoom in of different area, XY = 1.2 μm , Z = 970 nm/div.

(c) Zoom in of different area, XY = 1 μm , Z = 375 nm/div.

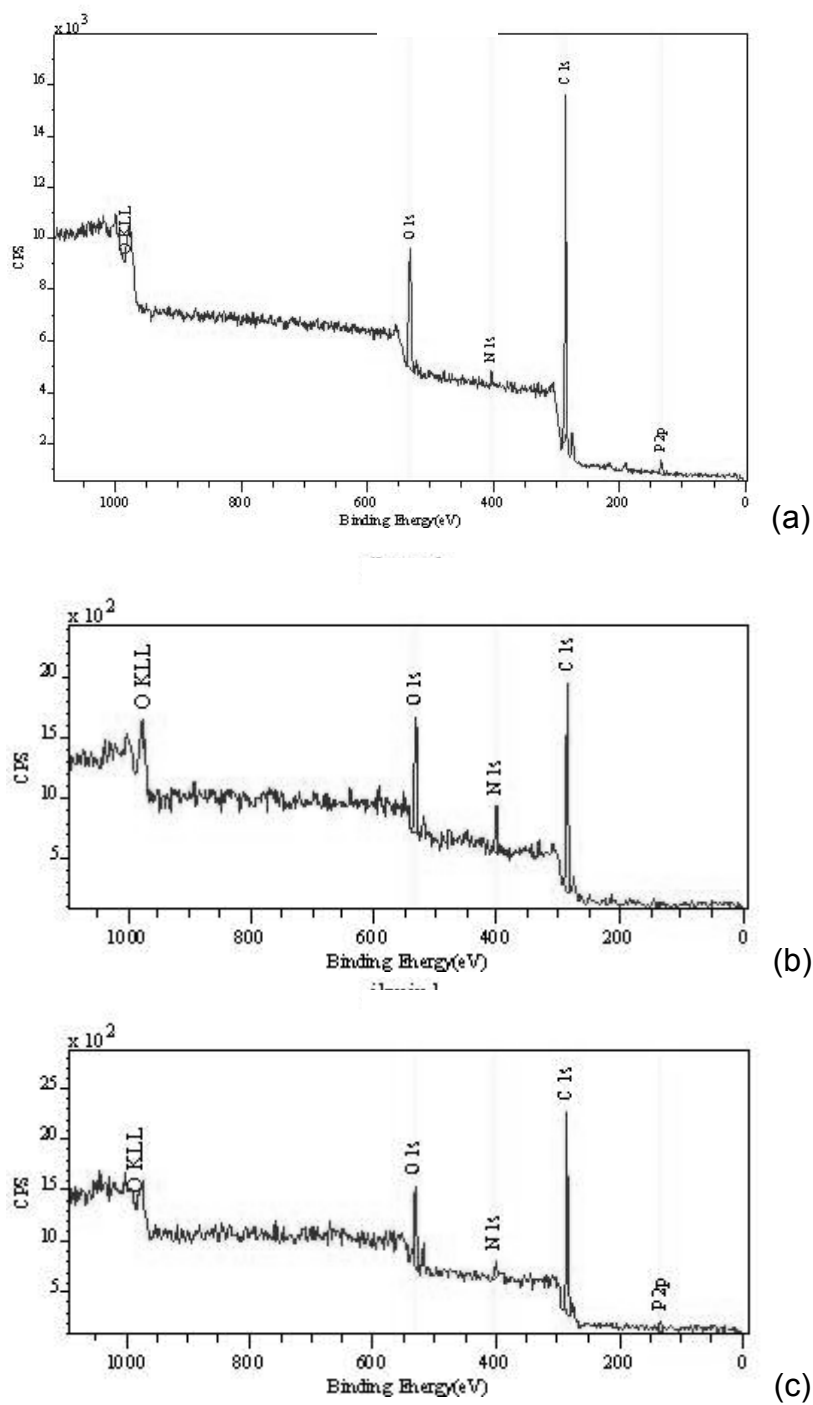


Figure 7.6. Overview spectra of the three samples.

- (a) Lipid.
- (b) Pregabalin.
- (c) 50:50 lipid:pregabalin.

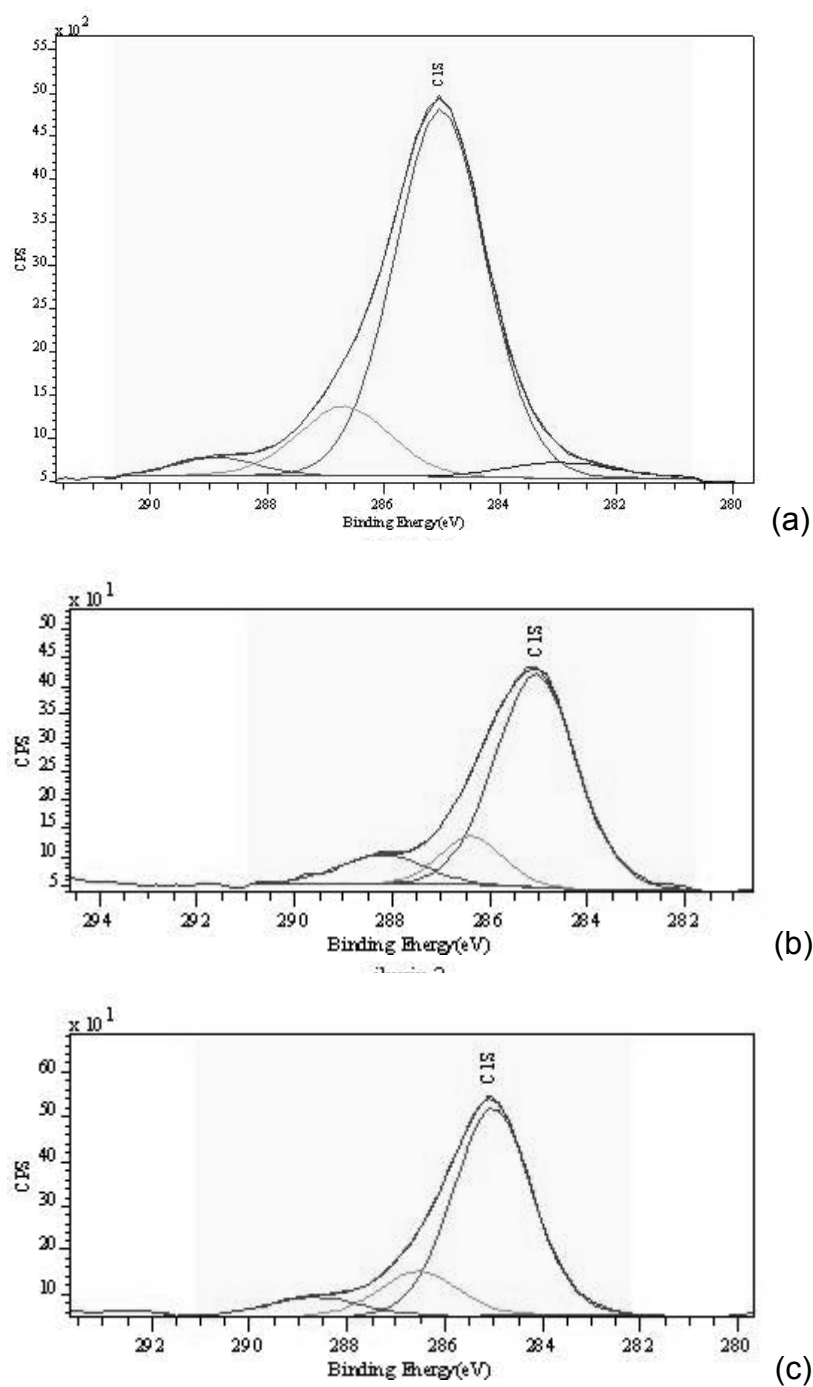


Figure 7.7. Carbon spectra of the three samples.

- (a) Lipid.
- (b) Pregabalin.
- (c) 50:50 Lipid:pregabalin.

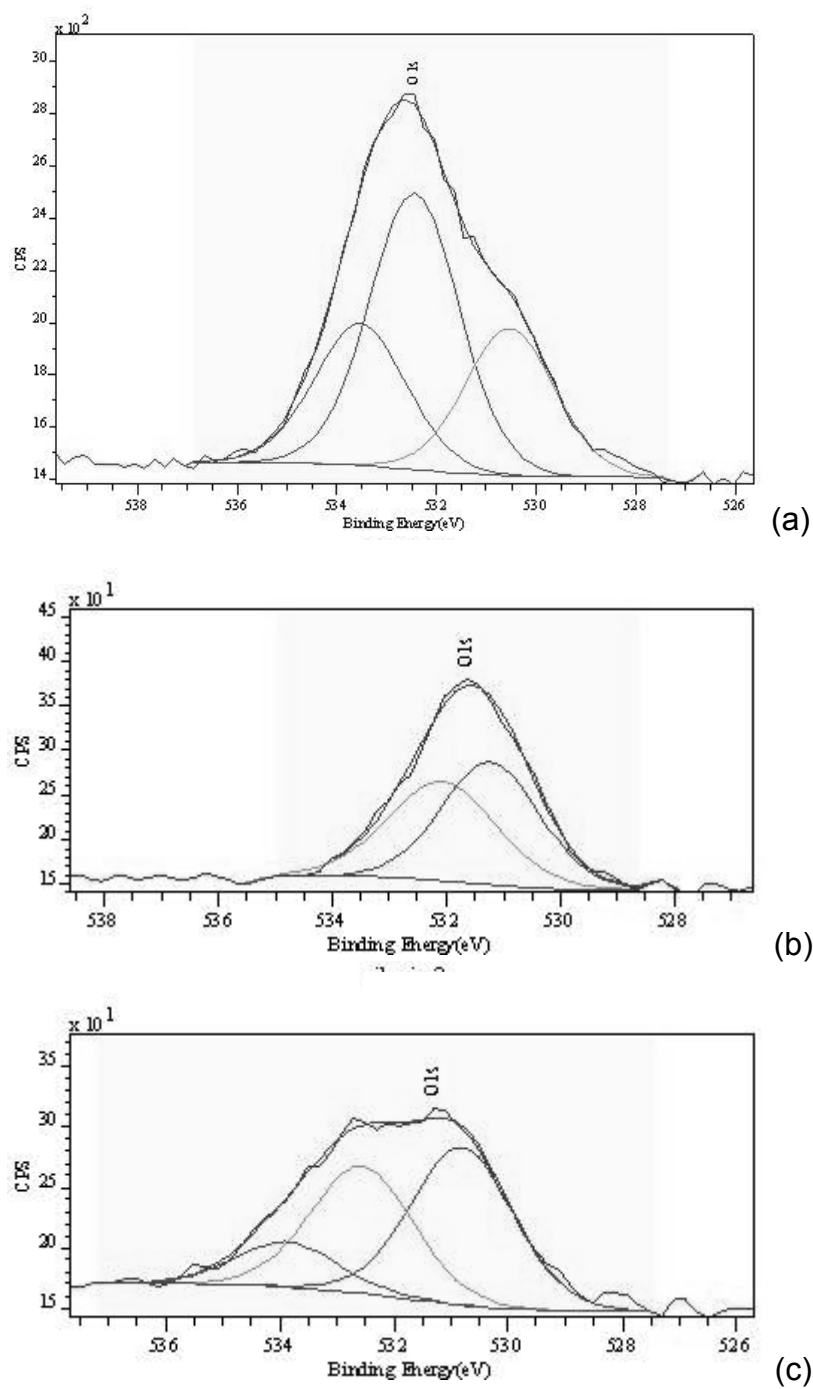


Figure 7.8. Oxygen spectra of the three samples.

- (a) Lipid.
- (b) Pregabalin.
- (c) 50:50 Lipid:pregabalin.

present in different quantities to that seen for the pure lipid, i.e. the C=O is more abundant in the pure drug than the lipid. In the case of the 50:50 spectra, shown in figure 7.8 (c), it is clear that C=O, C-O and P-O/P=O are present at 531 eV, 532 eV and 534 eV.

The nitrogen spectra are shown in figures 7.9 (a) to (c). For the lipid, figure 7.9 (a), it is seen that nitrogen is a single peak at 402.5 eV due to NH_3^+ . This is higher than found in the pregabalin, due to being in a different environment. For the pure pregabalin (figure 7.9 (b)), the high binding energy of the main peak (401.5 eV) indicates NH_3^+ , while the smaller component (399.5 eV) is a good fit with C-N. In the case of the 50:50 lipid:pregabalin spectra (figure 7.9 (c)), the main peak at 401.5 eV is NH_3^+ and the smaller peak at 398.5 eV is C-N.

The phosphorous spectra of the lipid and 50:50 sample are seen in figures 7.10 (a) and (b). The lipid (figure 7.10 (a)) has two peaks present at 285 eV and 286.5 eV, which is expected due The phosphorous spectra of the lipid and 50:50 sample are seen in figures 7.10 (a) and (b). The lipid (figure 7.10 (a)) has two peaks present at circa 133.0 eV and 134.5 eV, which is expected. The 50:50 sample is shown in figure 7.10 (b). Here, the same peak splitting and energies are seen as was observed for the pure lipid. There is only one peak because there is only one phosphorous atom and this is what is expected for PO_4 . The 50:50 sample is shown in figure 7.10 (b). Here, the same peak splitting and energies are seen as was observed for the pure lipid.

7.3.3. SIMS Data

When examining the spectra produced, it is of more use to examine the peaks at higher mass/unit values, as these produce the diagnostic regions of the spectra; however at lower mass ranges the fragments can provide a fingerprint region. The positive and negative ToF-SIMS data of the lipid is shown in figures 7.11 (a) and (b). In the positive spectra (figure 7.11 (b)), the

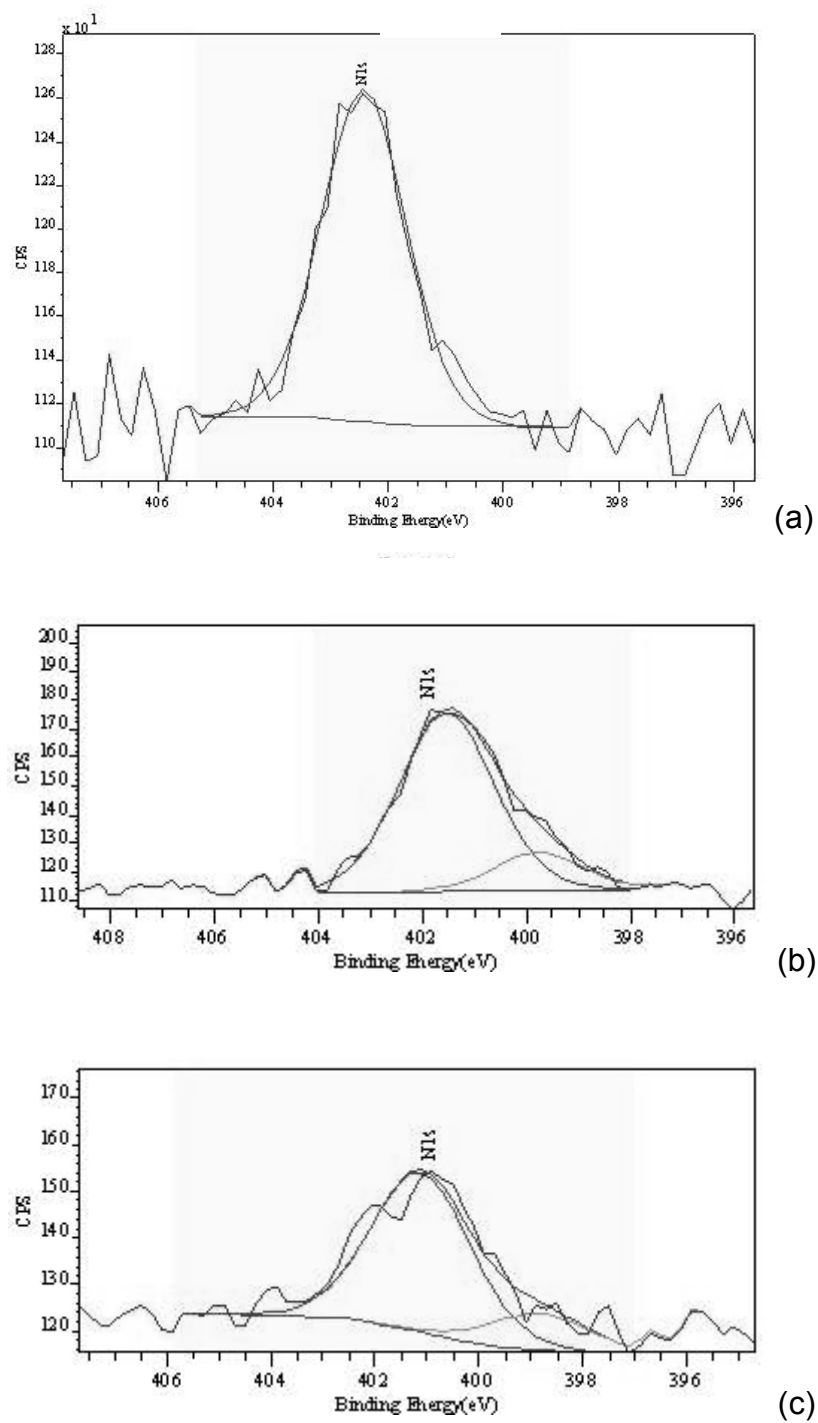


Figure 7.9. Nitrogen spectra of the three samples.

- (a) Lipid.
- (b) Pregabalin.
- (c) 50:50 Lipid:pregabalin.

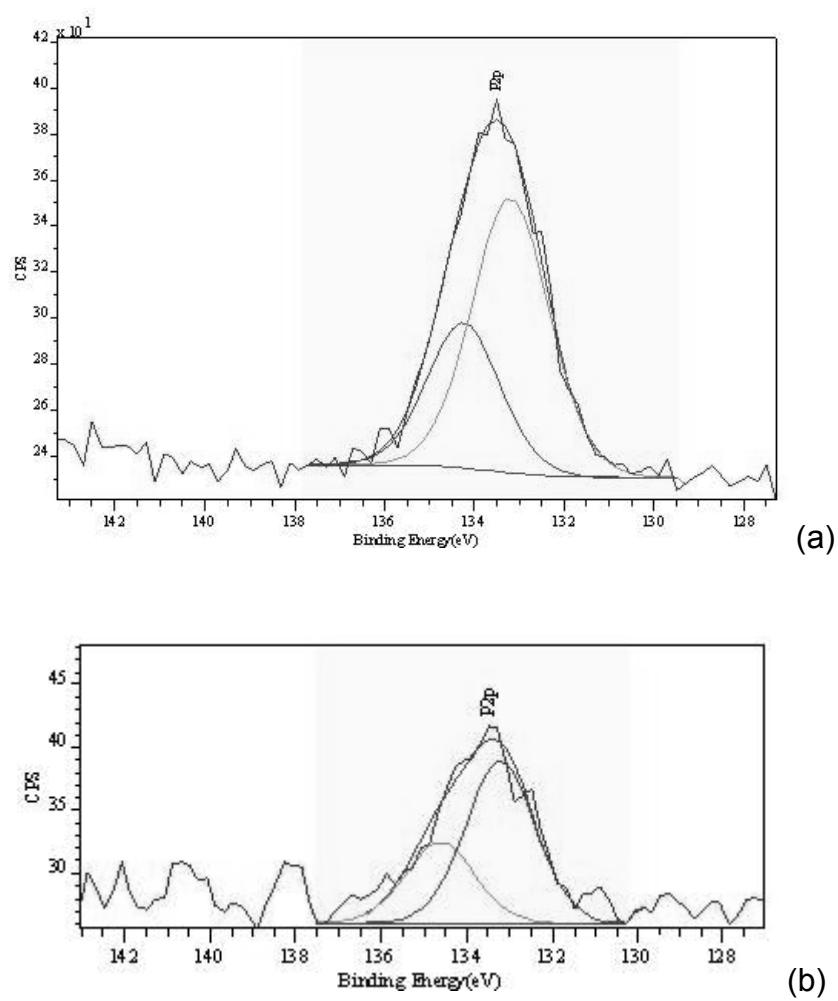


Figure 7.10. Phosphorous spectra of the lipid and 50:50 lipid:pregabalin samples.

(a) Lipid.

(b) 50:50 Lipid:pregabalin.

Sample Parameter		Spectrum Parameter	
Sample:	lipid	Polarity:	positive
Origin:		Area / μm^2 :	75x75
File:	1002S02.dat	Time / s:	200
		PI dose:	2.50E+008
Comments: ; ; SF5+ 9kV			

ION-TOF
TOF-SIMS IV

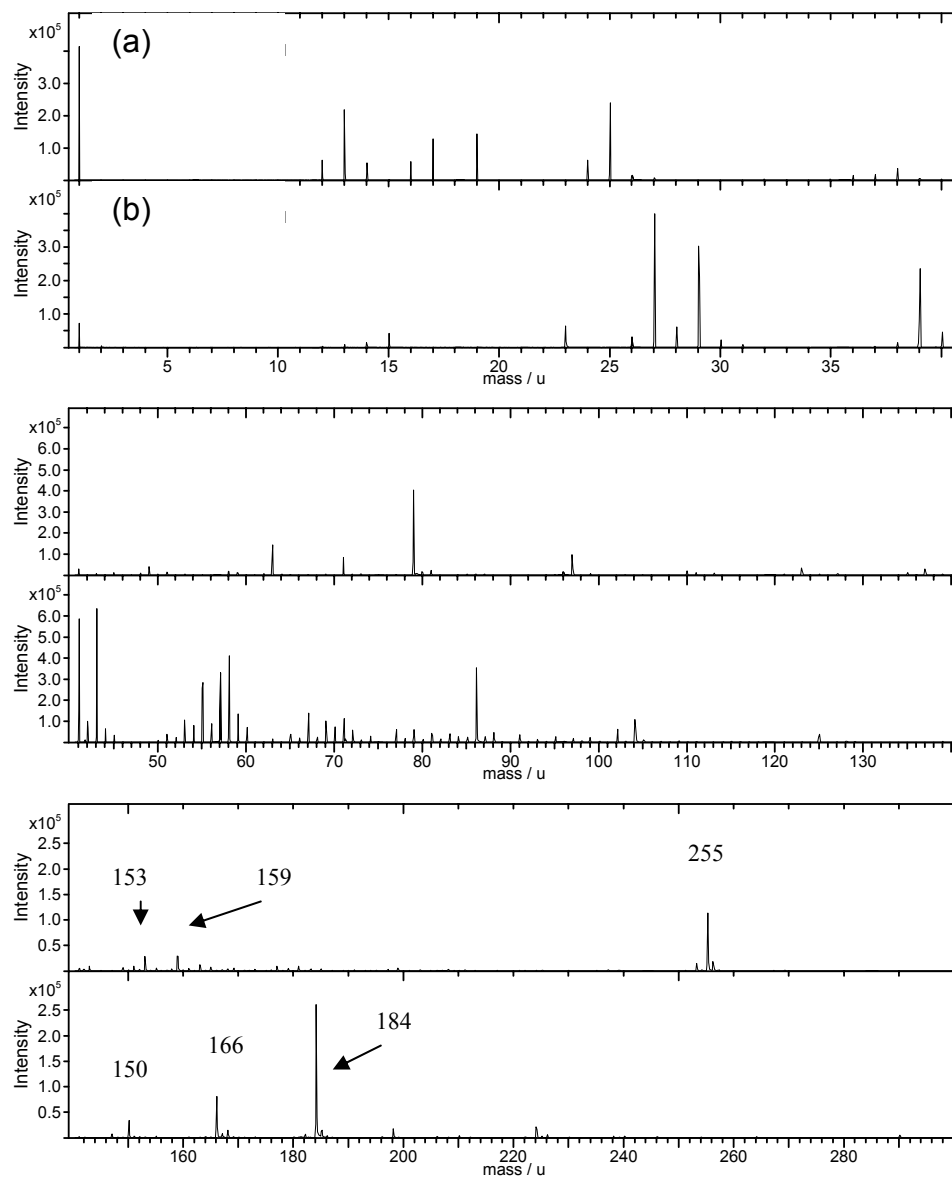


Figure 7.11. SIMS spectra of the lipid sample.

- (a) Negative spectra.
- (b) Positive spectra.

fingerprint fragments such as 58 m/z ($C_3H_8N^+$), 70 m/z ($C_4H_8N^+$), 72 m/z ($C_4H_{10}N^+$), 86 m/z ($C_5H_{12}N^+$), 104 m/z ($C_5H_{14}NO^+$), 125 m/z ($C_2H_6PO_4^+$), 150 m/z ($C_5H_{13}NPO_2^+$), 166 m/z ($C_5H_{13}NPO_3^+$), 184 m/z ($C_5H_{15}NPO_4^+$) and 224 m/z ($C_8H_{19}NPO_4^+$) can be observed as seen in previous work (Bourdous *et al.*, 2000; Ross *et al.*, 2001). However, in the negative spectra (figure 7.11 (a)), there are a number of smaller peaks seen between 150 m/z and 160 m/z, the two most distinctive being found at 153 m/z ($C_3H_5O_5P^-$) and 159 m/z ($C_3H_{11}O_5P^-$). In addition, a much larger peak is seen at 255 m/z ($C_8H_{17}O_6NP^-$).

The positive and negative 100% SEDSTM pregabalin spectra are shown in figure 7.12 (a) and (b). This sample displays the lower mass fragments associated with hydrocarbons (which will not be discussed further here). In the positive spectra (figure 7.12 (a)), there were three distinctive peaks at 142 m/z ($C_8H_{16}ON^+$), 160 m/z ($C_8H_{18}O_2N^+$) and 320 m/z (320 m/z peak not shown). In the negative spectra (figure 7.12 (b)) there was a distinctive peak at 159 m/z (the mass peak of the drug) and 195 m/z. It is noted that there was also a peak at 159 m/z in the lipid spectra, however, the peaks in the pregabalin have greater intensities (approximately 0.6×10^6) than those in the lipid (approximately 0.3×10^5).

The positive and negative 50:50 lipid:pregabalin spectra are shown in figure 7.13 (a) and (b). The main peaks seen in the positive spectra (figure 7.13 (b)) were found at 125 m/z, 142 m/z, 150 m/z, 160 m/z, 184 m/z, 224 m/z and 320 m/z. The main peaks found in the negative spectra (figure 7.13 (a)) were found at 159 m/z, 184 m/z and 255 m/z.

An additional control spectra of the glue used to adhere the particles to the silica was undertaken. This showed no similarities to the spectra of the lipid, 100% SEDSTM pregabalin or the 50:50 lipid:pregabalin (data not shown). Although the lower mass regions show fragments that would be expected for a hydrocarbon (C_xH_y).

Sample Parameter		Spectrum Parameter	
Sample:	Pregabalin	Polarity:	negative
Origin:		Area / μm^2 :	100x100
File:	1102S02.dat	Time / s:	200
		PI dose:	2.50E+008
Comments: ; ; SF5+ 9kV			

ION-TOF
TOF-SIMS IV

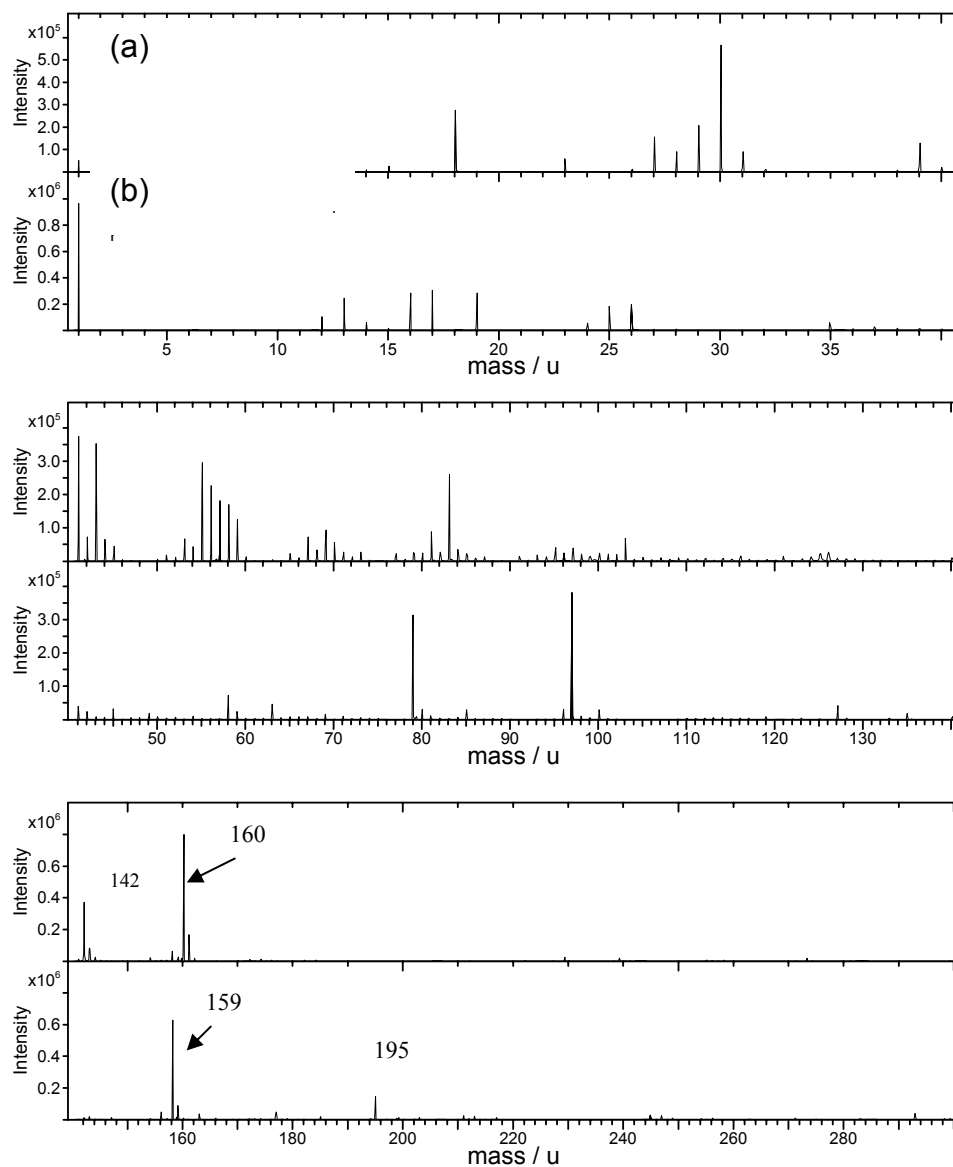


Figure 7.12. ToF-SIMS spectra of SEDS™ pregabalin.

- (a) Positive spectra.
- (b) Negative spectra.

Sample Parameter		Spectrum Parameter	
Sample:	50/50 Pregabalin/lipid	Polarity:	positive
Origin:		Area / μm^2 :	100x100
File:	1102S06.dat	Time / s:	200
		PI dose:	2.50E+008
Comments: ; ; SF5+ 9kV			

ION-TOF
TOF-SIMS IV

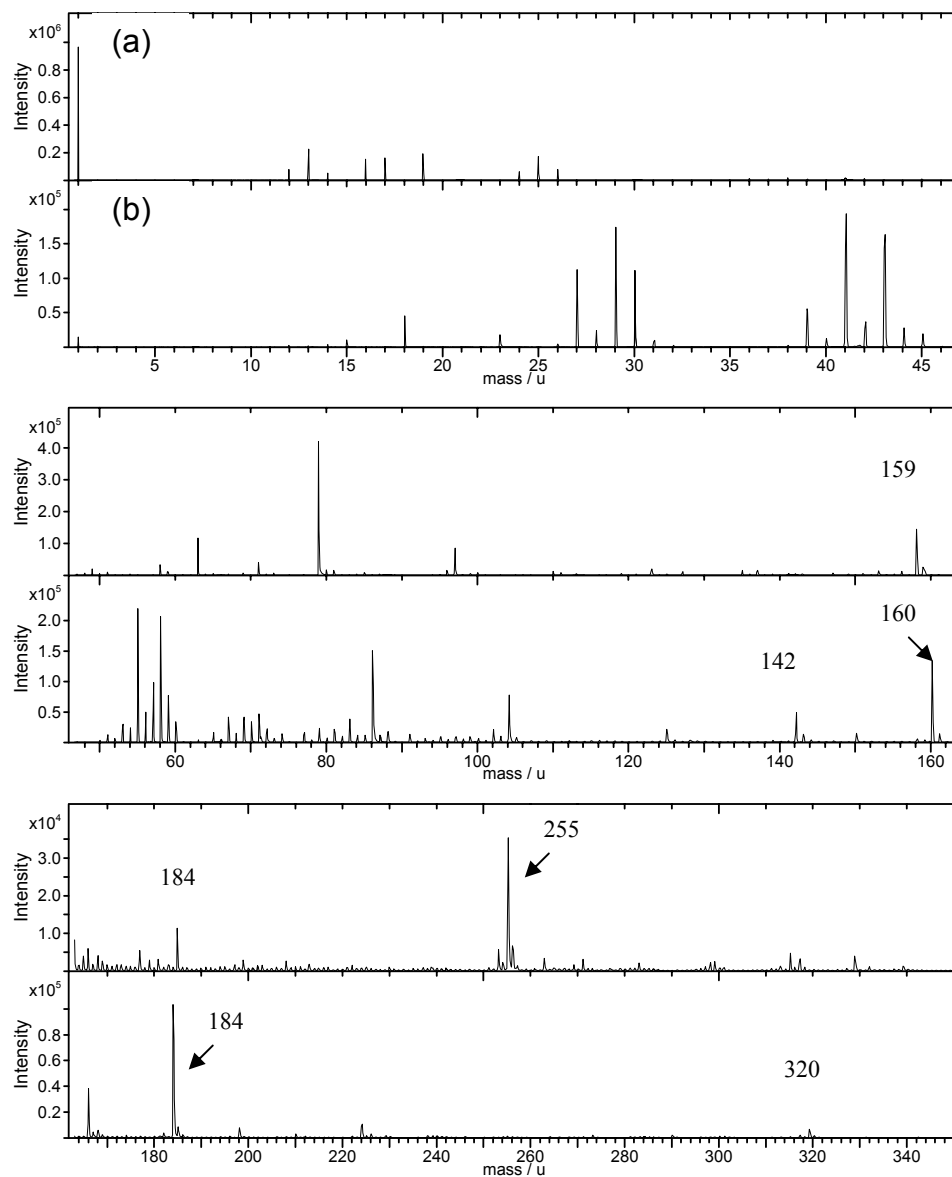


Figure 7.13. ToF-SIMS spectra of 50:50 lipid:pregabalin.

- (a) Negative spectra.
- (b) Positive spectra.

7.4. Discussion

7.4.1. Images

The SEM and AFM images (figures 7.2 to 7.5) showed that the 100% SEDSTM pregabalin and co-processed drug had different surface structures. The SEM images (figures 7.2 and 7.3) showed that the pure drug has a smaller, more uniform particle size than that of the co-processed drug. However the co-processed drug particles were more elongated and less aggregated than the pure drug. The AFM images (figures 7.4 and 7.5) also showed a difference in structure: the 100% SEDSTM material consisted of globular structures compared to the irregular steps present on the 50:50 lipid:pregabalin particles. The lack of any non-topographic phase contrast on any of the images indicates either that the surfaces of each are homogeneous or that the AFM is not sensitive under the conditions used to distinguish the areas of different chemical structure, as changes in this would lead to phase lag in the oscillation of the cantilever.

7.4.2. XPS

When the overview spectra of the three samples were compared (figure 7.6), the presence of phosphorous in both the pure lipid and 50:50 lipid:pregabalin indicated that there was lipid present on the surface of the molecule. The phosphorous spectra was due entirely to the presence of lipid, as no phosphorous was found in the pure drug. In order to decide if pregabalin was present, the individual spectra of the molecules needed to be examined to yield further information.

The carbon spectra (figure 7.7) of the 50:50 lipid:pregabalin sample showed the presence of C-C/C-H, COOH and C-O as were seen in the lipid spectra. However the spectra did not show any C-N⁺ as was seen in the 100% SEDSTM pregabalin. This means the 50:50 lipid:pregabalin carbon spectra is due entirely to the presence of lipid rather than the drug.

The oxygen spectra (figure 7.8) of the 50:50 lipid:pregabalin mix showed that C=O and C-O groups were present as seen in both the lipid and pregabalin spectra. As the proportions of the C-O and C=O groups were similar to those seen for the 100% SEDS™ pregabalin spectra, this indicated that pure drug was present. There were also P-O/P=O groups present in the 50:50 lipid:pregabalin spectra, similar to those seen in the pure lipid spectra, providing another indication that there was lipid present.

The nitrogen spectra (figure 7.9) for the 50:50 lipid:pregabalin material contained NH_3^+ and C-N groups. Both of these were found in the 100% SEDS™ pregabalin spectra, although only the NH_3^+ group was observed in the lipid spectra. This indicated again that pregabalin was present in the surface, in addition to the lipid.

The combined data from the XPS overview and individual element spectra showed that the 50:50 sample contained both lipid and the pregabalin. From the data it was possible to make an estimation as to how much lipid was present: the area covered by the phosphate group in the 50:50 lipid pregabalin spectra was 4.36%, and phosphorous is 0.8% of the number of atoms in the lipid molecule, so therefore lipid must cover only 5.45% of the drug particle. Because XPS samples the top 10 nm of a sample surface, it is possible that the largest proportion of lipid present may be concentrated in the core of the sample.

7.4.3. ToF-SIMS Data

The ToF-SIMS spectra of the pure lipid (figure 7.11) was similar to those previously seen for the sample. The fragments found at 58 m/z, 70 m/z and 72 m/z are present due to the cleavage of bonds in the choline moiety, and those at 104 m/z, 150 m/z and 166 m/z are due to cleavage in the phosphate region (Ross *et al.*, 2001). The peak at 125 m/z is due to cleavage of the choline moiety and phosphate region, at 184 m/z, due to the removal of the

polar head group and, at 224 m/z, due to the cleavage of both of the palmitoyl residues (Ross *et al.*, 2001). No data could be found for the negative spectra in the literature; however it is possible to speculate that the peaks (153 m/z, 159 m/z and 255 m/z) are all the result of the removal of the palmitoyl and polar head groups, leaving the carbon backbone and phosphate group.

The peaks seen in the 100% SEDSTM pregabalin (figure 7.12) can be explained by examining the mass of the drug. The relative atomic mass of pregabalin is 159 u, so the peak at 159 m/z in the negative spectra would be caused by the drug molecule only. In the positive spectra, the peaks were seen at 160 m/z, which would correspond to the mass peak of the drug with the addition of a proton and at 320 m/z which would correspond to two drug molecules passing through the detector.

The ToF-SIMS spectra of the 50:50 lipid:pregabalin sample (figure 7.13) shows the presence of both lipid and pregabalin peaks. Most of the peaks found below 100 m/z were common to both samples and will not be discussed here. In relation to the higher peaks, the positive spectra possess peaks at 125 m/z, 150 m/z, 184 m/z and 224 m/z, which indicate the presence of lipid, and peaks at 142 m/z, 160 m/z and 320 m/z, which indicates the presence of pregabalin. In the negative spectra, peaks are seen at 159 m/z and 255 m/z. The peak at 255 m/z is due to the lipid, whilst the peak at 159 m/z was seen in both the lipid and the drug. If the lipid negative spectra is re-examined, it is noted that the peak at 153 m/z was of similar size to the 159 m/z peak. As the 153 m/z peak is not present, and the 159 m/z peak in drug was much stronger than in the lipid, this peak is more likely to be due to the presence of drug and not lipid. The peak at 184 m/z was not seen in either sample, and so may be the result of a combination of both the pregabalin and the lipid.

These results support the data gathered using XPS, regarding the mixed nature of the surface. However, the sample depth of ToF-SIMS is approximately 1 nm (compared to 10 nm with XPS) (Vickerman, 1997). This

means that the surface is more likely to be composed of a mixture of lipid and drug instead of lipid coating the drug, as was previously envisaged from the XPS and AFM data as a complete lipid layer would be unlikely to be less than 1 nm thick. Although the AFM imaging showed no sign of phase contrast, it should be remembered that the AFM image sizes are approximately $5\ \mu\text{m} \times 5\ \mu\text{m}$ in size, compared to the ToF-SIMS data that was acquired over a $75\ \mu\text{m} \times 75\ \mu\text{m}$ area. This suggests that the area coverage of each component may be greater than the area imaged by the AFM in this work.

7.5. Conclusions

This chapter has examined the surface of a co-processed drug in order to determine its structure and composition. This work was undertaken using the AFM, as well as the complementary techniques of XPS and SIMS.

The AFM images obtained showed no phase contrast. However, when the XPS and SIMS data were examined, both techniques showed that there is both drug and lipid present in the surface. These techniques are surface sensitive and only involve the first few nanometers of a sample surface. XPS has a sampling depth of approximately 10 nm, so it could be possible that a thin layer of lipid is coating the drug. However, because SIMS is able to examine only the top 1 nm of the sample, the process suggests that the surface is a mixture of both lipid and drug and not a coating, as initially thought.

This work also highlights a potential limitation of the AFM in that some surface events either occur over larger areas than can be imaged, or are not sensitive to the AFM conditions. It also highlights the importance of using additional techniques to provide supporting information.

Chapter 8

Final Conclusions

This thesis has examined the application of AFM and other complementary surface analysis techniques to the understanding of particle adhesion and surface behaviour of drugs processed using a novel supercritical fluid technique and those produced using more traditional techniques. Work has focused on single particle studies aimed at developing an understanding of particle properties such as surface energy and morphology, in relation to the adhesion behaviour seen.

In chapter 3 it was shown that it is possible to make quantitative comparisons between particles of salbutamol sulphate produced using the SEDSTM technique and those produced by micronisation. This was achieved by the use of the artefact of tip imaging to produce an image of the contacting asperities of the particles of both types of salbutamol, and then applying contact mechanics to calculate the work of adhesion and the contact area. This was undertaken in a model liquid environment so that the effect of capillary forces could be eliminated. It was found that the SEDSTM salbutamol had a work of adhesion of 4 mJm^{-2} , compared to a value of 19 mJm^{-2} for the micronised sample. When corrected for contact area the SEDSTM was found to have a value of $3 \text{ mN}/\mu\text{m}^2$ compared to that of 13

$\text{mN}/\mu\text{m}^2$ for the micronised. The use of contact mechanics was found to be the best method of calculating contacting area as it took into account the mechanical properties of both the particle and the substrate.

Chapter 4 involved developing the imaging techniques in chapter 3 so that they could be applied to a non-liquid environment where capillary forces would be present, as is commonly found in the pharmaceutical industry. Force measurements were performed in air at controlled humidity using blank AFM tips and particle modified tips against HOPG and compressed salbutamol disk substrates. It was observed that for the measurements obtained for blank AFM tips against compressed disks that a peak in adhesion force with increasing humidity was seen at 22% RH for the SEDS™ material, and at 44% RH for the micronised. The same effect was also seen for some of the particle measurements against HOPG. This effect was linked to the geometry of the contacting asperities, which caused repulsive forces to be generated at higher humidities, coupled with the different surface chemistries creating different spreading effects, so that the capillary forces had a greater effect at lower humidity levels for the SEDS™ salbutamol than the micronised. This led to the generation of a three scenario model whereby the adhesion ranges from simple single asperity contact where peaks in adhesion with humidity are seen, to the situation where the asperity is saturated leading to a continual increase in the adhesion force with increasing humidity. When the data generated from particle against compressed disk measurements was examined, it was seen that this model could explain some of the behaviour seen, although not all.

Chapter 5 saw the application of this work to the differences in properties between different polymorphs of the drug sulphathiazole. Peaks in adhesion were seen when performing measurements against HOPG. These were seen at 22% RH for polymorphs I-Met and III, both of which were also observed to have similar surface energies when calculated using the data acquired below <10% RH. Polymorph IV also showed a peak in adhesion, although at 44% RH, and had a higher surface energy than polymorphs I-Met

and III. Polymorph I-Ace showed very different behaviour in that with increasing humidity no peaks in adhesion were seen, and the surface energy against HOPG was higher than the other polymorphs. From these results, it is postulated that the peaks in adhesion are related to lower surface energy and more stable crystal structure.

In chapter 6 the differences between SEDSTM and unprocessed insulin were examined in order to understand why the SEDSTM material was displaying aggregation phenomena. It was found that the SEDSTM possessed a higher surface energy than the unprocessed. It was also seen that in general neither sample showed peak behaviour, which supports the theory outlined in chapter 5 because both samples had a high amorphous content.

In chapter 7 the effect of co-processing two materials, the drug pregabalin and the lipid DPPC, was examined in order to understand the surface distributions of both components. Using the complementary techniques of ToF-SIMS and XPS it was seen that the surface coverage of the lipid was patchy due to the presence of both lipid and drug in the spectra, indicating that rather than forming a continuous surface coating, the lipid is incorporated into the particle during growth.

In conclusion, this project has shown that the AFM can make a valuable contribution to the understanding of particle properties that affect adhesion behaviour, not only against model systems, but also particle systems such as would be found in industry. These measurements have provided useful quantitative information, which when combined with available bulk techniques may provide a further understanding of the processes and factors involved in adhesion.

References

Allen, S.; Davies, M.C.; Roberts, C.J.; Tendler, S.J.B.; and Williams, P.M. Atomic force microscopy in analytical biotechnology. *Trends Biot.*, 15:101-105, 1997.

Alsten, J.G.V., and Eckert, C.A. Effect of entrainers and of solute size and polarity in supercritical fluid solutions. *J. Chem. Eng. Data*, 38:605-610, 1993.

Anwar, J.; Tarling, S.E.; and Barnes, P. Polymorphism of sulfathiazole. *Pharm. Sci.*, 78(4):337-342, 1989.

Apperley, D.C.; Fletton, R.A.; Harris, R.K.; Lancaster, R.W.; Tavener, S.; and Threlfall, T.L. Sulfathiazole polymorphism studied by magic-angle spinning NMR. *J. Pharm. Sci.*, 88(12):1275-1280, 1999.

Askeland, D. R.; and Phule, P. P. *The Science and Engineering of Materials*. Pacific Grove, C.A: Brooks/Cole-Thomson Learning, 2003.

Atkins, P.W. *The Elements of Physical Chemistry*. Oxford: Oxford University Press, 1996.

Aulton, M.E. *Pharmaceutics: The Science of Dosage Form Design*. London: Churchill Livingstone, 1988.

Beach, E.R.; Tormoen, G.W.; Drelich, J.; and Han, R. Pull-off force measurements between rough surfaces by atomic force microscopy. *J. Colloid Interface Sci.*, 247:84-99, 2002.

Beach, S.; Latham, D.; Sidgwick, C.; Hanna, M.; and York, P. Control of the physical form of salmeterol xinafoate. *Organic Pro. Res. Dev.*, 3:370-376, 1999.

Beale, J.P., and Grainger, C.T. DL-N-t-Butyl-2(4-hydroxy-3-hydroxymethylphenyl)2-hydroxyethylamine, (salbutamol, Ah. 3365), C₁₃H₂₁NO₃. *Cryst. Struct. Comm.*, 67(1):71-74, 1972.

Berard, V.; Lesniewska, E.; Andres, C.; Pertuy, D.; Iaroche, C.; and Pourcelot, Y. Affinity scale between a carrier and a drug in DPI studied by atomic force microscopy. *Int. J. Pharm.*, 247:127-137, 2002.

References

- Binggeli, M., and mate, C.M. Influence of capillary condensation of water on nanotribology studied by force microscopy. *Appl. Phys. Lett.*, 65(4):415-417, 1994.
- Binnig, G.; Quate, C.F.; and Gerber, C. Atomic force microscope. *Phys. Rev. Lett.*, 56(9):930-933, 1986.
- Binnig, G.; Rohrer, H.; Gerber, C.; and Weibel, E. Surface studies by scanning tunneling microscopy. *Phys. Rev. Lett.*, 49(1):57-61, 1982.
- Bleich, J.; Muller, B.W.; and Wabmus, W. Aerosol solvent extraction system - a new microparticle production technique. *Int. J. Pharm.*, 97:111-117, 1993.
- Bourdos, N.; Kollmer, F.; Benninghoven, A.; Ross, M.; Sieber, M.; and Galla, H.J. Analysis of lung surfactant model systems with time-of-flight secondary ion mass spectrometry. *Biophys. J.*, 79:357-369, 2000.
- Bowen, R.C.; DeMejo, L.P.; and Rimai, D.S. A method of determining the contact area between a particle and substrate using Scanning Electron Microscopy. *J. Adhesion*, 51:191-199, 1995.
- Briggs, D. *Surface Analysis of Polymers by XPS and Static SIMS*. Cambridge Solid State Science Series. Cambridge, UK: Cambridge University Press, 1998.
- Briscoe, B.J.; Liu, K.K.; and Williams, D.R. Adhesive contact deformation of a single microelastomeric sphere. *J. Coll. Interface Sci.*, 200:256-264, 1998.
- Brittain, H.G. *Polymorphism in Pharmaceutical Solids*. Drugs and the Pharmaceutical Sciences. New York: Marcel Dekker, Inc., 1999.
- Buckton, G.; Choularton, A.; Beezer, A.E.; and Chatham, S.M. The effect of comminution technique on the surface energy of a powder. *Int. J. Pharm.*, 47:121-128, 1988.
- Buckton, G. *Interfacial Phenomena in Drug Delivery and Targeting*. Drug Targeting and Delivery. Switzerland: Harwood Academic Publishers, 1995.
- Burnham, N.A., and Colton, R.J. Measuring the nanomechanical properties and surface forces of material using an atomic force microscope. *J. Vac. Sci. Technol. A*, 7(4):2906-2913, 1989.
- Burnham, N.A.; Dominguez, D.D.; Mowery, R.L.; and Colton, R.J. Probing the surface forces of monolayer films with an atomic-force microscope. *Phys. Rev. Lett.*, 64(16):1931-1934, 1990.
- Butt, H.J. Measuring electrostatic, van der waals, and hydration forces in electrolyte solutions with an atomic force microscope. *Biophys. J.*, 60:1438-1444, 1991.

References

- Cappella, B.; Baschieri, P.; Frediani, C.; Miccoli, P.; and Ascoli, C. Force-distance curves by AFM. *IEEE Eng. Med. and Biol. Mag*, March/April:58-65, 1997.
- Cappella, B., and Dietler, G. Force distance curves by atomic force microscopy. *Surf. Sci. R.*, 34:1-104, 1999.
- Carstensen, J.T. *Pharmaceutical Principles of Solid Dosage Forms*. Pennsylvania: Technomic Publishing Company, Inc., 1993.
- Clifford, T. *Fundamentals of Supercritical Fluids*. Oxford: Oxford University Press, 1998.
- Coelho, M.C., and Harnby, N. Moisture bonding in powders. *Powder Technol.*, 20:201-205, 1978.
- Daintith, J., ed. *A Dictionary of Chemistry*. Oxford Paperback Reference. Oxford: Oxford University Press, UK, 1996.
- Derjaguin, B.V.; Aleinikova, I.N.; and Toporov, Y.P. On the role of electrostatic forces in the adhesion of polymer particles to solid surfaces. *Powder Technol.*, 2:154-158, 1968.
- Derjaguin, B.V.; Muller, V.M.; and Toporov, Y.P. Effect of contact deformations on the adhesion of particles. *J. Colloid Interface Sci.*, 53(2):314-326, 1975.
- Dixon, D.J.; Johnston, K.P.; and Bodmeier, R.A. Polymeric materials formed by precipitation with a compressed fluid antisolvent. *AIChE J.*, 39(1):127-139, 1993.
- Dobbs, J.M.; Wong, J.M.; and Johnston, K.P. Nonpolar co-solvents for solubility enhancement in supercritical fluid carbon dioxide. *J. Chem. Eng. Data*, 31:303-308, 1986.
- Dobbs, J.M.; Wong, J.M.; Lahiere, R.J.; and Johnston, K.P. Modification of supercritical fluid phase behavior using polar co-solvents. *Ind. Eng. Chem. Res.*, 26:56-65, 1987.
- Ducker, W.A.; Senden, T.J.; and Pashley, R.M. Direct measurement of colloidal forces using an atomic force microscope. *Nature*, 353:239-241, 1991.
- Duncan-Hewitt, W.C., and Weatherly, G.C. Evaluating the hardness, Young's modulus and fracture toughness of some pharmaceutical crystals using microindentation techniques. *J. Mat. Sci. Lett*, 8:1350-1352, 1989.

References

Eve, J.K.; Patel, N.; Luk, S.Y.; Ebbens, S.J.; and Roberts, C.J. A study of single drug particle adhesion interactions using atomic force microscopy. *Int. J. Pharm.*, 238:17-27, 2002.

Feeley, J.C.; York, P.; Sumbly, B.S.; and Dicks, H. Comparison of the surface properties of salbutamol sulphate prepared by micronization and a supercritical fluid technique. *J. Pharm. Pharmacol.*, 50:S54, 1998.

Feeley, J.C.; Shekunov, B.Y.; Chow, A.H.L.; and York, P. Surface and aerodynamic characteristics of particles for inhalation produced using supercritical fluid technology. *Pro. Millennium World Congress Pharm. Sci.* San Francisco, USA., 2000.

Forbes, R.T.; Sloan, R.; Kibria, I.; Hollowood, M.E.; Humphreys, G.O.; and York, P. Production of stable protein particles: a comparison of freeze, spray and supercritical drying. *World Congress on Particle Technology.* Brighton, UK, 1998.

Florence, A.T., and Attwood, D. *Physicochemical Principles of Pharmacy.* London: Macmillan academic and professional Ltd, 1988.

Freund, J.; Halbritter, J.; and Horber, J.K.H. How Dry Are Dried Samples? Water Adsorption Measured by STM. *Micr. Res. Tech.*, 44:327-338, 1999.

Ghaderi, R.; Artursson, P.; and Carlfors, J. A new method for preparing biodegradable microparticles and entrapment of hydrocortisone in DL-PLG microparticles using supercritical fluids. *Eur. J. Pharm. Sci.*, 10:1-9, 2000.

Ghilzai, N.M.K. New developments in insulin delivery. *Drug Dev. Ind. Pharm.*, 29(3):253-265, 2003.

Gilbert, D.J.; Palakodaty, S.; and York, P. Production of salbutamol sulphate by the solution enhanced dispersion by supercritical fluids (SEDS) technique. *J. Pharm. Pharmacol.*, 52 S:164, 2000.

Haleblian, J., and McCrone, W. Pharmaceutical applications of polymorphism. *J. Pharm. Sci.*, 58(8):911-929, 1969.

Haleblian, J.K. Characterization of habits and crystalline modification of solids and their pharmaceutical applications. *J. Pharm. Sci.*, 64(8):1269-1288, 1975.

Hannay, J.B., and Hogarth, J. On the solubility of solids in gases. *Proc. R. Soc. London*, 29:324-326, 1879.

Hansma, H.G.; Kim, K.J.; Laney, D.E.; Garcia, R.A.; Argaman, M.; Allen, M.J.; and Parsons, S.M. Properties of biomolecules measured from atomic force microscope images: a review. *J. Struct. Biol.*, 119:99-108, 1997.

References

- Harwood, L.M., and Claridge, T.D.W. *Introduction to Organic Spectroscopy*. Oxford Chemistry Primers. Oxford: Oxford University Press, 1997.
- He, M.; Blum, A.S.; Aston, D.E.; Buenviaje, C.; and Overney, R.M. Critical phenomena of water bridges in nanoasperity contacts. *J. Chem. Phys.*, 114(3):1355-1360, 2001.
- Hegedus, B., and Gorog, S. The polymorphism of cimetidine. *J. Pharm. Biomed. Anal.*, 3(4):303-313, 1985.
- Heim, L.O.; Ecke, S.; Preuss, M.; and Butt, H.J. Adhesion forces between individual gold and polystyrene particles. *J. Adhesion Sci. Technol.*, 16(7):829-843, 2002.
- Heuberger, M.; Dietler, G.; and Schlapbach, L. Elastic deformations of tip and sample during atomic force microscope measurements. *J. Vac. Sci. Technol. B.*, 14(2):1250-1253, 1996.
- Hooton, J.C.; German, C.S.; Allen, S.; Davies, M.C.; Roberts, C.J.; Tendler, S.J.B.; and Williams, P.M. Characterization of Particle Interactions by Atomic Force Microscopy: Effect of Contact Area. *Pharm. Res.*, 20(3):508-514, 2003.
- Horn, R.G., and Smith, D.T. Contact electrification and adhesion between dissimilar materials. *Science*, 256:362-364, 1992.
- Hutter, J.L., and Bechhoefer, J. Calibration of atomic-force microscope tips. *Rev. Sci. Instrum.*, 64(7):1868-1873, 1993.
- Ibrahim, T.H.; Burk, T.R.; Etzler, F.M.; and Neuman, R.D. Direct adhesion measurements of pharmaceutical particles to gelatin capsule surfaces. *J. Adhesion Sci. Technol.*, 14(10):1225-1242, 2000.
- Ikai, A. ATM and AFM of bio/organic molecules and structures. *Surf. Sci. R.*, 26:261-332, 1996.
- Israelachvili, J.N. *Intermolecular and Surface Forces*. London, UK: Academic Press Inc., 1991.
- Jarzebski, A.B., and Malinowski, J.J. Potentials and prospects for application of supercritical fluid technology in bioprocessing. *Process Biochem.*, 30(4):343-352, 1995.
- Johnson, K.L.; Kendall, K.; and Roberts, A.D. Surface energy and the contact of elastic solids. *Proc. R. Soc. Lond. A*, 324:301-313, 1971.
- Jones, R.; Pollock, H.M.; Cleaver, J.A.S.; and Hodges, C.S. Adhesion Forces Between Glass and Silicon Surfaces in Air Studied by AFM: Effects of

References

Relative Humidity, Particle Size, Roughness, and Surface Treatment. *Langmuir*, 18:8045-8055, 2002.

Juppo, A.M.; Boissier, C.; and Khoo, C. Evaluation of solid dispersion particles prepared with SEDS. *Int. J. Pharm.*, 250:385-401, 2003.

Kappl, M., and Butt, H.J. The colloidal probe technique and its application to adhesion force measurements. *Part. part. Syst. Charact.*, 19:129-143, 2002.

Khoshkhoo, S., and Anwar, J. Crystallization of polymorphs: the effect of solvent. *J. Phys. D: Appl. Phys.*, 26:B90-B93, 1993.

Kim, J.H.; Paxton, T.E.; and Tomasko, D.L. Microencapsulation of naproxen using rapid expansion of supercritical solutions. *Biotechnol. Prog.*, 12:650-661, 1996.

Kitamura, M.; Yamamoto, M.; Yoshinaga, Y.; and Masuoka, H. Crystal size control of sulfathiazole using high pressure carbon dioxide. *J. Cryst. Growth*, 178:378-386, 1997.

Kitching, S.; Williams, P.M.; Roberts, C.J.; Davies, M.C.; and Tendler, S.J.B. Quantifying surface topography and scanning probe image reconstruction. *J. Vac. Sci. Technol. B*, 17(2):273-279, 1999.

Kordikowski, A.; York, P.; and Latham, D. Resolution of ephedrine in supercritical CO₂: a novel technique for the separation of chiral drugs. *J. Pharm. Sci.*, 88(8):786-791, 1999.

Kordikowski, A.; Shekunov, T.; and York, P. Polymorph control of sulfathiazole in supercritical CO₂. *Pharm. Res.*, 18(5):682-688, 2001.

Kulvanich, P., and Steward, P.J. Influence of relative humidity on the adhesive properties of a model interactive system. *J. Pharm. Pharmacol.*, 40:453-458, 1988.

Kumar, P., and Clark, M. *Clinical Medicine*. London: W. B. Saunders Company Ltd., 1994.

Lachman, L.; Lieberman, H.A.; and Kanig, J.L. *The Theory and Practice of Industrial Pharmacy*. Philadelphia: Lea and Febiger, 1986.

Lal, R., and John, S.A. Biological applications of atomic force microscopy. *Am. J. Physiol.*, 266:C1-C21, 1994.

Larson, K.A., and King, M.L. Evaluation of supercritical fluid extraction in the pharmaceutical industry. *Biotechnol. Prog.*, 2(2):73-82, 1986.

Lifshitz, E. M. The theory of molecular attractive forces between solids. *Sov. Phys. JETP*, 2(1):73-83, 1956.

References

Matson, D.W.; Fulton, J.L.; Petersen, R.C.; and Smith, R.D. Rapid expansion of supercritical fluid solutions: solute formation of powders, thin films, and fibers. *Ind. Eng. Chem. Res.*, 26:2298-2306, 1987.

Meyer, E.; Heinzelmann, H.; Grutter, P.; Jung, T.; Weisskopf, T.; Hidber, H.R.; Lapka, R.; Rudin, H.; and Guntherodt, H.J. Comparative-study of lithium-fluoride and graphite by atomic force microscopy (AFM). *J. Microsc.*, 152(1):269-280, 1988.

McFarlane, J.S., and Tabor, D. Adhesion of solids and the effect of surface films. *Proc. Roy. Soc. London*, A202:224-243, 1950.

McHugh, M.A., and Krukoni, V.J. *Supercritical Fluid Extraction: Principles and Practice*. Boston: Butterworth-Heinemann, 1994.

Muller, V.M.; Yushchenko, V.S.; and Derjaguin, B.V. On the influence of molecular forces on the deformation of an elastic sphere and its sticking to a rigid plane. *J. Coll. Interface Sci.*, 77(1):91-101, 1980.

Muster, T.H., and Prestidge, C.A. Face specific surface properties of pharmaceutical crystals. *J. Pharm. Sci.*, 91(6):1432-1444, 2002.

Myers, D. *Surfaces, Interfaces, and Colloids: Principles and Applications*. New York: John Wiley & Sons, 1999.

Moshashae, S.; Bisrat, M.; Forbes, R.T.; Nyqvist, H.; and York, P. Supercritical fluid processing of proteins I: lysozyme precipitation from organic solution. *Eur. J. Pharm. Biopharm.*, 11:239-245, 2000.

Muster, T.H., and Prestidge, C.A. Face specific surface properties of pharmaceutical crystals. *J. Pharm. Sci.*, 91(6):1432-1444, 2002.

Neto, C., and Craig, V.S.J. Colloid probe characterization: radius and roughness determination. *Langmuir*, 17:2097-2099, 2001.

Nogrady, T. *Medicinal Chemistry - A Biochemical Approach*. Oxford: Oxford University Press, 1988.

O'Brien, W.J., and Hermann, J.J. The strength of liquid bridges between dissimilar materials. *J. Adhesion*, 5:91-103, 1973.

Palakodaty, S.; York, P.; and Pritchard, J. Supercritical fluid processing of materials from aqueous solutions: the application of SEDS to lactose as a model substance. *Pharm. Res.*, 15(12):1835-1843, 1998.

Palakodaty, S., and York, P. Phase behavioral effects on particle formation processes using supercritical fluids. *Pharm. Res.*, 16(7):976-985, 1999.

References

Patton, J.S.; Bukar, J.; and Nagarajan, S. Inhaled insulin. *Adv. Drug Delivery Rev.*, 35:235-247, 1999.

The Pharmaceutical Journal, Manufacturing problems hit Abbott's HIV drug ritonavir. 1998. pp. 150.

Phillips, E.M., and Stella, V.J. Rapid expansion from supercritical solutions: application to pharmaceutical processes. *Int. J. Pharm.*, 94:1-10, 1993.

Podczeck, F., and Newton, J.M. Development of an ultracentrifuge technique to determine the adhesion and friction properties between particles and surfaces. *J. Pharm. Sci.*, 84(9):1067-1071, 1995.

Podczeck, F.; Newton, J.M.; and James, M.B. The estimation of the true area of contact between microscopic particles and a flat surface in adhesion contact. *J. Appl. Phys.*, 79(3):1458-1463, 1996.

Podczeck, F.; Newton, J.M.; and James, M.B. The influence of constant and changing relative humidity of the air on the autoadhesion force between pharmaceutical powder particles. *Int. J. Pharm.*, 145:221-229, 1996 a.

Podczeck, F.; Newton, J.M.; and James, M.B. Influence of relative humidity of storage air on the adhesion and autoadhesion of micronized particles to particulate and compacted powder surfaces. *J. Colloid Interface Sci.*, 187:484-491, 1997.

Podczeck, F. *Particle-particle Adhesion in Pharmaceutical Powder Handling*. London: Imperial College Press, 1998.

Pollock, H.M.; Burnham, N.A.; and Colton, R.J. Attractive forces between micron-sized particles: a patch charge model. *J. Adhesion*, 51:71-86, 1995.

Price, R.; Toby, M.; Stanniforth, J.N.; Thomas, M.; and Davies, M.B. Variation in particle adhesion due to capillary and electrostatic forces. *Respiratory Drug Delivery VII*. North Carolina, 2000. pp. 577-580.

Price, R.; Young, P.M.; Edge, S., Stanniforth, J.N. The influence of relative humidity on particulate interactions in carrier-based dry powder inhaler formulations. *Int. J. Pharm.*, 246:47-59, 2002.

Rabinovich, Y.I.; Adler, J.J.; Ata, A.; Singh, R.K.; and Moudgil, B.M. Adhesion between nanoscale rough surfaces; I. role of asperity geometry. *J. Colloid Interface Sci.*, 232:10-16, 2000.

Rabinovich, Y.I.; Adler, J.J.; Ata, A.; R. K, S.; and Moudgil, B.M. Adhesion between nanoscale rough surfaces; II. measurement and comparison with theory. *J. Colloid Interface Sci.*, 232:17-24, 2000.

References

Randolph, T.W.; Randolph, A.D.; Mebes, M.; and Yeung, S. Sub-micrometer-sized biodegradable particles of poly(l-lactic acid) via the gas antisolvent spray precipitation process. *Biotechnol. Prog.*, 9:429-435, 1993.

Rang, H.P.; Dale, M.M.; and Ritter, J.M. *Pharmacology*. Edinburgh: Churchill Livingstone, 1995.

Reverchon, E. Supercritical antisolvent precipitation of micro- and nanoparticles. *J. Supercrit. Fluids*, 15:1-21, 1999.

Reverchon, E.; Porta, G.D.; and Pallado, P. Supercritical antisolvent precipitation of salbutamol microparticles. *Powder Technol.*, 114:17-22, 2001.

Rhodes, M., ed. *Principles of Powder Technology*. Chichester: John Wiley & Sons, 1990.

Roberts, C.J.; Williams, P.M.; Davies, M.C.; Jackson, D.E.; and Tendler, S.J.B. Atomic force microscopy and scanning tunnel microscopy: refining techniques for studying biomolecules. *Trends Biot.*, 12:127-132, 1994.

Roberts, R.J., and Rowe, R.C. Brittle/ductile behavior in pharmaceutical materials used in tableting. *Int. J. Pharm.*, 36:205-209, 1987.

Roberts, R.J.; Rowe, R.C.; and York, P. The relationship between Young's modulus of elasticity of organic solids and their molecular structure. *Powder Technol.*, 65:139-146, 1991.

Roberts, R.J., and Rowe, R.C. Influence of polymorphism on the Young's modulus and yield stress of carbamazepine, sulfathiazole and sulfanilamide. *Int. J. Pharm.*, 129:79-94, 1996.

Rodriguez-Hornedo, N., and Murphy, D. Significance of controlling crystallization mechanisms and kinetics in pharmaceutical systems. *J. Pharm. Sci.*, 88(7):651-660, 1999.

Ross, M.; Steinem, C.; Galla, H.J.; and Janshoff, A. Visualization of chemical and physical properties of calcuim-induced domains in DPPC/DPPS Langmuir-Blodgett layers. *Langmuir*, 17:2437-2445, 2001.

Rubinson, J.F., and Rubinson, K.A. *Contemporary Chemical Analysis*. Upper Saddle River: Prentice-Hall Inc., 1998.

Sarup, L.; Servistas, M.T.; Sloan, R.; Hoare, M.; and Humphreys, G.O. Investigation of supercritical fluid technology to produce dry particulate formulations of antibody fragments. *Trans. IChemE*, 78(C):101-104, 2000.

Schaefer, D.M.; Carpenter, M.; Gady, B.; Reifenberger, R.; Demejo, L.P.; and Rimai, D.S. Surface roughness and its influence on particle adhesion

References

using atomic force techniques. *J. Adhesion Sci. Technol.*, 9(8):1049-1062, 1995.

Schulz, H. Mechanisms and factors affecting intrapulmonary particle deposition: implications for efficient inhalation therapies. *PSTT*, 1(8):336-344, 1998.

Sencar-Bozic, P.; Srcic, S.; Knez, Z.; and Kerc, J. Improvement of nifedipine dissolution characteristics using supercritical CO₂. *Int. J. Pharm.*, 148:123-130, 1997.

Shao, Z.; Mou, J.; Czajkowsky, D.M.; Yang, J.; and Yuan, J.Y. Biological atomic force microscopy: what is achieved and what is needed. *Adv. Phys.*, 45(1):1-86, 1996.

Shekunov, B.Y., and York, P. Crystallization processes in pharmaceutical technology and drug delivery design. *J. Cryst. Growth*, 211:122-136, 2000.

Skyler, J.S.; Cefalu, W.T.; Kourides, L.A.; Landschulz, W.H.; Balagtas, C.C.; Cheng, S.L.; and Gelfand, R.A. Efficacy of inhaled human insulin in type 1 diabetes mellitus: a randomised proof-of-concept study. *Lancet*, 357(February 3):331-335, 2001.

Sloan, R.; Tservistas, M.; Hollowood, M.E.; Sarup, L.; Humphreys, G.O.; York, P.; Ashraf, W.; and Hoare, M. Controlled particle formation of biological material using supercritical fluids. *6th Meeting on Supercritical Fluids - Chemistry and Materials*. Nottingham, UK, 1999.

Staniforth, J.N. Order out of chaos. *J. Pharm. Pharmacol*, 39:329-334, 1987.

Stewart, P.J. Particle interaction in pharmaceutical systems. *Pharm. Int.*, 7(6):146-149, 1986.

Subra, P., and Jestin, P. Powders elaboration in supercritical media: comparison with conventional routes. *Powder Technol.*, 103:2-9, 1999.

Subramaniam, B.; Rajewski, R.A.; and Snavely, K. Pharmaceutical processing with supercritical carbon dioxide. *J. Pharm. Sci.*, 86(8):885-890, 1997.

Tabor, D. A simple theory of static and dynamic hardness. *Proc. Roy. Soc. A*, 192:247-274, 1948.

Tabor, D., and Winterton, R.H.S. The direct measurement of normal and retarded van der Waals forces. *Proc. Roy. Soc. London*, A312:435-450, 1969.

Tabor, D. Surface forces and surface interactions. *J. colloid Interface Sci.*, 58(1):2-13, 1977.

References

Tai, C.Y., and Cheng, C.S. Supersaturation and crystal growth in gas anti-solvent crystallization. *J. Cryst. Growth*, 183:622-628, 1998.

Timoshenko, S.P., and Goodier, J.N. *Theory of Elasticity*. Engineering Societies Monographs. Singapore: McGraw-Hill Book Co, 1970.

Tom, J.W., and Debenedetti, P.G. Particle formation with supercritical fluids - a review. *J. Aerosol Sci.*, 22(5):555-584, 1991.

Tservistas, M.; Levy, M.S.; Lo-Yim, M.Y.A.; O'Kennedy, R.D.; York, P.; Humphrey, G.O.; and Hoare, M. The formation of plasmid DNA loaded pharmaceutical powders using supercritical fluid technology. *Biotechnol. Bioeng.*, 72(1):12-18, 2001.

Vansteenkiste, S.O.; Davies, M.C.; Roberts, C.J.; Tendler, S.J.B.; and Williams, P.M. Scanning probe microscopy of biomedical interfaces. *Prog. Surf. Sci.*, 57(2):95-136, 1998.

Vickerman, J.C. *Surface Analysis - The Principal Techniques*. Chichester: John Wiley & Sons Ltd, 1997.

Vickerman, J.C., and Briggs, D. *Tof-SIMS: Surface Analysis by mass Spectrometry*. Chichester: IM Publications and Surfaces Spectra Limited, 2001.

Villarrubia, J.S. Algorithms for scanned probe microscope image simulation, surface reconstruction, and tip estimation. *J. Nat. Inst. Stand. Technol.*, 102(4):425-454, 1997.

Walker, R., and Edwards, C. *Clinical Pharmacy and Therapeutics*. Edinburgh: Churchill livingstone, 1999.

Walls, J.M., ed. *Methods of Surface Analysis: Techniques and Applications*. Cambridge: Cambridge University Press, 1988.

Winters, M.A.; Knutson, B.L.; Debenedetti, P.G.; Sparks, H.G.; Przybycien, T.M.; Stevenson, C.L.; and Prestrelski, S.J. Precipitation of proteins in supercritical carbon dioxide. *J. Pharm. Sci.*, 85(6):586-594, 1996.

Xu, L.; Lio, A.; Hu, J.; Ogletree, D.F.; and Salmeron, M. Wetting and capillary phenomena of water on mica. *J. Phys. Chem. B*, 102:540-548, 1998.

Yeo, S.D.; Lim, G.B.; Debenedetti, P.G.; and Bernstein, H. Formation of microparticulate protein powders using a supercritical fluid antisolvent. *Biotechnol. Bioeng.*, 41:341-346, 1993.

Yip, C.M., and Ward, M.D. Atomic Force Microscopy of Insulin Single Crystals: Direct Visualization of Molecules and Crystal Growth. *Biophys. J.*, 71(August):1071-1078, 1996.

References

York, P.; Hanna, M.; Shekunov, B.Y.; and Humphreys, G.O. Microfine particle formation by SEDS (solution enhanced dispersion by supercritical fluids): scale up by design. *Respiratory Drug Delivery VI*. Hilton Head, South Carolina, USA: Interpharm Press Inc, 1998. pp. 169-175.

York, P. Strategies for particle design using supercritical fluid technologies. *PSTT*, 2(11):430-440, 1999.

York, P. Supercritical fluids ease drug delivery. *Manuf. Chem.*, June:26-29, 2000.

Young, P.M., Price, R., Tobyn, M.J., Buttrum, M., Dey, F. Investigation into the effect of humidity on drug-drug interactions using the atomic force microscope. *J. Pharm. Sci.*, 92(4):815-822.

Yu, L.X.; Furness, M.S.; Raw, A.; Outlaw, K.P.W.; Nashed, N.E.; Ramos, E.; Miller, S.P.F.; Adams, R.C.; Fang, F.; Patel, R.M.; Holcombe, F.O.; Chiu, Y.; and Hussain, A.S. Scientific considerations of pharmaceutical solid polymorphism in abbreviated new drug applications. *Pharm. Res.*, 20(4):531-536, 2003.

Zeng, X.M.; Martin, G.P.; and Marriott, C. *Particulate Interaction in Dry Powder Formulations for Inhalation*. London: Taylor & Francis, 2001.

Zimon, A.D. *Adhesion of Dust and Powder*. New York: Consultants Bureau, 1982.

Acknowledgements

I would like to thank all of my supervisors: Stephanie Allen, Martyn Davies, Clive Roberts, Saul Tendler and Phil Williams, particularly Clive for all of his input and assistance in reading my work. I would also like to thank Caroline German at Nektar for all of her help, and the BBSRC and Nektar for funding.

I also wish to acknowledge all those in the LBSA who have supported me during my studies, and in particular Roman for all of his efforts in the design and manufacture of the humidity control chamber, and Chen for his continued assistance and input in resolving the many difficulties I encountered with the AFM's. I would also like to thank Kim in the SSL for all of her help, particularly in reviewing and commenting on my work.

Finally, I would like to express my deepest gratitude to my mum, dad (whose park bench privileges will be replaced with the inheritance powders if he fails to reciprocate this acknowledgement in his next book), my sister Caroline and finally my friends Alison, Nisha and Malcolm, all of whom I am indebted to for their continual support through my undergraduate, pre-registration and postgraduate studies – Были бы кости, а мясо нарастёт.

Publications

Hooton, J.C.; German, C.S.; Allen, S.; Davies, M.C.; Roberts, C.J.; Tendler, S.J.B.; and Williams, P.M. Characterization of Particle Interactions by Atomic Force Microscopy: Effect of Contact Area. *Pharm. Res.*, 20(3):508-514, 2003.

Hooton, J.C.; German, C.S.; Allen, S.; Davies, M.C.; Roberts, C.J.; Tendler, S.J.B.; and Williams, P.M. The Effect of Contact Geometry and Surface Chemistry on the Adhesion of Pharmaceutical Particles. To be submitted to *Pharm. Res.*
